Power Generation from Solar Pond Using Thermoelectric Generators

A thesis submitted in fulfilment of the requirements for the degree of Doctor of Philosophy

Baljit Singh Bhathal Singh

M.Sc. Mechanical Engineering

B.Eng. (Hons) Mechanical Engineering

School of Aerospace Mechanical and Manufacturing Engineering

College of Science Engineering and Health

RMIT University

February 2015

Declaration

I certify that except where due acknowledgement has been made, the work is that of the author alone; the work has not been submitted previously, in whole or in part, to qualify for any other academic award; the content of the thesis/project is the result of work which has been carried out since the official commencement date of the approved research program; any editorial work, paid or unpaid, carried out by a third party is acknowledged; and, ethics procedures and guidelines have been followed.

Baljit Singh Bhathal Singh

25 /02/ 2015

Acknowledgements

I would like to express my heartfelt gratitude to my primary supervisor Professor Aliakbar Akbarzadeh for his guidance, support, and expertise throughout my research work. He has instilled professionalism and core values in me. Despite his hectic and busy time schedule, the guidance provided to me will be cherished forever.

Sincere thanks to my second supervisor, Dr. Abhijit Date for his endless encouragements and support for the experimental work and as well as helping in critically review my writing.

Special thanks all my colleagues from the Conservation and Renewable Energy (Energy-CARE) group for their advice, help and helping me to keep things in perspective. All the social events we organised together helped the much needed escape the study routines.

I would like to also thank the technical support I received from the SAMME workshop staff. It would have been impossible to complete my studies without your input and valuable ideas. Thank you to Don Savvides, Patrick Wilkins, David Goodie, Eliecer Bonilla and others for their invaluable advice and support.

Special thanks to University Technology MARA, Malaysia and Education Ministry of Malaysia (KPT) for providing scholarship for study at RMIT University.

Finally, I must express my special gratitude to my wife, Wandeep Kaur for her support given to me and her willingness to proof read pages of technical writings without any complains and expectations. Thank you for your support, encouragements, understanding and patience throughout my study. I would also like to express my thanks to my parents, in-laws, siblings and friends for their encouragements and well wishes.

Abstract

Renewable energy is becoming an important source of energy due to the rise in crude oil prices and the increase in greenhouse effects due to burning of fossil fuels. With only finite source of fossil fuel and exponential increase in the demand of power because of increase in human population, power generation from renewable energy promises a sustainable future for the mankind. Solar energy can be harnessed to meet our energy needs for a sustainable future. Currently, solar thermal technologies convert energy from the sun into useful thermal energy. Solar energy is intermittent in nature and most solar thermal technologies require separate collectors and storage systems. This makes them expensive to operate. Furthermore, power generation from low grade heat is currently restricted to vapour compression cycles with low reliability and high maintenance cost. There is a need to explore low cost integrated solar thermal collector and storage system and an alternative technology to convert this low grade heat into electricity.

A salinity gradient solar pond is a low-cost solar collector with long term thermal storage capability. It utilizes a large body of saline water with increasing density gradient from top to bottom that absorb solar radiation and stores the thermal energy. The solar pond technology has been used for power generation and low-temperature process heat applications respectively. Solar ponds have been simple and low cost solar energy system for a relatively longer period of time and very stable with the intermittent supply of solar energy.

A thermoelectric generator (TEG) has the advantage that it can operate from a low grade heat source such as waste heat energy. Heat is supplied to the hot side of the thermoelectric cell while the other end is maintained at a lower temperature by a heat sink. As a result of the temperature difference, Seebeck voltage is generated that result in current flow through an external load resistance. There are no moving components in the TEG and this will lead to a reliable, quiet and maintenance free operation for power generation. Although Organic Rankine Cycles (ORC) engine is currently used to generate electricity from solar pond using low grade heat, it still requires a certain threshold in the temperature difference of the system. The TEGs however works without any temperature difference threshold needed for its operation. In other words, TEGs can produce power even at low temperature differences and can be fully passive.

The main aims of this project are to develop a system for conversion of low grade heat (< 100 ˚C) to work and effective utilisation of low driving temperature differences from low grade heat for heat to work conversion. This thesis examines the potential of power generation from solar pond using TEGs with innovative new designs. Theoretical analysis was developed to investigate the performance of TEGs with low grade heat input. Potential of solar pond as an integral collector and storage system is explained in detail with the maintenance and operation requirements. Simple experimental tests performed shows that TEGs can replace ORC engines for low grade heat power generation with higher reliability and lower maintenance. The thesis also explains the systematic procedure of design and manufacturing of TEG heat exchangers. Experimental test rigs and instrumentations used for testing the prototypes are explained in detail. The effect of thermal adhesives on power output from TEGs without any mechanical fixtures presented in the thesis shows remarkable potential for large scale TEG heat exchangers. The effect of thermal variation on the performance of TEGs are also studied and highlighted in the thesis.

This thesis presents an innovative method to convert low grade heat from solar pond using TEGs. The proposed systems has been developed for electricity generation and has the potential to provide continues electricity without disruption from solar energy at low cost and high reliability.

Table of Contents

Chapter 2 Literature Review

List of Figures

List of Tables

Nomenclature

A	Heat transfer area (m^2)
A_c	Cross sectional area (m^2)
A_s	Surface area (m^2)
A_{TEG}	Area of thermo element (mm^2)
C	Circumference (m)
C_c	Concentration of the salt in storage zone (kg/m^3)
c_p	Specific heat capacity of the working fluid (J/kg K)
C_s	Humid heat capacity of air (J/ kg ˚C)
C_y	Final concentration of the salt(m^3)
D	Diameter (m)
D_h	Hydraulic diameter (m)
dP	Difference in pressure (Pa)
dS	Difference in salt concentration value for a given depth (kg/m^3)
dz	Difference in the vertical distance from the bottom of solar pond (m)
f	Friction factor
Fr	Froude number
f_ρ	Reflection loss adjustment factor
Gr	Grashoff number
h_c	Convective heat transfer coefficient (W/m^2K)
h_{conv}	Heat transfer coefficient (W/m^2K)

H_I	Solar radiation in available at a depth in the pond (W/m^2)
h_L	Head loss (m)
$h_{L,minor}$	Minor head loss (m)
I	Electrical current (A)
i	Fluid enthalpy (J)
I_{mpp}	Maximum power point current (A)
I_{out}	Output current TEG (A)
I_{sc}	Short circuit current (A)
I_{total}	Total current (A)
K	Calibration factor
k_G	Thermal conductivity material of the ground below the surface of solar pond (W/mK)
K_L	Loss coefficient
K_n	Thermal conductivity of N type TEG leg (W/mK)
K_p	Thermal conductivity of P type TEG leg (W/mK)
k_s	Molecular diffusivity (m^2/s)
L	Gradient zone thickness (m)
L_c	Thickness of solder/contact in module (m)
L_v	Latent heat of evaporation of water (J/kg)
$\dot{m}$	Mass flow rate (kg/s)
n	Contact parameter
N	Number of thermo elements per module

Nu	Nusselt number
P	Perimeter (m)
P_1	Vapour pressure of water at the surface temperature (Pa)
P_a	Partial pressure of water vapour in the ambient air (Pa)
P_{in}	Power input (W)
P_{loss}	Power losses (W)
P_{net}	Net power output (W)
Pr	Prandtl number
P_{TEG}	Electrical power generated by TEG (W)
Q_c	Heat removed (W)
$Q_{conv-loss}$	Heat loss to the ambient environment due to convection (W)
$Q_{evap-loss}$	Exaporative heat loss from the solar pond (W)
Q_h	Heat supplied (W)
Q_{hlg}	Heat loss to the ground/soil (W)
Q_{HR}	Total heat removal from the solar pond (W)
Q_I	Amount of solar radiation reaching the storage zone (W)
Q_{in}	Energy input (J)
Q_{LCZ}	Heat storage in storage zone (W)
$Q_{peltier}$	Heating/cooling of Peltier cell (J)
$Q_{rad-loss}$	Radiative heat loss from the solar pond (W)
R	Electrical resistance (Ω)

r’	Dimensionless contact parameter
R, r	radius (m)
R’	Capacity ratio
Ra	Raleigh number
$R_{ceramic}$	TEG ceramic plate resistance (Ω)
R_{conv}	Convective thermal resistance (˚C/W)
R_{cu}	TEG copper resistance (Ω)
Re	Reynold number
RH	Relative humidity (%)
$R_{inner\ pipe}$	Pipe thermal resistance (˚C/W)
R_{int}	Internal resistance TEG (Ω)
R_L	Load resistance (Ω)
R_n	TEG N-type element resistance (Ω)
R_o	Internal resistance TEG (Ω)
R_p	TEG P-type element resistance (Ω)
R_{sol}	TEG solder resistance (Ω)
R_{TEG}	Thermal resistance of TEG (˚C/W)
R_{th}	Thermal resistance (˚C/W)
S	Salt concentration (kg/m^3)
S, α_s	Seebeck coefficient (V/K)
S_i	Normalised spectrum distribution function of the incident solar radiation for wavelength band i

S_o	Salt concentration of the fluid at reference temperature (K)
s_T	Soret coefficient
T_A	Ambient temperature (°C)
T_c	Cold junction temperature (°C)
T_G	Solar pond ground temperature (°C)
T_h	Hot junction temperature (°C)
T_{in}	Temperature in (°C)
T_{inwf}	Inlet temperature of the working fluid (°C)
T_{LCZ}	Solar pond storage zone temperature (°C)
T_{out}	Temperature out (°C)
T_{sky}	Sky temperature (°C)
T_{UCZ}	Solar pond upper convective zone temperature (°C)
U	Overall heat transfer coefficients (W/m^2 K)
V	Voltage (V)
V_a	Avearge monthly wind speed (m/s)
V_{avg}	Average velocity (m/s)
V_e	Volume of water loss by evaporation (m^3)
V_f	Volume of water supplied for the flushing (m^3)
V_{mpp}	Maximum power point voltage (V)
V_{ocv}	Open circuit voltage (V)
V_{out}	Output voltage TEG (V)

V_{total}	Total voltage (V)
V_b	Volume of brine above the diffuser (m^3)
V_{flow}	Volume flow rate (m^3/s)
W_{pump}	Pumping power (W)
x_G	Ground thickness (m)
y_d	Starting height for gradient establishment (m)
y_s	Position of the diffuser at height (m)
z	Light path (m)
ZT	Figure of merit
α	coefficient of thermal expansion of water (K^{-1})
β	coefficient of expansion of water due to salinity (m^3/kg)
α_n	Seebeck coefficient of N type TEG leg (V/K)
α_p	Seebeck coefficient of P type TEG leg (V/K)
δ	Angle of declination
$\delta(\lambda)$	Characteristic wavelength attenuation length (m)
ΔQ	Change in heat energy (J)
ΔT	Tempearture difference (˚C)
ΔT_{lmtd}	Log mean temperature differences (˚C)
ΔT_m	Mean temperature differences (˚C)
δ_i	Characteristic attenuation length for wavelength band i
δ_{total}	Total uncertainty

ΔV	Potential Difference (V)
Δx	Change in length (m)
ε	Surface roughness
ϵ_w	Emissivity of water
$\eta_{max\ TEG}$	Maximum TEG efficiency (%)
η_{pump}	Efficiency of pump (%)
η_{sp}	Efficiency of solar pond
Θ_r	Reflected angle
λ	Wavelength (m)
μ	Median
Π	Peltier coefficient
ρ	Density of the fluid (kg/m^3)
ρ	Electrical resistivity of thermo element material (Ω cm)
ρ_r	Reflectance
σ'	Standard deviation
σ	Stefan Boltzmann’s constant (W/m^{2}K^4)
τ_T	Thomson coefficient (V/K)
τ_l	Transmission of light in water
τ_s	Fraction of the incident radiation penetrating the surface
τ_w	Wall shear stress (Pa)
τ'	Average wall shear stress (Pa)

φ	Angle of latitude
ω	Hour angle

List of Acronyms

DC	Direct current
FNU	Formazin Nephelometric Units
HDPE	High density polyethylene
HEX	Heat exchanger
LCZ	Lower convective zone
LED	Light emitting diode
MEF	Multi effect distillation
MgCl	Magnesium Chloride
MPPT	Maximum Power Point Tracker
MSF	Multi flash desalination
NaCl	Sodium Chloride
NCZ	Non Convective Zone
ORC	Organic Rankine cycle
ppm	Parts per million
PV	Photovoltaic
PVC	Poly vinyl chloride
SGSP	Salinity Gradient Solar Pond
TEG	Thermoelectric generator
TDS	Total Dissolved Salt
UCZ	Upper Convective Zone

List of Publications

Journals

1. **Singh, B.**, Varthani, J., Remeli, M.F., Tan, L.P., Date, A. and Akbarzadeh, A. (2013). "Experimental Investigation of Power Generation from Salinity Gradient Solar Pond Using Thermoelectric Generators for Renewable Energy Application." Journal of Applied Mechanics and Materials 393: 809-814.

2. **Singh, B.,** Ding, L.C., Remeli, M.F., Oberoi, A., Date, A. and Akbarzadeh, A.(2015) "Experimental Investigation on Effect of Adhesive on The Performance of Thermoelectric Generator." *Journal of Electronic Materials*.

3. **Singh, B.**, Gomes, J., Tan, L.P., Date, A. and Akbarzadeh, A (2012). "Small Scale Power Generation Using Low Grade Heat from Solar Pond." *Procedia Engineering* 49: 50 – 56.

4. **Singh, B.,** Tan, L.P., Date, A. and Akbarzadeh, A. (2014). "The Effects of Temperature Difference and Compressive Force to the Electrical Characterization of Peltier Cell for Artificial Concentrated Solar Power Thermoelectric Application." *Journal of Mechanical Engineering* 11: 15-30.

5. Orr, B., **Singh, B.,** Tan, L.P. and Akbarzadeh, A. (2014). "Electricity generation from an exhaust heat recovery system utilizing thermoelectric cells and heat pipes." *Applied Thermal Engineering* 73: 588-597.

6. Remeli, M.F., Date, A.,Tan, L.P., **Singh, B.** and Akbarzadeh, A. (2015). "Simultaneous power generation and heat recovery using a heat pipe assisted thermoelectric generator system" *Energy Conversion and Management* 91:110-119.

International Conferences

1. **Singh, B**., Remeli, M. F., Pedemont, A., Oberoi, A., Date, A. and Akbarzadeh, A. (2014). “Thermal Heat Storage Gain of Salinity Gradient Solar Pond using Evacuated Tube Solar Collectors”. *International Conference On Global Sustainability And Chemical Engineering (ICGSE), Kuala Lumpur, Malaysia*

2. **Singh, B.,** Remeli, M. F., Poong, Z.K., Oberoi, A., Date, A. and Akbarzadeh, A. (2014). “Design Fabrication of a Control Flow Mechanism for Flushing Fresh Water System for RMIT University Solar Pond.” *Conference on Humanity, Science and Engineering (CHUSER 2014), Kuala Lumpur, Malaysia.*

3. **Singh, B.,** Orr, B., Remeli, M.F., Tan, L.P., Date, A. and Akbarzadeh, A (2013). “Power Generation by Thermoelectric Cells With Heat Pipes Using Engine Exhaust Gas.” *11th International Heat Pipe Symposium (11th IHPS), Beijing, China*.

4. **Singh, B.,** Tan, L.P., Date, A. and Akbarzadeh, A.(2012). “Power Generation from Salinity Gradient Solar Pond Using Thermoelectric Generators for Renewable Energy Application.” *Power and Engineering Conference (PECON 2012), Kota Kinabalu, Malaysia: 89-92.*

5. **Singh, B.,** Remeli, M.F., Oberoi, A., Tan, L.P., Date, A. and Akbarzadeh, A.(2014). “Electrical Power Generation from Low Grade Heat Of Salinity Gradient Solar Pond Using Thermoelectric Generators.” *Proceedings of the 52nd Annual Conference, Australian Solar Energy Society (Australian Solar Council) Melbourne May 2014 ISBN: 948-0-646-92219-5.*

6. Ding, L.C., **Singh, B.,** Remeli, M. F., Oberoi, A., Date, A. and Akbarzadeh, A. (2015). “Prospects of Power Generation from Geothermal Energy Using Thermoelectric Modules.” *Proceedings World Geothermal Congress 2015, Melbourne, Australia.*

7. Remeli, M.F., **Singh, B.,** Tan, L.P., Date, A. and Akbarzadeh, A (2013). “Combined Thermosyphon Thermoelectric Model (TTM) for Waste Heat Recovery And Power Generation.” *11th International Heat Pipe Symposium (11th IHPS), Beijing, China.*

8. Tan, L.P., **Singh, B.,** Date, A. and Akbarzadeh, A. (2012). “Sustainable Thermoelectric Power System Using Concentrated Solar Energy and Latent Heat Storage.” *Power and Engineering Conference (PECON 2012), Kota Kinabalu, Malaysia: 105-109.*

9. Remeli, M.F., Date, A., **Singh, B.,** Tan, L.P. and Akbarzadeh, A (2014). “Combined Thermosyphon Thermoelectric Model (TTM) for Waste Heat Recovery And Power Generation.” *International Conference on Global Sustainability and Chemical Engineering (ICGSE), Kuala Lumpur, Malaysia.*

1.0 Introduction

1.1 Background and Significance

Renewable energy is becoming an important source of energy due to the rise in crude oil prices and increase in the greenhouse effects due to burning of fossil fuels. Most of our electricity is generated by fossil fuels. These types of fuels are non-renewable and also pollute the environment. With only finite source of fossil fuel and exponential increase in the demand of power due to increase in the human population, power generation from renewable energy promises a sustainable future for mankind. Figure 1.1 shows the global energy generation in 2014. From Figure 1.1, it is shown that 81 % of global energy generation was obtained from fossil fuels and only 19 % renewable energy sources were used for power generation purposes.

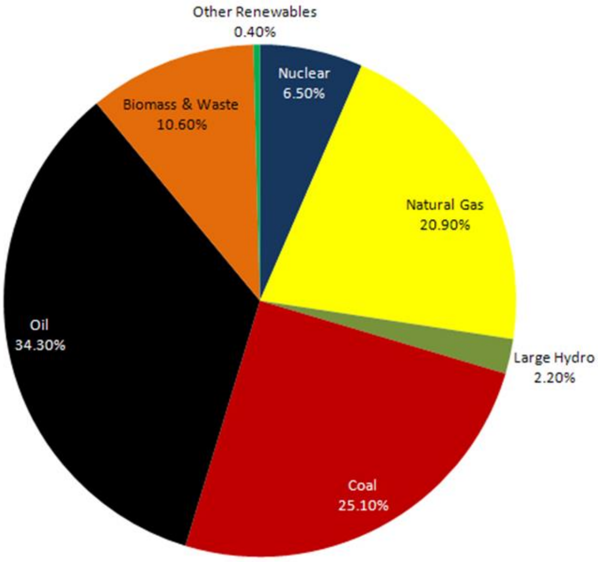

Figure 1.1 Global energy generations (http://www.worldenergyoutlook.org/ 2015)

Figure 1.2 shows the global carbon dioxide emissions from 1850 to 2030. It is projected that the carbon dioxide emissions are going to increase at an exponential rate in the future. This is due to burning of fossil fuels to meet our energy needs. Global warming is the result of carbon dioxide emission into the atmosphere mainly due to human activities. It is very important to reduce our reliance on fossil fuels to protect our planet for future generation. A more sustainable way to generate energy is by using renewable energy. Renewable energy sources have the potential to replace fossil fuel to meet our energy demands. Energy from the sun can be harnessed to fulfil our energy needs and at the same time reduce our reliance on fossil fuels.

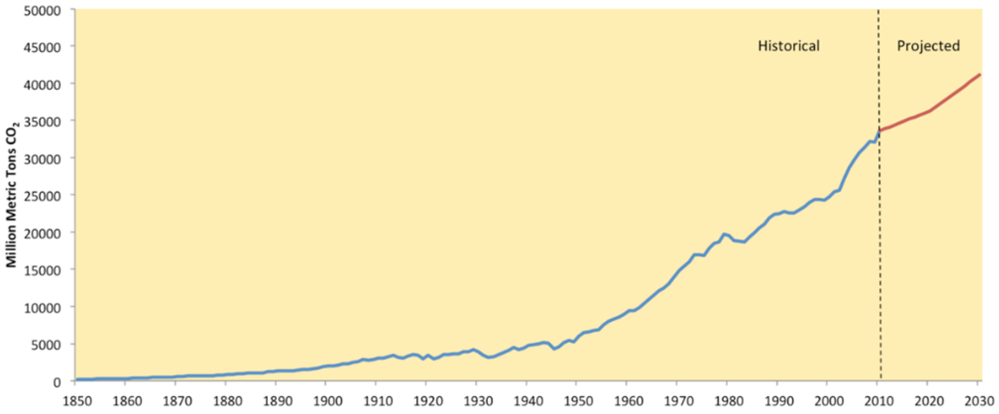

Figure 1.2 Carbon Dioxide Information Analysis Center, Oak Ridge National Laboratory (World Energy Outlook , 2012)

A salinity gradient solar pond is a low-cost solar collector with long term thermal storage capability. Solar ponds have been simple and low cost solar energy system for a relatively longer period of time and they can be an alternative to fossil fuel for generation of electricity. A thermoelectric generator (TEG) has the advantage that it can operate from a low grade heat source such as waste heat energy. Although Organic Rankine Cycles (ORC) engine is currently used to generate electricity from solar pond using low grade heat, it still requires a certain threshold in the temperature difference of the system. The TEGs however works without any temperature difference threshold needed for its operation and can be fully passive.

1.2 Solar Energy

Our current needs for electricity are mainly fulfilled by fossil fuels. Renewable energy sources can meet our energy demands by many folds. One of the major sources of renewable energy is the energy from the sun. Energy from the sun can be considered an infinite source of energy that will not deplete over time, when compared to fossil fuels. Furthermore, solar energy is non-polluting with no air and water pollution. Besides environmental benefits, using solar energy also creates economic, social, political and technological gain. Figure 1.3 shows renewable energy resources of the world. It is clearly shown in the figure that solar energy promises a sustainable future with enormous potential.

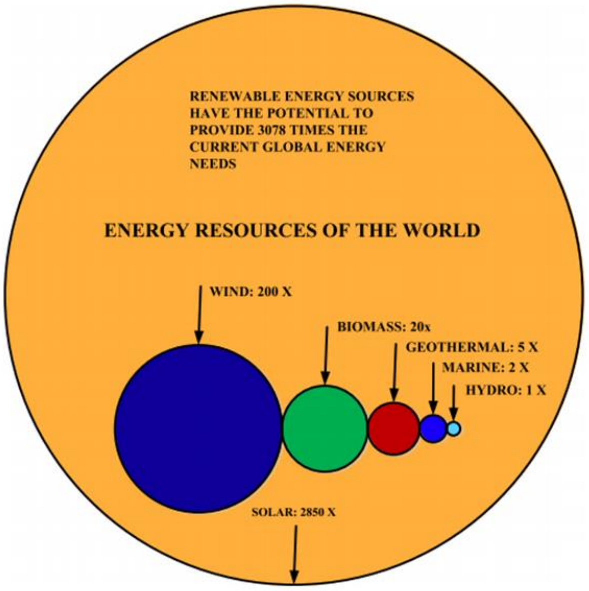

Figure 1.3 Renewable energy resources of the world (Ellaban et al., 2014)

Solar energy can be converted into heat. It can be collected at low temperature thermal heat (< 100 ºC) or at high temperature with concentrators. Solar thermal is the most economical alternative among the renewable energy systems (Mekhilef, 2011). Solar energy converted into thermal heat energy is generally used for heating air or water for domestic and commercial applications in the industries. High grade heat from concentrators is used for heat engine operations. One of the disadvantages of the current solar thermal technology is that it is not cost effective to compete with conventional heating systems. The reliability of these solar thermal systems depends on the availability of sunlight. In the absence of sunlight, these solar thermal systems will cease to operate. Besides that, these systems require a separate storage and collector systems.

One of the most widely used forms of low grade heat application for low cost operations is the solar pond technology (Swift et al., 1987). Solar pond can collect and store thermal energy from the sun at temperatures between 70˚C to 90˚C. Solar pond differs from other solar thermal systems where solar pond is an integrated collector and storage system. This makes solar pond an inexpensive and simple technology. Solar pond reliability is not affected even with a few cloudy days.

1.3 Solar Pond

The density of a body of fluid decreases with the increase in temperature. An ordinary pond will absorb sunlight incident on it and this will lead to heating of water at the bottom of the pond. The warmer fluid at the bottom will rise to the surface and the colder fluid will sink to the bottom as a result of the buoyancy effect. This phenomenon is called natural convection. The warm fluid loses heat to the environment by means of convection, radiation and evaporation. Due to the presence of this convection current in the body of fluid, it is impossible to retain heat in the body of fluid. The absorbed heat in the body of fluid is lost due to the continuous mixing caused by the convection current. A solar pond eliminates the heat loss caused by convection current with the help of an artificially created salinity-density gradient. This results in heat retention at the bottom of the pond and increase in temperature with time. Solar pond is a body of fluid with increasing salinity density gradient along its depth and bottom of the pond being fully saturated.

Solar pond consists of three zones as shown in figure 1.4. The top layer is the thinnest zone called Upper Convective Zone (UCZ). The density of the fluid solution is lowest in this zone. The middle layer of the solar pond is called Non-Convective Zone (NCZ). The salinity gradient in this zone varies linearly from the top to the bottom of NCZ. The presence of salinity gradient in NCZ suppresses the convection current in the solar pond. NCZ provides an insulating barrier for the solar pond to prevent heat loss from the bottom of the pond. As result of that, the temperature at the bottom of the pond can increase up to 90 ° C. The bottom zone of the solar pond is called Lower Convective Zone (LCZ). The salinity in this zone is highest and reaches the saturated level between 20 % -30 % depending on salt used to establish the salinity gradient. For a typical solar pond with a depth of 3 m, LCZ is between 1 m to 1.5 m thick, UCZ thickness is around 0.8 m to 1.5 m thick and the UCZ is normally not more than 0.3 m thick.

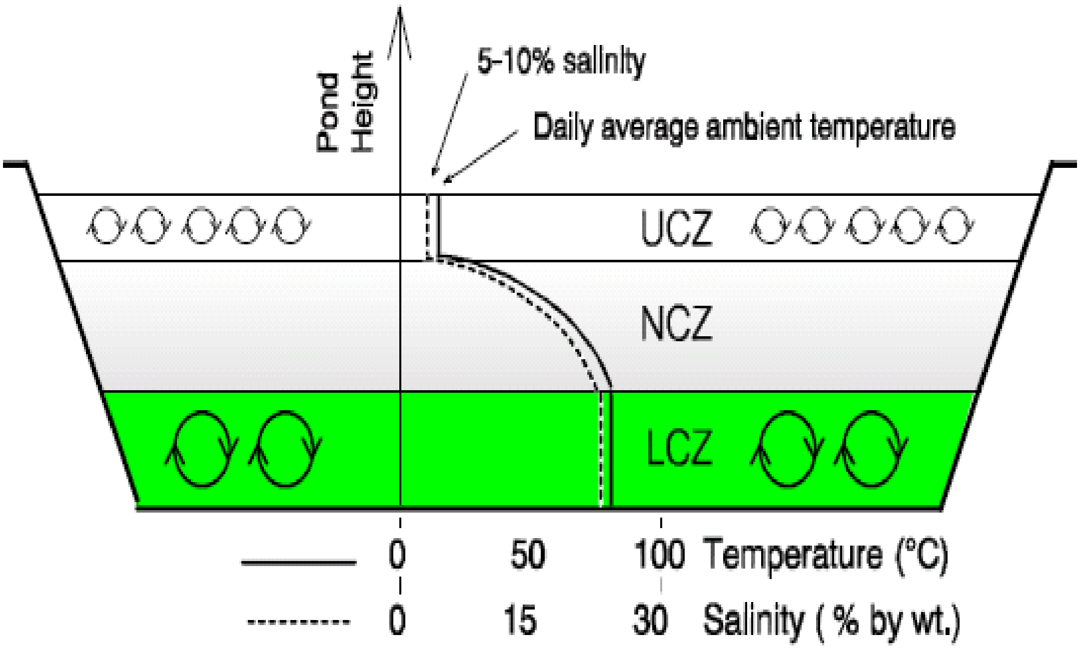

Figure 1.4 Schematic of salinity gradient solar pond (Leblanc et al., 2011)

Vapour heat engines currently dominates the power generation using heat energy. These systems use many moving parts to convert the heat energy obtained from combustion of fuel or waste heat. Many of the components in vapour heat engines move at very high speeds and incur dynamic forces that limit their operation in the long run. These systems often require lengthy maintenance and shut down service times. Additionally, the heat energy required for these systems must be made available at high temperatures (> 150˚C) as the working fluid is mostly in the form of steam. But, Thermoelectric Generator (TEG) based waste heat conversion system is much simpler compared to their conventional vapour power plants. TEGs based system do not require boiler, condenser, working fluid pump or turbine. It is purely a solid state device acting as compact heat exchanger (Singh, 2011). This build up makes TEG as a reliable and maintenance free device. Additionally, the operation of the TEG system is quiet, due to the absence of any moving parts in them. This makes TEG a new attraction for power generation from renewable energy where temperature gradients are available.

With a quarter of the population on this planet living without electricity, generating power from solar pond using TEG system promises a future to these people. In remote areas, where the electricity grid is not available and the sun shines year round, TEG with solar pond power generation system can be used to provide an alternative to other high cost power generation system (Singh, 2011). The energy of the sun is abundant and limitless and is more than enough to meet our current energy needs by manyfold. TEG system provides an attractive means of converting solar energy to electricity and can definitely help to connect the remote area to the grid. The relative simple, low cost and with almost zero maintenance promises TEG system to be a good source of power generation system from solar energy for remote areas.

TEG can convert electricity directly to DC electricity and have been used extensively worldwide for power generation for at least 40 years now (Rowe, 1995). Power generation based on the TEG system offers great advantage compared to photovoltaic (PV) system, in terms of cost. The cost for TEG system is as low as 750 to 1100 $/kWh, compared to the cost of PV system at 2500 to 5000 $/kWh (Agarwal and Markanda, 2012). This makes TEG based system a cheaper alternative to PV systems for power generation (Liu et al., 2014). Besides that, PV load factors are also low and lowest in winter, when the demand is highest. This makes the PV system operate at low performance. The proposed TEG systems with solar pond enable solar energy to be converted easily to DC electricity using TEGs. Solar pond also allows the storage of heat energy at a much lower cost compared to PV system. This stored heat can be converted to electricity using TEG and eliminates the use of batteries for electricity storage. Furthermore, as shown in Figure 1.5, thermoelectric based technologies shows high probability of success with high impact for successful applications when compared to some energy harvesting methods.

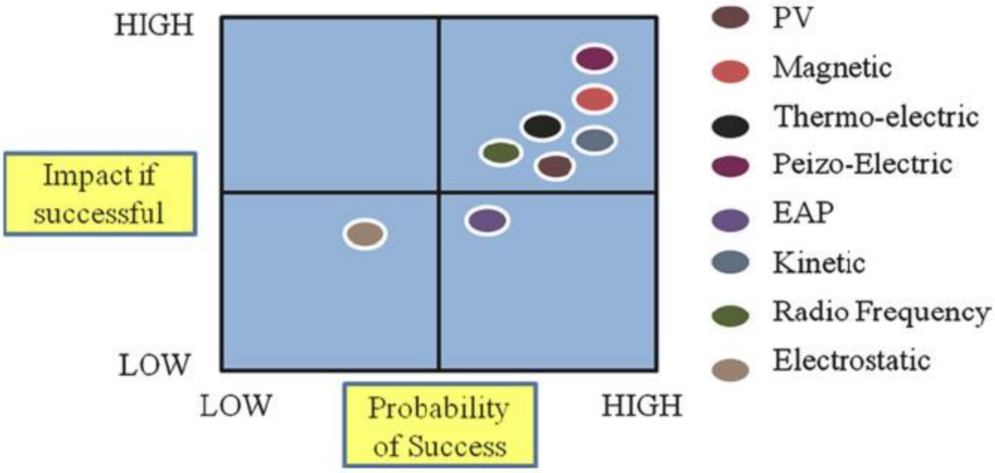

Figure 1.5 Frost &Sullivan’s opportunity analysis matrix of various micro energy harvesting (10 W – 100 kW) technologies (Vijay et al., 2013)

1.4 Problem Statement

Low grade heat power generation using Organic Rankine Cycle (ORC) engine requires certain threshold for operation. This limits the operating temperatures for such systems at low temperatures below the boiling point of organic fluid of ORC engine. Thermoelectric generators works even at low temperature applications and is most suited for low grade conversion for power generation when compared to ORC engine. Currently, solar thermal technologies convert energy from the sun into useful thermal energy. Solar energy is intermittent in nature and most solar thermal technologies require separate collectors and storage systems. This makes them expensive to operate. Furthermore, power generation from low grade heat is currently restricted to vapour compression cycles with low reliability and high maintenance cost. There is a need to explore low cost integrated solar thermal collector and storage system and an alternative technology to convert this low grade heat into electricity.

1.5 Objectives, Research Questions and Scope of Study

In this research, heat exchangers with thermoelectric generators utilising low grade heat of solar pond, was designed and tested, both indoor and outdoor environment. The main aim of this project is to develop a system for power generation from solar pond using thermoelectric generators.

The objectives of this research are,

I. To analyse the potential of solar pond as a source of low grade heat (source temperature < 100 °C) for power generation using TEG with natural and forced convection heating coupled with forced convection cooling.

II. To design and evaluate suitable TEG heat exchanger designs for very low driving temperature differences.

III. To investigate the effects on TEG performance due to uneven temperature distribution.

IV. To investigate the effective strategy of constructing TEG heat exchanger for corrosive salty environment.

Before achieving the project aims, the following research questions are needed to be addressed:

I. What is the maximum temperature difference available in a solar pond in terms of low grade heat for potential electrical power generation from TEGs?
II. How the geometric design will affect the heat transfer of TEG heat exchanger for low driving temperature differences?
III. What are the effects on TEG performance due to uneven temperature distribution?
IV. What are the prospects of using non-mechanical fixtures for effective TEG heat exchanger design to be used with very low driving temperature differences?

This project provides a new method to convert the low grade heat energy from solar pond into electricity for possible use in industry or at remote areas that are not connected to electric grid. Power is generated using renewable source of energy. TEGs are reliable to be used for long term applications and they are quiet and maintenance free as they operate without any moving parts. The system is also capable of generating power even with low temperature differences across the TEG. This research embarks on providing a clean energy for a more sustainable future with minimal or no reliance on fossil fuel. The available low grade heat (<100˚C) in the solar pond will be sufficient enough to power the TEGs while the cooling for the heat sink section of the TEG side can be maintained by siphoning action of the surface water, or maintained by an external pump. The system developed in this work acts like a heat engine, but without any moving parts. This increases the reliability of the system and also provides a low maintenance and noise free operation. As the solar pond acts as heat storage, the developed system can also be operated at night for power generation for remote areas and will continue to operate even at low temperature differences.

1.6 Methodology

1.6.1 Literature Review

The proposed system is considered a new approach in which no similar approach has been reported and published in journals, conferences, thesis and books. Extensive literatures are required to survey on solar pond, TEGs, power generation from TEGs and solar ponds for gaining through understanding.

1.6.2 Development of Computer Model and Experiment of Test Rigs

A computer model was developed to predict the performance and output of the system before embarking on the actual experimental setup.

A small scale testing unit with 16 TEGs will be developed in the Renewable energy Lab at RMIT University to understand the performance of the TEGs for various temperatures. The thermal and electrical characteristics were studied in the lab before embarking on a full scale model with hundreds of TEGs in the solar pond.

1.6.3 Data Analysis

The experimental results recorded will be imported into Microsoft Excel spreadsheet for graphing the results. The formulas used to calculate the heat transfer and flow in the heat exchanger were used to obtain parameters for gap analysis of the heat exchanger. This was then compared in graphical form to obtain the theoretical results for optimum heat exchanger design. Excel spreadsheet programming allows for quick data analysis with good graphical output. Graphical presentation is a good tool for data analysis and trend observation of parameters such as temperatures, powers and pressures. To ensure the reliability of the experimental results, it must be compared with the numerically calculated results to determine the level of accuracy between experiments and numerical models.

1.6.4 Thesis Preparation

A summary of the project significance, research outcomes and methodologies for answering the research questions of the project. Possible recommendation for future works is required to be illustrated for continuation on the same research work or for other prospective researchers who wish to investigate in the same research field.

1.7 Structure of the Thesis

The thesis is divided into seven chapters including the introduction, and the remaining chapters are as follows:

Chapter 2 describes the available literature for solar thermal systems. Solar pond technology and thermoelectricity literature was reviewed. The potential of thermoelectric generators to generate electricity from low grade heat was presented and discussed in this chapter.

Chapter 3 describes the concept of solar pond technology. The chapter includes design criteria, site selection, construction methods and lining installation, establishing a salinity gradient and maintaining pond stability. The chapter also addresses routine maintenances including salt management, clarity maintenance, wave suppression and manual monitoring of salinity, temperature and pH level. Augmentation and automation design and application is also discussed.

Chapter 4 presents a testing of thermoelectric generators for power production using a simulated heat source. This will then be used as benchmark for computer programming for design and construction of heat exchangers for thermoelectric power generation from solar pond.

Chapter 5 presents an analysis of a natural convection and forced convection heating applied to a heat exchanger for power generation from solar pond using thermoelectric generators. This chapter will focus analysis, design and fabrication of power generation using passive and active method to induce the cooling and heating flow rate in the heat exchanger for temperature difference required for the power generation from solar pond.

Chapter 6 presents experimental procedure and results for TEG heat exchanger for power generation using low grade heat from solar pond. A 12V pump used to deliver the hot fluid needed for the power generation from TEG. Flow for the hot and cold fluid at forced convection used to maximise the heat transfer from both the fluid in a counter flow arrangement.

Chapter 7 concludes the analysis of the proposed power generation from low grade heat of solar pond using thermoelectric generators. In addition, some recommendations for future work and suggested research directions are presented.

2.0 Literature Review

2.1 History of Solar Energy

Solar energy is the earliest and the oldest form of renewable energy used by humans. Humans have been using solar energy as early as 8000 BC. It was mainly used for food and animal skin drying. The ancient civilizations of Greeks, Indians, Chinese, Egyptians and American-Indians worshipped the sun as their gods (Kapur, 1964). These ancient civilizations used the energy from the sun for various applications. Before the Renaissance period in Europe, the main application of solar energy was focussed on water pumping using air heated by solar energy (Dickinson & Cheresiminoff, 1980). After the 18th century, solar energy was converted into heat to power the steam engines (Goswami et al., 1999). In the late 19th century, some researchers used low boiling-point fluid such as sulphur dioxide and aqueous ammonia solution for solar powered pump in a closed loop flat-plate collectors to drive a steam engine. Concentrated solar energy was also utilised for melting metals. Temperatures as high as 3500 ^{0}C were recorded by Russian scientist at the end of 19th century (Boer, 2005).

Most of the technology developed using the solar energy during the industrial revolution was mainly for demonstration purposes or experimental devices used for proof of concept. It was not applied extensively in the industry due to the problem of unpredictable and cyclic availability of solar energy.

In the early twentieth century, the development of solar energy was mainly concentrated in the United States. The technology used to concentrate the solar energy was much more efficient compared to earlier predecessors. This lead to many solar energy devices with efficiency ranging 50-85 % developed and patented at that time (Robinson, 1956). The clever use of coating materials, high conductivity metal like copper coupled with heat pipes, evacuated tubes solar collectors, and the development of Fresnel lenses together with the development of electronics for sun tracking made solar energy once more and attractive source of renewable energy. The developments of solar technology in the twentieth century made it a strong contender to replace the fossil fuel in terms of power generation, and not just being developed for “curiosity” purposes (Butti & Perlin, 1977). Although fossil fuels can meet our energy needs for another four generations, but it will be at the expense of very high environmental costs. Solar energy promises a sustainable future for all. Furthermore, with continues research and developments, we can ensure that all our energy needs can be fulfilled by solar energy alone, and reduce or eliminate our reliance on fossil fuels.

2.2 Solar Thermal Power Generation

The main sources of power generation today are fossil fuel, hydro power, wind power, tidal power, solar power and nuclear power (Rivera and Cruz, 2009). Fossil fuel pollutes and contributes to global warming. Solar power generation promises a more sustainable and promising future. Solar thermal power generations are making a comeback as the industry is developing renewed activity and interest. The classification of solar thermal power generation is shown in Figure 2.1.

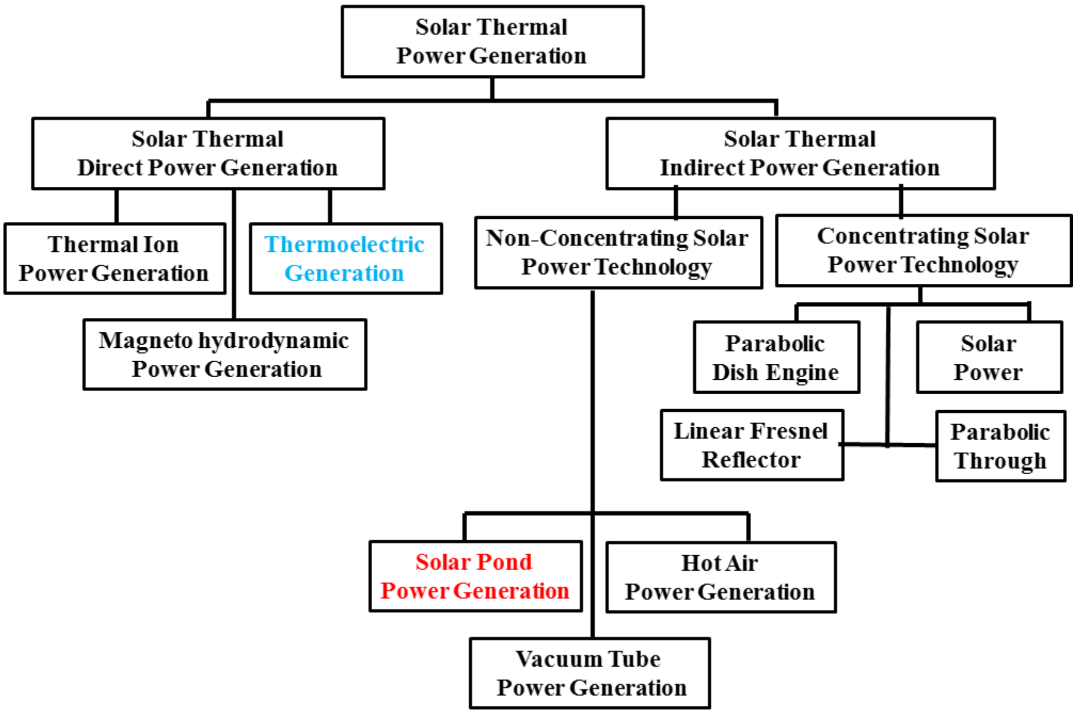

Figure 2.1 Classification of solar thermal power generation (Zai et al., 2011)

Solar pond power generation is classified as non-concentrating solar power energy. It uses indirect solar energy converted into thermal energy. Shallow solar pond has been used to run engine to pump water as early as 1909 where solar energy was transferred to a storage tank as sensible heat (Mills, 2001). Solar pond is the only solar thermal power generation system with integrated thermal and storage system. This makes solar pond a competitive system compared to other solar thermal power generation system in terms of economic and large scale application (Fiorenza, 2006). The main aim of this project was to develop new method to combine the solar pond technology with thermoelectric power generation. The next section explains in detail on solar ponds and thermoelectricity.

2.3 Solar Pond

2.3.1 History of Solar Pond

Salt-water solar ponds are the most common form of solar pond. The first solar pond was discovered at the beginning of 20th century in Eastern Europe. Medve Lake in Transylvania ($42^{0}44^{'}$N, $28^{0}45^{'}$E) recorded a maximum temperature of up to 70 ˚C at a depth of 1.32 m in summer and a minimum temperature at 26˚C during early spring (Hull et al., 1989). It was observed that the high temperatures in the pond were due to the presence of natural salinity gradient in the lake. A shallow lake in Washington State recorded temperatures up to 50˚C at a depth of 2 m. In Antarctica region, direct solar radiation resulted in a temperature difference of 45˚C for Lake Bonney and Lake Vanda at a depth of 60 m. Other natural solar lakes in Castle Lake, California and Eliat, Israel were reported with a temperature difference of 20 ˚C between the surface and a depth of 5 m (Wilson and Nielson 1962).

From the observations above, it was found that the salinity gradient plays an important role in storing thermal energy collected from solar radiation. Dr Rudolph Bloch in Israel first raised the idea hinted by Kalecsinsky for solar energy storage system using artificial solar ponds (Kalecsinsky, 1902). This was further investigated by Rabl and Nielsen from USA in 1974 with the interest of energy storage and space heating using solar ponds.

2.3.2 Solar Pond Classifications

Figure 2.2 shows the types of solar ponds studied since the early 1900s. All solar ponds can be divided into non-convecting, convecting and augmented solar pond. In the non convecting type solar pond, various techniques are used to suppress the natural convection in solar pond with salt stabilised salinity gradient, membranes, salt basins, viscosity and gel stabilised.

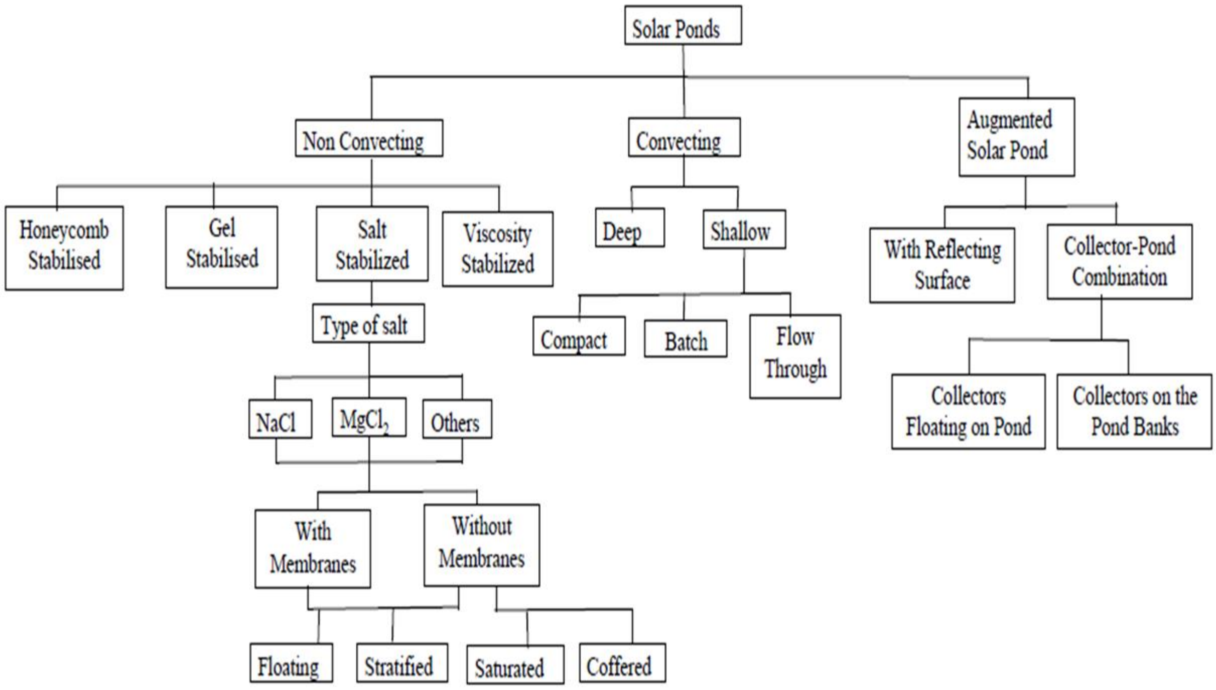

Figure 2.2 Types of solar pond (Salem and Probert, 1986)

In convecting solar ponds, the convection current is not suppressed. For shallow convecting solar ponds, the body of water is heated by the insolation in a shallow pond not more than 10 cm deep. Augmented solar ponds are normally equipped with solar energy harnessing devices to augment the capability of solar pond in terms of solar capturing capability. Both convecting and non convecting solar pond can be augmented with solar collectors.

2.3.3 Sources of Salt

The salt used for salinity gradient must be chemically stable. The salt should not be toxic and must be safe to handle. The salt must not inhibit the insolation transmission characteristic of the water and also prevent the rate of organic growth in water which will affect the clarity of the solar pond. The upward diffusion of heat from solar pond can be reduced by choosing the type of salt that is temperature dependant (Elwell et al., 1977). Magnesium and sodium chlorides fits most of the criteria above *(*Hull et al., 1989*).*

2.3.4 The Design and Performance of Solar Ponds

The design of a solar pond depends on specific application. It is very important to identify the main application of the solar pond before the start of the design stage. A solar pond supplying hot water above 80˚C for power generation purposes will require different design parameters as compared to the one supplying hot water at 35˚C for aquaculture applications. The desired delivery temperature for any application needs to be considered carefully. The storage temperature in the solar pond must be kept 3˚C – 5˚C higher than the delivery temperature in order to compensate the heat transfer losses.

2.3.5 Site Selection

The site chosen for solar pond construction must be appropriately selected. The main characteristics for solar pond sites are listed as below:

- High solar radiation insolation
- Low wind speed for minimum mixing of the top surface of the solar pond
- Flat site with minimum vegetation and trees for ease of construction and minimum earthmoving
- Water table more than 5 m deep from the storage zone for minimum thermal losses
- Good soil cohesion properties for stable walls

2.3.6 Design Considerations and Sizing

The size of solar pond depends on the availability of solar radiation together with the temperature and demand of the heat required for application. It is important to have access to the local long term weather and solar data. For research application with a surface area of less than 500 m^2, a circular shape pond is preferred due to heat loss criterion and practical reasons (Nielsen, 1980). This is because the circular shape provides least perimeter for a given surface area. For larger ponds, rectangular shape is preferred as ground heat loss is not an important factor.

2.3.7 Excavation and Lining

Before preceding the earthwork, the design of the solar pond should include the design for evaporation ponds/storage ponds. The drainage pattern and site layout that includes the pipeline for heat extraction, instrumentation for monitoring and recording purposes must be considered at the design stage. This design process should be done thoughtfully as the excavation cost contributes to almost 40 % of the total cost for a solar pond construction. The soil for the solar pond construction site should be with low permeability. A slope of not more than 1:3 (vertical: horizontal) is used for the constructions of the sloping wall.

Liners are very important to prevent the saline water from the solar pond leaking into the underground water table and endangering the environment (Boegli et al., 1982). This leakage will carry away the salt from saturated storage zone together with heat and this will affect the overall operation of the pond. The polymeric liner not just need to withstand the anticipated maximum temperature of the pond, but it needs to be resistant to ultraviolet radiation (Lu et al. 2004). Leak detection system should also be incorporated in the construction of the solar pond. Figure 2.3 shows the typical cost sharing relevant to the construction of a solar pond.

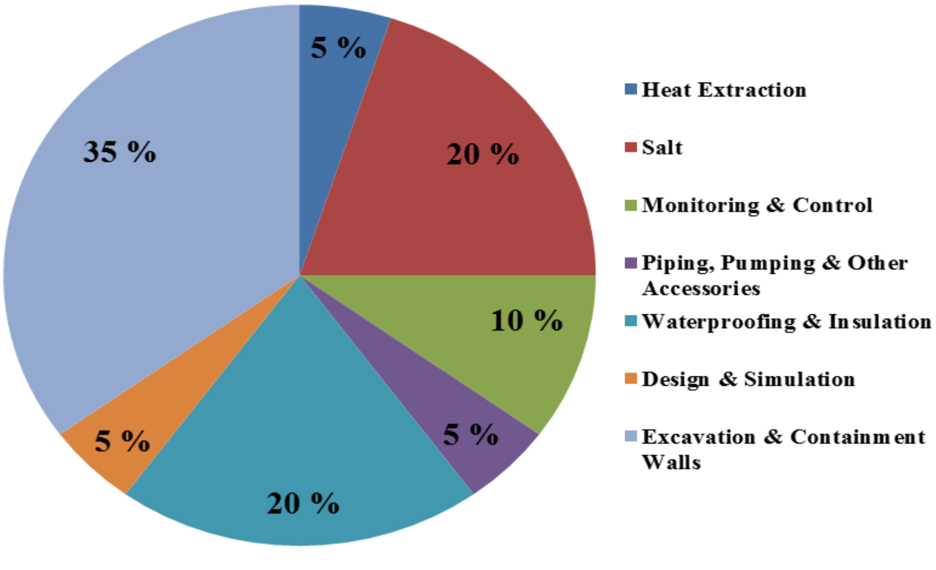

Figure 2.3 Typical cost sharing relevant to construction of solar pond (Fiorenza, 2006)

2.3.8 Salinity Gradient Establishment

There are a few methods to establish the salinity gradient of solar pond. The methods are:

i. Natural Diffusion
ii. Stacking
iii. Redistribution

Most of the solar ponds in the world are established using the redistribution method (Zangrando, 1980). In this method, a solar pond is first filled with a saturated brine mixture up to a depth of the lower storage zone and half the thickness of the gradient zone. From the interface of the lower storage zone and the gradient zone, fresh water will be injected with a diffuser. The fresh water is injected in a stepwise manner. The point of injection of fresh water should rise twice as fast as the pond surface rises. This will allow for uniform gradient establishment. This method is the commonly used method worldwide at present.

The salinity gradient of the pond is maintained at a ‘stability margin’ number greater than two (Xu, 1990). The ‘stability margin’ number is defined as the ratio of the measured stability coefficient to the calculated stability coefficient to satisfy the dynamic stability criterion. This is to ensure that the density gradient in the pond is kept at a certain minimum level. If this is not done, the convection currents will develop in the gradient zone and it will compromise the stability of the salinity gradient in the pond.

2.3.9 Heat Extraction

The heat stored in the storage zone and the gradient zone can be used for numerous applications. Two methods have been used to extract heat from a solar pond. In the first method, a submerged heat exchanger is used to circulate fresh water (Hull et al., 1985). This submerged heat exchanger can be made of metal or plastic.

The second method to extract heat from the solar pond is by using brine extraction method (Fynn et al., 1980). In this method, hot brine from the bottom of the interface of gradient zone is passed through an external heat exchanger with the help of a diffuser. After the heat exchange, the hot brine is pumped back into the storage zone of the solar pond. This brine withdrawal method requires a small heat exchange surface when compared to the submerged heat exchanger heat extraction method.

Heat extraction from the gradient zone addition to the storage zone can help to improve the overall efficiency of the solar pond (Akbarzadeh et al., 2005). A selective withdrawal method can be used to extract hot brine from different depths of the gradient zone. This brine can then be passed through a series of heat exchanger where a heat transfer fluid is preheated using the heat from the gradient zone at different depth.

2.3.10 Solar Ponds Applications

2.3.10.1 Industrial Process Heat

Solar ponds are suitable for supplying low-temperature heat at competitive cost when the solar ponds are situated at suitable locations. Hot water obtained from solar ponds can be used for town water heating, laundries, salt drying, dairies, food processing plants (Reid et al., 1986) and solution mining operations.

2.3.10.2 Agricultural and Aquaculture

Solar ponds provide readily available heat energy at low temperatures. This low temperature heat is suitable for yearly agricultural cycles with enhanced ability to provide food on a continual basis (Hull et al., 1986). Solar ponds can be used to meet many low temperature agricultural needs (Akbarzadeh et al., 2005). Using fossil fuel to supply low temperature heat is not sustainable in the long term.

2.3.10.3 Fresh Water Production –Desalination

Multistage flash desalination (MSF) and multieffect distillation (MEF) technology could operate at temperatures around 70 ˚C. This allow for heat from solar ponds to be used for the above low pressure thermal desalination processes where fresh water is lacking and seawater or brackish water is available in abundance. The use of solar ponds for desalination purposes allows minimum environmental footprint operation. Additionally, the waste brine from the process can be recycled and fed to the storage zone of the pond for salinity gradient maintenance (Akbarzadeh and Date, 2014).

2.3.10.4 Electrical Power Production

Low temperature heat from the solar ponds can be converted into electricity for daily applications. 5 MW of electrical energy output was successfully produced with a 250 000 m^2 solar pond at Bet Ha Arava, at the Dead Sea in Israel. Solar ponds in Alice Springs, Australia and El Paso, USA produced electrical power output of 15 kW and 70 kW respectively. Conventionally, ORC engines are used to convert the low temperature heat from solar ponds to electrical energy. ORC engines have a reported heat to net electricity efficiency of around 6 % (Collins, 1983).

2.3.10.5 Chemical Productions

Solar ponds are used for producing many chemical related products such as sodium sulphate (Lesino et al., 1982), chloride salts, Lithium Carbonate, fertilisers and other industrial chemicals. The low temperature heat from the solar ponds provides a cost effective method for chemical productions at large scale applications.

2.3.10.6 Salinity Mitigation

With the rising salinity levels around the world, many productive agricultural lands are abandoned and neglected. The salinity mitigation schemes at these areas with unproductive land can be integrated with solar ponds as an attractive potential application. Solar ponds can be successfully incorporated with these evaporative basins to produce heat or electricity. The salt produced by the evaporative basins can be supplied to the storage zone of the solar ponds and the underground saline water can be utilised for surface flushing of the ponds before channelled to the evaporative basins (Akbarzadeh et al., 2005).

2.3.11 Solar Ponds Worldwide

2.3.11.1 Solar Ponds – Israel

Artificial solar ponds were developed and the successful demonstration of the solar ponds technology influenced the development of solar ponds all over the worlds. The solar pond at En Boqeq was the first solar pond to generate 150 kW of electrical power in 1979. In 1984, a 250 000 m^2 solar pond at Bet Ha Arava utilised the low temperature heat from the solar pond to produce 5 MW of electrical power output, as shown in figure 2.4. This solar pond was connected to the grid as a peaking plant. The brine for the solar ponds in Israel was obtained from Dead Sea. Figure 2.4 also shows the aerial view of the Dead Sea solar pond near Bet Ha Arava, Israel.

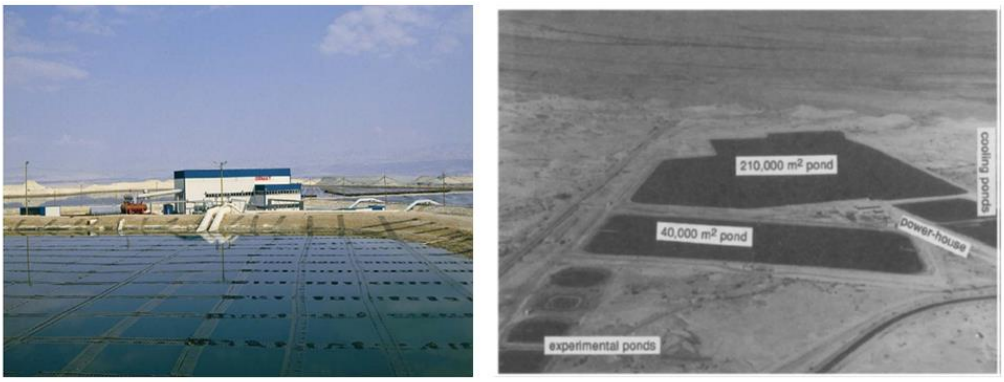

a.) The Dead Sea solar pond near Bet Ha Arava, Israel. (Grossman, G ,1999)

b.) Aerial View of the Dead Sea solar Pond near Bet Ha Arava, Israel. (Tabor and Doron, 1990)

Figure 2.4 The Dead Sea solar ponds near Bet Ha Arava, Israel

2.3.11.2 Solar Ponds – USA

Solar ponds research began in the USA around 1973, mainly by Rabl & Nielsen at the Ohio State University. Solar Ponds with a size less than 5000 m^2 has been successfully operated in a varied climate conditions both for electricity generation and industrial heat processing. Solar ponds with an area of 2000 m^2 in Ohio, USA have been used to heat the municipal swimming pools and to heat a greenhouse for another application. A 3700 m^2 solar pond was constructed in 1983 with cooperation between University of Texas El Paso and Bruce Foods, Inc. This solar pond, as shown in Figure 2.5 was used to supply heat to the food processing industry. Additionally, with well-designed procedures for maintaining the gradient, the storage zone temperature remained above 80 ˚C consistently throughout the year. A maximum electrical power output of 120 kW was achieved using an Ormat ORC engine coupled with the pond. Large solar ponds with an area of 300 000 m^2 were used in Nevada by Nevada Power Co for solution refining by preventing the precipitation of epsomite salt in winter by the heat of the storage zone. A 2000 m^2 solar pond was constructed at the University of Illinois, USA for cost effective construction methods study (Newell et al., 1987).

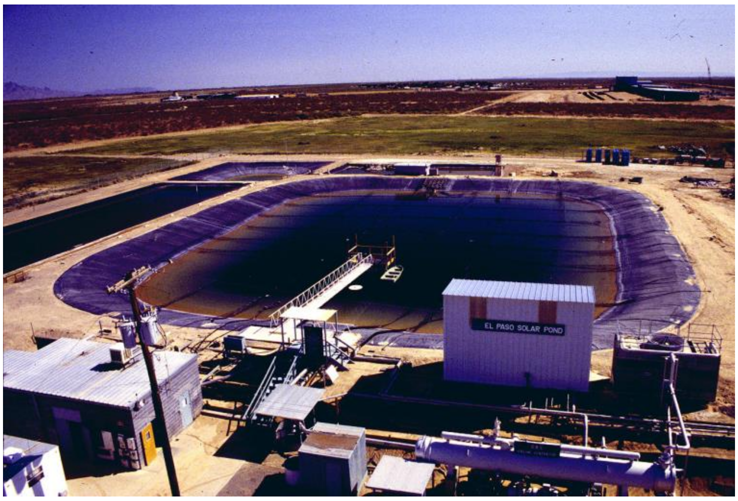

Figure 2.5 Solar pond at University of Texas, El Paso (Lu et al., 2014)

2.3.11.3 Solar Ponds – Australia

Solar ponds were investigated as research projects since 1964 in Australia by the Commonwealth Scientific and Industrial Research Organisation (CSIRO). The University of Melbourne and Cheetham Salt Ltd, Laverton operated two solar ponds with surface area of 900 m^2 each for research purpose. One of the ponds was unlined for research study utilising the underground brines. Enreco also built a 150 kW unit to supply power to Birdsville using Great Artesian Basin hot water which has been running for many years.

In early 2000, RMIT University together with two industrial partners designed and constructed 3000 m^2 solar pond at Pyramid Hills, Victoria, as shown in figure 2.6. The pond was designed with a depth of 2.3 m, storage zone thickness of 0.8 m and the gradient zone thickness of 1.2 m. The heat from the solar pond was used for salt drying process at Pyramid Salt Factory. Heat was also used at the site for aquaculture farming. Up to 60 kW of process heat was supplied consistently to the salt production process at the factory. The underground saline water used in the factory for salt production was used for surface flashing before collected at two large evaporation ponds. The pond has ceased operating after massive flash floods in Victoria in 2011.

At RMIT University, a 53 m^2 experimental solar pond was constructed in the late 90s. The pond is in a circular shape with a diameter of 8m and a depth of 2.5 metres, as shown in Figure 2.6. A 1600 m^2 solar pond was built at Alice Springs, Northern Territory in 1984 for power generation using Organic Rankine Cycle Engine, as shown in Figure 2.7. 20 kW electricity output was obtained for the isolated communities located in the outback regions there (Collin R, 1985).

a.)Pyramid Hill solar pond (3000 m^2) **b.) RMIT University solar pond (53 m^2)**

Figure 2.6 Pyramid Hill solar pond (3000 m^2) and RMIT solar pond

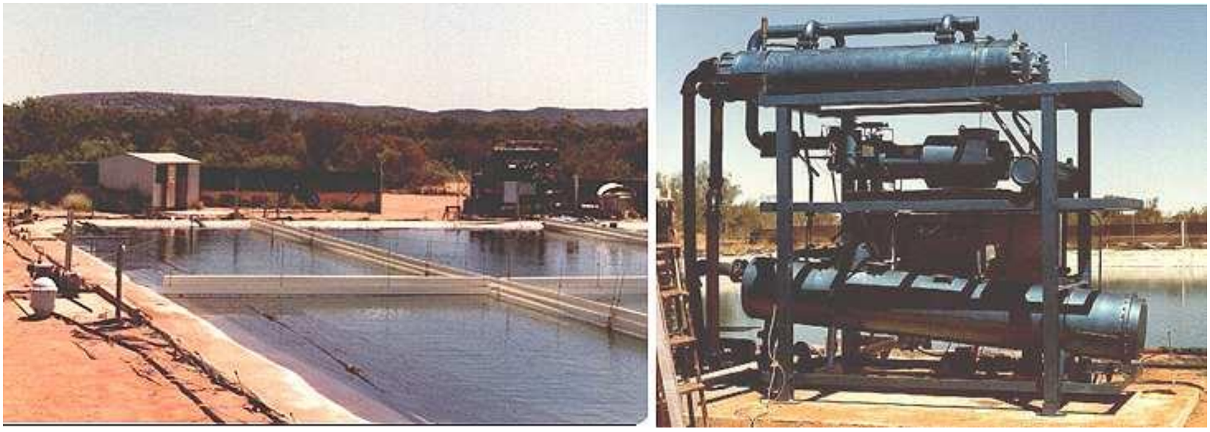

Figure 2.7 Alice Spring, Northern Territory solar pond (left) and ORC engine (right) (Hull et al., 1989)

2.3.11.4 Solar Ponds – China

Salt lakes in China’s Qinghai, Tibet Plateau area are mainly constructed to extract lithium carbonate salt for the lithium production for battery storage. The solar ponds in Tibet, China are constructed on high latitudes (>3000 m) and on a hilly barren land. The region lacks conventional energy resources and the solar energy can be utilised with the help of solar pond for mineral processing. A solar pond was built with a surface area of 2500 m^2 and depth of 3 m near the Zabunye salt lake in Tibet (Nie, Bu et al., 2011). The slope of the side wall is 1.5:1. The solar pond was built after excavating 1 m below ground. The pond bottom and side walls were completely compacted with clay from the lakeside. A 0.5 mm thick sheet of high density polyethylene (HDPE) was paved on the top of the clay layer to prevent brine leakage. An automatic temperature measurement system was installed before the start of the operation of the pond. Another solar pond was built in Lianyungang, Jiangsu in China in 1983 with an area of 1000 m^2 utilising the by-product of salt production called bittern, as shown in Figure 2.8.

Figure 2.8 Clockwise from top left: (1) Zabuye salt lake; (2) Solar pond after evaporation; (3) Lithium Carbonate sheets, and (4) Lithium Carbonate harvesting (Nie, Bu et al., 2011).

2.3.11.5 Solar Ponds – India

Many solar ponds were constructed in India since the 1970s for both research and industrial applications. A 1200 m^2 pond was constructed at Central Salt and Marine Chemicals Research Institute (CSMCR) in Bhavnagar, Gujarat in 1970. Magnesium Chloride, which is a waste product from the edible salt production process, was used to create the salinity gradient of the pond. The institute built another solar pond with an area of 1600 m^2 in 1980 utilising sodium chloride for the salinity gradient establishment. From 1980-1982, Tata Energy Research Institute built and operated a 100 m^2 sodium chloride based solar pond in Pondicherry. Indian institute of Science built a 240 m^2 solar pond in Bangalore for research purpose. The data from the pond provided valuable information in regards to the technical and economic viability of a small solar pond.

Solar ponds in India were also used to supply heat to the industrial and town water heating applications. A 400 m^2 solar pond supplied hot water for the rural community located in Masur, Satara. Another solar pond with an area of 300 m^2 was used for hot water supply to student hostels in Hubli, Karnataka.

The largest solar pond in India was operated in Bhuj, as shown in figure 2.9. The solar pond was constructed with an area of 3000 m^2. The heat from the solar pond was used in the dairy production in the Kutch Dairy factory. The pond recorded a maximum temperature of

99.8 ˚C. The pond was constructed with local materials with mined clay and plastics to reduce the construction cost. External heat exchangers were used to extract heat from the hot brine through a shell and tube heat exchanger. Feed water was heated up to a temperature of 70 ˚C and used in the dairy factory for cleaning and washing. The solar pond at the dairy farm, as shown in Figure 2.9 successfully supplied up to 80 000 litres of hot water for the heating process in the dairy factory.

Figure 2.9 Solar Pond in Bhuj, India (Kumar and Kishore. 1999)

2.3.11.6 Other Countries

Almost all parts of the world showed interest in the solar pond technology and it continues to increase. One of the largest solar ponds used for sodium carbonate production is located in Ethiopia. It is operated by Ethiopian Mineral Resources Development Corporation since 1988. The surface area of the pond is 300 000 m^2 with a depth of 1.5 m. In Argentina, a solar pond with an area of 600 m^2 and a depth of 2.4 m is used to produce sodium sulphate since 1982. A 700 m^2 solar pond was used in Canada for grain drying from 1981- 1984. In Portugal, a 1000 m^2 solar pond with a depth of 3.1 m was used for greenhouse heating since 1983. In Japan, the heat from a 1500 m^2 solar pond was used to produce hot water at 75 ˚C for can washing. In Barcelona, Spain, a 500 m^2 solar pond was used to supply hot water for industrial mining applications. A 53 m^2 above ground solar pond was constructed at Solvay-Martorell facilities, Catalonia, Spain for research works, as shown in Figure 2.10. Many other countries like France, Italy, Mexico, Kuwait, Qatar, Togo, Iran, Finland, Greece, Bangladesh, Egypt, Tunisia, and Croatia have explored the potential of solar pond either for research or industrial application. This indicates the high interest by many nations to use the solar pond for a wide variety of industrial application with good sustainability practices.

Figure 2.10 Solar pond at Solvay-Martorell facilities, Catalonia, Spain (Bernad et al., 2013)

Table 2.1 shows the some salinity gradient solar pond locations in the world with information on area, maximum temperature, capacity, efficiency and applications.

Table 2.1 Salt Gradient solar pond operating worldwide (Lodhi, 1996, Kumar & Kishore, 1999)

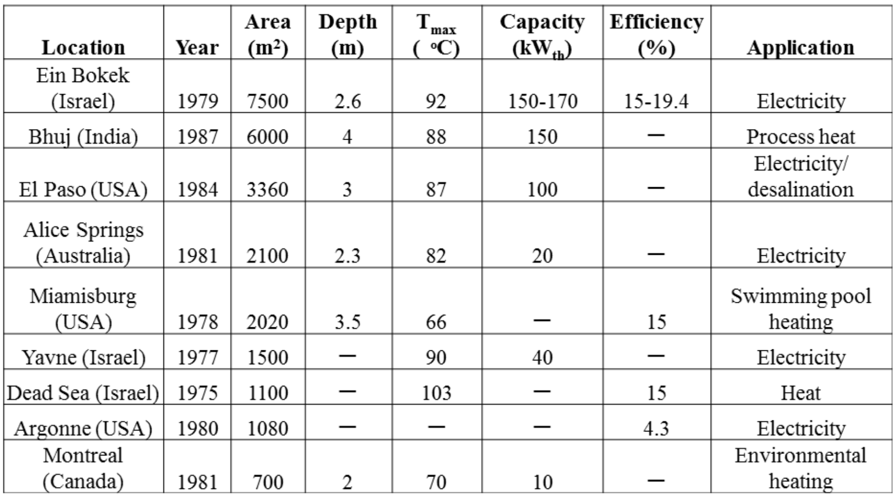

Location	**Year**	**Area (m^2)**	**Depth (m)**	**T_{max} (°C)**	**Capacity (kW_{th})**	**Efficiency (%)**	**Application**
Ein Bokek (Israel)	1979	7500	2.6	92	150-170	15-19.4	Electricity
Bhuj (India)	1987	6000	4	88	150	–	Process heat
El Paso (USA)	1984	3360	3	87	100	–	Electricity/ desalination
Alice Springs (Australia)	1981	2100	2.3	82	20	–	Electricity
Miamisburg (USA)	1978	2020	3.5	66	–	15	Swimming pool heating
Yavne (Israel)	1977	1500	–	90	40	–	Electricity
Dead Sea (Israel)	1975	1100	–	103	–	15	Heat
Argonne (USA)	1980	1080	–	–	–	4.3	Electricity
Montreal (Canada)	1981	700	2	70	10	–	Environmental heating

2.3.12 Energy, Environment & Economic (EEE) Evaluation of Solar Pond

One of the main advantages of a solar pond over other thermal systems is that it is an integrated energy collection and storage system. Due to the built-in storage capacity of the solar pond, the pond can deliver heat whenever it is required on a reasonable continuous basis. Solar pond situated at a suitable location with the ability to use local resources can operate at a relatively lower cost when compared to other technologies for large scale collection, storage and solar thermal energy delivery systems. Solar pond operation is environmentally friendly which is sustainable.

Solar pond for heating can be highly competitive and economical when compared to providing heat energy utilising Liquefied Petroleum Gas (LPG) or oil. Solar pond technology can also compete with natural gas where the price for this fuel is high. One of the main benefits of a solar pond is that it is a zero greenhouse emission source of heat. Figure 2.11 shows the cost of industrial heat and cost of base load of solar pond compared to conventional fuels and power plant. Both the costs reduce significantly as the size of the solar pond increases. This shows that the economic viability of the solar pond power generation depends on the size of the pond. For industrial process heat in the range of 50 ˚C to 90 ˚C, large solar pond is very competitive when compared to natural gas and coal. For electricity generation from solar pond, large solar ponds are competitive to conventional coal plants, when impact of environmental costs due to pollution caused by fossil fuel burning in the conventional plants is considered.

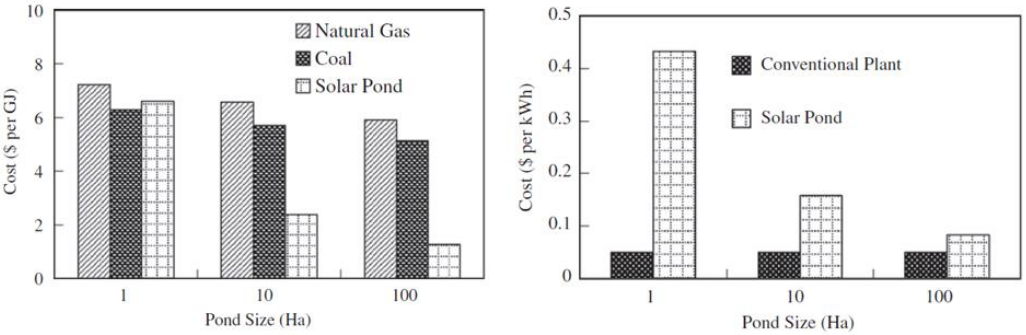

Figure 2.11 Cost of industrial heat (left) and cost of base load (right) (Leblanc et al., 2011)

Organic Rankine cycle (ORC) is currently used for electrical power generation from solar ponds. This results in higher unit costs of producing base load electric power when compared to conventional energy sources. This is due to the high capital cost for ORC and the low overall efficiency of the conversion of thermal energy from solar ponds to electrical energy (≤ 7%). Nevertheless, it is very important not to compare the cost of solar pond power generation with today's emission-intensive technologies heavily relying on coal. Comparison should be made with other renewable technologies such as photovoltaic systems. Other means of power generation methods from solar pond using alternative technology like thermoelectric generators are currently being investigated for better conversion efficiency.

For solar pond power generation in winter months, ORC engine will cease to operate since the threshold temperature required for the boiling of organic fluid is lower than the required temperature. In this case, it is worthy to explore technologies like TEG power generation for all year long power generation even at low temperatures in winter months.

2.3.13 Solar Pond Advantages and Disadvantages

One of the main advantages of solar pond is that it is an integrated solar thermal collector and storage system. Unlike PV systems, where the PV panels acts as the collector and a different batteries system acts as the storage system. This makes solar pond an inexpensive and a simple in concept without any complicated technology. The cost of setting up a solar pond is not high because all we need to do is ground excavation and then fill it up with water and salt. As we know, water and salt are available in abundance. Additionally, the large thermal mass of water makes solar pond very stable thermally. Even with several consecutive cloudy days, the overall temperature in the storage zone drops only be a few degrees, and can be recovered easily with the next available sunny days. This makes solar ponds suitable as a long-term thermal storage system.

As the solar pond is made of water and salt, the maximum possible temperature attainable is not more than 100 ˚C. This makes solar pond as a source of low grade heat only. It is not possible to obtain medium grade heat (250˚C – 600˚C) or high grade heat (> 600 ˚C). This is because the water at storage zone cannot exceed the boiling temperature of water. Besides that, solar pond is highly dependent on site as large dedicated land/ site is required for the establishment of solar pond, as some sites might create limitations for building a large solar pond. As salt is required for the operation of solar pond on a constant basis, there should enough salt supply at site for a sustainable operation of the solar pond. Therefore, solar ponds need to be built near the sea, or slat lakes or salt affected areas.

With the known advantages and limitations of the solar pond, there is a need to look for an alternative to ORC engines for power generation. Thermoelectricity provides a better alternative for power generation from solar pond. Even with small solar ponds at low temperatures, TEG modules are capable of generating power and can be utilised to build heat exchangers that are not technologically complicated, when compared to ORC engines. Next section discusses about potential of TEG modules used for power generation from solar ponds.

2.3.14 Future Directions of Solar Ponds

Solar ponds principles have evolved greatly since the start of the pioneering work in the 1950s. Various solar ponds have been constructed all over the globe for experimental purposes as well as for large scale applications. The applications presently of greatest interest are industrial process heating, thermal desalination, saline effluent management and biogas production. As with other renewable energy technologies, it is hard to compete economically with conventional fossil fuels while no cost penalty is imposed on the latter for the impending major global costs of the irreversible climate change their greenhouse emissions are causing.

Numerous research and development of solar ponds technology has been learned throughout the world and this adds to the benefit in terms of the design and installation of new pond projects. Further investigations on the alternative salts, new lining techniques, cost effective and simple construction methods, artificial solar pond liquids and methods to limit wind mixing on the surface of the pond can provide the possibility of development of new generation solar ponds.

With abundant, exceptional sites for solar ponds and the increase in the fossil fuel prices, solar ponds technology can become economically viable that provides for a sustainable energy system.

2.4 Thermoelectric Generator

2.4.1 History

Thermoelectricity was first discovered in 1821 by Thomas Johann Seebeck (Xi et al., 2007). He observed that when two dissimilar metals in a closed loop were maintained at a certain temperature difference at the junctions. Initially, it was the phenomenon was thought to be caused by magnetism force, as evidenced by deflection in the compass magnet. Further investigations then proved that electrical current that flows in the dissimilar metals caused the magnetic field presence. Thermal energy was successfully converted to electrical energy with conversion efficiency of 3 %, which was comparable with the most efficient steam engine at that time (Rowe, 1978).

In 1834, Jean Charles Athanase Peltier discovered Peltier effect. In Peltier effect, when a current is passed through two dissimilar metals in a loop, a cooling and heating junction was observed at the end of the loop, depending on the direction of current flow. Both Peltier and Seebeck effects are thermodynamically reversible process.

Later in 1855, William Thomson, also known as Lord Kelvin predicted a phenomenon called Thomson effect. Thomson effect explained comprehensively the Seebeck and Peltier effects and described their relationships. This effect explains the cooling and heating effect on a current-carrying conductor/semiconductor with temperature gradient. A net flow of electrons due to the temperature differences causes the electromotive force to flow in the conductor. Figure 2.12 below shows the Seebeck, Peltier and Thomson effect.

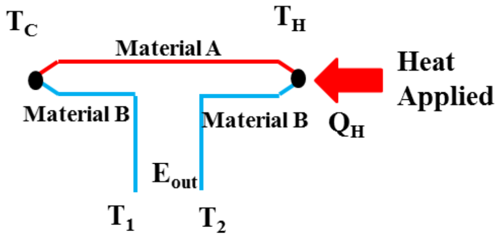

a.) Seebeck Effect

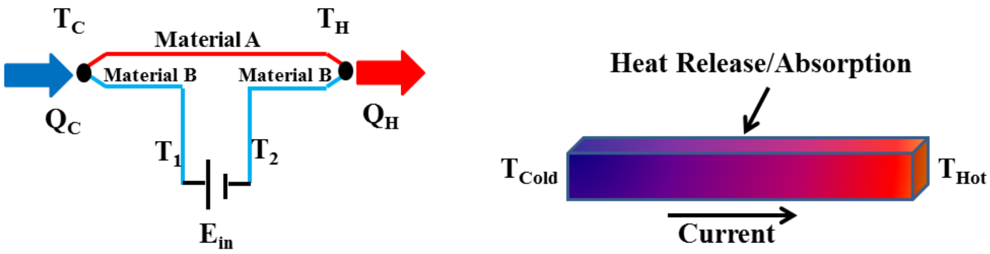

b.) Peltier Effect

c.) Thomson Effect

Figure 2.12 Illustrative representation of: a.) Seebeck b.) Peltier and c.)Thomson effect

The relations for Seebeck, Peltier and Thomson effects are given as follow:

$$\text{Seebeck coefficient, } S = -\Delta V/\Delta T \quad (2.1)$$

where ΔV is the potential difference in V

ΔT is the temperature difference in K.

$$Q_{peltier} = (\Pi_1 - \Pi_2)I \quad (2.2)$$

where Π_1 and Π_2 are Peltier coefficients

I is the current from point 1 to 2 in A

$Q_{peltier}$ is the heating or cooling rate of junctions in J

Thomson coefficient, $\tau_t = \frac{1}{I}\frac{\Delta Q}{\Delta x} / \frac{\Delta T}{\Delta x}$ (2.3)

Where ΔQ is the change in heat in J

I is the current in A

Δx is length in m

ΔT is the temperature difference in K

I is the current in A

In the early 1900s, thermoelectric principle was explored to generate electricity. However, the use of metals and metal alloys as conductors the in thermoelectric modules limited its application. In the late 1930s, thermoelectricity as a source of electrical power received renewed interest with the development of synthetic semiconductors with better Seebeck coefficients at 5 % thermal to electrical conversion efficiency (Telkes, 1947). In 1950s, with improved thermal to electrical conductivity ratio led to even higher conversion efficiencies to up to 10 %. This was possible by alloying semiconductor materials with isomorphous elements, as demonstrated by Russian scientist named Ioffe (Rowe,1978). With better efficiencies and Seebeck coefficient, thermoelectric generators were used in real applications for space explorations in United States of America. Radioisotopes replaced fossil fuel as the source of heat in power generation for spacecraft using TEG modules for long periods, unattended (Ewert, 1998). Since then, TEG modules have been successfully used to for terrestrial and remote area power generation, pacemaker, cooling and heating of trains (Bojic et al., 1997), powering wrist watches (Snyder, 2008), waste heat recovery (Yodovard, 2001), solid state heat pump cooling below ambient temperature and many more. The first commercial TEG module was used to power radio receivers in rural araes in Russia. The heat was obtained from a kerosene lamp (Vedernikov and Iordanishvili, 1998). Hot stove with TEG were also used by Russian soldiers during world war two to power communication devices. Figure 2.13 shows the earliest application of TEG power generation on commercial scale.

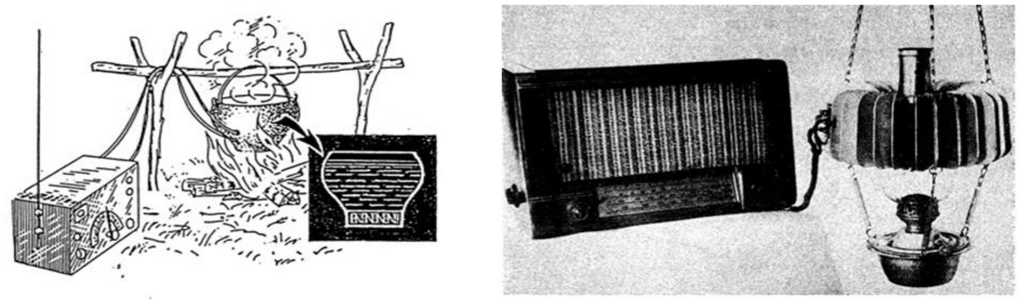

a.) Partisan's Canteen : thermoelectric generation by campfire

b.) Kerosene lamp: thermoelectric generation used for radio

Figure 2.13 Early application of TEG power generation (http://www.kelk.co.jp)

2.4.2 Materials Development for TEG

With new discovery in materials and alloys used for TEG modules, TEG power generation continues to fascinate researchers. New ideas and methods have allowed development of TEGs with higher efficiency and figure of merit. The figure of merit of TEG is defined as:

$$Z = \sigma S^2/k \tag{2.4}$$

where σ is the electrical conductivity in S/m

S is the Seebeck coefficient in V/K

K is the thermal conductivity in W/mK

The dimensionless figure of merit, ZT is obtained by multiplying Z with average temperature across TEG. TEG modules with ZT values are considered good and ZT values of between 3 -4 ranges are important for TEGs to compete with mechanical devices in terms of efficiency (Hsu et al., 2004, Boukai et al., 2008).

Figure 2.14 shows the ZT values for various bulk thermoelectric materials as a function of temperature.

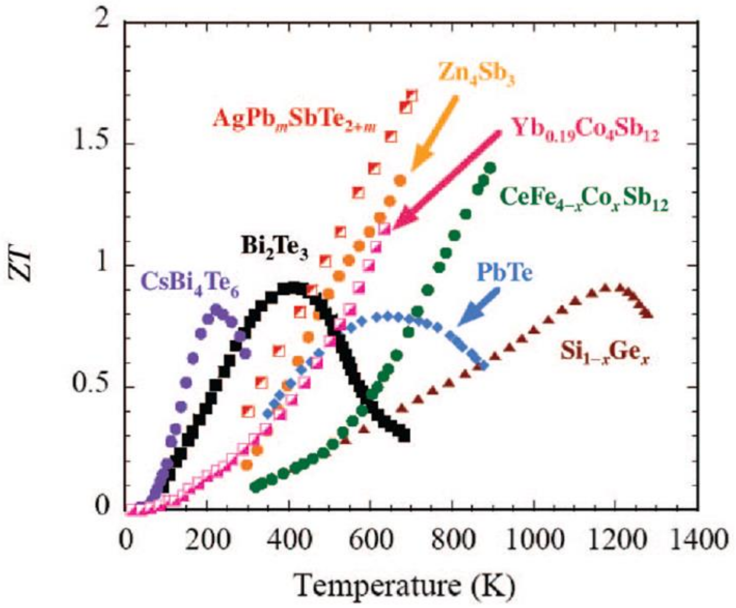

Figure 2.14 ZT values for various bulk thermoelectric materials as a function of temperature (Tritt and Subramaniam, 2006)

Most common thermoelectric materials with ZT values ranging from 0.8 to 1.0 are Bismuth Telluride (Bi_2Te_3) (Goldsmid et al., 1980). This bulk material is suitable for TEG operation at temperatures between 200 – 500 K. At higher temperatures, lead tellurides (PbTe) can be operated at ZT of 1.5 at temperatures up to 700 K (Heremans et al., 2008). New bulk materials such as skutterudites, Heusler alloys, complex calcogenides and oxide allow TEG to operate at high temperatures around 1000 K with ZT around 1 (Rowe, 1995). Recent developments in quantum dot and nano-technology have further enhanced the ZT values to be around 1.5 (Kim et al., 2010).

2.4.3 Advantages of TEGs as Heat Engine

One of the main advantages of TEG module is that the device acts as a solid state heat engine without any moving parts. This allows for a noiseless and vibration free operation. When compared to other mechanical heat engines, the presence of many moving parts results in dynamic forces that can cause maintenance issues in the long term operation (Nolas et al., 2001). The absence of moving parts in TEG allows for long continuous operation life with high reliability. Furthermore, TEG modules have good potential for miniaturisation when compared to conventional heat engines. The heat source needed for TEG operation is also not specific, where heat transfer from gas, liquid and radiation can be used to power them. TEG modules used in space applications proved that they are resilient and highly reliable and not susceptible to the elements of the environment. Even at low temperature differences, TEG modules are capable of generating power and make them a good candidate for waste heat and miniature devices applications. With better conversion efficiencies in the future, TEG modules are going to revolutionise the conversion of thermal energy to electrical energy and replace current conventional bulky mechanical heat engines.

2.4.4 Thermoelectric Power Generation

Thermoelectric power generation can be obtained by maintaining temperature difference across the TEG module when connected to an external load. The charge carriers in TEG module element legs act as the working fluid of the heat engine. Generally, TEGs are categorised either as isotopic and non- isotopic generators (Date, 2014). TEG power generation can meet wide range of power requirements and can be a source of sustainable source of electrical generation system.

2.4.4.1 Isotopic Generators

In isotopic generators, radioactive fuel such as Plutonium -238 and Strontium 90 are used as the heat source for TEGs. The long half-life of the radioactive materials allows the TEG module to operate unattended for long periods. Plutonium -238 based generators are mainly used for space exploration due to absence of oxygen for fossil fuel burning. It is also used for medical devices due to minimal shielding requirements. Strontium-90 based generators, which are one fortieth the cost of Plutonium-238, are mainly used for terrestrial application with heavy shielding due to its low cost (Carney, 1972). These isotopic generators are also used for remote area for oil pipelines and sea buoys where cost is not considered as principle criteria.

2.4.4.2 Non-Isotopic Generators

Non-isotopic generators are much more straightforward with less sophistication when compared to isotopic generators. The heat at the hot junction is provided by many sources like fossil flame, solar radiation, geothermal energy, waste heat from heat engines and many more. This type of generator is also widely used in remote areas where conventional electrical power is not reachable. Non-isotopic generators can be categorised into low power generation and high power generation including solar thermoelectric generation and waste heat thermoelectric generation.

2.4.4.2.1 Low Power Generators

Batteries are currently used as energy supply for terrestrial wireless and remote sensing devices. With a limited lifetime of batteries, the batteries in these systems need to be replaced after a few years. Additionally, the harmful chemical contents in batteries require expensive procedure for the disposal. To overcome the problems arising from the use of batteries, small and inexpensive TEG can be used to power these low powered devices. Small temperature differences of less than 20˚C are enough to generate power for these small devices (Glosch et al., 1999). Catalytic combustion of fuel without the production of flame can lead to high density power generation using TEG modules with simple and compact designs. This will lead to cost reduction and simplifies miniaturisation. (Federici, 2006)

TEG was also successfully used to power wrist watches using only body heat (Kishi et al., 1999). A thin TEG bulk materials and temperature difference of 1.5 K, an open circuit voltage at 300 mV was generated by the TEG module to power a wrist watch with normal operation power requirement of only 22 μW. A fuel cell with TEG was used for small portable power applications. Unreacted mixture after fuel cell reaction can be catalytically combusted to power TEG with special heat exchangers (Ahn et al., 2007).

Many thermal energy sensors utilising TEG modules have been developed and used successfully. These include cryogenic heat flux sensors (Haruyama, 2001), ultrasonic intensity sensors (Romdhane et al., 1995), water condensation detection sensors (Vancauwenberghe et al., 1996), fluid flow sensors (Stachowiak, 1998), and infrared sensors. (Volklein et al., 1999).

2.4.4.2.2 High Power Generation

2.4.4.2.2.1 Solar Power generation

Solar hybrids systems with TEG have been used to boost efficiencies of solar devices and at the same time improve the stability of performance. To increase the electricity production of the photovoltaic (PV) modules, TEG was used to increase electricity production from PV modules. The heat flux from PV modules is passed through TEG and then to the heat extractor system of the PV system (Urbiola et al., 2011). Thermal concentration systems have been widely used to generate power from TEG modules (Kraemer et al., 2011). With recent advances in tracking system and high ZT TEG modules, solar power generation using TEG modules can be used to generate electricity and supplied to main grid. Solar TEG system has been used for terrestrial applications with solar hot water systems for cogeneration electricity at minimal extra cost. Figure 2.15 shows the schematic hybrid system of PV and TEG power generation.

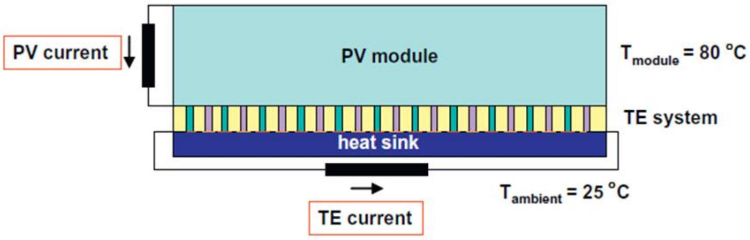

Figure 2.15 Schematic hybrid system of PV and TEG power generation (Sark, 2011)

Power generation from low grade heat of solar pond was obtained from ORC engines. The requirement of certain threshold temperature for the operation of ORC engines limits the power generation from solar pond at temperatures lower than 50 ˚C. To overcome this problem, TEG modules can be used with low grade heat of solar pond even at low temperatures. There is no scale limit in terms of heat energy conversion to electricity. However little in amount, heat energy is converted directly to electricity. Furthermore, small solar ponds limit the application of ORC engines. The operation of power generation from solar pond with passive systems like thermosiphon proves that low grade heat at low temperatures can be converted to electricity using TEG (Singh et al., 2011). Figure 2.16 shows the schematic of power generation from solar pond using TEG.

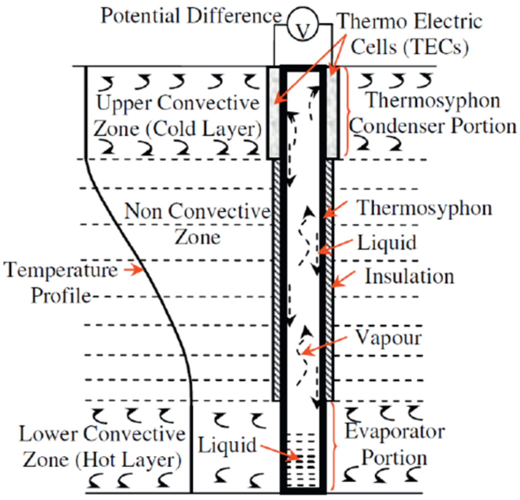

Figure 2.16 Schematic of power generation from solar pond using TEG (Singh et al., 2011)

Integrated heat pipe with TEG modules for power generation from evacuated tube solar collectors was developed for its simplicity in operation and high reliability with low investment and maintenance cost (He et al., 2012). Thermionic converter with TEG generator was able to convert thermal energy at 1800 K with high efficiency into electricity (Natito et al., 1996). Solar energy converted into electrical energy by TEG modules headgear as shown in Figure 2.17 was successfully tested to provide thermal comfort for people active with outdoor activities.

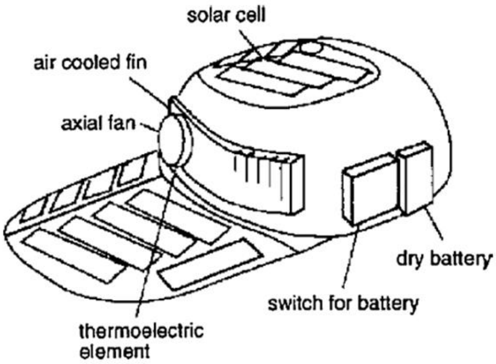

Figure 2.17 Schematic of solar-driven thermoelectric cooling headgear (Hara et al., 1998)

2.4.4.2.2.2 Waste Heat Power Generation

Vapour heat engines currently dominates the power generation using heat energy. These systems use many moving parts to convert the heat energy obtained from combustion of fuel or waste heat. Many of the components in vapour heat engines move at very high speeds and incur dynamic forces that limit their operation in the long run. These systems often require lengthy maintenance and shut down service times. Additionally, the waste heat required for these systems must be made available at high temperatures (> 150 ^{0}C) as the working fluid is mostly in the form of steam. But, TEG based waste heat conversion system is much simpler compared to their conventional vapour power plants. TEGs based system do not require boiler, condenser, working fluid pump or turbine. It is purely a solid state device acting as compact heat exchanger (Hsu, 2011). This build up makes TEG as a reliable and maintenance free device. Additionally, the operation of the TEG system is quiet, due to the absence of any moving parts in them. This makes TEG a new attraction for power generation from renewable energy where temperature gradients are available.

Almost 66 % of the available heat energy is wasted currently. Thermal energy from thermal power plants, automobiles, incinerators, glass and steel factories, gas industry and nuclear power plant utilises only 34 % of the available thermal energy for useful applications (Ghosh, 2012). TEG system can be used to convert this waste heat directly into electricity. This helps in creating a sustainable future and also helps to increase the overall efficiency of thermal systems. Even 1 % increase in the overall efficiency levels in the industry by using TEG can considerably reduce our reliance on fossil fuel. TEG recovery waste heat is attractive as the low conversion efficiency of TEG makes it unnecessary to consider the cost of the thermal input. Figure 2.18 shows the conceptual design of TEG power generation from industrial waste heat.

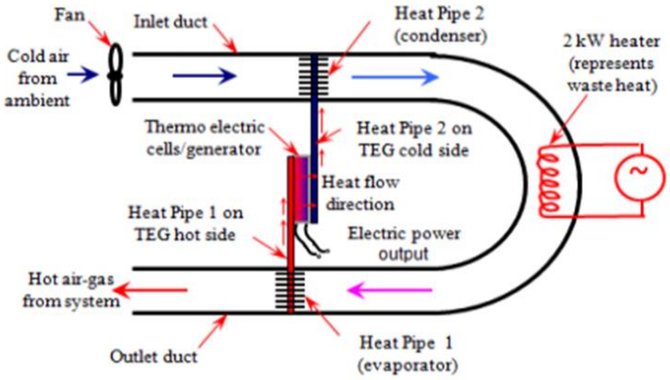

Figure 2.18 Conceptual design of TEG power generation from industrial waste heat (Remeli et al., 2014)

Automobiles and trains have successfully converted the waste heat from the exhaust into useful electricity using TEG, as shown in Figure 2.19. Successful recovery waste heat from exhaust of IC engine into electricity of up to 1 kW using TEG has been demonstrated (Naskar and Kulkarni, 2011). These TEG system uses the vehicle exhaust or body heat as heat source and separate cooling system. The cooling system can be either forced convection cooling with external device or ram air heat sink.

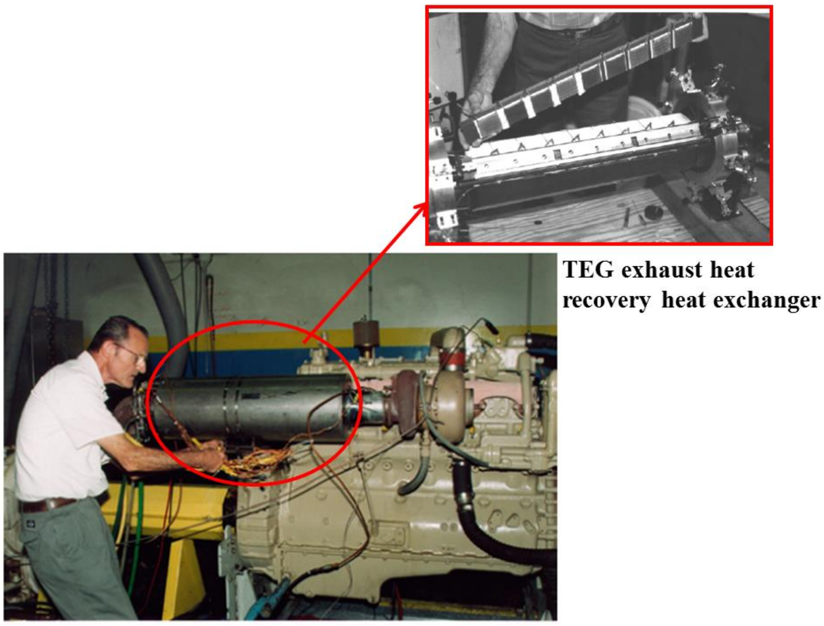

Figure 2.19 One kW TEG power generation from diesel engine (Bass et al., 1994)

TEG power generation in regions with unreliable power supply can be used to supply electricity. The availability of biomass fired stoves with constant temperatures of up to 250˚C can produce 100 W of electricity with only thirty six TEG modules (Lertsatitthanakorn, 2007). TEG power generation from stoves can overcome the low PV load factors in winter, where demand is highest in isolated rural homes (Rinalde, 2010). The limitation of natural convection heat sink for TEG power generation can be overcome with thermosyphonic heat pipe design, where temperature difference for TEG operation is higher than finned heat sink (Nuwayhid and Hamade, 2005). TEG modules are also used for outdoor camping where the electrical output from the module connected to cooking stove is used to recharge electrical appliances like hand phone in camping areas.

2.4.5 Other TEG Applications

Geothermal TEG power generation has been explored for large scale TEG heat exchanger using geothermal heat (Bistchi, 2009). Figure 2.20 shows the overview of proposed TEG geothermal system. Thermoelectric refrigerators driven by solar cells for cold storage of vaccines and perishables have potential for outdoor applications where there is no electricity (Dai et al., 2003). Thermolectric power generation combined with roof solar collectors has been demonstrated for use to supply electrical power, roof heat gain reduction and indoor ventilation of spaces (Maneewan et al., 2004). Themoelectric refrigeration has many advantages when compared to vapour compression and absorption air conditioning. TEG refrigeration is CFC free, lightweight, silent in operation, reliable, fast start-up and can be converted to heating mode by switching the direction of the current flow (Xi et al., 2007).

TEG power generation from human body heat successfully generated electrical power of 50 nW with a temperature differences of only 7 ˚C (Jo et al., 2012). Researchers are currently working on TEG power generation such as glass fabric and felt embedded with thermos elements using body heat for electronic devices charging purposes.

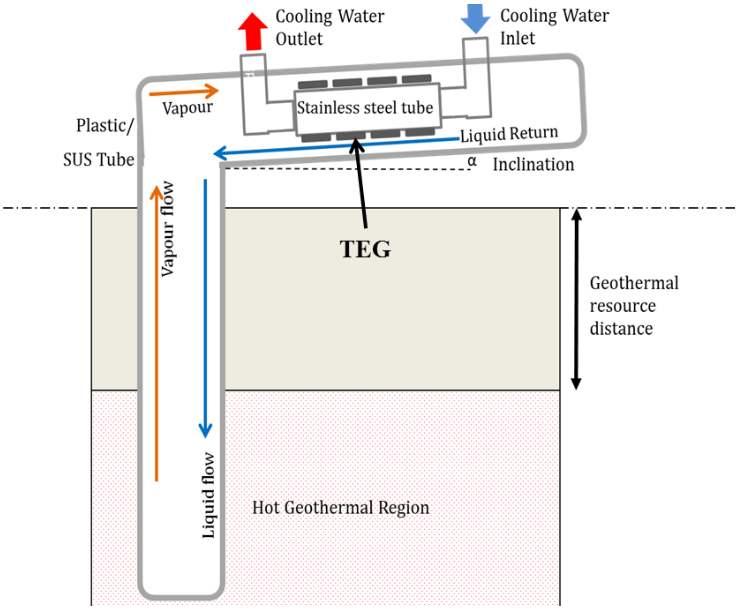

Figure 2.20 Overview of proposed TEG geothermal system (Ding et al., 2015)

2.5 Chapter Summary

TEG can convert electricity directly to DC electricity and are used extensively worldwide for power generation for at least 100 years now. TEG systems with solar pond enable solar energy to be converted easily to DC electricity. Solar pond also allows the storage of heat energy at a much lower cost compared to PV system. This stored heat in solar pond can be converted to electricity using TEG and helps to eliminate the use of batteries for electricity storage. The system is also capable of generating power even with low temperature differences across the TEG. This research provides an alternative source of clean energy for a more sustainable future with minimal or no reliance on fossil fuel.

3.0 RMIT University Experimental Solar Pond

3.1 Introduction

In this chapter, the RMIT University experimental solar pond is described in detail. The operation, maintenance and the 24 hours monitoring system are discussed. The theoretical analysis is compared with the experimental results. Routine procedure to maintain the density, pH and turbidity within the desired limits is discussed. New designs to boost the storage zone temperature and new innovative control system developed for surface flushing are also discussed in this chapter.

3.2 RMIT University Solar Pond Description

3.2.1 Construction

A 53 m^2 circular solar pond was constructed at Renewable Energy Park, Bundoora East Campus, RMIT University in 1988. The diameter of the circular solar pond is 8 m and water is filled to 2.05 m from the floor of the solar pond. This water level is maintained by an overflow system on the northern part of the pond. The overflow system channels the overflow water to the evaporation ponds located in the southern part of the solar pond. The solar pond is 1.35 m above ground for ease of observation. The walls are made of 0.2 m thick reinforced concrete. 1 mm thick epoxy resin is coated on the inside wall of the solar pond to protect it from corrosion and chemical reaction. 30 mm thick polystyrene foam insulation was sprayed to the outer above ground wall to prevent heat loss from the wall of the solar pond. At the bottom of the pond, a 0.2 m thick concrete layer forms the bed of the solar pond. 100 mm thick polystyrene foam was laid on this reinforced concrete bed to prevent heat loss from the solar pond to the ground. The density and thermal conductivity of the foam are 35 kg/m^3 and 0.03 W/m˚C. Another 0.18 m thick layer of reinforced concrete was poured onto the polystyrene insulation layer to negate the buoyancy effect due to the low density insulation material. An observational window was installed at the western part of the solar pond for clarity observational purposes and also for internal heat exchanger tubes monitoring. A 10 mm thick glass with a width of 0.4 m and 1.5 m in length was used to construct the observational window. A cylindrical salt charger made from polyethylene with a diameter of

0.6 m was fixed to the wall of the solar pond. This salt charger is used to replenish the sodium chloride salt lost by diffusion. The bottom of the salt charger is open and it is fixed at 0.56 m from the bottom of the solar pond. The solar pond was designed with a 0.56 m thick bottom storage zone, 1.35 m thick gradient zone and 0.14 m thick to convective zone. Figure 3.1 shows the RMIT University experimental solar pond with the observational window.

Figure 3.1 RMIT University experimental solar pond

T-type thermocouples are used to measure the temperature of the pond at fixed intervals. As shown in Figure 3.2, a total of nine thermocouples are embedded between the concrete structure and the insulation layer to monitor the temperature for heat loss calculation to the ground. The locations of the thermocouples are given in Figure 3.2. Another set of thermocouples are used to measure the in pond water temperature and the heat exchanger tube temperature. The thermocouples for the heat exchanger tubes are placed on the surface of the polyethylene pipe and insulated with Armaflex insulation material. These thermocouples are connected to a data acquisition system for constant temperature recording and monitoring.

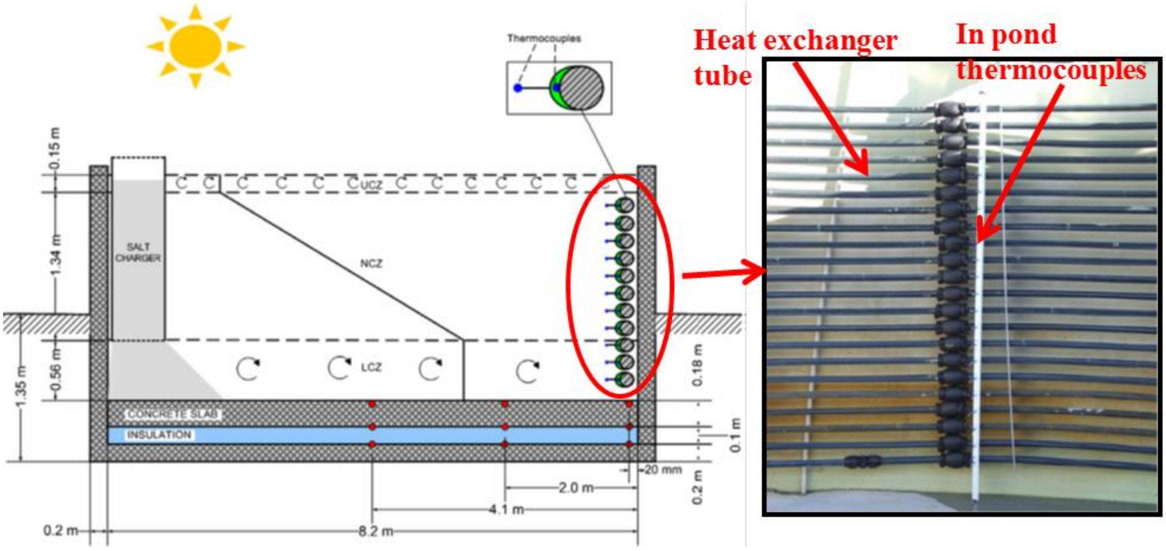

Figure 3.2 Schematic view of solar pond with thermocouples position (Leblanc et al., 2011)

3.3 Theoretical Operation of Solar Pond

3.3.1 Solar Radiation

Figure 3.3 shows the spectral energy curve of solar radiation at sea level and extrapolated outside the atmosphere (Lacis, 1973). Based on the figure, the available solar radiation on earth’s surface is less than the solar energy outside of the atmosphere for the same location. This is due to the absorption and reflection of solar radiation by the earth’s atmosphere. The available solar radiation outside the earth’s’ atmosphere is all beam radiation, where the radiation received from the sun without any change in its direction. On a clear sunny day, majority of the radiation that is available will be beam radiation and only less than 10 % will be diffusive radiation. Diffusive radiation is caused by the scattering effect of the atmospheric conditions. On a fully overcast day, almost all radiation will be of diffusive in nature with negligible bema radiation.

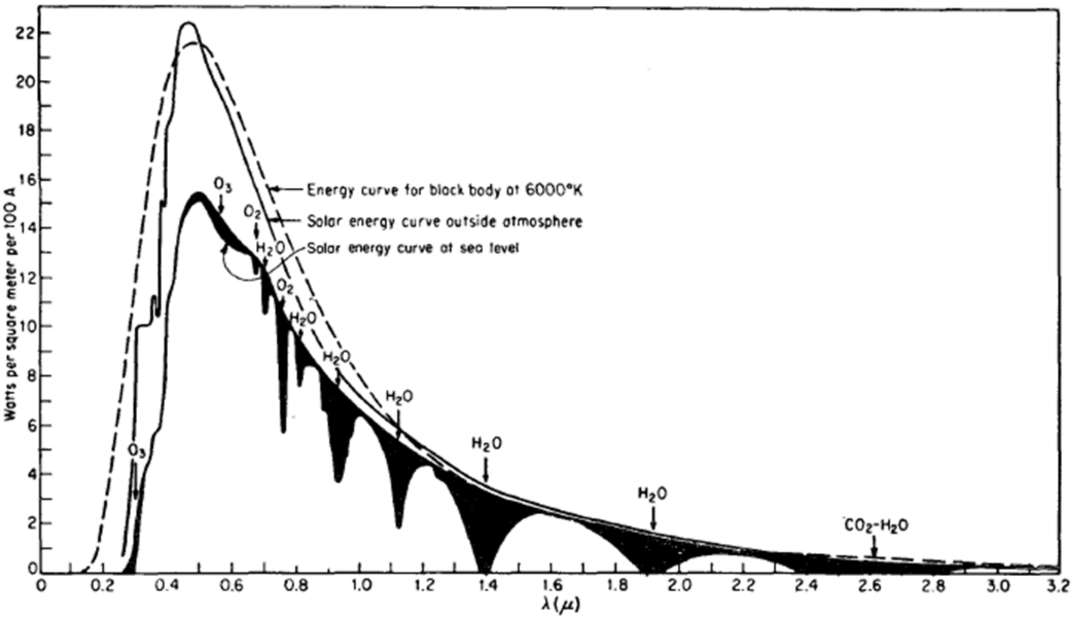

Figure 3.3 Spectral energy curve of solar radiation at sea level and extrapolated outside the atmosphere (Lacis, 1973)

3.3.2 Solar Radiation Transmission in Water

Radiation from the sun that strikes the surface of the body of water will be absorbed, and the remainder reflected back into the atmosphere. The absorbed radiation in the body of water can be converted into useful thermal energy. Water absorbs mostly short wavelength solar radiation. This makes water a good absorber of solar radiation. The radiation can also be transmitted into the bottom storage zone of solar pond via transmission of solar radiation. The transmission of solar radiation through the pond water is one of the most important factors in determining the solar pond efficiency. The clarity of the solar pond must be kept as high as possible to avoid suspended particulate matters from absorbing and scattering the solar radiation in the pond. There is not much difference in light attenuation in fresh water and water dissolved with NaCl salt (Smith and Baker, 1981).

For a given wavelength, λ of light, the transmission of light in water through a distance d is given by

$$\tau_l = (\lambda, d) = \exp[\, - d/\delta(\lambda)] \tag{3.1}$$

where $\delta(\lambda)$ is given as characteristic wavelength attenuation length.

If particle scattering were very important, the total transmission of a beam solar radiation incident to the surface of water through a distance d is given by:

$$\tau_l(d) = \tau_s \int_0^\infty S(\lambda)\tau(\lambda, d)d\lambda = \tau_s \int_0^\infty S(\lambda) \exp\left[-\frac{d}{\delta(\lambda)}\right] d\lambda \qquad (3.2)$$

where τ_s is fraction of the incident radiation penetrating the surface of the pond in relation to reflectance, ρ_r given as:

$$\tau_s = 1 - \rho_r \qquad (3.3)$$

The function of depth, z in a pond is an important factor to calculate the thermal performance of solar pond. This function is given as:

$$d = z/\cos \Theta_r \qquad (3.4)$$

where Θ_r is the refracted angle.

From equation, substituting (3.4) into (3.3) gives:

$$\tau_l(z, \theta_r) = \tau_s \int_0^\infty S(\lambda)\exp[-z\, sec\theta_r\, /\delta(\lambda)]d\lambda \qquad (3.5)$$

As the integral of the equation 3.5 is time-consuming, approximate simplified representation by Rabl and Neilsen (1975) is given below:

$$\tau_l(d) = \tau_s \sum_{i=1}^{4} S_i \exp(-\frac{d}{\delta_i}) \qquad (3.6)$$

where $\tau(d)$ is the total transmission solar radiation incident on a water surface through a distance d

τ_s is the fraction of solar radiation that penetrates the air/water interface

S_i is a normalised spectrum distribution function of the incident solar radiation for wavelength band i.

δ_i is the characteristic attenuation length for wavelength band i.

The four term series above can be adequately fitted to most transmission function for 0.1 m < z <3 m as shown in Figure 3.4.

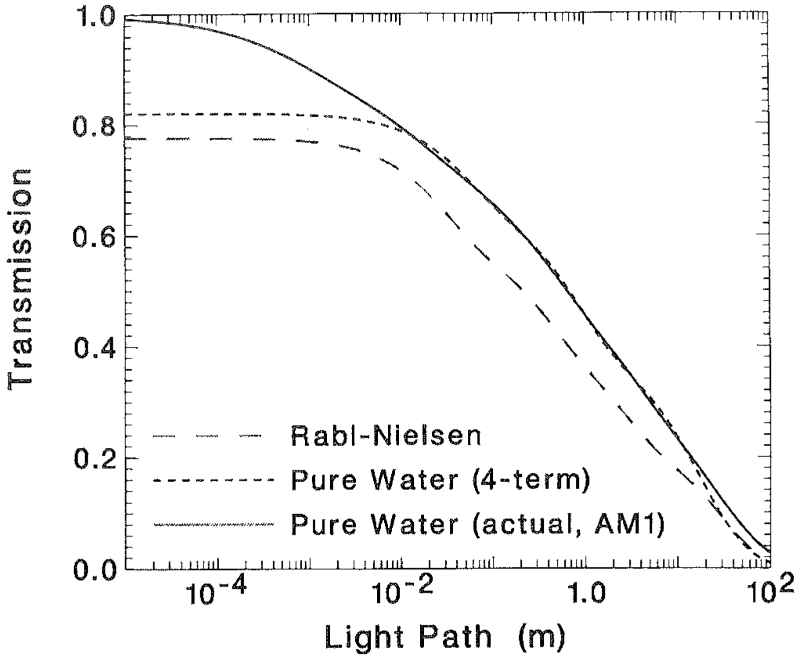

Figure 3.4 Light transmissions versus light path (Hull et.al., 1989)

Table 3.1 Parameters for four terms series fit of pure water transmission (Hull et al., 1989)

i	**S_i**	**δ_i(m)**
1	0.156	34.7
2	0.249	13.3
3	0.259	0.781
4	0.156	0.0509

As the parameters in Table 3.1 represent the transmission in pure distilled water, in practice the solar pond will never achieve this transparency. A clean sea water transparency can be used to approximate the transmission of solar radiation. Table 3.2 provides the parameters for four terms series fit of clean sea water transmission Rabl and Neilsen (1975). From figure 3.4, the transmission curves are almost straight lines for the light path range from $0.1 < z < 3$ m. This lead to the following transmission functions by Bryant and Colbeck, 1977.

$$\tau_l(d) = a - b \ln (d/\delta), \quad (3.7)$$

where the values of constants are given as $a = 0.36$, $b = 0.08$ and $\delta = 1.0$.

Although this transmission function has no physical basis, it provides a reasonable fit for the region in the range $0.1 < z < 3$ m and has been adopted by many researchers (Hull, 1980).

Table 3.2 Parameters for four terms series fit of clean sea water transmission Rabl and Neilsen (1975)

i	**S_i**	**δ_i(m)**
1	0.237	31.2
2	0.193	2.22
3	0.167	0.333
4	0.179	0.0286

.

Figure 3.5 shows the attenuation of solar radiation in a solar pond with increasing depth. Assuming a solar pond with a total depth of 2.5 m, where UCZ, NCZ and LCZ zones is 0.4 m, 1.4 m 0.7 m thick respectively, the amount of solar radiation available in the UCZ and NCZ interface is only 43 %. The rest is absorbed by the UCZ zone. Only 32 % of the total solar radiation is available in the NCZ and LCZ interface.

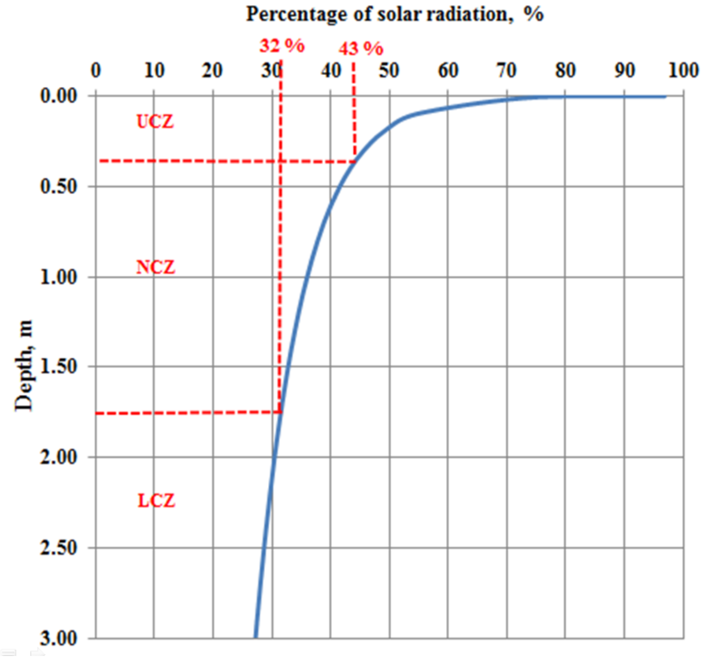

Figure 3.5 Penetration of sunlight into solar pond

3.3.2 Steady State Heat Storage at LCZ Zone

Steady state analysis provides a good a reliable tool for solar pond thermal analysis. A quick thermal change in the environment does not change thermal environment of the pond (Kooi, 1979). The gradient zone in a solar pond utilises the heat in the NCZ zone for maintaining and building the temperature gradient. The amount of heat input and output from this zone is equal. The UCZ and NCZ zones are considered to be a lumped system as these zones are assumed to be well thermally mixed regions (Akbarzadeh, 2005). A one-dimensional conduction flux can be used for steady state thermal analysis of solar pond. Figure 3.6 shows the energy balance in a typical solar pond.

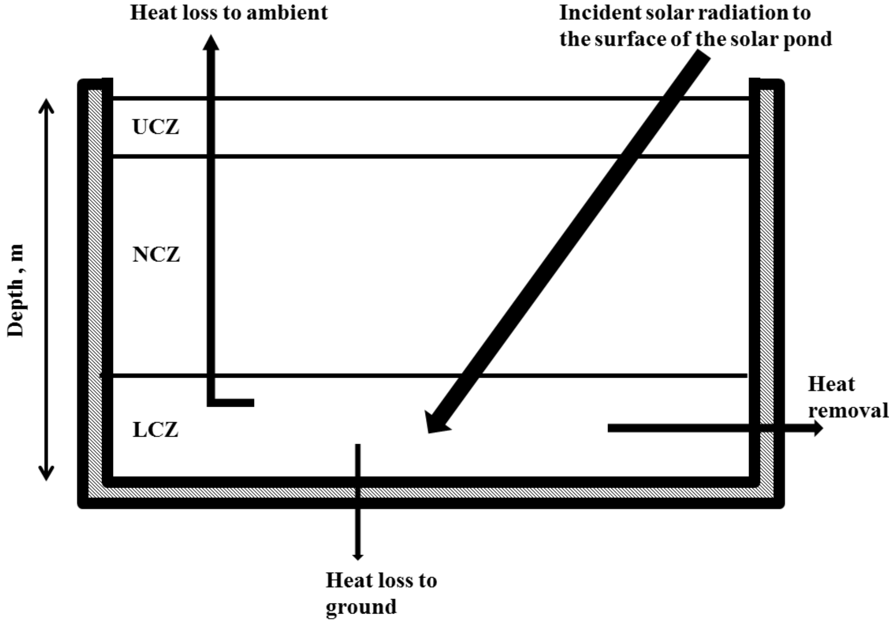

Figure 3.6 Energy balance in solar pond

The equation representing heat storage in the storage zone, Q_{LCZ} based on one dimensional energy balance is given below:

$$Q_{LCZ} = Q_I - Q_{HR} - Q_{hlg} - Q_{conv\text{-}loss} - Q_{rad\text{-}loss} - Q_{evap\text{-}loss} \tag{3.8}$$

The heat losses to the walls are assumed to be negligible and the walls are assumed to be well insulated for one-dimensional steady state analysis.

Q_I is the amount of solar radiation incident to the top the UCZ. The equation to calculate Q_I is given by equation 3.7.

Q_{hlg} represents the heat loss to the ground/soil. This equation is represented by:

$$Q_{hlg} = k_G A (T_{LCZ} - T_G)/x_{G,} \tag{3.9}$$

where k_G (W/m K) is the thermal conductivity material of the ground below the surface of solar pond. x_G is the thickness of the ground material. T_G is the ground temperature and T_{LCZ} is the LCZ zone temperature, both in ^{0}C.

The following equations ($Q_{conv\text{-}loss}$, $Q_{rad\text{-}loss}$, $Q_{evap\text{-}loss}$) are referred from Kanan et.al., 2014. $Q_{conv\text{-}loss}$ represents the heat loss to the ambient environment due to convection. The equation is given by:

$$Q_{conv\text{-}loss} = h_c A (T_{UCZ} - T_A) \tag{3.10}$$

where h_c (W/m^2 K) is the convective heat transfer coefficient given by :

$$h_c = 5.7 + 3.8V_a \tag{3.11}$$

where V_a is the average monthly wind speed in m/s. T_{UCz} is the temperature of UCZ . T_A is the ambient temperature.

$Q_{rad\text{-}loss}$ is the radiative heat loss from the solar pond. The equation to calculate $Q_{rad\text{-}loss}$ is given below.

$$Q_{rad\text{-}loss} = \sigma\epsilon_w\{(T_{ucz}+273)^4+(T_{sky}+273)^4\} \tag{3.12}$$

Where σ is the Stefan Boltzmann's constant.

ϵ_w is emissivity of water (0.83)

T_{sky} is the sky temperature given as follow:

$$T_{sky} = T_A-(0.55+0.061(P_1^{0.5}))^{0.25}$$

Where P_1 = vapour pressure of water at the surface temperature

$= \exp(18.403 - 3885/(T_{ucz}+230))$

$Q_{evap\text{-}loss}$ is given by following equation:

$$Q_{evap\text{-}loss} = L_v h_c(P_1-P_a)/(1.6C_sP_{atm}) \tag{3.13}$$

where L_v = latent heat of evaporation of water (J/kg)

C_s = Humid heat capacity of air (J/ kg ^{0}C)

P_a = Partial pressure of water vapour in the ambient air

$$=\exp(18.403-3885/(T_A+230))RH \tag{3.14}$$

Wher RH is the relative humidity in %.

Q_{HR} is the total heat removal from the solar pond. A pump circulates working fluid through the in-pond heat exchangers to remove heat from the storage zone of the solar pond. The equation for heat removal from solar pond can be represented as:

$$Q_{HR} = \dot{m}\, c_p (T_{LCZ} - T_{inwf})\, t \tag{3.15}$$

where $\dot{m}$ is the mass flow rate through the pump in the heat exchanger in kg/s. c_p is the specific heat capacity of the working fluid and T_{inwf} is the inlet temperature of the working fluid in ° C. t is the time taken for the heat removal in seconds. Figure 3.7 shows the heat exchangers used for the heat removal from the LCZ and also NCZ zones. These submerged tubes are made of reinforced polyethylene pipes. The outer diameter of these tubes is 32 mm with 3 mm thickness. The wall heat exchanger is 560 m long with a heat transfer area of 56 m^2. The bottom heat exchanger is shorter with a total length of 83 m and total surface area of 8 m^2. The thermal conductivity of the heat exchanger pipes are given as 0.37 W/m K.

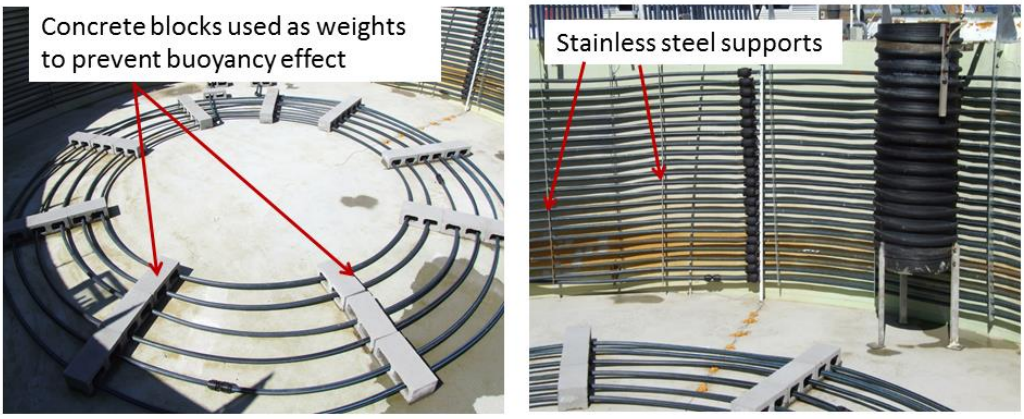

Storage zone heat exchanger

Wall (NCZ and LCZ zone) heat exchanger

Figure 3.7 Heat exchanger tubes used for the heat removal from the LCZ and also NCZ zones

Based on the equation (3.8), the efficiency of the solar pond can be calculated from the following equation:

$$\eta_{SP} = \frac{Solar\ Radiation\ input\ in\ LCZ - Total\ Losses - Heat\ Removal\ from\ LCZ}{Solar\ radiation\ input\ at\ surface\ of\ the\ solar\ pond}$$

$$= [Q_I - (Q_{hlg} + Q_{conv} + Q_{rad} + Q_{evap}) - Q_{HR}]/Q_{I=0} \quad (3.16)$$

The solar radiation input at the surface of the solar pond can be written with a reflection loss adjustment factor, f_ρ as shown by equation below:

$$H_I(x) = f_\rho\ H_I(x=0)\ (a - \left\{b ln \frac{x}{cos\theta_r}\right\}) \quad (3.17)$$

where H_I (x) is the solar radiation in W/m^2 available at a depth of x m in the pond.

Q_I (x=0) is the solar radiation in W/m^2 available at the surface of the pond.

x is the distance of the LCZ from the surface of the pond in metres.

a and b are constants equal to 0.36 and 0.08 respectively.

f_ρ is the reflection loss adjustment factor given in table 3.3.

Θ_r is the angle of refraction.

The angle of refraction can be calculated from Snell's Law (Jafarzadeh, 2005), as follow:

$$\sin\Theta_i/\sin\Theta_r=1.333 \tag{3.18}$$

where Θ_i is the angle of incidence of direct radiation to a horizontal plane with normal.

Given

$$\cos\Theta_i = \cos\delta\cos\varphi\cos\omega+\sin\delta\sin\varphi \tag{3.19}$$

where δ is the angle of declination, ϕ is the angle of latitude and ω is the hour angle.

The declination angle is given as :

$$\delta = 23.45 \sin (360(284+N)/365.25) \tag{3.20}$$

where N is the day of the year.

The hour angle is given by :

$$\omega = 2\pi(h-12)/24 \tag{3.21}$$

where h is the hour.

Table 3.3 Reflection loss adjustment factor (Tabor and Weinberger, 1981)

Latitude (degrees)	**Reflection Loss Adjustment Factor, f_ρ**
0 - 29	0.98
30 -43	0.97
44 -49	0.96
50 -53	0.95
54 -56	0.94
57 – 58	0.93
59 – 60	0.92
61 -62	0.91

Typical solar pond efficiency is about 15 – 20%. Heat should be extracted at a rate proportional to the monthly average solar radiation for optimum operation of a solar pond. This will result in higher thermal efficiency at variable load when compared to constant heat extraction (Al Jammal and Kasshan, 1996). For combination of heat extraction from NCZ and LCZ, the thermal efficiency of solar pond can be improved further to 25% (Date et al., 2013). The overall thermal efficiency of a solar pond could be enhanced by up to 50% when compared to heat extraction solely from the LCZ. (Yaakob, 2011).

3.4 Gradient Establishment

The salinity gradient profile of the RMIT University solar pond was re-established in early 2012 after the changing of the steel brackets supporting the heat exchanger tubes. These earlier steel brackets were made from galvanised steel. It was badly corroded after being exposed to the highly corrosive environment of the solar pond over a decade long. New stainless steel bracket were made to refurbish the old ones. The stainless steel used for these new brackets was of grade 316 that can withstand highly corrosive environment. The salinity gradient of the solar pond was then established once the new stainless steel brackets were installed. The pond was filled with the redistribution technique used by Zangrando, 1980. With a given proposed depth of the solar pond as D = L + H, with the storage zone depth taken as L and the H as the gradient zone thickness. The concentration of the salt in storage zone is taken as C_c and the concentration of salt in the gradient zone will be at $\frac{1}{2}C_c$. The pond is initially filled with saturated brine with maximum concentration, C_c to a depth of L + $\frac{1}{2}$H. The fresh water is then injected with a diffuser at height L. The diffuser is raised at a constant rate and fresh water injected will mix with saturated brine at top of the diffuser and diluting the solution as the diffuser is moved upward until the pond is filled to D, the maximum capacity of the solar pond. The diffuser is moved in a proportional rate to the surface motion.

If the diffuser position is taken as y_d starting from height L and the y_s is the position of the diffuser at height L +$\frac{1}{2}$ H, the proportionality can then be written as:

$$y_d = c_1 y_s + c_2 \text{ , where at } t = 0,\ y_d = L \text{ and } y_s = L + \frac{1}{2}H \tag{3.22}$$

$$\text{at } t = t_f,\ y_d = y_s = L+H$$

In the final position,

$$y_d = 2y_s - (L + H) \text{ and } \dot{y}_d = 2\,\dot{y}_s \tag{3.23}$$

where $\dot{y}$ is the time derivatives and $\dot{y}_s$ is the flow into the diffuser divided by the area of the pond, A.

The evolution of the concentration in the mixed layer above the diffuser is governed by:

$$\dot{C}_a(t) = \frac{d}{dt}\left(\frac{M}{V_a}\right) = \frac{\dot{M}}{V_a} - C_a(t)\frac{\dot{V}_a}{V_a}, \tag{3.24}$$

where $V_a(t)$ is the volume of brine above the diffuser,

$$V_a(t) = A[y_s(t) - y_d(t)] = \frac{A}{2}[L + H - y_d(t)] \tag{3.25}$$

Brine of concentration C_a is lost due mixing at the bottom of the diffuser at a rate of $\dot{y}_d$, therefore

$$M(t) = \dot{-}C_a(t)\dot{y}_d\mathrm{A} \tag{3.26}$$

which yields:

$$\dot{C_a}(t) = C_a(t)\left[-\frac{2\dot{y}_d}{L+H-y_d} + \frac{\dot{y}_d}{L+H-y_d}\right]$$

$$= -\frac{C_a(t)\dot{y}_d}{L+H-y_d} \tag{3.27}$$

when $C_a(0) = C_c$ and $y_d = L$, after integrating equation (3.6), we get:

$$C_a(t) = C_c\left(\frac{L+H-y_d}{H}\right) \tag{3.28}$$

The layers below the diffuser never moves once the diffuser passes over them, that gives $C_a(y_d(t))$ as the salinity profile left at a distance of $y_d(t)$ from the bottom, hence the final profile within the gradient zone is given as:

$$C_y = C_c\left(\frac{L+H-y}{H}\right) \tag{3.29}$$

The storage zone and gradient zone thickness was identified. Then based on the above technique, the solar pond was filled with saturated brine until the middle of the gradient zone. A diffuser as shown in Figure 3.8 was used to inject fresh water into the saturated brine starting from the storage and gradient zone interface. The diffuser was made with two semicircular discs with a diameter of 350 mm and a vertical gap of 3 mm. The thickness of the each semicircular plate was 25 mm. The horizontal gap in the diffuser was at 8 mm. As the thickness of the storage zone was set at 0.56 m, this point was chosen as the start of the injection of the fresh water. The diffuser was then raised twice the rise in the water level in a stepwise manner. A 5 cm rise in the water level that leads to a 10 cm rise in the diffuser level is the most widely applied experience in the salinity gradient establishment in practice today. The diffuser was risen in such that the diffuser reaches the predetermined final level at the surface of the pond. Fresh water at rate of 0.3 kg/s was injected into each layers of the saturated brine. This fresh water was obtained from the town water supply available at the Renewable Energy Park, RMIT University. The above flow rate kept the Froude number below 16, as suggested by Zangrando, 1979. Fresh or low salinity water is injected horizontally into the body of water in the solar pond. The mixing occurs only in the region above the level of injection.

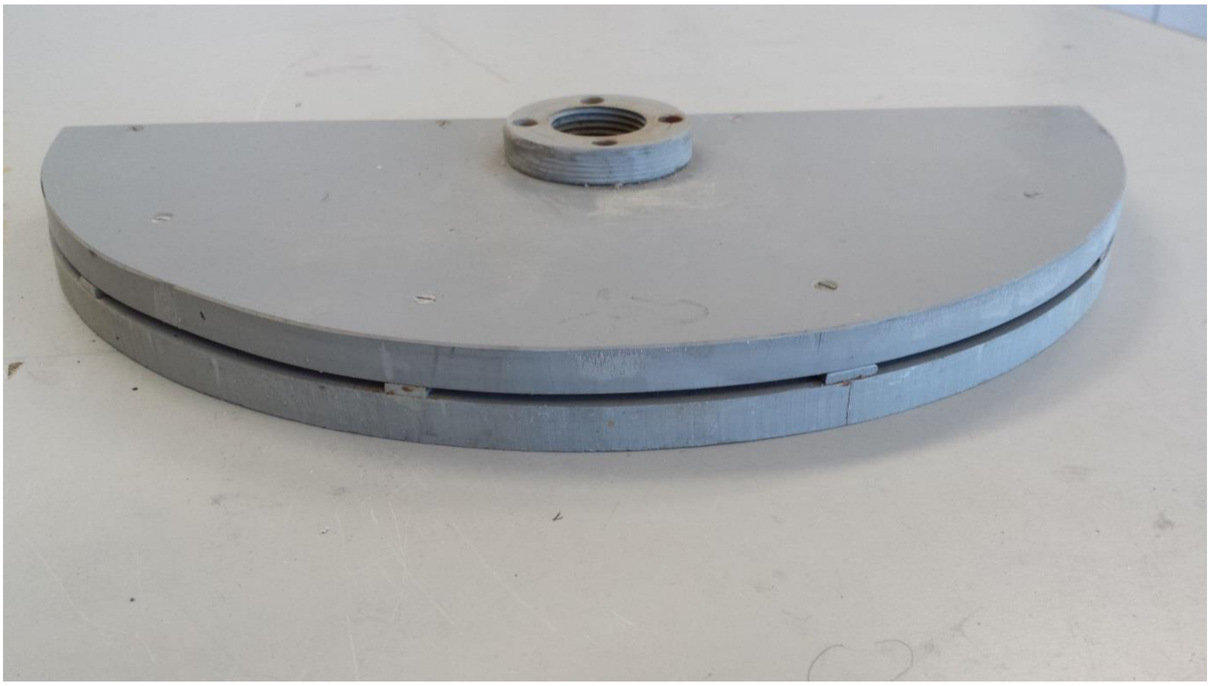

Figure 3.8 Diffuser used for gradient establishment

The density gradient of the RMIT University solar pond was established in 4 days as shown in Figure 3.9. The evolution of the density gradient is evident from the density profile shown in the Figure 3.9. The diffuser injected fresh water starting from the storage and the gradient zone interface. As the pond was filled with saturated brine initially, the fresh water injected with the help of diffuser diluted the saturated brine above the diffuser level. This created a lower density fluid as the diffuser moved upwards in a stepwise manner. The density gradient was fully established once the diffuser reached the top level of the solar pond.

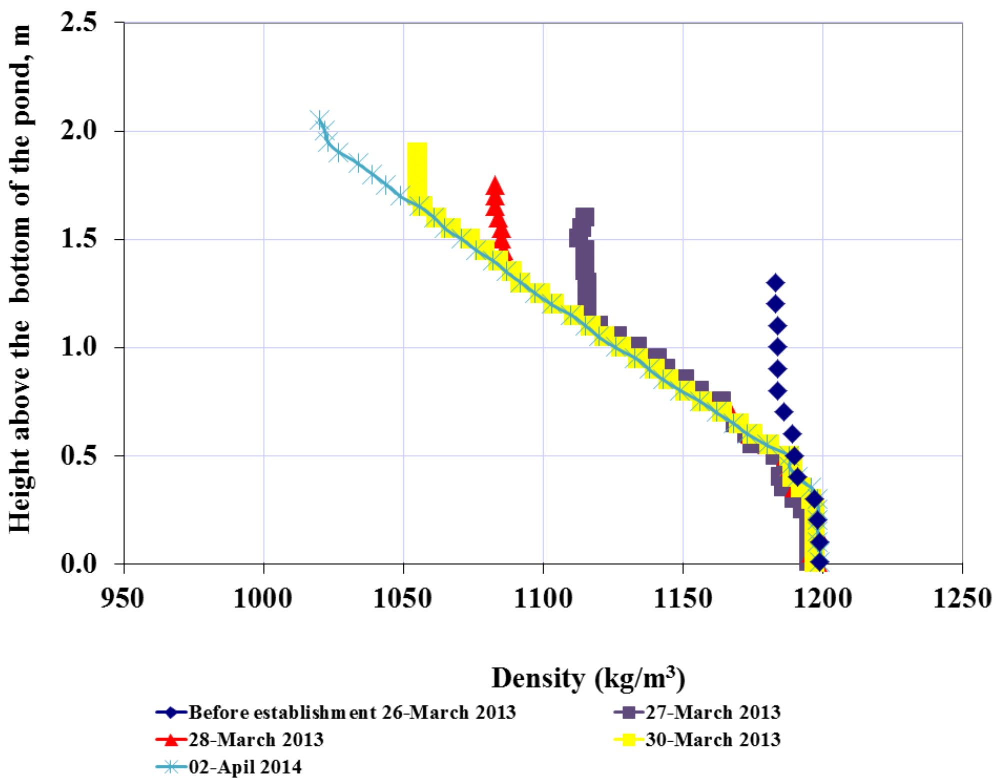

Figure 3.9 Evolution of the density gradient

3.5 Instrumentation and Data Acquisition System

3.5.1 Temperature Tracking

Data acquisition system was used to record and monitor the temperature of the RMIT University solar pond. A DataTaker (DT500 & channel expansion module (CEM) series) was used to achieve the above. The data acquisition system is shown in Figure 3.10. A computer system located 50 m away from the data acquisition system records the data. The temperature of the solar pond is measured every 30 minutes in a day. The data acquisition system also measures the solar irradiance for every 10 seconds in a day. A total of fifty-seven thermocouples (T-type) are used for temperature measurements. Forty-four thermocouples are used to measure the in pond temperature and also the heat exchanger wall temperature in the solar pond. These thermocouples are arranged vertically with a distance of 80 mm between each thermocouple. The first thermocouple in the vertical direction is located 0.2 m from the bottom of the solar pond. A thermocouple is located above the UCZ of the solar pond to record the ambient temperature. Another nine thermocouples are embedded between the reinforced concrete and the insulation layer at the bottom of the solar pond for ground heat losses monitoring. The positions of the embedded thermocouples from the wall of the solar pond was set at 20 mm, 2 m and 4 m, as shown in Figure 3.2. The thermocouples used to measure wall temperature of the heat exchanger tubes are insulated and covered with Armaflex insulation.

Figure 3.10 Data acquisition system for temperature and solar radiation data logging

Figure 3.11 shows the dial thermometer used for top and bottom zones temperature of the solar pond. These dial temperatures are installed on the southern side of the top concrete wall.

Figure 3.11 Dial thermometers on the concrete wall

3.5.2 Solar Radiation Tracking

A solar cell pyranometer (SolData 80SPC) was used to record the global solar radiation data. The solar cell pyranometer consist of a photovoltaic cell that provides the output in mV. The solar cell was placed on a horizontal plane 2.5 m above ground to obtain the amount of solar radiation striking the surface of the solar pond. The output of the solar cell pyranometer was connected to the data acquisition system and solar radiation data were recorded every 10 s in a day. The calibration factor, K provided by the manufacturer was given as 154 mV/(kW/m^2). This means for a 1 kW/m^2 solar radiation received on a clear sunny day, the voltage produced will be 154 mV. The voltage output varies linearly with the solar radiation striking the solar cell. After operating for more than 12 years, the solar cell pyranometer was calibrated by Vipac Engineers & Scientist facility in Melbourne of early 2012. The new calibration factor was set as 143 mV/ (kW/m^2). Figure 3.12 shows the solar cell pyranometer used to record the solar radiation data for RMIT University solar pond.

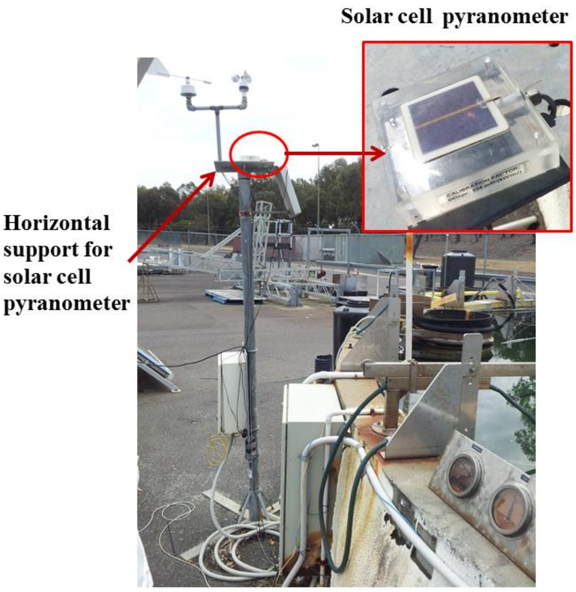

Figure 3.12 Solar cell pyranometer located 2.5 m above ground for solar irradiance data acquisition.

Figure 3.13 shows the daily solar radiation obtained by the solar cell pyranometer at RMIT University on 30/12/2013 in 24 hours. The solar cell pyranometer recorded the global solar radiation every 10 seconds. The maximum radiation was recorded at 1:36 PM with a value of 1106 W/m^2. The dip in the values of the radiation as shown in Figure 3.13 was due to the momentary overcast by the clouds. This caused the drop in the readings. The readings are taken daily throughout the year. From the daily global solar radiation data, an average value can be obtained for the radiation data. For a month, a mean value for the daily global solar radiation can be calculated from the recorded data. This is then compared with the data obtained from the Bureau of Meteorology (BOM) website. The nearest station for the BOM is located at distance of about 5 km away from the RMIT University solar pond at La Trobe University.

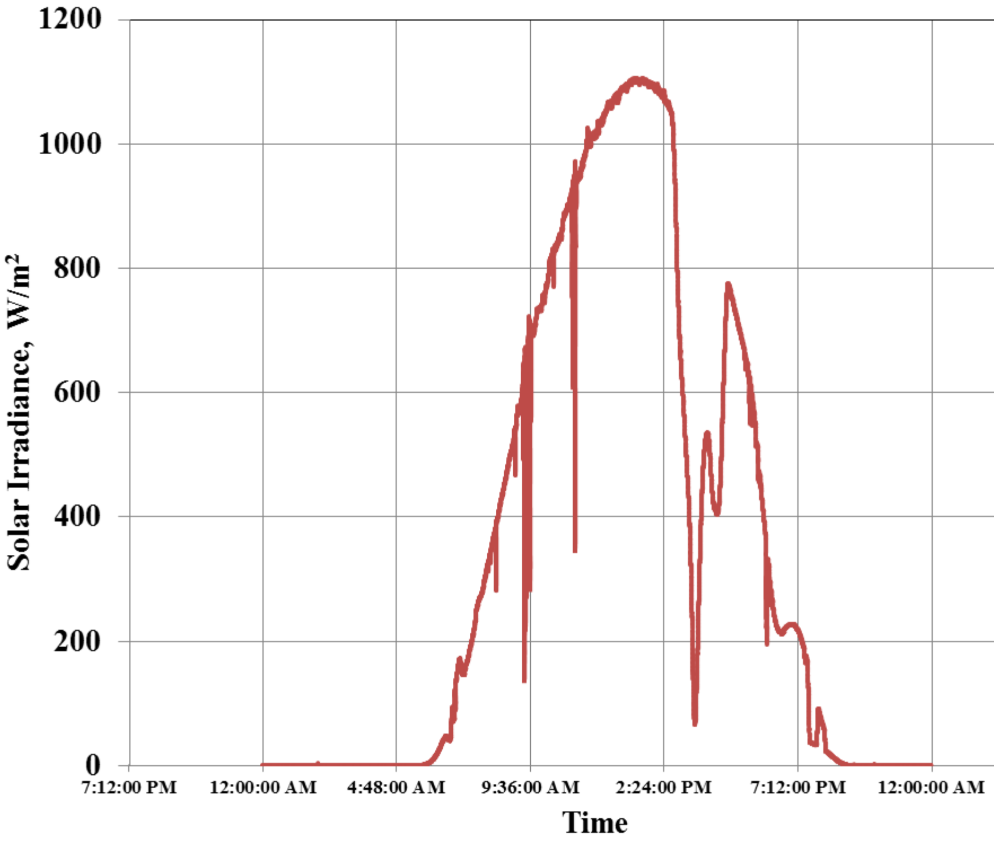

Figure 3.13 Daily solar irradiance obtained by the RMIT University solar cell pyranometer on 30/12/2013

Figure 3.14 shows the average monthly daily global solar irradiation from April 2013 to July 2014. The figure also shows the average daily monthly ambient temperature. The readings obtained from the RMIT University solar cell pyranometer was compared with the readings obtained from BOM website (Appendix A). Both the average monthly daily global solar irradiation for the above period shows similar trend and with little variation between the values obtained from RMIT University and BOM. The slight discrepancy between the data obtained from both the sources could be due to the different instrumentation used for data recordings at both the above locations. From Figure 3.14, it can be seen that the readings obtained from the RMIT University solar cell pyranometer was reasonably comparable to the data obtained from Bureau of Meteorology, Australia. The highest average monthly daily global solar irradiation was recorded at 286 W/m^2 in January 2013. The lowest average monthly daily global solar irradiation was recorded at 58 W/m^2 in June 2014. Both the maximum and minimum values of the average monthly daily global solar irradiation were obtained in summer and winter respectively. On average, 151 W/m^2 of average monthly daily global solar irradiation for the above period was received at RMIT University solar pond site. The average ambient temperature for the same period was recorded at 17 ˚C.

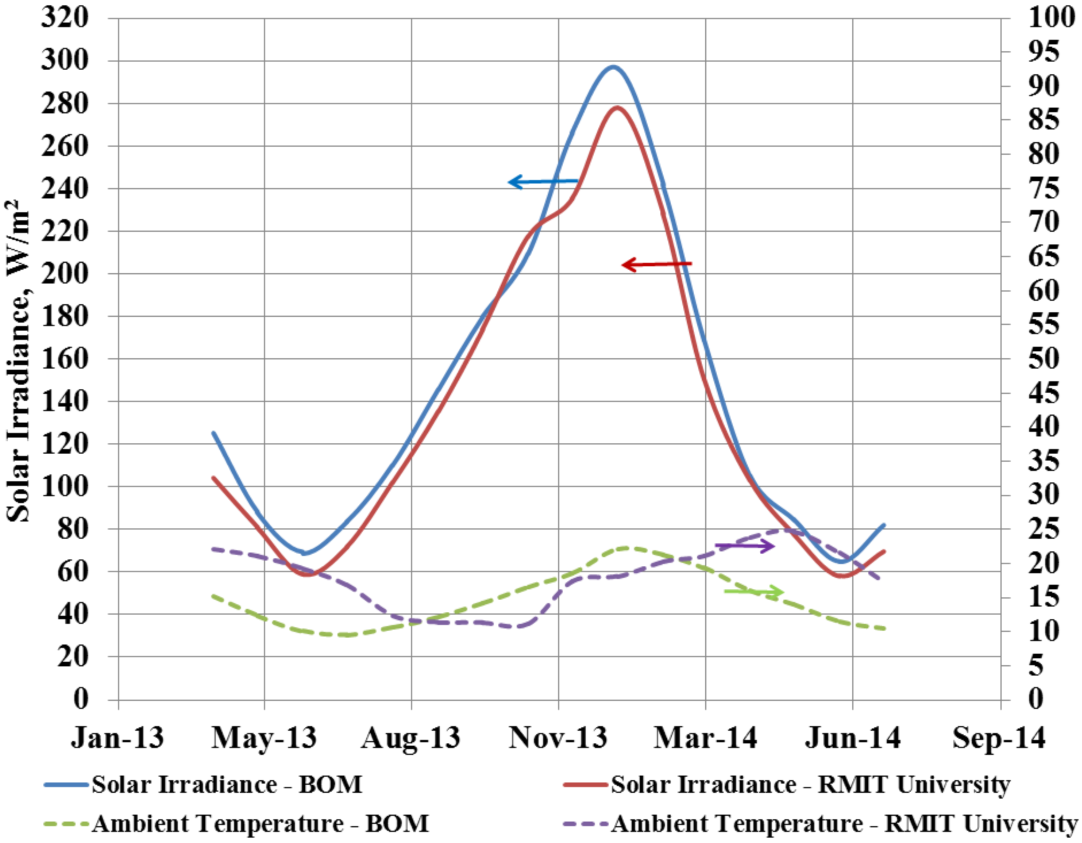

Figure 3.14 Monthly average global solar irradiance from April 2013 to July 2014

3.6 Solar Pond Density and Temperature Profiles

3.6.1 Density Profile

Solar pond can be divided into three distinctive zones, namely LCZ, UCZ and NCZ. These three zones need to be maintained for optimum performance of the solar pond. The thickest region in the solar pond is NCZ. This zone plays the most important role in suppressing the convection currents in the solar pond. Figure 3.15 shows the evolution of thickness of all three zones for RMIT University solar pond from April 2013 to July 2014. It is shown that the thickness of LCZ was maintained at a fixed level between 0.5 – 0.6 m. The thickness of the UCZ varies according the environmental factors. UCZ tends to increase when there are strong wind conditions and during rainy days. High ambient temperatures during the summer months also contribute to thicker UCZ zone. These external elements cause mixing in the upper layers and allow UCZ to penetrate deeper into the NCZ and decreases the thickness of NCZ. Internal factors like salt transportation from the saturated region in LCZ to low saturated region in UCZ also affects the NCZ zone thickness. This can be overcome with constant flushing of the surface of solar pond with fresh water and salt addition to the LCZ. The typical thickness of the UCZ is around 0.1 m to 0.25 m for the above mentioned period. The NCZ zone was maintained around 1.4 m throughout from April 2013 to July 2014. Overall, the thickness of the three zones in the RMIT University solar pond was maintained reasonably according to the initial designated thickness throughout the 16 months period.

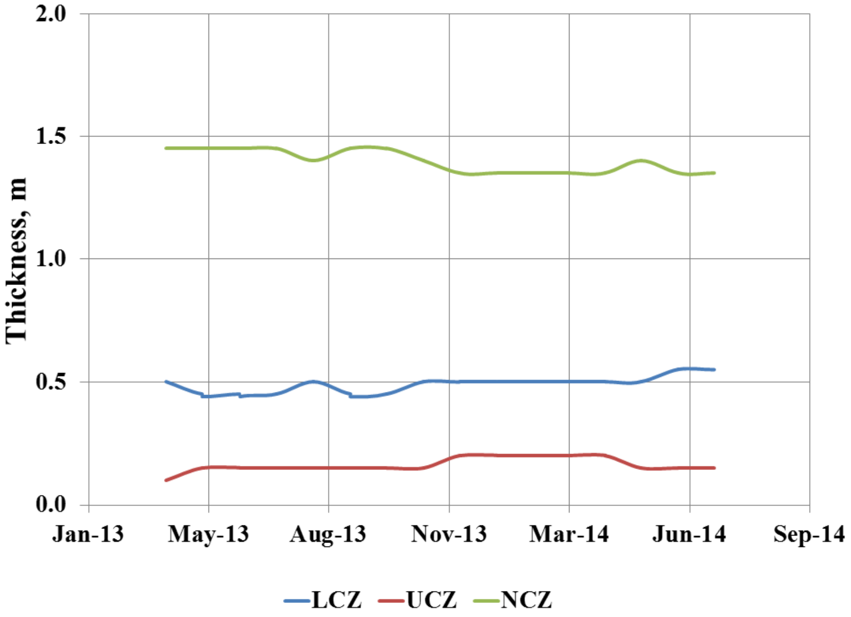

Figure 3.15 The evolution of LCZ, NCZ and UCZ over 16 months

Figure 3.16 shows a typical salinity profile of RMIT University solar pond. This profile was obtained 10th of February 2014. The profile shows the thickness of each zones and its corresponding thickness. From the profile shown, it can be identified that the LCZ zone is 0.5 m thick, NCZ is 1.4 m thick and the UCZ is about 0.25 m thick. The density in the LCZ zone was maintained at 1200 kg/m^3. The density in the UCZ zone was measured to be around 1006 kg/m^3. The density profile taken on a regular basis from a solar pond allows for the maintenance of the density profile of a solar pond. If the density profile of a solar pond is compromised, remedial actions can be taken to rectify the density profile for optimum performance of the solar pond operation, as outlined by Yaakob, 2014. Figure 3.17 shows the average monthly density profile taken from April 2013 to July 2014. From the figure, we can see that the density profile of RMIT solar pond was maintained very well for the 16 months period. The top density profile in the UCZ zone was affected by the external strong wind conditions as well as the rainy seasons that induce mixing the upper zone of the solar pond. Eventually, the profile healed itself overtime. Also from the same figure, the NCZ thickness and gradient was maintained reasonably well in the above-mentioned period.

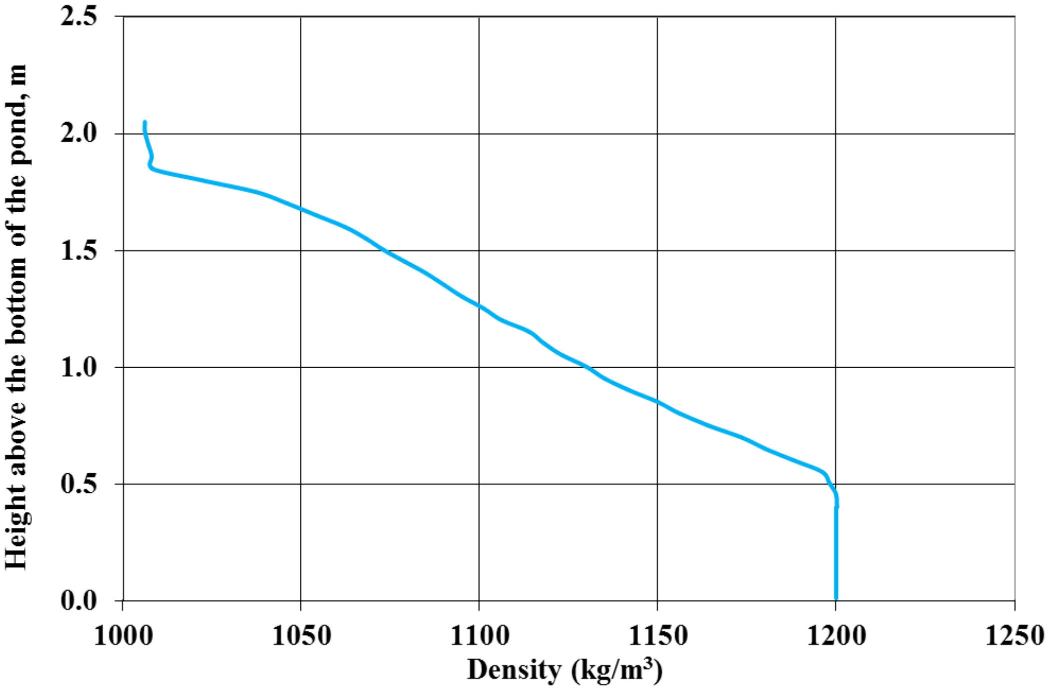

Figure 3.16 Density profile of RMIT University solar pond taken on 10/2/2014

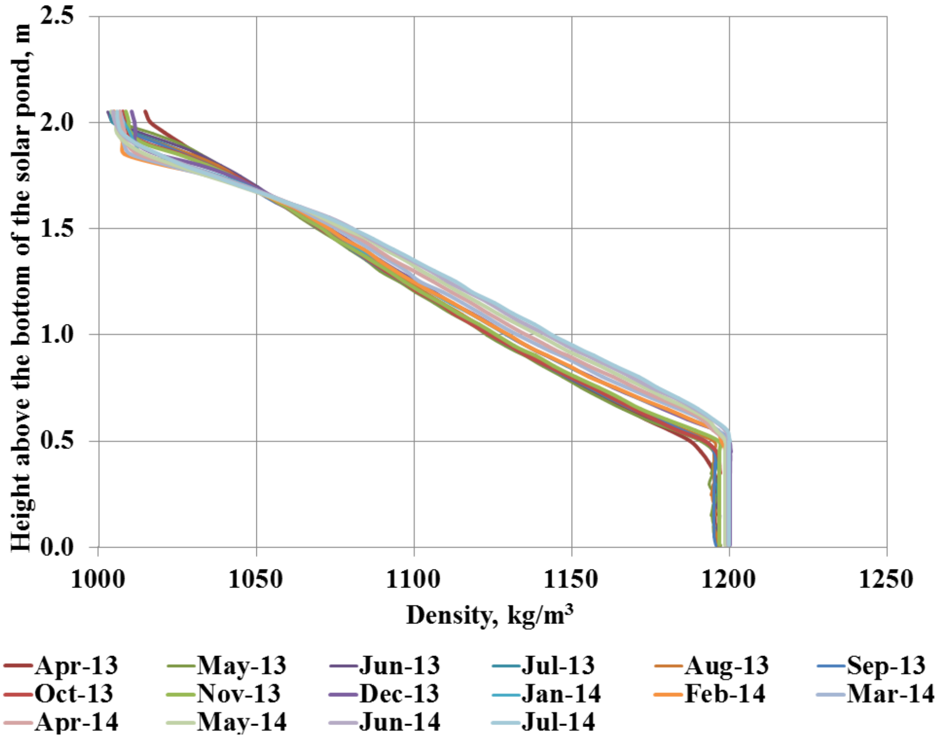

Figure 3.17 Evolution of average monthly density profiles for RMIT University solar pond from April 2013 to July 2014

3.6.2 Temperature Profile

Figure 3.18 shows a typical temperature profile for RMIT University solar pond. The temperature profile was taken on 10th of February 2014. The maximum temperature at the bottom of the storage zone was recorded at 74.9 ˚C. The temperature profile in the LCZ zone is not in a vertical line due to ground heat losses. As the temperature in the ground is much lower than the LCZ zone, heat is lost to the ground from the LCZ zone via conduction. The lowest temperature was recorded at the top of UCZ at 22.0˚C. The temperature difference available from the temperature profile was at 52.9˚C between the UCZ and LCZ zones. The temperature in the NCZ drops from a maximum in the LCZ-NCZ interface to 24.3˚C in the NCZ-UCZ interface. It is also possible to distinguish the thickness of LCZ, NCZ, and UCZ zones of the solar pond from the temperature profile, as shown in the figure. The maximum temperature obtained in this period was highest recorded for RMIT University solar pond. This was possible with good clarity and profile maintenance of the solar pond.

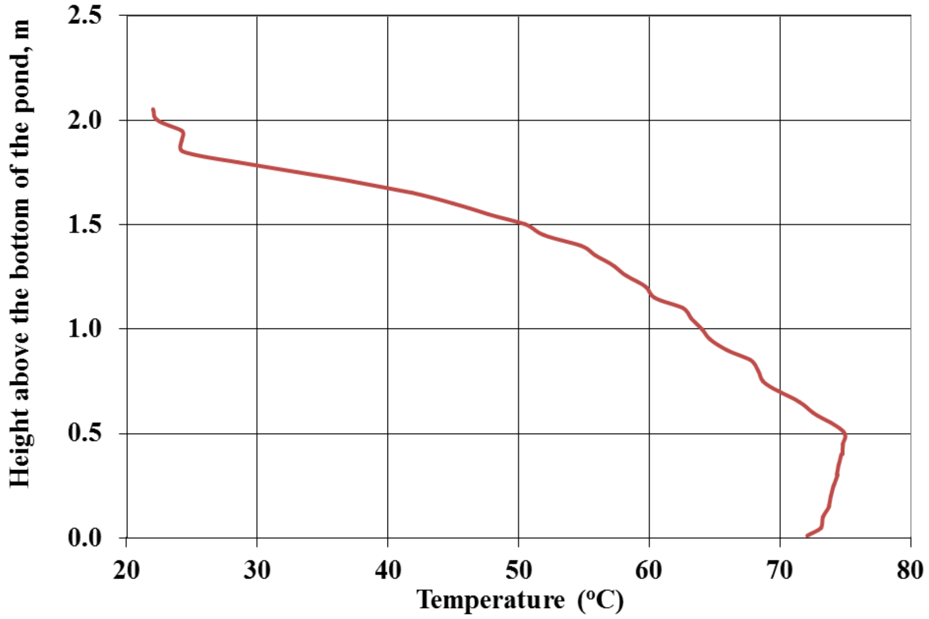

Figure 3.18 Temperature profile of RMIT University solar pond taken on 10/2/2014.

Figure 3.19 shows the evolution of average monthly temperature profiles for 16 months from April 2013 to July 2014 for RMIT University solar pond. The maximum temperature in the UCZ was recorded in the month of February 2014 during the summer seasons. The average temperature in LCZ over this period was recorded at 70.8 ˚C, while UCZ zone recorded an average monthly temperature of 24.1˚C. The minimum temperature in the LCZ zone was recorded during the winter period in July 2014 at 27.8˚C. The UCZ zone average monthly temperature for the same period was recorded at 11.4˚C. As the solar irradiance differs from the summer months to the winter months, the average monthly profiles also change according the amount of solar irradiance received by the solar pond. The minimum and maximum average monthly temperatures differences between LCZ and UCZ zone available in the RMIT solar pond in winter and summer are 16.4˚C and 46.7˚C, respectively.

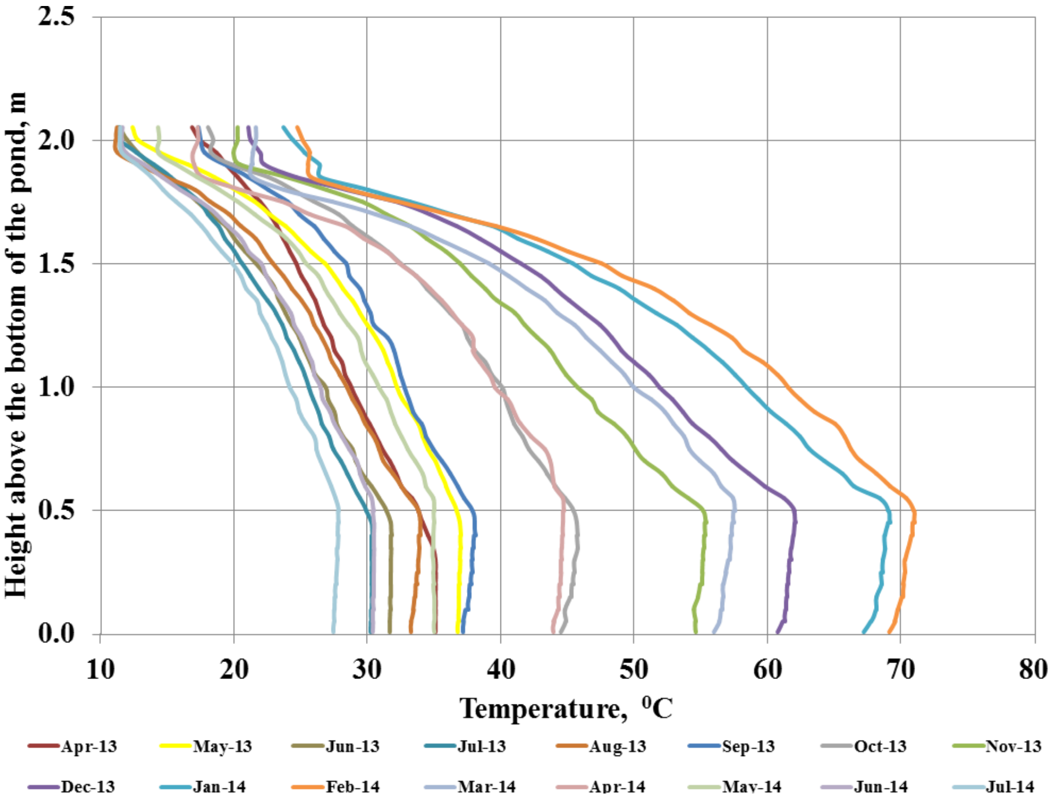

Figure 3.19 Evolution of average monthly temperature profiles for RMIT University solar pond from April 2013 to July 2014

3.7 Solar Pond Maintenance and Clarity

3.7.1 Salt Charging

The salinity profile developed due to the molecular diffusion of salt from the concentrated region to a less concentrated region in the UCZ zone will lead to gradient erosion over a period of time. Salt moves upwards due to the molecular diffusivity despite the absence of convection currents in the NCZ zone. The salt transport upward into the boundary zones depends on the seasonal changes that occur in a year (Alagao et al., 1994). Molecular diffusivity from the lower convective zone to the upper convective zone affects the shape of the salinity profile. This will result in increase in the salinity in the UCZ over a period. The initial density profile which consists of low salinity level in the UCZ zone and high salinity level in the lower storage zone will approach overall uniformity at a rate controlled by the rate of diffusion (Hull et al., 1989). There is a need to flush the excess salt collected at the top surface of the solar pond and replace the salt loss by diffusion in the LCZ zone. Figure 3.20 shows the salt charger used to replace the salt loss by diffusion in the solar pond. The salt charger is filled with sodium chloride salt on a weekly basis to compensate the loss of salt by diffusion. The salt pile collected at the bottom of the LCZ zone diffuses in the upward direction. Excess salt diffused upward is flushed by the fresh water into the evaporation ponds. This process maintains the stability of the salinity gradient of the solar pond for optimum and stable operation of the pond. The stability of the solar pond is given as the function of the height or depth (Xu et al., 1991). The performance and stability of the solar pond depend on the integrity of the insulating layer of NCZ.

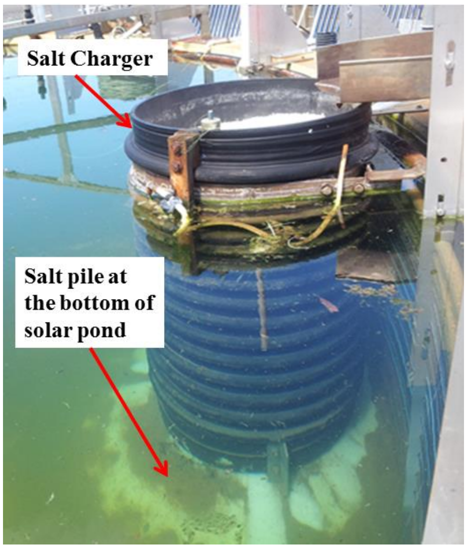

Figure 3.20 Salt Charger

Salt diffusion in the solar pond affects the salinity profile based on the distance and salt concentration differences between the UCZ and LCZ zones, and molecular diffusivity, k_s. For a solar pond with aqueous solution with only a single salt candidate, the diffusion is called a binary system (Rothmeyer, 1980). The salt transport rate per unit area for the binary system from molecular diffusion is proportional to the negative of the concentration gradient and to the molecular diffusivity; k_s where the temperature is assumed uniform (Hull and Mehta, 1987). If the temperature gradient is present, there will be additional transport proportional to the negative of the temperature gradient, to the concentration and to the thermal diffusion or Soret coefficient, s_T. The Soret coefficient, s_T for NaCl is positive and for other salts is negative (Schott. 1973). The soret term for salt transport in salinity gradient solar pond can be neglected as the salt diffusion with this term differed by less than 10%

when compared the value of salt diffusion calculated without this term (Nielsen, 1975). Rate of salt loss by diffusion is given by the equation below (Malik, 2011).

$$\dot{m} = -k_s \frac{dS}{dz} \tag{3.30}$$

Where $\dot{m}$ is the salt loss by diffusion in kg/s, k_s is the molecular diffusivity, dS is difference in salt concentration value for a given depth in kg/m^3 and dz refers to the difference in the vertical distance from the bottom of solar pond. The relations of salinity and temperature of the aqueous solution in a solar pond is given by the following relation (Hull et al., 1989).

$$\rho = \rho_0[1 - \alpha(T - T_0 + \beta(S - S_0)] \tag{3.31}$$

Where ρ_0 in kg/ m^3 is the density of the fluid at reference temperature, T_0 in Kelvin.

S_o in kg/ m^3 is the salt concentration of the fluid at reference temperature T_0 in Kelvin.

α is the coefficient of thermal expansion of water given as 0.4 X 10^{-3} K^{-1}.

β is the coefficient of expansion of water due to salinity given as 0.65 X 10^{-3} m^3/kg.

S and ρ are the salt concentration and density of the fluid at temperature T (Kelvin), respectively.

The above equation can be arranged into the following equation:

$$S = S_0 + \left\{\left[\frac{\rho}{\rho_0} + \alpha(T - T_0) - 1\right] x \frac{1}{\beta}\right\} \tag{3.32}$$

Where the reference temperature is given as T_0=293K, ρ_0= 998 kg/m^3 and S_0 = 0.

The flushing water transports the extra salt from the top surface of the solar pond to the evaporation ponds. The rate of water used for flushing is set at twice the local evaporation rate. Given the volume of water supplied for the flushing is given as V_f and the volume of water loss by evaporation is given as V_e. The difference between the two will result in the volumetric flowrate of water into the evaporation pond (m^3/s), given by equation below.

$$V_f - V_e = V_{ep} \tag{3.33}$$

The rate of mass transport of salt to evaporation pond is given as :

$$\dot{m} = V_{ep} \text{ x } S_T \tag{3.34}$$

Where S_T is the salinity of the top surface layer.

This rate of mass transport in equation (3.34) is the same with the mass transport in equation (3.30).

The molecular diffusivity can be affected by the wind speed and the fetch length of the solar pond (Akbarzadeh and Ahmadi, 2005). Figure 3.21 shows the salt consumption for RMIT University solar pond for 16 months. The salt consumption increased two fold in the summer months due to the increase in the salt diffusion at higher temperatures. This is because the high temperature, the molecular diffusivity increases with the temperature as a result of decrease in solvent viscosity (Hull et al., 1989). Molecular diffusivity, k_s increases in the order of 1.0 X 10^{-9} m^2/s at 10˚C to 5 X 10^{-9} m^2/s at 90 ˚C. The actual average monthly consumption was estimated to be around 106 kg and the theoretical actual monthly consumption calculated was estimated at 75 kg. These estimates are vital for the salt record analysis. The available record helps in budget estimation and also provides early warning signs underground leakages (Lu et al., 2004)

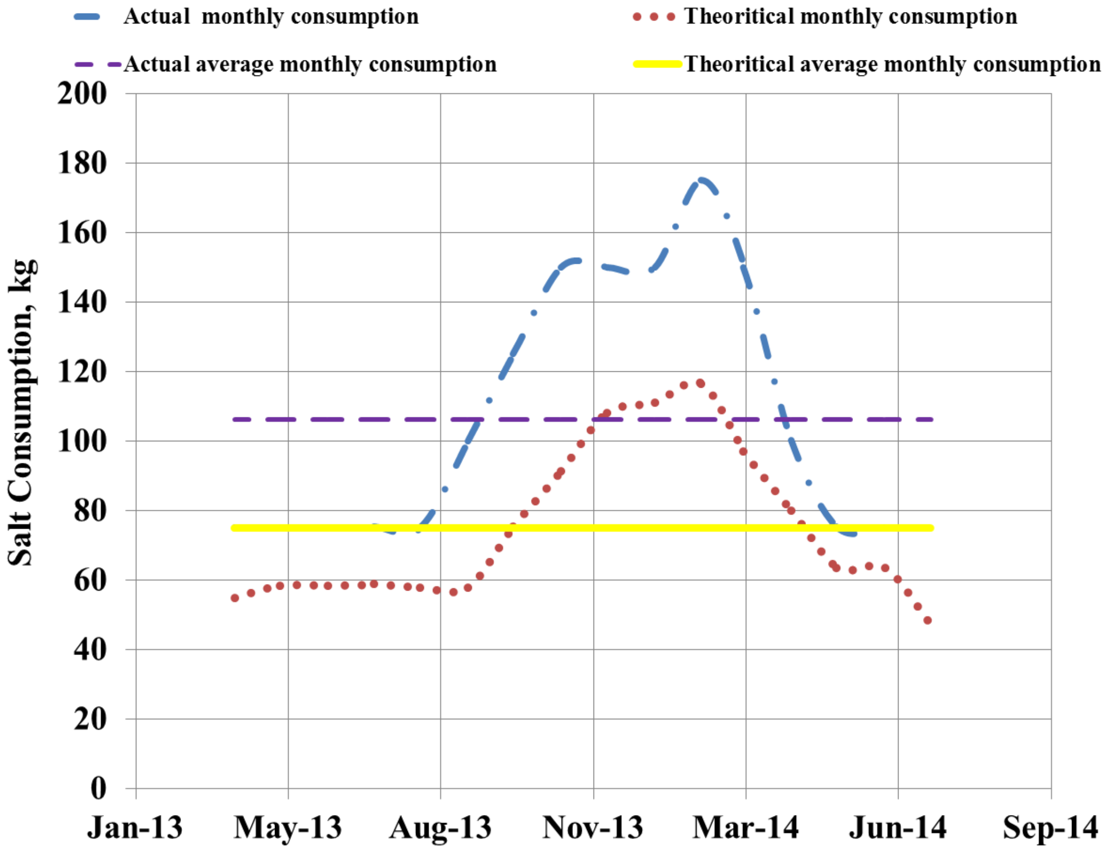

Figure 3.21 Salt consumption at RMIT University solar pond from April 2013 to July 2014.

3.7.2 Surface Washing

Figure 3.22 shows the flushing system used to overcome the upward salt diffusion from the LCZ zone in the solar pond. As the salinity of the UCZ zone increases due to the salt diffusion, the overall thickness of the gradient zone will be compromised (Schladow, 1984). To overcome this problem, fresh water is supplied to the top surface of the solar pond as shown in Figure 3.22. The fresh water washes the surface of the solar pond from the excessive salt build up to maintain the integrity of the salinity gradient for optimum performance of the solar pond. The excess water with salt overflow from the solar pond to evaporation ponds via an overflow pipe outlet located at the top of the solar pond. Water is channelled to the evaporation ponds by gravitational force as the solar pond top surface zone is located at higher elevation than the evaporation ponds. The salt from the surface washing can be reused in the solar pond once all the water is evaporated in the evaporation pond. Usually, the size of the evaporation pond is twice the area of the solar pond. The rate of water used for surface washing depends on the evaporation rate at the solar pond location. Conventionally, the rate of water used for surface washing is twice the rate of evaporation rate. This helps in salt transport to evaporation ponds and at the same time maintains the level of water in the solar pond at all times.

Figure 3.22 Flushing system (left) and evaporation ponds at RMIT University solar pond.

3.7.3 Automatic Control of the Surface Washing System

The surface washing system used traditionally for solar pond technology relies on the estimation of evaporation rate at the site. Water is then delivered twice the amount of this evaporation rate. Water is supplied at this rate 24 hours a day throughout the year. Although this generalised technique is widely applied for surface washing system worldwide today, there is a need to innovate the surface washing system to overcome the ceaseless water flow for surface washing system. The traditional water surface washing system was replaced by an automatic control system at RMIT University. A conductivity probe with total dissolved salt (TDS) controller and a floating switch was used to design the new flushing system. A solenoid valve was used to control the water flow for surface washing. This solenoid valve operates based on the signal received form the conductivity probe and the floating switch. When the surface water falls 10 mm below the original level and the TDS value reaches more than 9 000 parts per million (ppm), the solenoid valve opens and fresh water is supplied to flush the salt from the surface and to maintain the level of the solar pond. 9 000 ppm TDS corresponds to the UCZ salinity at 1008 kg/m^3. This salinity value is the maximum allowable salinity level at the surface zone before fresh water is supplied for the surface washing. The solenoid valve shuts off once the desired salinity and level is achieved at the top surface. This helps in reducing the amount of fresh water used for surface washing. The new design also provides a much precise amount of water to the solar pond and avoids incessant flow of water.

Figure 3.23 shows the automatic surface washing system located at RMIT University solar pond with its major components. The system is fixed on the east side of the solar pond wall and has been running successfully for more than twelve months automatically. The salinity gradient was well maintained throughout the period of the use of this automatic surface flushing system.

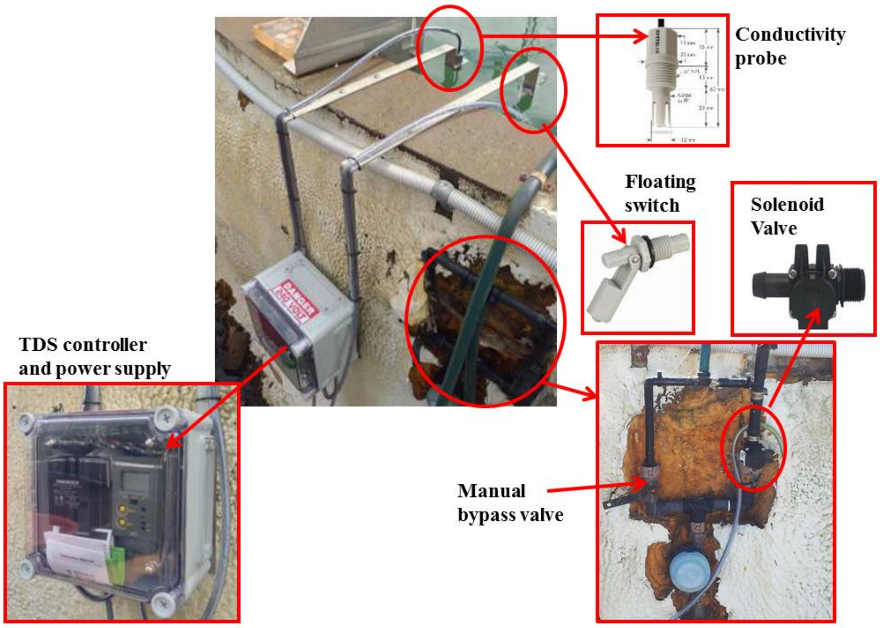

Figure 3.23 Automatic surface washing system located at RMIT University solar pond with its major components.

3.8 Clarity and Turbidity Control

3.8.1 Sources of Turbidity

For artificial solar ponds, the maintenance of water clarity is not only one of the main requirements but also recognised as potential problem (Tabor, 1963). Water transparency plays an important role in achieving good thermal efficiency in a typical solar pond. Bacteria, algae and wind–borne debris contribute to a drop of clarity in the solar pond. Light attenuation due to the suspended algae and microorganisms tend to reduce the thermal efficiency of the solar pond (Kirk, 1980). *Dunaliella viridis* is the type of algae that remains green in salt concentrations (Felix, 1979). Halophilous bacteria also thrive in solar ponds and contribute to the turbidity. Sulphur bacteria normally strive in the saturated storage zone and at this zone, the high optical quality is not mandatory (Post, 1977). The decomposition of the suspended organic materials produce inorganic forms of nitrogen, sulphur and phosphorous that yields a complex substance called “humic substance” (Schnitzer, 1978). Blue green algae depend on the sunlight to produce food and thrive in a warm environment. Blooms often occur in solar ponds in summer conditions due to the favourable warm environment for the algae. Heavy metals like lead, copper, chromium and ferrous oxide are also present in the body of water of solar ponds (Malik, 2011). This is due to the corrosion of metal supports in high saline environments. The UCZ and LCZ zones in a solar pond need to be maintained at good clarity levels for optimum light transmittance to the bottom storage zone. Therefore, there is a need to maintain the clarity of solar pond to a certain desired level for best thermal efficiency. Figure 3.24 shows some of the contamination due to algae and foreign particles on the top surface of RMIT University solar pond.

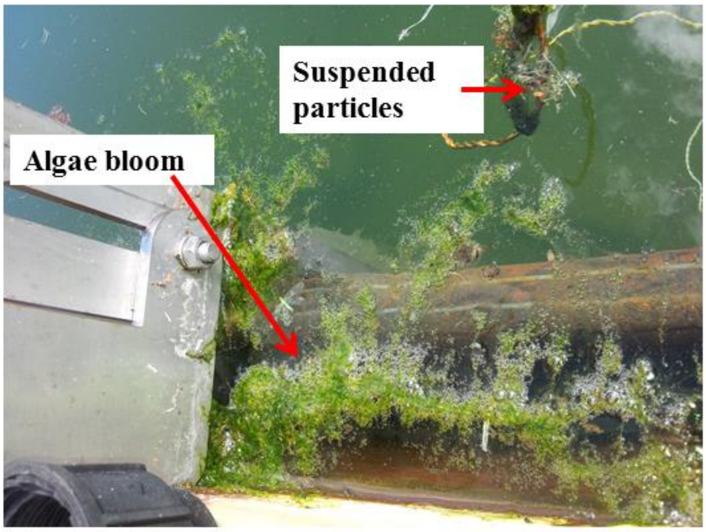

Figure 3.24 Contamination due to algae and foreign particles on the top surface of RMIT University solar pond.

3.8.2 Turbidity Control Methods

3.8.2.1 Acidification

Hydrochloric acid (HCL) can be used to control the turbidity caused by algae bloom. Low pH environment reduces the survival rate of most of the algae in a solar pond. It is very important to maintain pH level between 3- 4 for effective control of the algae bloom. The low pH provides a shock treatment for the algae and bacteria in the solar pond. At RMIT University solar pond, pool acid with 32 % HCl concentration was used to treat the problem caused by the algae bloom. Acid was injected into the affected layers of the solar pond in the UCZ and NCZ zones. No acid was injected into the LCZ as the high salinity environment in this zone will inhibit any algae growth. Besides that, the high salinity in this zone will cause crystallisation of salt when acid is added. For the radiation from the sunlight to reach the bottom of the pond in the storage zone, the NCZ and UCZ need to be free from any foreign particles. This will ensure that the pond can be operated at the maximum thermal efficiency.

When the pH level in the NCZ and UCZ increase to a level more than 4, diluted acid will be injected to the affected zone. 5 litres of saline water from the affected zone will be siphoned and mixed with 1 litre of HCL acid with 32 % concentration. This mixture is then injected back into the affected zone using a diffuser. The diffuser minimise the mixing while the acid solution is injected into the solar pond. A tank filled with the acid solution is kept at higher platform, 1 m from the top surface of the solar pond and the flow is maintained into the solar pond via the diffuser by means of gravitational force. Figure 3.25 shows the arrangement used at RMIT University to inject acid into the solar pond.

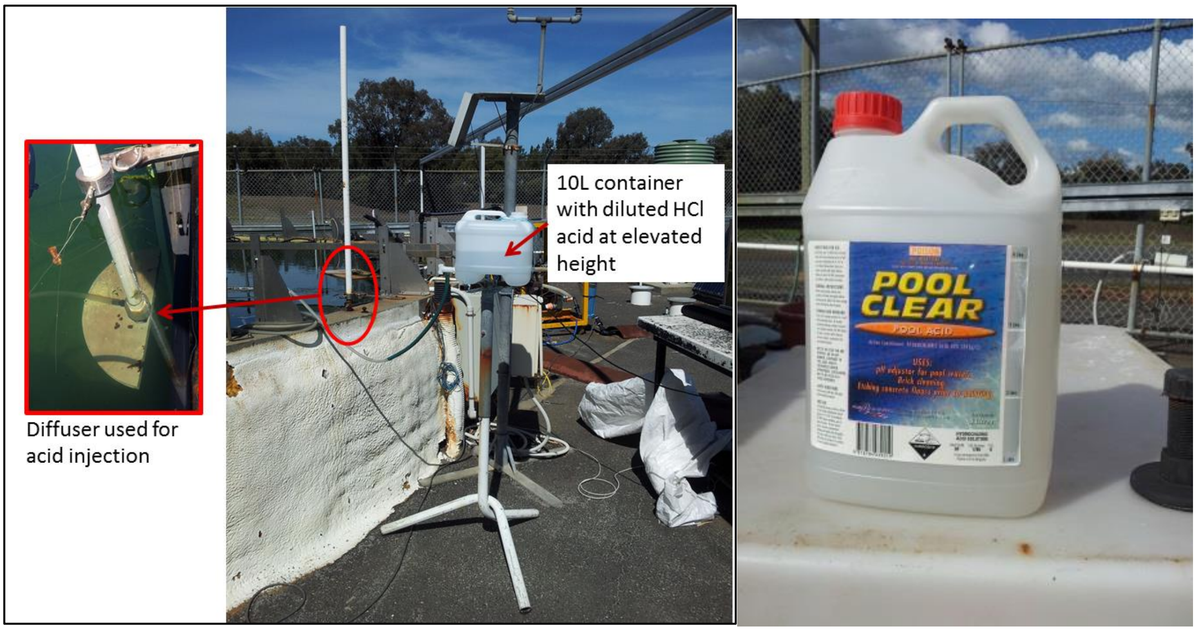

Figure 3.25 Acid injection into solar pond (right) and pool acid used for acid treatment (left)

Figure 3.26 shows the average monthly evolution profiles of pH profile in RMIT solar pond before and after acid injection. In March 2013, the pond was refurbished and filled with brine. The pH level remained around 7, which provides a healthy environment for algae to strive. Acid was added into the NCZ and UCZ zones in April 2013 and the pH level shifted towards a more acidic level on the pH scale. From May 2013 to July 2014, the pH level in the UCZ and NCZ level was maintained around 3 - 4. When the pH level in this two zones increased to more than 4 on the pH scale, acid solution would be added as described above to bring the pH to the desired level. The low pH environment in these two zones helped to maintain a good clarity and algae free solar pond throughout the period from April 2013 to July 2014.

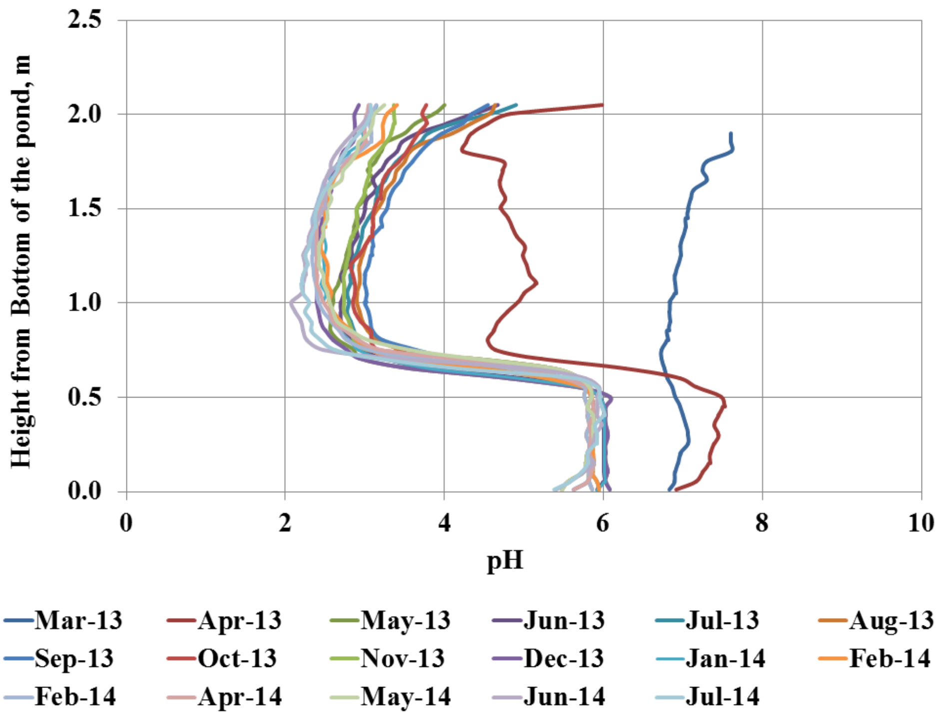

Figure 3.26 Average monthly pH evolution profiles for RMIT University solar pond from March 2013 to July 2014.

Turbidity measurements are based on the formazin turbidity units (FTU) or nephtalometric turbidity units (NTU). A noticeable difference can be detected by human naked eye when the turbidity level is more than 5 FTU (Myre and Shaw 2006). A turbidity level of less than 3 FTU is desired for optimum operation of solar pond (Xu et al., 1993). Figure 3.27 shows the average monthly turbidity profiles for RMIT University solar pond. The turbidity level in NCZ and UCZ zones was kept at a value below 3 FTU throughout the period from April 2013 to July 2014. The turbidity level in LCZ was above there due to the suspended dust particles. These dust particles are believed to be beneficial to the storage zone as it absorbs radiation from the sunlight transmitted into this zone (Akbarzadeh, 2005). The turbidity profile allows one to identify the clarity of the pond and any remedial actions can be performed to maintain a good clarity in a solar pond. The tap water turbidity at RMIT University solar pond was found to be at 0.65 FTU. The turbidity of the solar pond in the UCZ and LCZ zones were kept at 0.65 FTU for better clarity and performance. The acid treatment successfully maintained good clarity throughout the operation of the solar pond for good penetration of solar radiation into the storage zone.

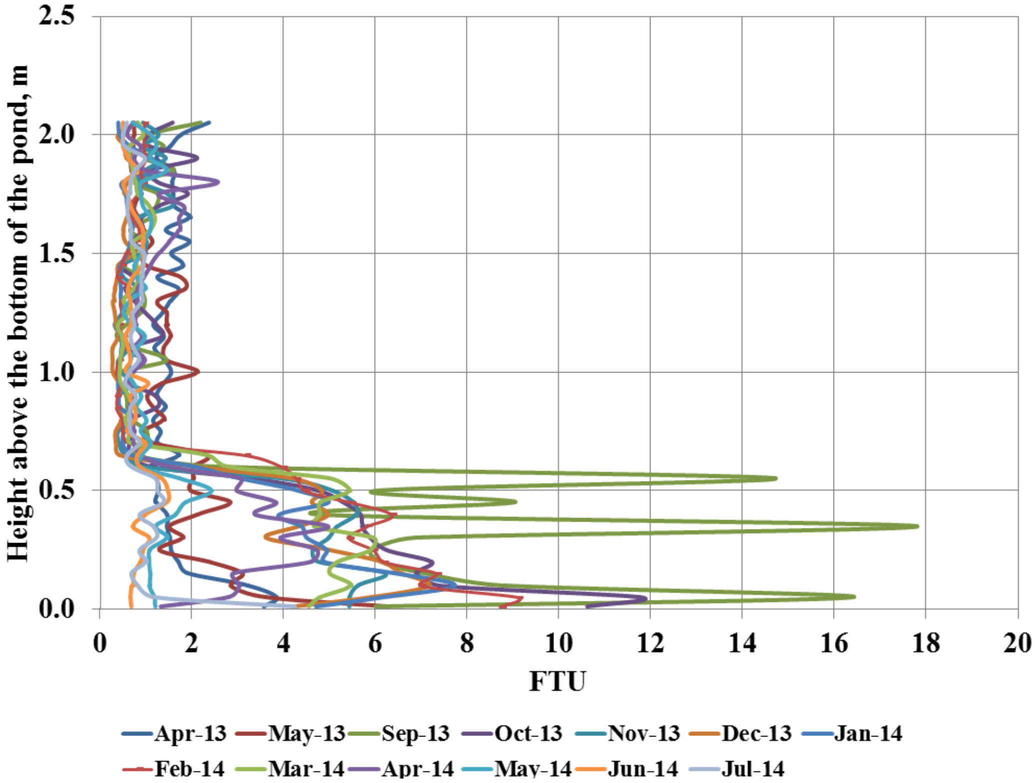

Figure 3.27Average monthly turbidity profiles for RMIT University solar pond

3.8.2.2. Biological control

Brine shrimps can be used as a biological control to maintain the clarity of the pond. The most common species is the Artemia Salina (Tackaert and Sorgeloos, 1993) and they have been quite successful in maintaining the clarity of saline ponds. Brine shrimps from will feed on the algae to control their growth. The algae is ingested and finally excreted as dense faecal matter that sinks to the bottom of storage zone. This biological control is highly recommended to maintain the clarity of the pond due to its effectiveness, cost and environmental benefits (Gasulla, 2011). However, these brine shrimps are very susceptible to the hot condition when the solar pond temperature reaches more than 60˚C. They simply cannot survive in a warm environment. Other than that, the acidic environment and step changes of salinity in the solar pond are not favourable for the brine shrimps to thrive. Another species of brine shrimp, *paratemia zietziana*, was found to be able to survive in an extreme saline environment (Geddes, 1981).

3.8.2.3 Flocculation

Many suspended nonliving particulate matter can cause scattering of light that is transmitted into the solar pond (Kirk, 1980). These particulate includes dust, soil, sediments and decomposing algae. These particulates are influenced by the density gradient of the solar pond and they may reach static equilibrium where the particle and the fluid density are equal. These suspended particulates can be treated with flocculants. Flocculants cause particulates to coagulate into larger sizes which then sink to the bottom of the solar pond. At RMIT University solar pond, flocculants based on the aluminium chloride was used for flocculation. A litre of the flocculants was used to treat 50 000 litres of water in the solar pond. The clarity of the pond was visibly improved after a few days of application of the flocculants.

3.8.2.4 Chlorination

Algae grow mostly in the UCZ zone and the top of NCZ zone. This is because the temperature at these levels is not extreme and this allows the algae to strive. One way to treat this problem is by using chlorine. Chlorine when dissolved in water quickly hydrolyses to hydrochloric and hypochlorous acids, and partially ionised as shown by the formulas below:

$$Cl_2 + 2\ OH^- \rightarrow Cl^- + OCl^- + H_2O \qquad (3.35)$$

This chemical reaction due to the chlorination is effective in controlling the algae bloom. The chlorination kills the algae due to the shock treatment and prevents further growth. The chlorination method helps in maintaining the transparency of the solar pond by preventing microorganism growth (Bronicki, 1986). At RMIT University solar pond, chlorine tablets are used for the chlorination with a floating dispenser. The floating dispenser was filled with three chlorine tablets and left floating on the surface of the solar pond. The tablets are replaced with new ones every two months. Figure 3.28 shows the floating dispenser and the chlorine tablets used for the chlorination of RMIT University solar pond.

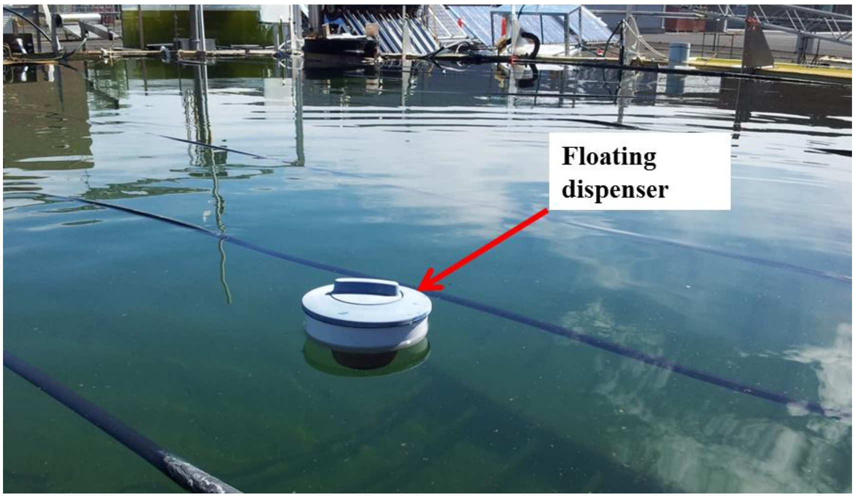

Figure 3.28 Floating dispenser used for the chlorination of RMIT University solar pond.

3.8.2.5 Other Methods

An alternative to HCL for chemical treatment is copper based algaecide known as cupricide (Gasulla et al., 2011). HCL tends to corrode the metal supports in solar pond. Cupricide is more stable compared to HCL. However, cupricide cost is higher than HCL and limits its application for solar pond clarity treatment. Other chemicals used to improve clarity of solar pond are copper sulphate (Cohen, 1981), Diuron (Stewart and Pearson, 1970), trazines (Walsh 1972) by inhibiting the photosynthesis of the algae. Heavy metals such as Cu^{++}, Pb^{++} and Zn^{++} can also be used to inhibit the growth of algae and bacteria in solar pond. Peroxidation using hydrogen peroxide for clarification was used earlier but discontinued due to the effervescence of gas at elevated temperatures which effects the pond

3.8.3 Density, Temperature, pH and Turbidity Measurement Devices

The weekly profiles for the density, temperature, pH and turbidity are taken manually for observation and monitoring purposes. A siphon tube as shown in Figure 3.29 was used to extract the sample from the desired level. The density, pH and turbidity of a sample were taken with the devices shown in the same figure. The temperature was measured using a k-type thermocouple attached at the bottom of the siphon tube. A digital thermometer connected to the thermocouple provides the readings for the temperatures taken at regular interval. The siphon tube is moved every 5 cm interval from the bottom to the top surface of the pond. A total of 100 ml was extracted from the each 5 cm interval level of the solar pond.

After measurement, the samples are collected in a plastic container and returned back to the solar pond via the salt charger.

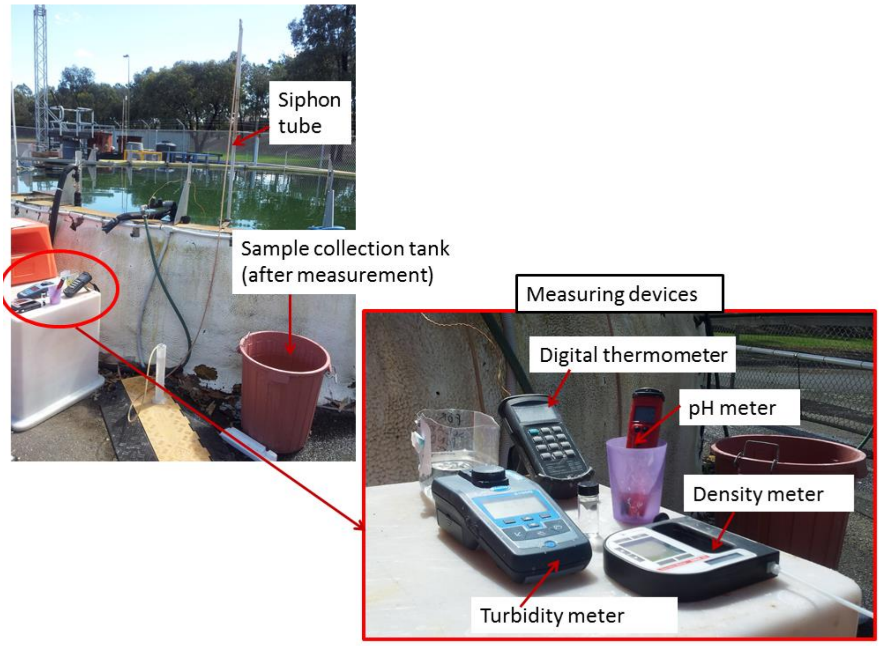

Figure 3.29 Siphon tube and electronic devices used for weekly data measurement of solar pond

Figure 3.30 shows the average monthly temperature profiles of LCZ and UCZ from April 2013 to July 2014. Maximum temperature differences between the two zones were recorded in February 2014, during summer season. In winter season, minimum temperature difference of 16°C was observed for the two zones in solar pond. Organic Rankine cycle (ORC) engines works well with the hot side temperatures of more than 50°C in the LCZ. LCZ temperatures lower than 50°C inhibit the operation of ORC engine. This is because ORC engines require a certain threshold in hot fluid temperature to evaporate the organic fluid for ORC engine operation. In most cases, the threshold temperature to boil the organic fluid is more than 50 °C. Due to this reason, the LCZ temperature available in winter season will not operate any ORC engines. Alternatively, thermoelectric generators (TEG) can be operated even at low-temperature environment. This allows TEG modules to operate continuously throughout the year in both winter and summer conditions. This provides an edge when compared to the ORC engine. The next chapter will discuss the experimental investigation of TEG for power generation from solar pond using low-grade heat.

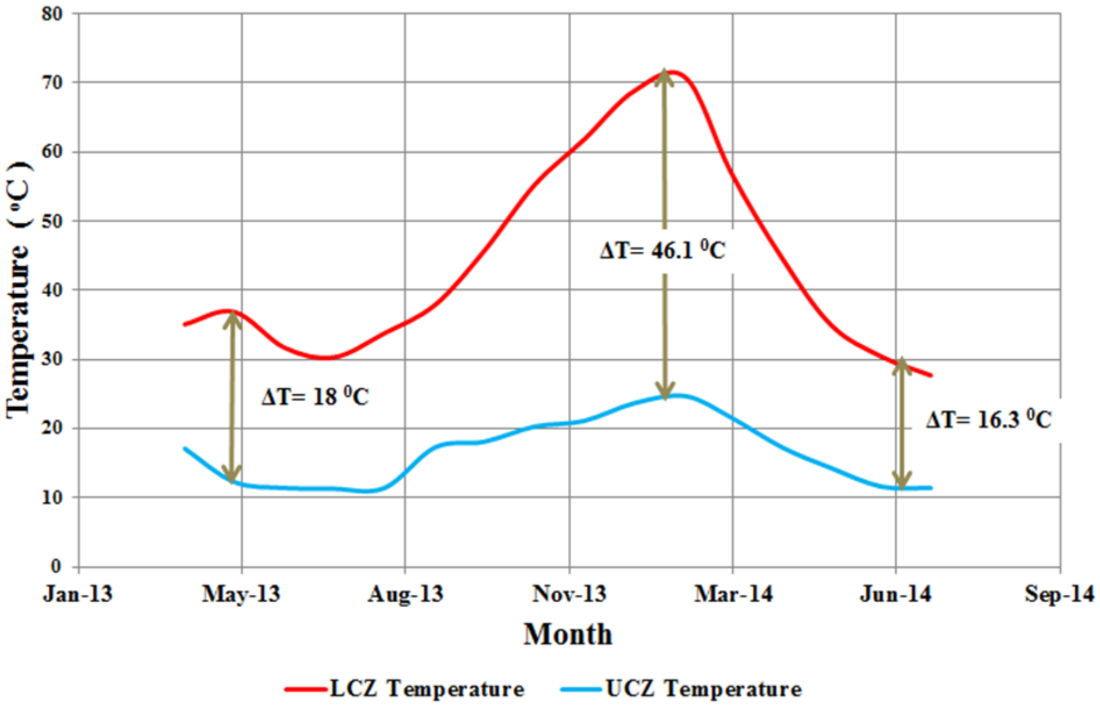

Figure 3.30 Average monthly temperature profiles of LCZ and UCZ from April 2013 to July 2014

3.9 Heat Addition to the Thermal Storage System

3.9.1 System Setup

Solar pond acts as a thermal storage and collector. When the temperature in the LCZ is high, heat can be extracted from this zone and utilised for desired applications. However, the low temperatures of LCZ in off summer seasons restrict heat removal from LCZ. This is because the low temperatures in LCZ are not viable for meaningful heat transfer applications. However, heat can also be added via the heat exchanger in the storage zone of the solar pond. Usually, this heat exchanger is only used for heat removal from the storage zone. But the reserve is also true if one needs to add thermal energy in storage zone to boost the temperature.

One of the easiest methods available to achieve the above is by using evacuated tube solar water heaters. An array of solar evacuated tube collectors to collect heat energy and transferred into the LCZ in order to boost the temperature. An array of direct flow solar evacuated tube collectors supplied by Greenland Systems was installed in RMIT's

Renewable Energy Laboratory. Table 3.4 below outlines the technical specifications given for model GL 100-16DF type collectors installed at the site.

Table 3.4 Technical Specifications for Solar Collector (Greenland Systems, 2012)

Collector Model	**GL - 100-16DF**
Collector Structure (Heat Pipe Vacuum Type Solar Collector)	**Solar Collector**
Construction	**DF (Direct Flow)**
Dimensions (mm)	**1920W x 2160L x 187H**
Number of Tubes per Collector	**16**
Collector Dimensions excl. Condensor	**100 x 2015**
Collector Manifold Fluid Capacity (Dry Heat Interface)	**3L**
Mass (kg)	**97**
Fluid Pressure Drop: @ 120L/hour (kPa)	**0.84**
Fluid Pressure Drop: @ 480L/hour (kPa)	**5.4**
Solar Aperture	**2.95 m^2**
Peak Power (Peak Power at 100W/m^2 of Normal Isolation)	**6.1MJ/hour 2.35 kW**
Hail Test to AS/NZS 2712	**Pass**
Stagnation Temperature	**276 °C**

There are a total of 8 collectors installed, with 2 rows of 4 units connected in series facing north, installed at an angle of 35°. This was done in order to maximise the power output during the summer months when the sun is higher in the sky.

The potential for increasing the performance of a solar pond by combining the system with solar evacuator tubes provides a motivation for the heat addition system to the storage zone. The concept behind it is that the solar evacuated tubes will collect additional thermal energy and transfer this to the solar ponds thermal energy store. As a result raising the temperature of the solar pond and increasing the efficiency.

The system comprised of a series of solar evacuated tube collectors connected via a photovoltaic pump to a heat exchanger located in the LCZ of the solar pond. The final schematic of the experimental rig used is shown below in Figure 3.31. The experimental plan shows a number of features including the solar evacuated tube collectors, piping, piping fixtures, visual gauges, solar pond and heat exchanger.

The working fluid is circulated through the 2 rows of 4 units, then into a 400 Litres insulated storage tank. A Type T (Copper – Constantan) thermo couple is located in the bottom of the tank for measuring the temperature of the water inside the tank. An inlet pipe runs directly to the circulation pump in order to top up the level of water in the system, which can be monitored visually from the water level gauge on located on the side of the tank. Water can be extracted from the system via a ball valve located at the bottom of the tank.

A positive-displacement vane pump power by a solar photo voltaic panel was used to circulate water through the evacuated tubes and solar ponds heat exchanger. The solar panel powering this pump also served as a control system for when the pump operates. Pump operates only with solar radiation and shuts down when solar radiation is zero. A header tank wase installed to ensure that the vane pump stays primed as changing temperature alters the volume of water in the system.

In order to accurately measure the necessary temperatures T-type thermocouples were positioned at both the inlet and outlet pipe of the heat exchanger. This will allow the heat transfer rate to be calculated using the follow equation:

$$\dot{Q} = \dot{m}C_p(T_{in} - T_{out}) \tag{3.36}$$

The flow rate was measured using a flow meter (Grundfos Vortex Flow sensor Standard, 2-40 l/min). Heat was transferred directly to the LCZ via a coil type heat exchanger located in LCZ region. By inserting heat via a heat exchanger, the salinity gradient has little disturbance as opposed to physically adding and extracting water from the pond itself. The coil type heat exchanger is made out of 32 mm outside diameter Blueline Nylex poly pipe and an approximate length of 80 meters submerged in the LCZ, where the highest temperatures are contained. The poly pipe has an approximate wall thickness of 3 mm.

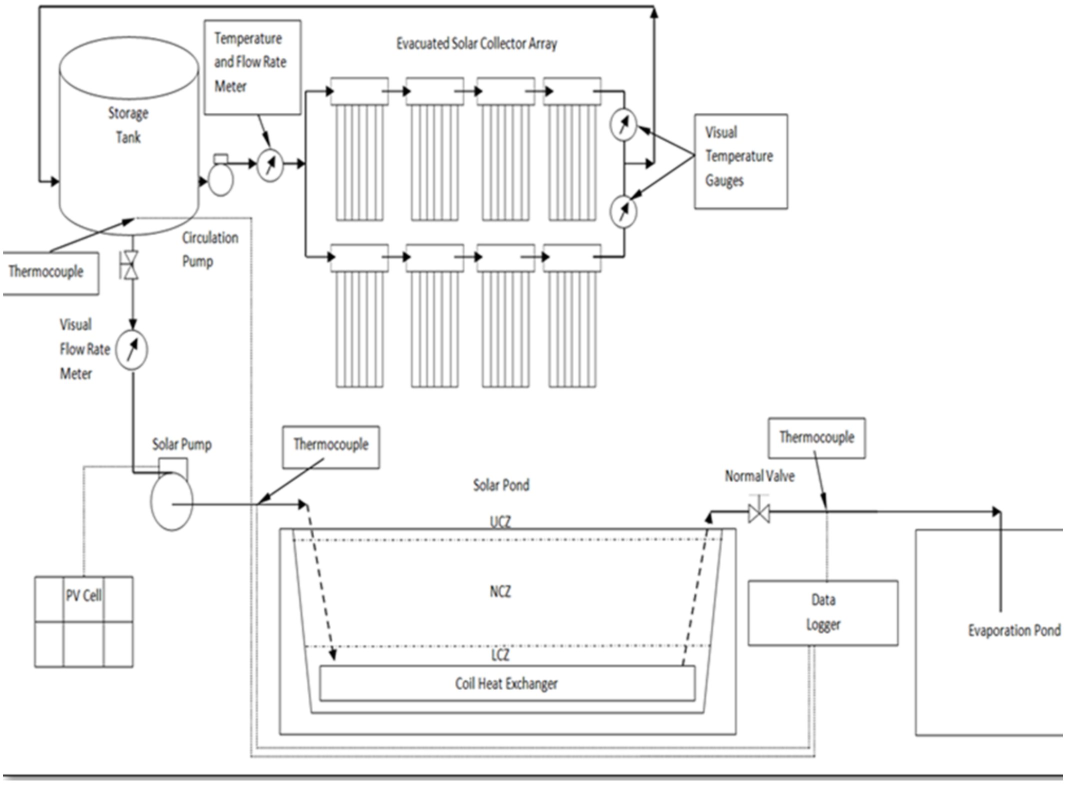

Figure 3.31 Schematic of the heat addition system used for the RMIT solar pond

3.9.2 Results and Discussions

The heat energy added to the LCZ using the addition system was maximum at 52 kWh on 27/9/2014. The average heat energy added daily was 25 kWh. Total heat energy added to LCZ by the heat addition system depended on the pump working hours which depend on the solar radiation condition itself and water temperature in the isolated water tank. Due to the maintenance of the pump on the between 16 – 18/9/2014, the heat energy output from the heat addition system was zero.

The total average heat energy added to the LCZ by the heat addition system and solar radiation including heat losses to the top and the ground was 61 kWh and the maximum at 110 kWh on 22/9/2014. However, on 16/9/2014, the heat losses were more than the heat added to the LCZ. As mentioned previously, the pump was under maintenance while the average solar radiation was 25 W/m^2 which means only 7 W/m^2 penetrated to the LCZ. These two factors resulted in a 6 kWh heat energy loss on 16/9/2014 from LCZ instead total heat energy added. Figure 3.32 shows the heat addition to the storage zone of RMIT University solar pond using evacuated tube solar heaters, solar energy and total heat energy added to LCZ.

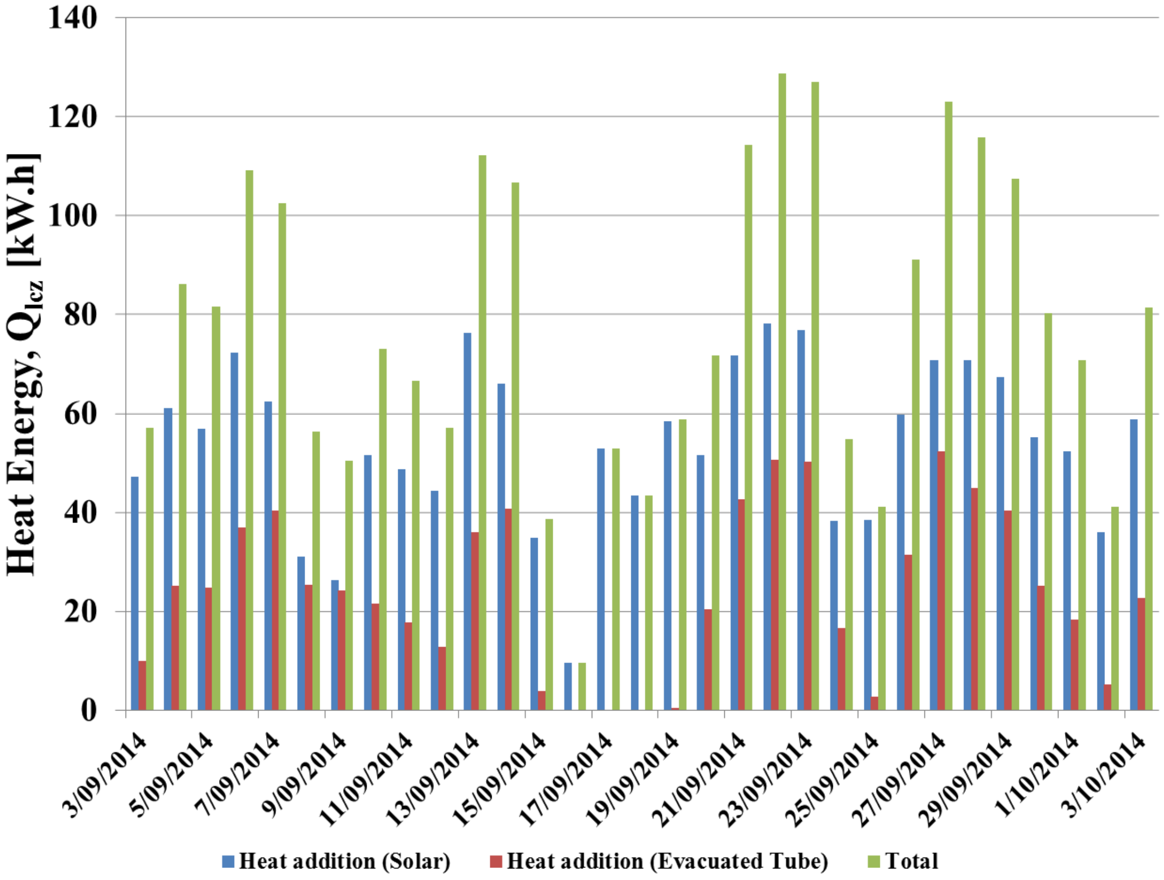

Figure 3.32 Heat additions to the storage zone of RMIT University solar pond

The heat energy added to the LCZ by solar radiation without the heat energy added by the heat addition system was found to be on an average of 53 kWh. Comparing the average value of the heat energy added to LCZ by solar radiation to the heat addition system, heat energy added to LCZ by solar radiation is greater than the heat energy added to LCZ by the heat addition system. The maximum was on 22/9/2014 when average solar radiation hitting the surface of the pond was 202 W/m^2. On the other hand, the minimum was on 16/9/2014 when the average solar radiation hitting the surface of the pond was 25 W/m^2. The contribution of the heat addition system in adding heat to the pond was found to be 31 % as shown at Figure 3.33.

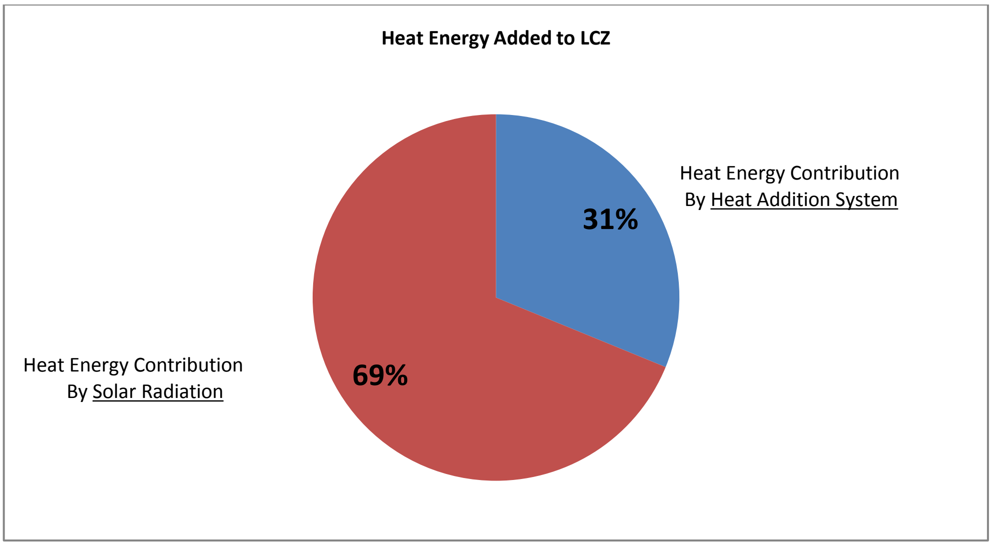

Figure 3.33 Heat energy additions to LCZ breakdown by percentage.

Figure 3.34 shows the average daily LCZ temperature in both 2013 and 2014 and average horizontal solar radiation received at the surface of the pond. The maximum temperature in the LCZ in 2013 was clearly higher. This was expected because of the higher solar radiation in 2013. However, on 5/9/2014, the temperature recorded in the LCZ for 2014 was higher, despite the solar radiation for 2013 still being higher. This indicates that the heat addition system was viable in adding the heat to the LCZ. This resulted in higher temperature in the LCZ. This method can be used to boost the temperature of the solar pond when the solar radiation is lower in the non-summer seasons.

All equipment including electronic load, thermocouples, voltmeter and ammeter used for experiment were calibrated to ascertain their accuracies. The relative uncertainty of the equipment used is defined as

Relative uncertainty = 0.5 x resolution/ (operating or measuring value) (3.37)

The total uncertainty was obtained by combining the sensor accuracy and measuring instruments accuracy using the root sum of square method as follows;

$$\delta_{total} = \sqrt{(\delta_{Sensor})^2 + (\delta_{Instruments})^2} \tag{3.38}$$

Where, δ is the uncertainty of the measured value.

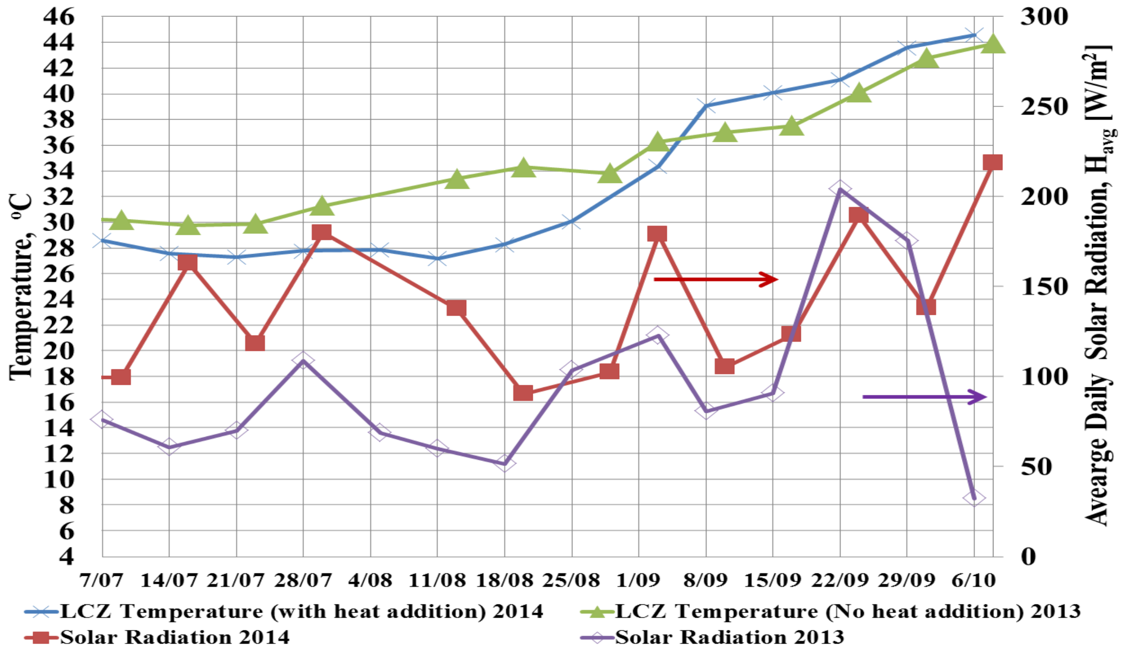

Figure 3.34 Average daily LCZ temperature and solar radiation comparison for 2013 and 2014 with and without heat addition

3.10. Chapter Conclusion

Solar pond acts as thermal collector and storage system. Solar energy is stored in the storage zone of solar pond. NCZ acts as an insulation layer and prevents heat loss from the storage zone. A maximum average monthly temperature of 71 ˚C was recorded for RMIT University solar pond. The minimum and maximum average monthly temperatures differences between LCZ and UCZ zone available in the RMIT solar pond in winter and summer are 16 ˚C and 47 ˚C, respectively. The available temperature difference in the solar pond can be used to generate electricity using thermoelectric generators throughout the year. Both LCZ and UCZ temperatures are suitable to power the hot side and cold side of the thermoelectric generator for power generation application. Furthermore, the maintenance of the solar pond assures maximum penetration of solar radiation to the storage zone of the solar pond. Clarity of the solar pond must be kept at optimum level all the time. An automatic control system for the surface washing allows for fresh water addition only when it is required and helps in water conservation in the long run. The heat addition system used in this project successfully helped to boost the storage zone temperature. This method can be used to increase the storage zone temperature in non-summer conditions

4.0 Electrical and Thermal Characteristics of Thermoelectric Generator

4.1 Introduction

This chapter focused on the electrical and thermal characteristics of thermoelectric generators (TEG). The chapter begins with a theoretical background of TEG to explore the potential of TEG being used for power generation from solar pond. TEG can operate even at low temperature conditions and is suitable for power generation using low grade heat from solar pond. Experiments were conducted to analyse the maximum power output from TEG at various temperature differences and the experimental results are presented in this chapter. To avoid mechanical fixtures in highly corrosive environment of solar pond, TEGs were tested with various adhesive for optimum power output. Finally, the effect of series and parallel array connections on the power output of TEG are examined and reported in this chapter.

4.2 Theoretical Background of TEG

The TEG works on the principle of Seebeck effect, conduction effect and Joule effect. As seen from Figure 4.1, when heat source is applied to a pair of P-N TEG couple, heat energy, Q_h creates a temperature difference, ΔT between the both sides of the P-N TEG couple.

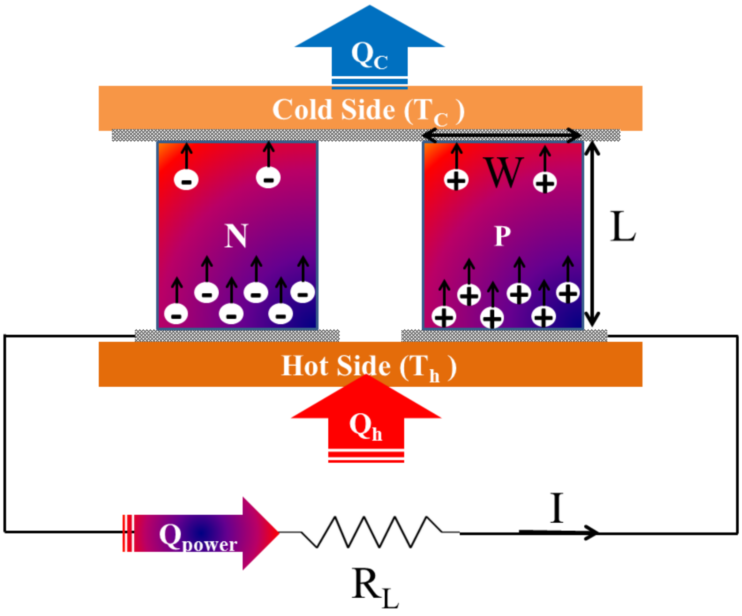

Figure 4.1 Single TEG couple with P-N leg (Hsu et al., 2011)

As a result of thermoelectric effect, electrical current, I flow in the circuit. The conduction effect is proportional to the thermal conductivity, k and the temperature difference, ΔT across the P-N leg. The electrical current in the P-N circuit will generate Joule effect internally, which heats the cold and hot side. The Joule effect is proportional to the electrical resistance of TEG, R_{TEG} and square of the current, I. The P-N ingot in a TEG is sandwiched between two copper electrical conductors on the inner part and electrically insulated ceramic plates on the outer side.

For theoretical analysis, the internal properties of TEG are assumed to be constant, independent of temperature with no heat losses from the system. The rate of heat supplied and heat removal can then be estimated at the hot and cold junction respectively as follow (Hsu et al., 2011):

$$Q_h = (K_p + K_n)(T_h - T_c) + (\alpha_p - \alpha_n)IT_h - (I^2R/2) \tag{4.1}$$

$$Q_c = (K_p + K_n)(T_h - T_c) + (\alpha_p - \alpha_n)IT_c - (I^2R/2) \tag{4.2}$$

Where K_p and K_n are thermal conductivity of P and N type TEG leg. T_h and T_c represent the hot and cold junction temperature respectively. α_p and α_n are the Seebeck coefficient of P and N type TEG leg respectively.

The electrical power generated from TEG is given as

$$P_{TEG} = Q_h - Q_c \tag{4.3}$$

Equation (4.3) can also be written in the form of voltage, V and current, I.

$$P_{TEG} = IV \tag{4.4}$$

Rearranging equation (4.1) to (4.4), we obtain,

$$(\alpha_p - \alpha_n)I(T_h - T_c) - I^2R = (I)V \tag{4.5}$$

Equation (4.5) is then divided with I, resulting:

$$V = (\alpha_p - \alpha_n)(T_h - T_c) - (I)R \tag{4.6}$$

Rearranging equation (4.6) where $(\alpha_p - \alpha_n) = \alpha$ and $(T_h - T_c) = \Delta T$, we obtain a simplified form equation as follow:

$$V = \alpha_s \Delta T - (I)R \tag{4.7}$$

When I = 0, from equation (4.7) we get

$$V_{ocv} = \alpha\Delta T \tag{4.8}$$

For TEG containing N number of couples, the following equation can be used for open circuit and short circuit relations.

$$V_{ocv} = 2N\alpha\Delta T \tag{4.9}$$

$$V_{mp} = V_{ocv}/2 = N\alpha\Delta T \tag{4.10}$$

$$I_{sc} = (\alpha/\rho)(A_{TEG}/L)\ \Delta T \tag{4.11}$$

$$I_{mp} = 0.5(\alpha/\rho)(A_{TEG}/L)\ \Delta T \tag{4.12}$$

Maximum power obtained when the load resistance, R_L is equal to the internal resistance of TEG, $R_{TEG.}$

Maximum power output of a typical TEG is given as follow (Rowe and Min, 1998):

$$P_{max\ TEG} = \frac{\alpha^2}{2\rho}\frac{NA_{TEG}(T_h - T_C)^2}{(L+n)(1+2rL_c/L)^2} \tag{4.13}$$

Where

contact parameter, n =0.1 mm,

dimensionless contact parameter, r = 0.2

Length of thermo element, L = 1.2 mm

Thickness of solder/contact in module, L_c = 0.8 mm

Seebeck coefficient, $\alpha = 2.12 \times 10^{-4}\ VK^{-1}$

Number of thermo elements per module, N = 126.

Electrical resistivity of thermo element material, $\rho = 2.07 \times 10^{-3}\ \Omega$ cm.

Area of thermo element, $A_{TEG} = 1.96\ mm^2$.

The thermoelectric power is related to dimensionless figure of merit given by

$$ZT = \alpha^2\sigma T/k \tag{4.14}$$

Where α is the Seebeck coefficient of TEG, σ and k are the electrical and thermal conductivity respectively and T is the absolute temperature.

For calculating the efficiency of TEG, the following equation is used.

$$\eta_{\max TEG} = \frac{T_h - T_c}{T_h}\left[\frac{(1+ZT)^{0.5}-1}{(1+ZT)^{0.5}+\left(\frac{T_c}{T_h}\right)}\right] \tag{4.15}$$

The temperature difference across the TEG can be obtained through the resistance network shown in the Figure 4.2.

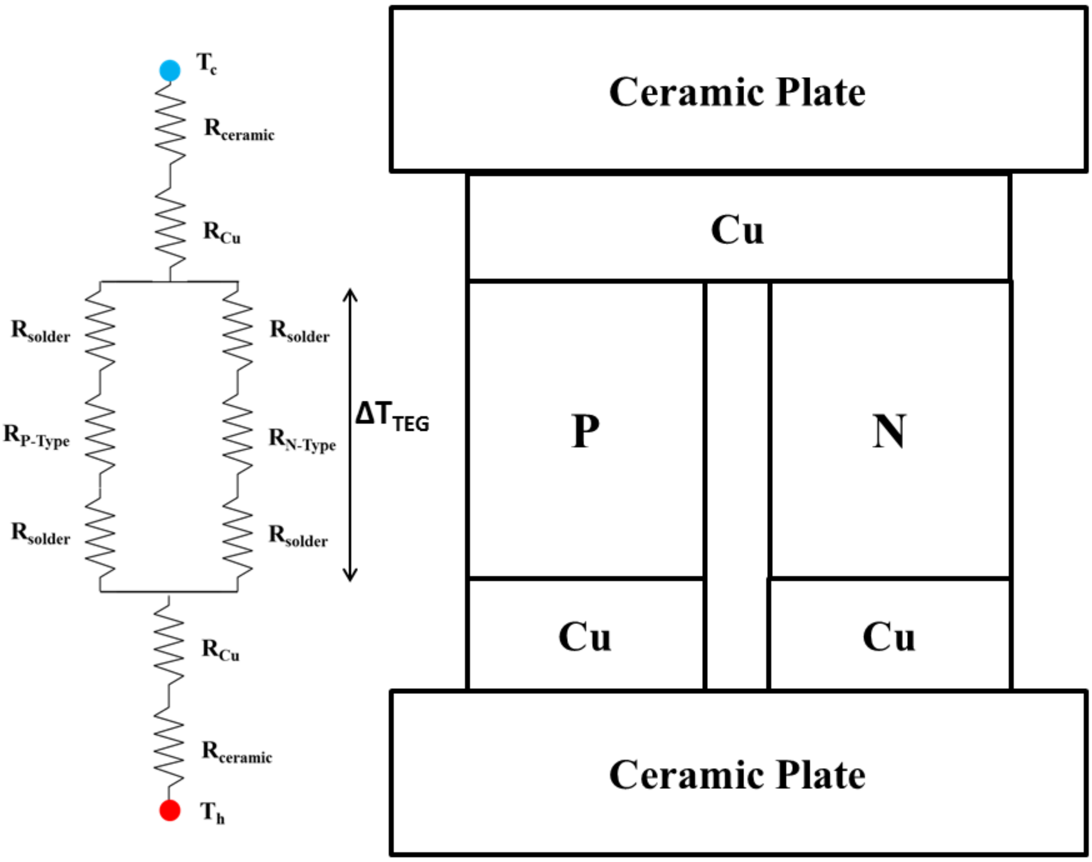

Figure 4.2 Schematic diagram and resistance network for single P-N couple (Hsu et al., 2011)

The exact temperature difference across the TEG is calculated with equation 4.16 (Hsu et.al, 2011), as shown below:

$$\Delta T_{TEG} = \frac{(R_N+2R_{sol})//(R_p+2R_{sol})}{2(R_{cer}+R_{Cu})+(R_N+2R_{sol})//(R_p+2R_{sol})}(T_h - T_C) \tag{4.16}$$

The values for the individual thermal resistance in equation 4.16 can be obtained from the manufacturer of TEG and ΔT_{TEG} can then be computed from this equation based on the hot side and cold side temperature.

Figure 4.3 below shows the TEG for present analysis. The TEG was obtained from Beijing Huimao Cooling Equipment Co. Ltd, China. The maximum continuous hot side temperature was specified at 125 ˚C. The maximum current and maximum voltage for each module was specified at 10 A and 15.2 V respectively. The size of each TEG module is 40 mm (length) and 40 mm (width) with a thickness of 3.2 mm. Each module weighs 22 g. There are 127 thermo elements in each module and the code for the TEG module was given as TEC1-12710T125 (Appendix B).

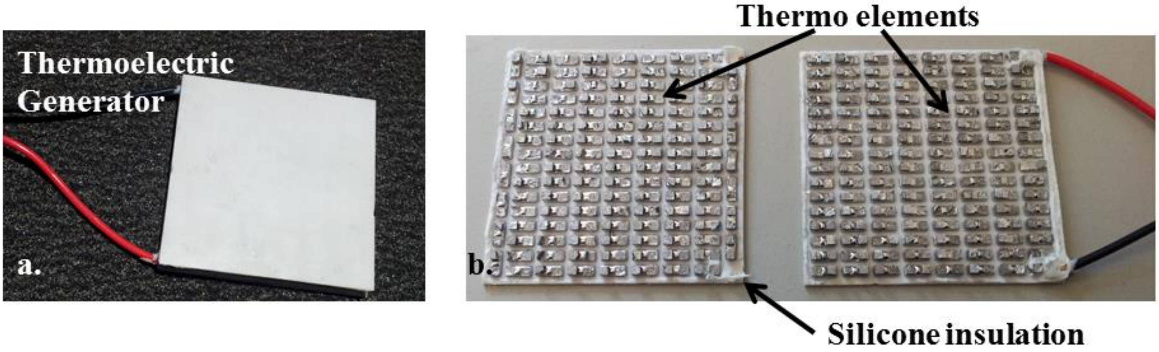

Figure 4.3 a) Thermoelectric generator, b) Inside view of the TEG with thermo elements and insulation

4.3 Single TEG Testing

4.3.1 Experimental Set Up

In order to determine the optimal design and settings for a water-based cooling TEG system, various heating and cooling conditions were conducted indoor on a single TEC. The objective was to explore the thermoelectric output power performance under different parameters such as cooling water flow rates, heating concentrations and compressive stresses at TEG contact interface. This analysis was important knowledge during the preliminary stage of development of a water-cooled TEG system to achieve optimal design settings and reduce operational cost. In addition, Peltier cell was used as TEG as it is relatively inexpensive compared to Seebeck cell which is specially designed for high temperature thermoelectric generation. Peltier cell is widely used as thermoelectric refrigeration such as portable coolers. Providing a temperature gradient across this cell leads to the Seebeck effect where the output power is similar to Seebeck cell at low temperature environment (<150 ^{o}C). It is also noted that the Peltier cell used in this analysis has a maximum operating temperature of 125 ^{o}C.

The test set-up is shown in Figure 4.4 and the schematic diagram of the setup in Figure 4.5. One side of the TEG is heated using a heat simulator made of copper block inserted with cartridge heater. The cold side is cooled using liquid cooled heat sink where water is pumped into the cooling block in which is installed with internal fins to provide a greater heat transfer performance. The temperatures were measured on the hot and cold side of the TEG using T-type thermocouples that where fixed inside the grooves machined on the heater block and liquid heat sink. In order to avoid any heat losses to the ambient, the test sample was completely shielded using polystyrene insulation. The formula to calculate the efficiency, η of the TEG is given below:

$$\begin{aligned} \eta &= P_{out} / P_{in} \\ &= [\dot{m} \text{ x } c_p \text{ x } (T_{out} - T_{in}) + P_{TEG}] \;/\; (VI)_{heater} \end{aligned} \tag{4.17}$$

The input power of the heater is given by the voltage (V) and the current (I) applied for the different set of heating. The power output is calculated from the mass flow rate of cooling water ($\dot{m}$) with specific heat capacity (c_p) and the temperature difference between the cold water at inlet (T_{in}) and cold water at outlet (T_{out}). The formula to calculate Carnot efficiency, η_c is given by the formula below:

$$\eta_c = \frac{T_h - T_c}{T_h} \tag{4.18}$$

where T_h is the hot surface absolute temperature and T_c is the cold surface absolute temperature of the TEG.

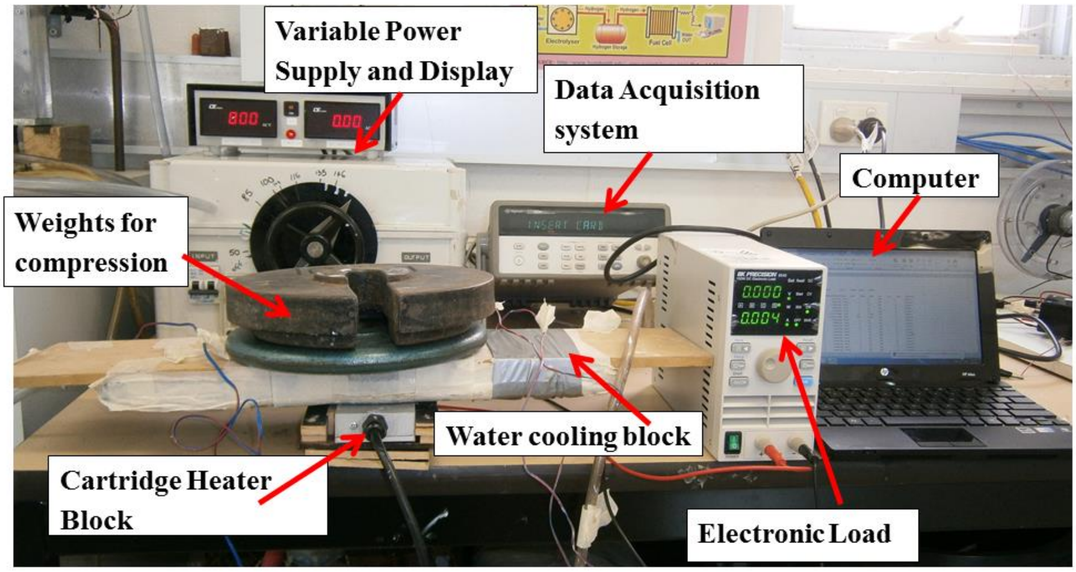

Figure 4.4 Experimental facility showing details of set-up used to test the performance of TEG

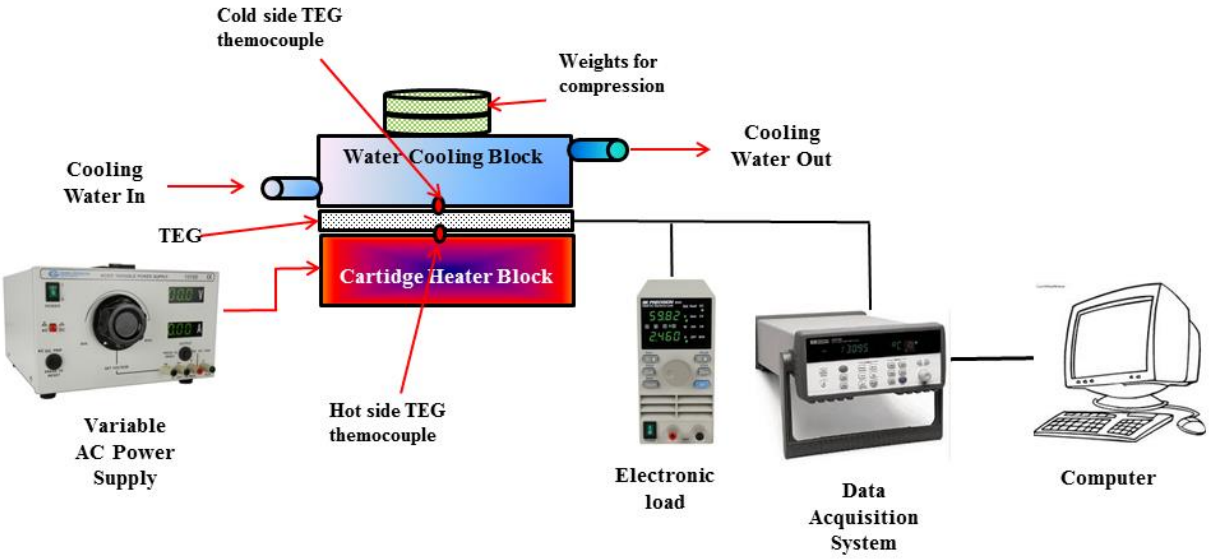

Figure 4.5 Schematics of experimental set-up used to test the performance of TEG

In order to understand the thermal effect of compressive forces between the TEG faces and heat exchange surfaces, interfacial pressure was applied using weights (in kg) of 10,15..etc as shown in Figure 4.4. Data from the thermocouples were recorded on the computer using Agilent 349070A data logger unit. The maximum power output was determined by a digital rheostat (model: BK Precision 8540, 150W DC). Figure 4.6 shows the heater and the cooling block and the set-up when weights were used for compression in order to reduce thermal contact resistance for the experimental set-up.

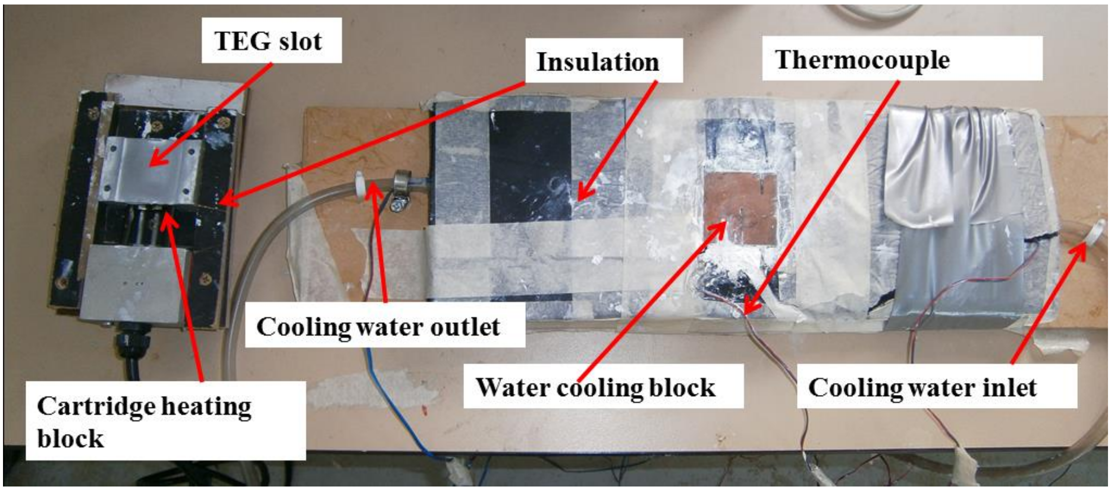

Figure 4.6 Electric heater (left) and water-cooling heat sink (right)

4.3.2 Results and Discussion

The first test objective was to determine the cooling water flow rate required on the cold side for steady state operation of the experimental set-up. Three different flow rates were used to obtain the performance of the cell. The external power supplied to the hot side of the TEG was chosen at 20 W. Figure 4.7 shows that by increasing water flow rate on the cold side of the TEG, the power output from the TEG increases. The results for 11 ml/s and 25 ml/s are identical and higher than 6 ml/s, as seen in Figure 4.7. This is because the cooling rate for both the flow rates provides the same effect. It can be concluded that the optimum cooling rate required for the cold side is 11 ml/s, as the higher flow rates will not increase the power output of the TEG. The subsequent experiments were conducted with this flow rate. These experiments were conducted to obtain results for a single TEG cell to obtain electrical and thermal characteristics.

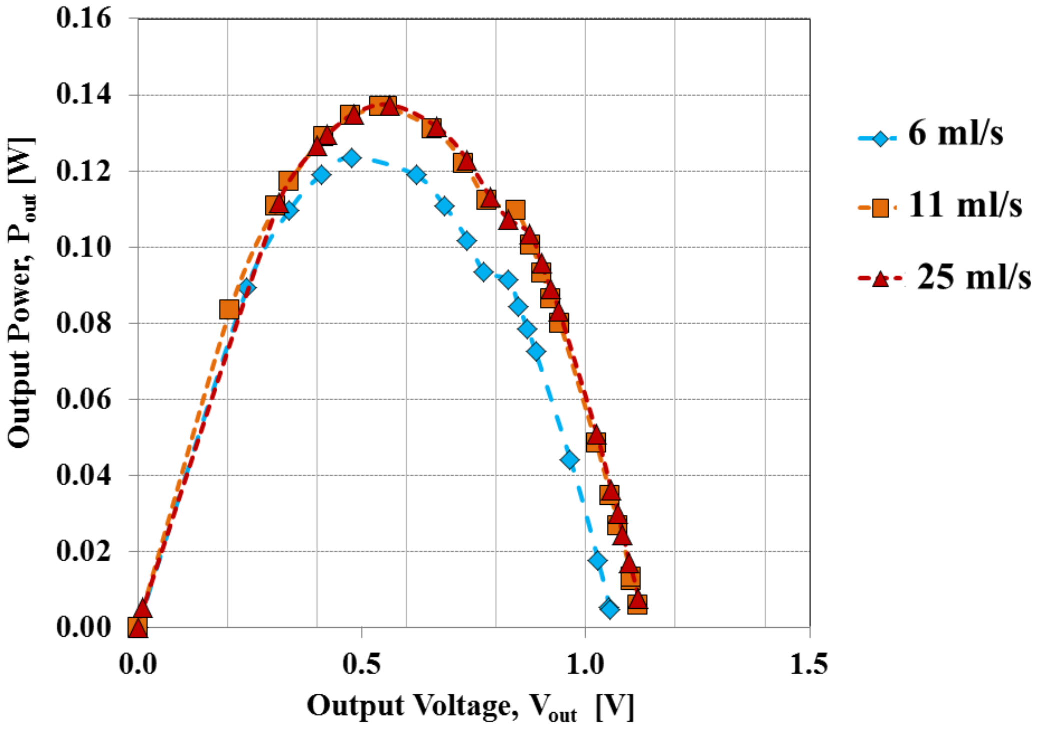

Figure 4.7 Effect of Flow Rate to Output Power

Few set of weights were used to apply the compression needed for the experimental setup. Weights from 10 kg to 40 kg, with an increase of 5kg between them were applied to the experimental set up. The result of this analysis is shown in Figure 4.8. From Figure 4.8, it is evident that the output power increases with the increase in the weights applied. The maximum power occurred at 30 kg. From Figure 4.8, the difference between 25 kg weight and 30 kg weight is negligibly small. From the results, it was shown that the 30 kg weights applied provides the maximum compression for maximum power output. The experiment is then continued with this weight for all other external power supply to the hot side of the TEG.

At 40 kg compression weight, significant drop in power was observed. This is due to the cracks in the TEG developed because of high compression. Based on the results obtained, the maximum loading stress for the TEG is at 245 kPa and it should not be exceeded in order to avoid damage to the TEG. The loading stress was obtained by dividing the weight (Newton) applied to the set-up with the surface area of TEG.

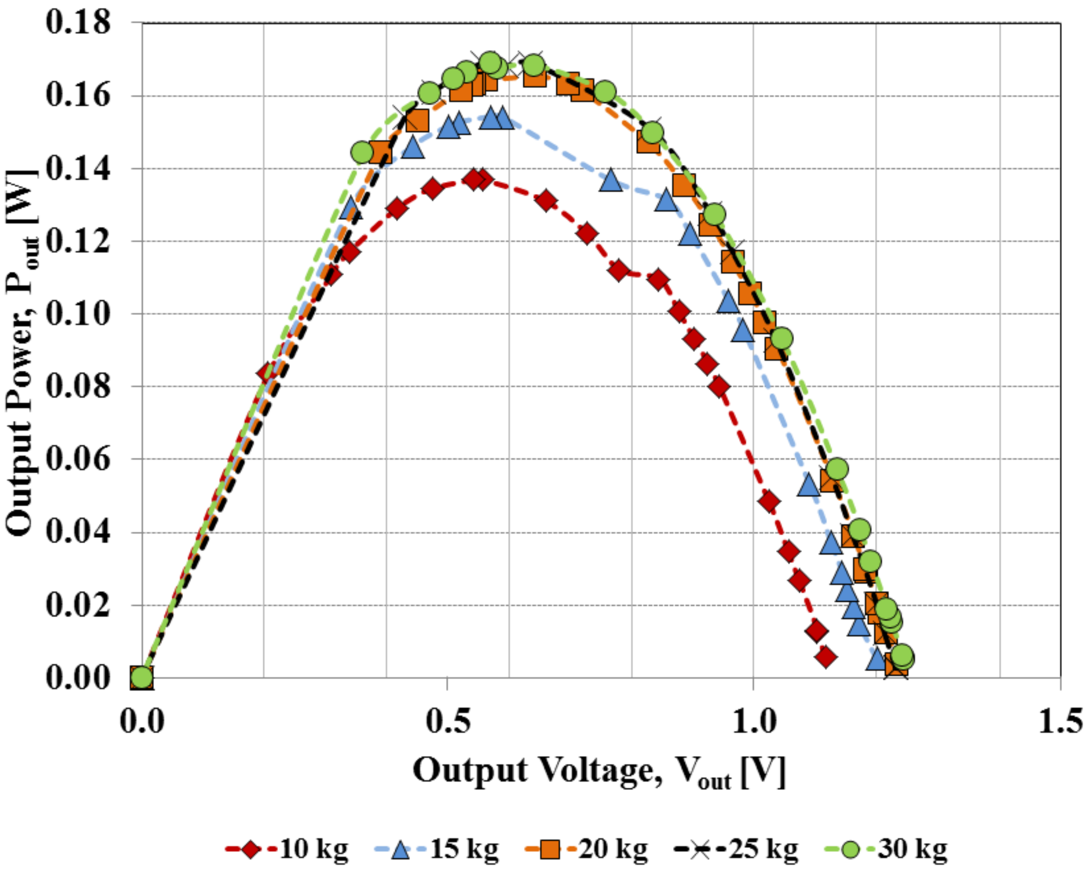

Figure 4.8 Output power with different compression weights

Figure 4.9 shows the temperature profiles of the single TEG testing. The hot side TEG temperature reached steady state after 28 minutes. The cartridge heater was set at 120 W power input. Once steady state was achieved, the electronic load was applied to the TEG to obtain the maximum power.

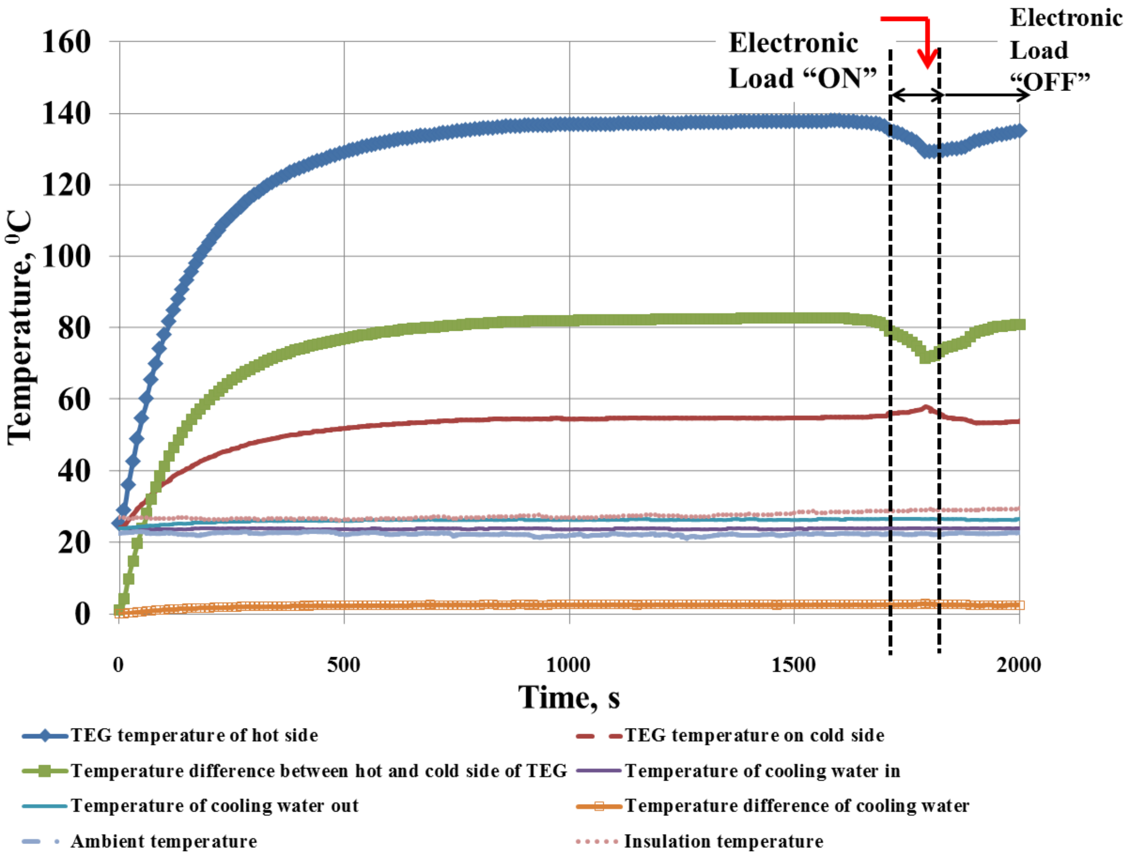

Figure 4.9 Temperature profiles of the single TEG testing

The resistance on the electronic load was varied from a maximum value to a minimum. Maximum power was obtained when the resistance of the TEG matches the resistance of the electronic load. From figure 4.9, it can be seen that when the electronic load was applied, a drop in the hot side TEG temperature was observed. At the same time, the cold side TEG temperature experienced an increase in its temperature. This is because of the electron transport phenomenon in the TEG module. The electrons move from the hot side of the TEG to the cold side of the TEG. As a result of that, current was induced in the TEG module. The heat transfer across the TEG transforms part of the thermal energy into electrical energy due to the electron transport phenomenon. When the electronic load was switched off, the temperature profiles of the cold and hot side of the TEG returns to its original state. The cold side of the TEG was maintained by a constant flow rate of cooling water. The steady state temperature difference between the cooling water inlet and outlet was observed at 2.6 ˚C.

With a known mass flow rate of water through the cooling system, the rate of heat transfer due to the cooling of TEG can be obtained. The maximum temperature difference across the TEG was recorded at 81.4 °C with a maximum power output from TEG at 2.6 W.

Once the flow rate and the required compression was established, the output power supply was varied to obtain the I/V (output current versus the output voltage) characteristic of the TEG. Figure 4.10 shows the performance curve of the TEG module at 120 W cartridge heater power input. The blue line shows the current versus voltage (I-V) relationship of the TEG. The red curve shows the power output of the TEG module versus the voltage output. The maximum power point for the TEG module lies when $I_L = I_{sc}/2$ and $V_L = V_{ocv}/2$. This point was obtained when the load resistance matches the internal resistance of the TEG module. The value of R_{int} can be obtained from the slope I-V line. The value of R_{int} depends on the operating temperature of the TEG module and varies with change in temperature (Montrecucco, 2014). For operation of TEG to the left of maximum power point, the effective thermal conductivity of the TEG module reduces as a result of reduced current flow. This results in lower thermal energy than the maximum power point which leads to increased thermal efficiency of the system. When the TEG module is operated to the right side of the maximum power point, the thermal conductivity of the system increases. This results in lower thermal efficiency. The thermal conductance increases from the left to the right of the power curve. The maximum power obtained for the above figure was recorded at 2.6 W with a corresponding output voltage and output current at 2.9 V and 0.9 A, respectively.

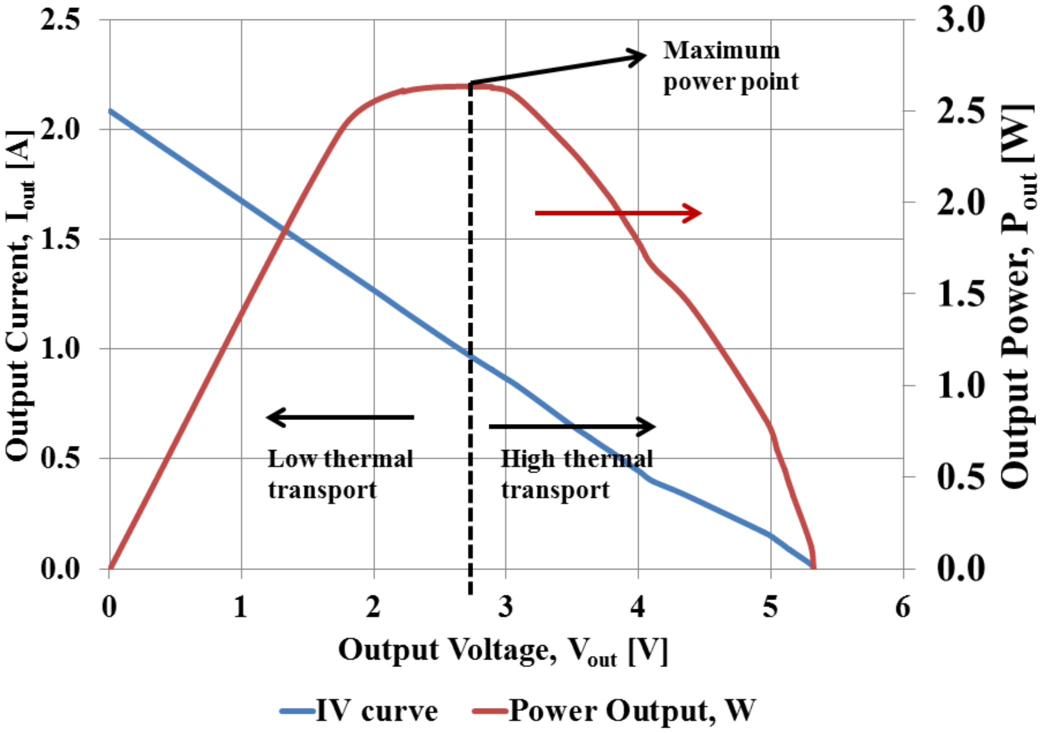

Figure 4.10 Output current and output power at 20 W heat input

Figure 4.11 shows the output current, I_{out} [A], versus the output voltage, V_{out} [V] for several temperature gradients, $\Delta T = T_H - T_C$ [^{0}C]. The output current increases with increase in external power supply, P_{in}. External power supply, P_{in} [W] of 20 to 160 Watts was applied to the hot side of the TEG.

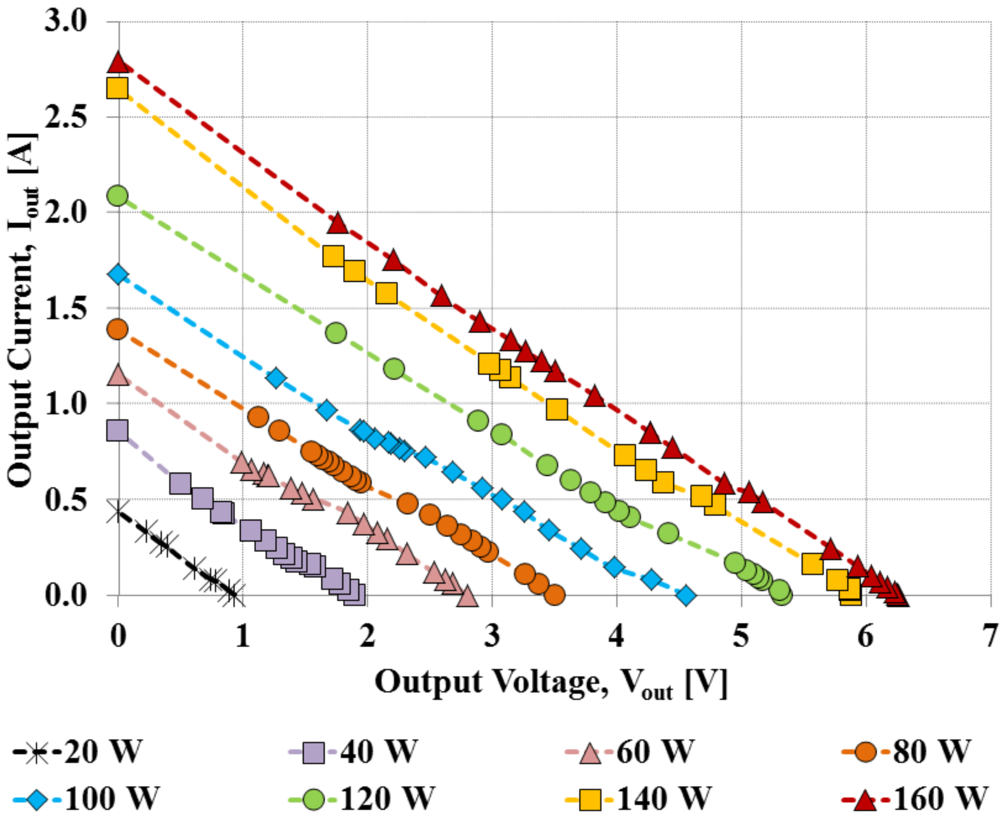

Figure 4.11 The output Current versus the Output voltage for several input power.

From Figure 4.11, a high linearity can be observed in all I/V plots with the same slope. This means that the internal resistance of the TEG is constant with the test temperatures on the hot side and the load operations. This will result in clear existence in clusters of internal resistances, as shown in Figure 4.12. In order to calculate the statistical behaviour of these clusters, their medium ($\mu_i \in$ 2.4, 2.2, 2.4, 2.4, 2.5, 2.5, 2.3, 2.4 Ω) and standard deviation ($\sigma_i \in$ 0.1, 0.2, 0.4, 0.2, 0.4, 0.2, 0.3, 0.5 Ω) were calculated and shown in Figure 4.13.

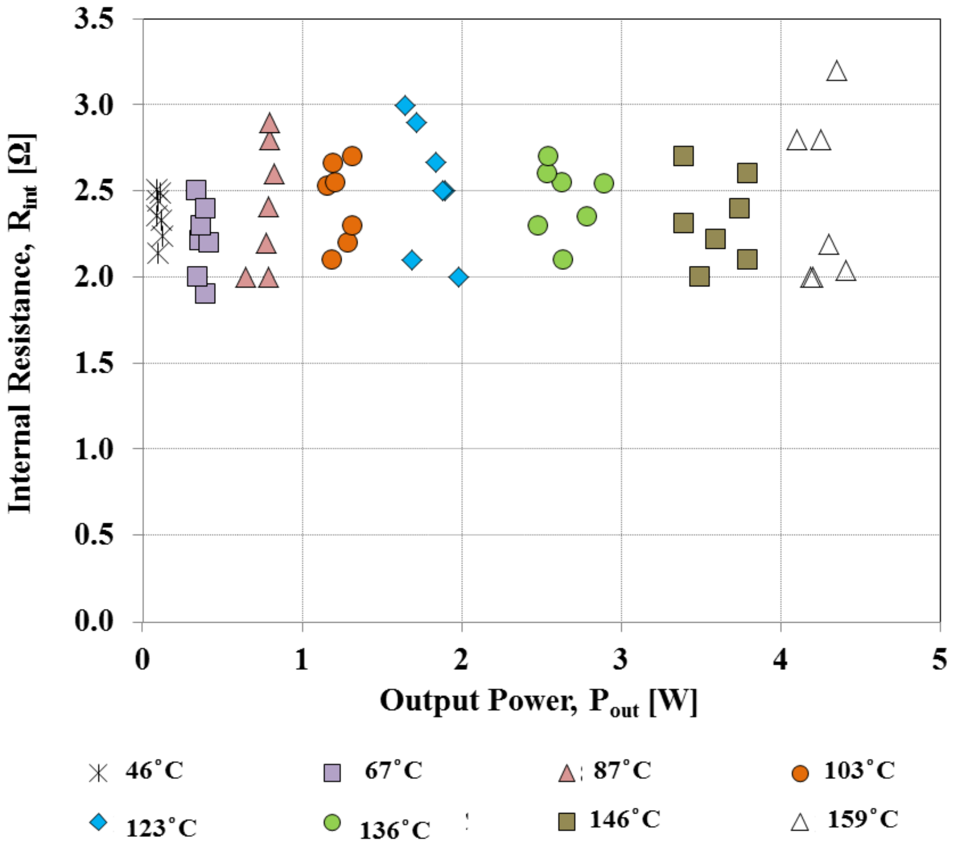

Figure 4.12 The internal resistance of thermoelectric converter versus the output power for several test temperatures.

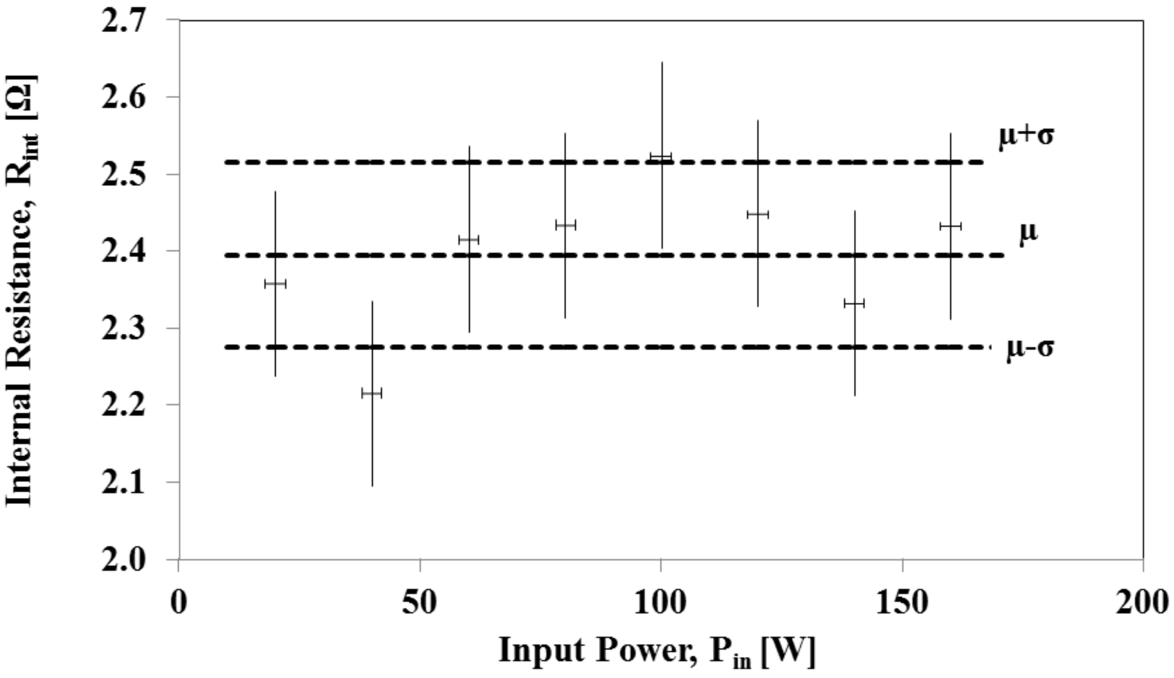

Figure 4.13 The medium and standard deviation values of the internal resistance of the TEC, versus the output power

The length of the intervals (the standard deviation) around the centre values of the clusters (their medium) can be considered to have the same order magnitude. This indicates repetition of certain pattern on the behaviour of TEG. The possible explanation for this discrepancy is the variability of the measuring conditions due to the high test temperature involved in the characterisation process (e.g., calorimetric leaks and convection around hot plate). The central line of the three horizontal line in figure 4.13 represents the medium of the mediums (e.g., $\mu = [\mu_1 + \mu_2 + \mu_3 + \mu_4 + \mu_5 + \mu_6 + \mu_7 + \mu_8]/ 8 = 2.4\ \Omega$), while the equal distances between the central line (μ) to the top and the bottom lines is the standard deviations ($\sigma = \sigma_1, \sigma_2, \sigma_3, \sigma_4, \sigma_5, \sigma_6, \sigma_7, \sigma_8, \approx 0.1\ \Omega$). These last two lines are located on $\mu + \sigma$ and $\mu - \sigma$, respectively. From this analysis, it is possible to conclude that the internal resistance of the analysed TEC is equal to $R_0 = 2.4\ \Omega$, with a tolerance equal to $\Delta R_{int} = 0.1\ \Omega$, thus $R_{int} = R_0 \pm \Delta R_{int} = 2.4 \pm 0.1\ \Omega$.

It is also observed from figure 4.14 that the output power increases with the increase in input power. This is due to the rise in output voltage, V_{out} [V] as the temperature gradient, $\Delta T = T_H - T_C$ [^{0}C] increases. This will then result in an increase in the output current, I_{out} [A].

The dissipated power corresponds to the external load resistance applied, R_L [Ω]. Maximum power occurs when the external load resistance R_L [Ω] is equal to the internal resistance, Rint [Ω] of the TEC, e.g, $P_{out} = R_L I_{out}$ [W]. Figure 4.14 shows the output power P_{out} [W] versus the output voltage V_{out} [V]. The output power increases P_{out} [W] with the increase in temperature difference, $\Delta T = T_H - T_C$ [^{0}C] or external power applied P_{in} [W] to the hot side of the TEC. Figure 4.15 is an alternative set of plots, but for the output power P_{out} [W] versus the output current I_{out} [A].

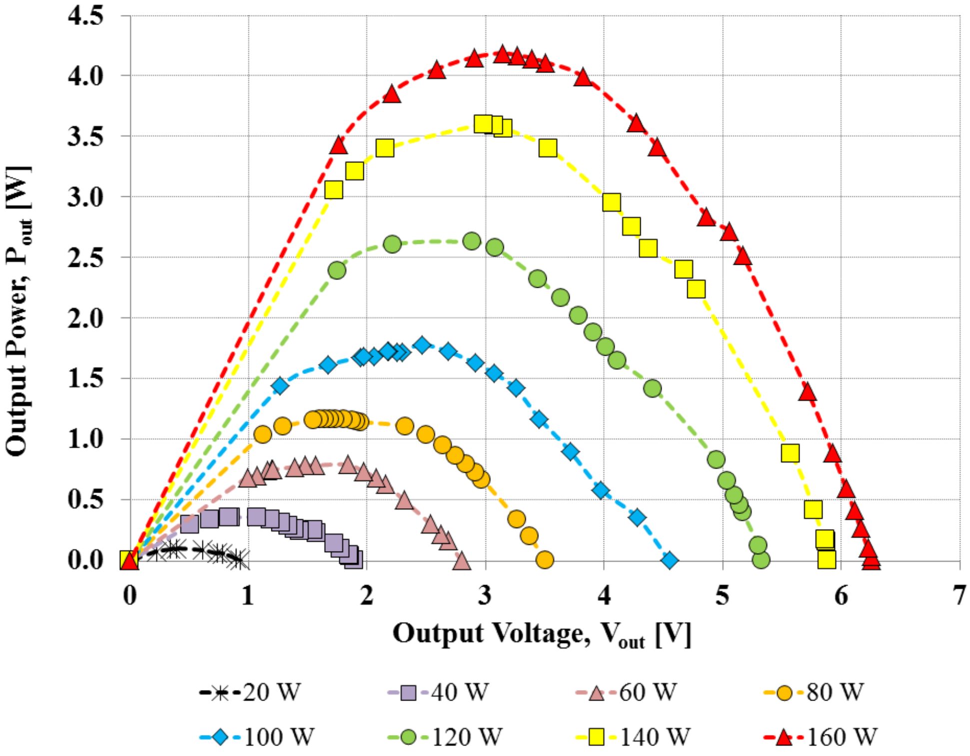

Figure 4.14 Output power versus the output voltage

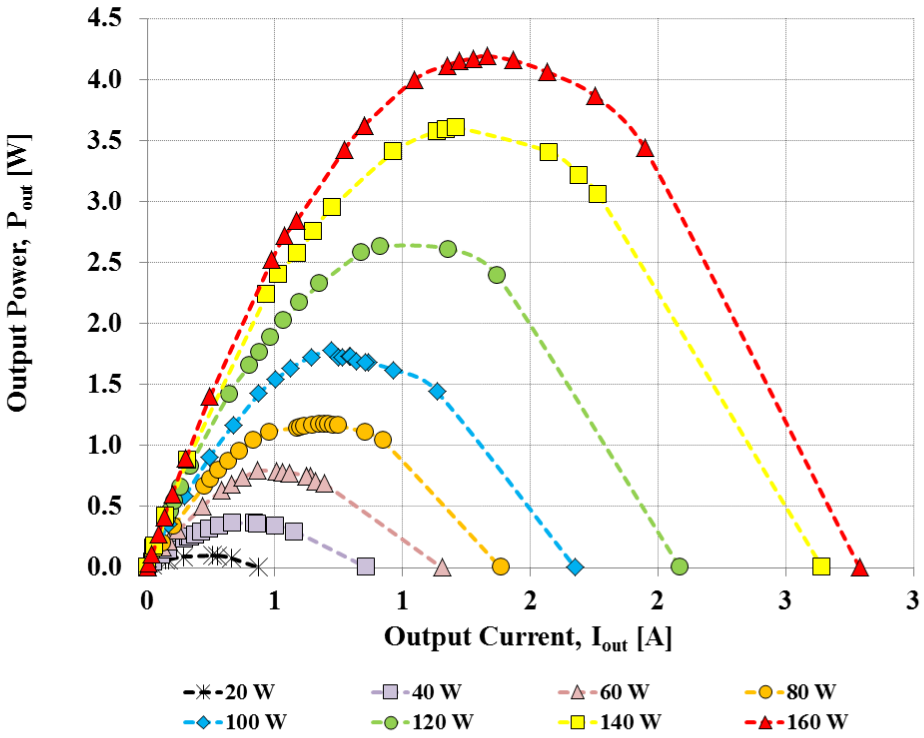

Figure 4.15 Output power versus the output current

Figure 4.16 shows the plot for open-circuit voltage, V_{open} [V] versus the temperature difference, $\Delta T = T_H - T_C$ [^{0}C] across the TEC. The open-circuit voltage, V_{open} [V] was measured at the output of the TEG without any external resistance load, R_L [Ω] applied to the TEG. An open- voltage function was obtained by curve-fitting the plot for figure 4.16, as shown below.

$$V_{open} = 0.064\,\Delta T \text{ [V]} \tag{4.19}$$

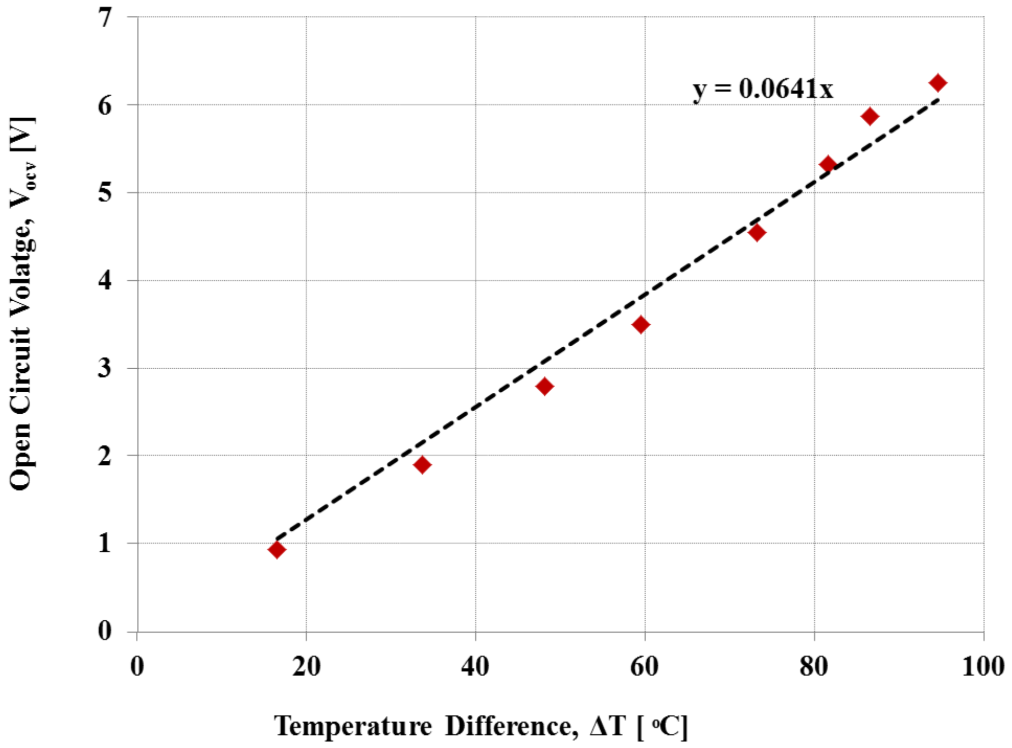

Figure 4.16 Open circuit voltage versus the temperature difference across the TEG

Figure 4.17 shows the TEG hot and cold side temperature and maximum power output for different power input to the cartridge heater. Maximum temperature 175˚C was recorded for the TEG hot side temperature at 160 W power input to the cartridge heater. Although the maximum continuous temperature for the TEG was specified at 125˚C on the hot side, the TEG was able to operate at higher temperature than the specified maximum temperature. This is because the TEG module is capable of handling intermittent high temperature up to 200˚C before the solder material in the module fails. Based on figure 4.16 it is evident that the hot side temperature varies linearly with the power input. The temperature range required by the TEG to operate using thermal energy of solar pond is between 30 ˚C to 90 ˚C. TEG module was proven to be able to produce electrical power within the specified range as mentioned for solar pond applications. This proves that the TEG module can be operated for power generation from solar pond using low grade heat below 90˚C. TEG cold side temperatures was maintained below 100˚C throughout the experiment using forced convection cooling.

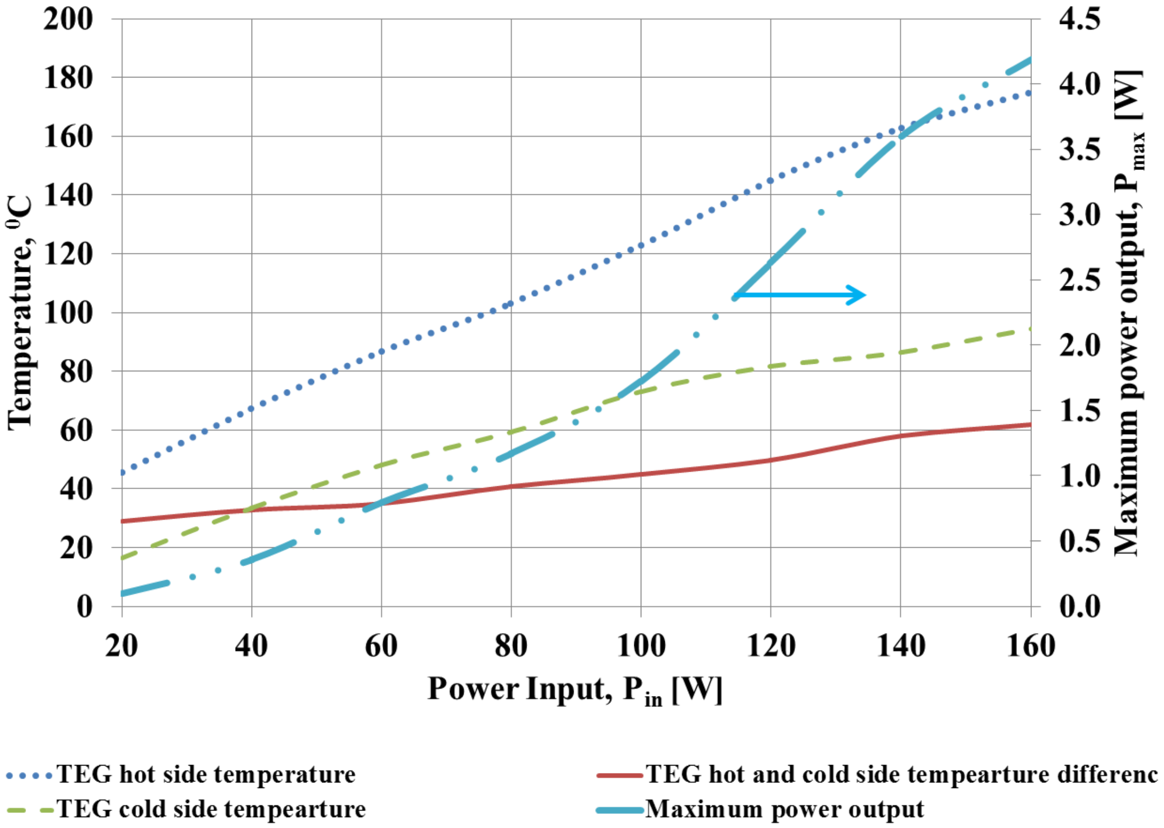

Figure 4.17 TEG hot and cold side temperature and maximum power output for different power input to the cartridge heater

Figure 4.18 shows TEG thermal resistance and TEG internal electrical resistance. These values can be calculated using the equations given below

$$R_{th\ TEG} = (T_h - T_c)/Q_{in} \tag{4.20}$$

$$R_{int\ TEG} = V_{mpp} / I_{mpp} \tag{4.21}$$

The average TEG internal electrical resistance was recorded at 2.4 Ω. As can be seen from figure 4.17, maximum TEG internal electrical resistance was 2.7 Ω at cartridge heater input of 160 W. The maximum and minimum TEG thermal resistance was recorded at 0.8 ˚C/W and 0.7 ˚C/W, respectively. The average TEG thermal resistance was calculated to be 0.8˚C/W.

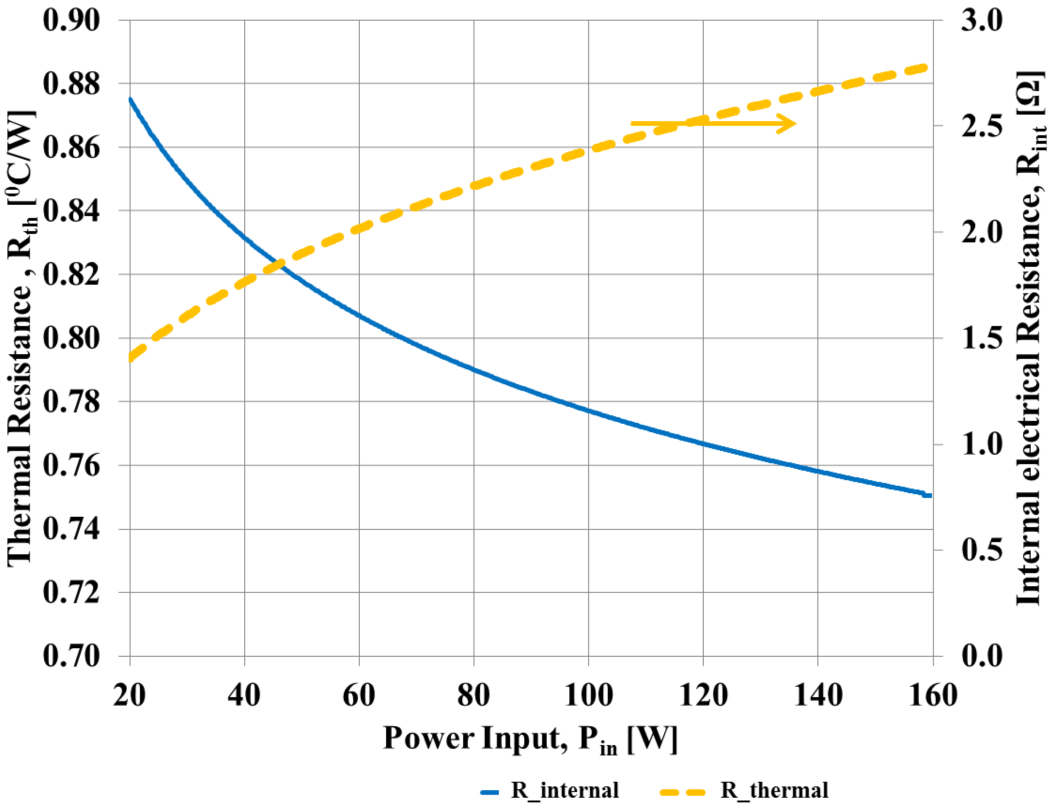

Figure 4.18 TEG thermal resistance and TEG internal electrical resistance

Figure 4.19 shows the maximum power point current output (I_{mpp}), maximum power point voltage output (V_{mpp}), Open circuit voltage (V_{ocv}), and short circuit current (I_{sc}). Open circuit voltage varies linearly with the cartridge heater power input with a maximum value recorded at 6.3 V. Both the maximum power point current output (I_{mpp}) and maximum power point voltage output (V_{mpp}) varies linearly with higher TEG hot side temperature or power input. Maximum power point current output (I_{mpp}) and short circuit current (I_{sc}) reached stagnation point after 140 W power input. This is because of the limitation of Bismuth Telluride (Bi_2Te_3) materials of the TEG module reaching its maximum operating limit. In other words, the increase in maximum power output with increase in cartridge heater power input will not result in higher output. It is best to operate the TEG below this maximum point for higher thermal efficiency.

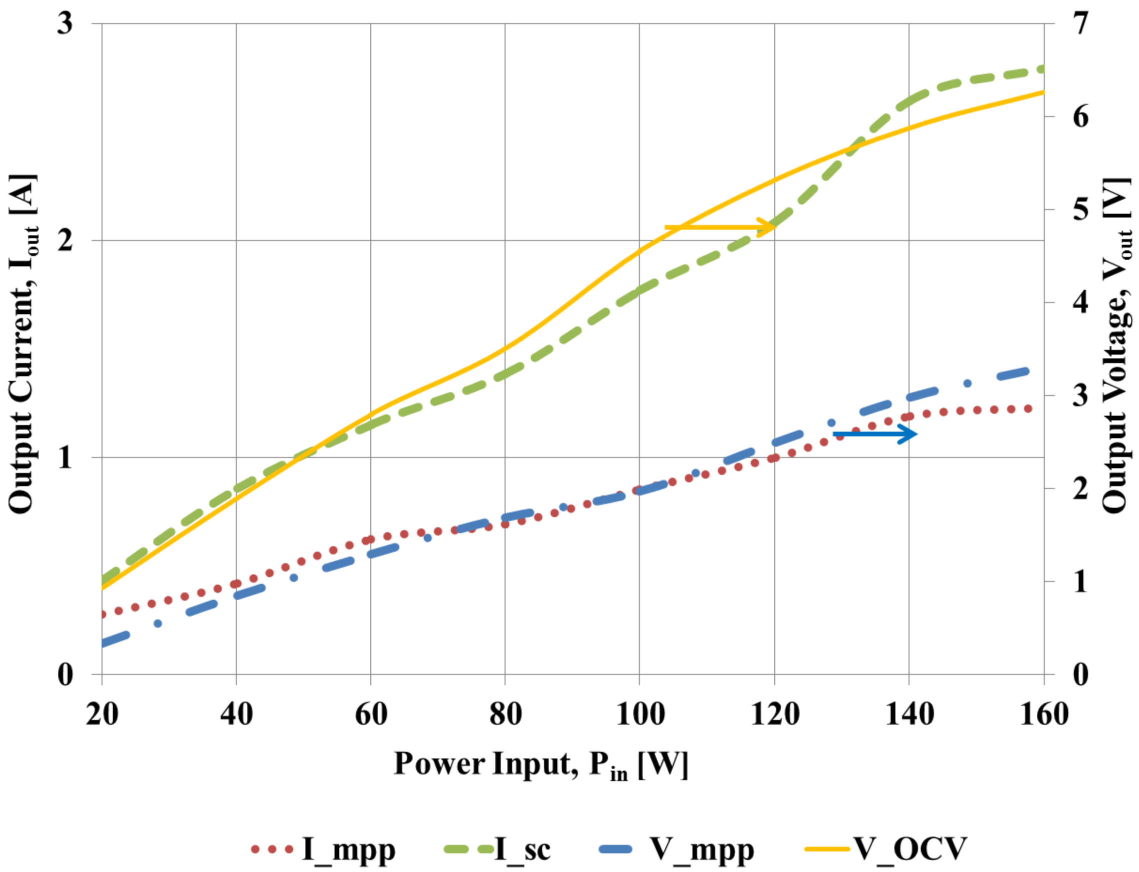

Figure 4.19 Maximum power point current output (I_{mpp}), maximum power point voltage output (V_{mpp}), Open circuit voltage (V_{ocv}), and short circuit current (I_{sc})

4.4 Experimental Investigation on Effect of Adhesive on the Performance of Thermoelectric Generator

4.4.1 Introduction

TEG is mainly used to convert heat energy to electrical energy by using a heat exchanger. These thermoelectric modules are secured in the heat exchanger either by mechanical clamps or with fixtures with nut and bolts (Casano and Piva, 2011). This presents a challenge when these thermoelectric modules are to be used under harsh conditions where corrosion plays a very important factor. Solar pond acts as a thermal storage system and this technology has the potential to be coupled with TEG. One of the key problem with solar pond is with the high concentration of salt content (>20%) in the water of the pond (Andrews and Akbarzadeh, 2005). The corrosion from the saltwater from solar pond actually requires a highly corrosion resistance metal or coating to overcome the problem of corrosion for heat exchangers used with thermoelectric modules in these harsh conditions. The above problem also applies to other industry where the thermoelectric modules are actually held by mechanical fixtures and requires a maintenance schedule to replace these fixtures overtime. This actually increases the overall cost of the system and the task becomes very labour intensive. Besides that, the overall thermal resistance of the thermoelectric modules increases with the addition of these fixtures and this will reduce the overall heat transfer across the TEG. As heat transfer is reduced, the amount of power generated will also drop and this will affect the overall efficiency of the system.

In this project, a TEG is attached to a substrate without any mechanical fixtures. A variety of adhesives are used to attach the TEG and the effect of the adhesive on the thermal resistance of the thermoelectric module was investigated. A single TEG was first tested on various heating loads without any attachment. Then a stainless steel plate of 1mm thick was attached to one side of the TEG and the tests were repeated with different adhesives. A 316 grade stainless steel was used for the experiment as it is designed for many industrial processes that require a higher level of resistance to corrosion. This makes this type of steel suitable for solar pond applications. The thermal conductivity of stainless steel plate used was taken as 16 W/m K. Finally, two stainless steel plates were sandwiched to the TEG and the tests were repeated again. Results are discussed in terms of the effect of adhesive to the overall thermal resistance of the TEG and also the effect of adhesive on the overall power output of the TEG. Three types of adhesives were used for this experiment and all three were chosen for its stability to perform in harsh environment and economic reasons. The names of the adhesives used for the experimental investigation of this paper are given as follow:

I. Arctic Silver® Thermal Adhesive (adhesive A).
II. BOSTIK® Industrial Grade Silicone glue (adhesive B)
III. Omegabond® 101 Epoxy adhesive. (adhesive C)

The above are the three common types of adhesives for strong adhesive bonds in harsh environments. In the following sections, the adhesives will only be referred to as adhesive A, B and C respectively as indicated above.

4.4.2 Experimental Set Up

The thermoelectric module characteristic test set-up is shown in figure 4.4. This is the same experimental set up used for single TEG testing. One side of thermoelectric module was heated using heat simulator made of copper block with cartridge heater inserted. The cold side was cooled using liquid cooled heat sink where water was pumped into the cooling block in which is installed with internal fins to provide a greater heat transfer performance. The temperatures were measured on the hot and cold side of the thermoelectric module using T-type thermocouples that where fixed inside the grooves machined on the heater block and liquid heat sink. In order to avoid any heat losses to the ambient, the test sample was completely shielded using polystyrene insulation. A series of weights were used to reduce the thermal resistance across the experimental setup. These weights ensure that the TEG is well clamped between the heater block and also the cooling block and minimises the air gap between them. A high conductive thermal paste was used to provide a good thermal contact between the surfaces.

The experiment was conducted with a single TEG attached with a single stainless steel plate of 1 mm thickness. As the size of each TEG is 40mm X 40mm, the same dimensions were used for the stainless steel plate. The adhesives were applied to attach the stainless steel plate to the TEG and it was compressed to ensure the thickness of the adhesive applies is not more that 1mm. The experiment was repeated for the TEG attached to the stainless steel plate under various heating conditions and this is repeated for the other two adhesives as well. Finally, another stainless steel was attached to the other side of the TEG and the experiment was repeated again for all three adhesives. The effect of different adhesives on the thermal resistance of the TEG is presented in the following section. Figure 4.20 shows the TEG attached with the stainless steel plate.

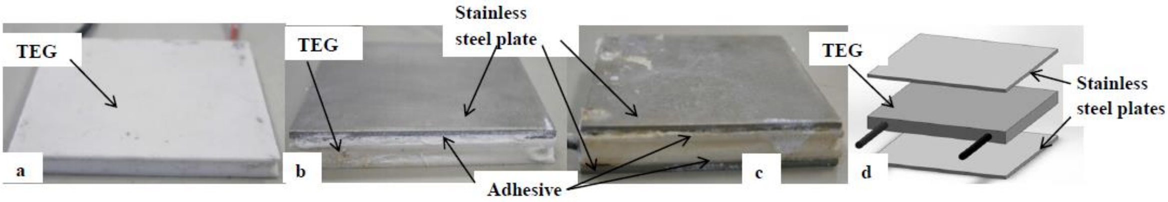

Figure 4.20 a) TEG, b) TEG attached to a single stainless steel plate with adhesive, c) TEG attached to double stainless steel plate with adhesive, d) model of TEG and stainless steel plates.

4.4.3 Results and Discussions

External power supply, P_{in} [W] of 20 to 160 Watts was applied to the hot side of the TEG. The thickness of all three adhesive used for the experiment was measured using a vernier calliper to be approximately 1 mm thick.

The experiment was repeated with TEG attached to a stainless steel plate with three different kinds of adhesives the adhesives The same setup as the above experiment was used and the TEG with one stainless steel plate attached with adhesives was tested under various heating conditions. The experiment was then repeated with two stainless steel plate attached with the above adhesives and the experiment was repeated again. The formula used to calculate the thermal resistance of the thermoelectric module is shown below.

$$Q = \Delta T / R_{th} \tag{4.22}$$

where Q (W) is the rate of heat transfer, ΔT (°C) is the temperature difference between the hot and cold side of the thermoelectric module, and R_{th} is the thermal resistance across the thermoelectric module. As adhesive and stainless steel will increase the thermal resistance of the thermoelectric module, the overall heat transfer across the thermoelectric module will drop and this will result in the drop in the power generated, as shown in Figure 4.21.

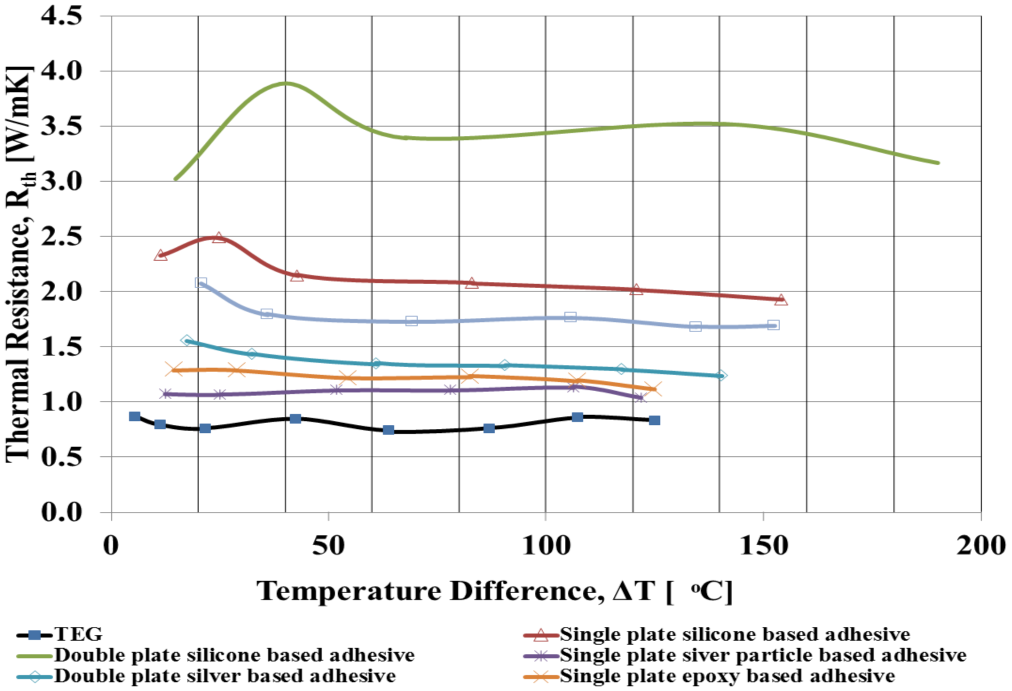

Figure 4.21 Thermal resistances versus external power supply

From Figure 4.21, the thermal resistance of a single TEG used on average calculated to be 0.8 ˚C/W. The legend in Figure 4.21 shows the type of adhesive used for the TEG stack with stainless steel plate. The number after the letter denoting type of adhesive refers to the number of stainless steel plate used for the stack. The thermal resistance increases to 1.30˚C/W when a single plate stainless steel was attached to the TEG with adhesive A. For a plate of thermal conductivity k, area A and thickness L, its thermal resistance can be calculated using the formula given below:

$$R_{th} = L/kA \qquad (4.23)$$

Figure 4.21 shows the thermal resistance, R_{th} [˚C/W] versus external power supply, P_{in} [W]. From Figure 4.21, it is shown that the thermal resistance of adhesive B and C is 1.1˚C/W and 0.2 ˚C/W. From the results, thermal resistance value of adhesive B and C is 16 % and 483 % higher than adhesive A, respectively. This proves that adhesive A is the best adhesive to attach TEG to any heat transfer surface as the thermal resistance is the lowest among the adhesives. Adhesive C is the least favoured as the thermal resistance of it is very high compared to other adhesives and this will cause a drop in the heat transfer across the TEG and subsequently reduce the amount of electrical power produced.

Figure 4.22 shows the resistance network used to calculate the thermal resistance of the adhesive for this experiment. T_{hot} refers to the hot side temperature and T_{cold} refers to the cold side temperature. R_1 is the resistance of the stainless steel plate, R_2 is the resistance of the adhesive and R_3 is the resistance of the TEG. For the experiment using a single plate, total resistances are given by the sum of $R_{1,}$ R_2 and R_3. For double stainless steel plate, the total resistances will be based on two plates attached with adhesives to the TEG as shown by Figure 4.22 (b).

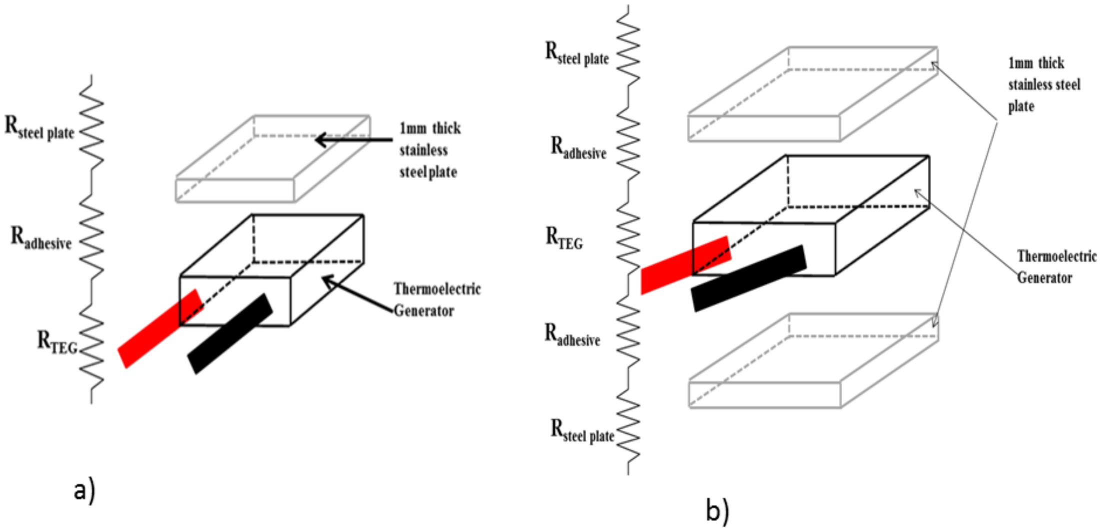

Figure 4.22 a) Thermal resistance network for single stainless steel plate attached to TEG with adhesive; b) Thermal resistance network for double stainless steel plate attached to TEG with adhesive

As the thickness of the stainless steel plate was 1 mm and the area at 40 mm X 40 mm and the thermal conductivity of stainless steel plate is 16 W/m K, the thermal resistance of the stainless steel plate was calculated to be 0.04 ˚C/W. As the total increase in the thermal resistance was caused by the TEG, stainless steel plate and the adhesive A, the thermal resistance of the adhesive A can be subtracted from the thermal resistance value of TEG and stainless steel plate. This gives a value of 0.2 ˚C/W for the thermal resistance of adhesive A. The same method can be applied to calculate the thermal resistance of adhesive A when two stainless steel plates were attached to the TEG. From Figure 4.21, the thermal resistance of TEG with two stainless steel plate attached with adhesive A is 1.6 ˚C/W. The total thermal resistance caused by adhesive A calculated to be 0.2˚C/W. This is approximately same with the thermal resistance calculated for the adhesive A with a single stainless steel plate. The values differ by 7 % due to the contact resistance arising from the uneven layer of the adhesive used to attach the stainless steel to the TEG. The values for the thermal resistance of all three adhesives were within less than 10 % of the published values of each of the manufacturers of the adhesives used in the experiment.

Figure 4.23 shows the output power of TEG for various heating conditions. Maximum power output, P_{out} (W) recorded for a single TEG was maximum at 3.56 W with a power input of 160 W. This gives a maximum efficiency of 2.3 %. The other three lines on Figure

4.23 shows the maximum power output, P_{out} (W) obtained for the TEG when a stainless steel plate was attached to the surface of TEG with adhesive. All three adhesives were analysed and adhesive B affects the power output of the TEG drastically. The drop in power is more than 60 % as the thermal resistance across the TEG increased and this caused huge resistance for the heat transfer flow from the hot side to the cold side. With a reduced heat transfer rate, the amount of power generated will also drop proportionally. Adhesive C causes slightly higher thermal resistance as compared to the adhesive A.

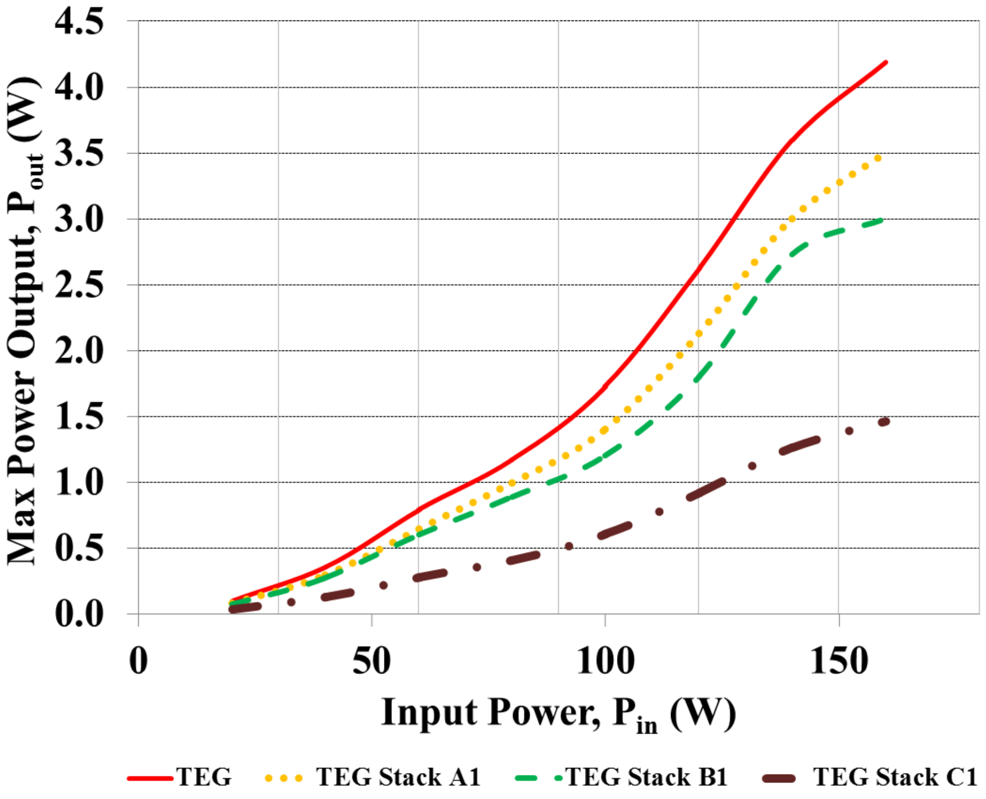

Figure 4.23 Maximum power output of TEG versus the input power

Thermal resistance of a TEG plays an important role in the amount of heat transfer across a TEG. A lower thermal resistance will provide more heat transfer across the surface of TEG and results in higher power output. Arctic Silver® Thermal Adhesive provides the least thermal resistance when used to attach stainless steel plate to a TEG. This is followed by Omegabond® 101 Epoxy adhesive and the least favourable adhesive is BOSTIK® Industrial Grade Silicone glue. This is because BOSTIK® Industrial Grade Silicone glue causes very high thermal resistance to the entire setup and this will cause the amount of heat transfer across the TEG to reduce drastically. The Arctic Silver® Thermal Adhesive and Omegabond® 101 Epoxy adhesive increases the thermal resistance of the TEG stack with a single stainless steel plate by 16 - 22 % and the BOSTIK® Industrial Grade Silicone glue increased the thermal resistance of the same stack by 109 %. The drop in power for BOSTIK® Industrial Grade Silicone glue was more than 60 % as the thermal resistance across the TEG increased and this caused huge resistance for the heat transfer flow from the hot side to the cold side. From the work done, it was shown that Arctic Silver® Thermal Adhesive can be used to attach TEG to any heat transfer surface with a minimum increase in the overall thermal resistance of the system. This method allows the attachment of TEG without any mechanical clamps and fasteners.

4.5 Parallel and Series Array Connections Study

4.5.1 Introduction

In actual thermoelectric systems practice, several arrays consisting of series and parallel connections are deployed to achieve the desired voltage and current output. These connections can help to achieve larger values of current and voltage depending on applications. Generally, maximum power point trackers (MPPT) electronic converters are used to maximise the power extracted from the TEG systems (Laird and Lu, 2013). The TEG arrays connected to the MPPT subsystems are controlled independently, similar to photovoltaic systems (Pilahwa and Perrault, 2013). The MPPT system helps to reduce the effect on the power output from the TEG systems due to thermal mismatch. Thermal mismatch is caused by thermal variability because of uneven heating and irregular thermal contact resistance arising from mechanical clamping forces. These thermal mismatches cause irregular power output from the array of TEG systems. As a result of this, the load impedance applied to the TEG array systems causes decrease in thermal to electrical conversion efficiency of the system. MPPT allows each TEG in the arrays controlled independently electronically (Wu et.al, 2013). However, this increases the overall cost of the TEG system and at the same time increases the complexity of the TEG system. For low cost and simple TEG applications, a compromise must be reached between the series and parallel connections to reach the required operating conditions. A series connection of all the TEG system will compromise the operation of the system if one TEG in the array fails due to the unforeseen circumstances. The parallel connections of the TEG systems will result in higher joule heating due to the higher current output. Therefore, a combination of series and parallel arrays are desired for a low cost TEG system. A number of TEG can be connected in series and then be connected in parallel arrays to increase the reliability of the TEG system. The type of combination for series and parallel depends on the end use of the TEG system The desired output current and voltage can be customised depending on the application. Figure 4.24 and 4.25 shows the TEG modules arranged in series and parallel arrays. From Figure 4.24 it is shown that the output current in the series array remain the same but the voltage is the sum of the individual voltage of the TEG modules used in the arrays, as shown by equation 4.24. From Figure 4.25, it is shown that the voltage across the parallel array system remain the same. The output current of the parallel array is the sum of the individual output current of the TEG modules, as shown by equation 4.25. In practical application, a balance between the series and parallel arrays must be found to suit the requirement of the desired implementation of the TEG systems.

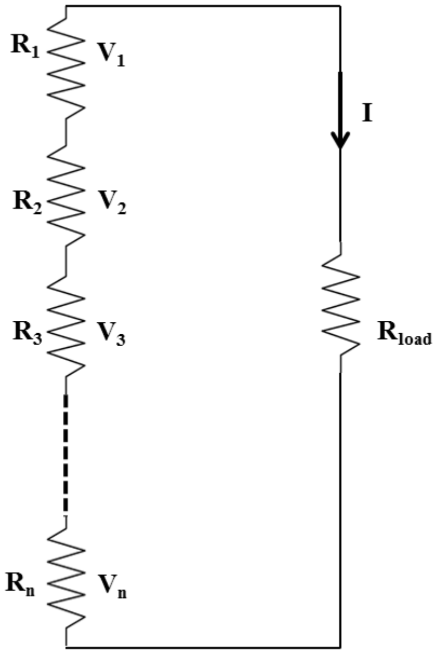

Figure 4.24 Series connection array resistance network

$$V_{total} = V_1 + V_2 + V_3 + \ldots\ldots\ldots\ldots + V_n$$

$$= \sum_{i=1}^{n} V \qquad (4.24)$$

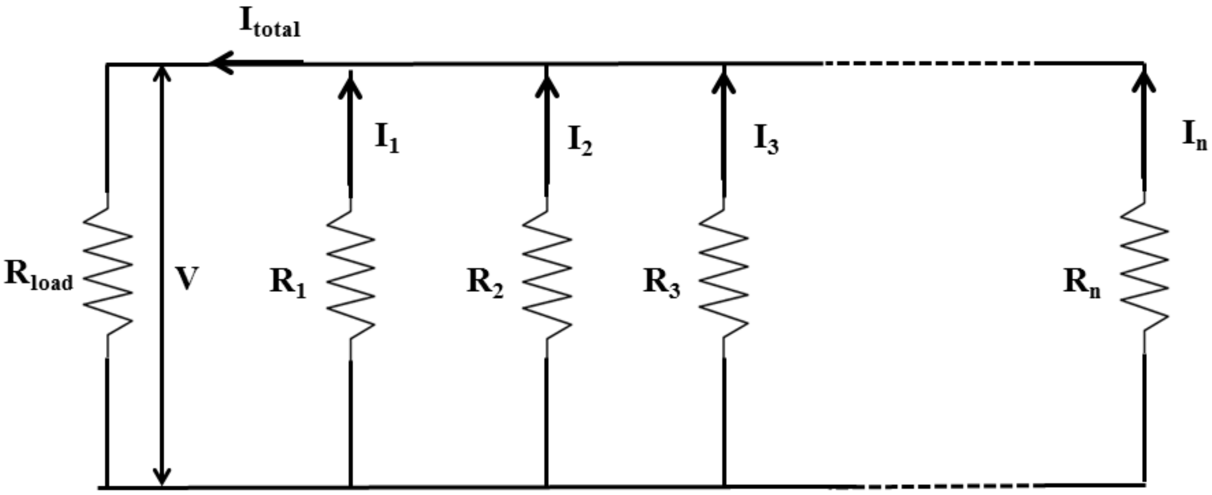

Figure 4.25 Parallel connection array resistance networks

$$I_{total} = I_1 + I_2 + I_3 + \ldots\ldots\ldots\ldots + I_n$$

$$= \sum_{i=1}^{n} I \tag{4.25}$$

4.5.2 Experimental Analysis of Series and Parallel Connections on the Performance of TEG Systems

In order to evaluate the performance of TEG systems operating in series and parallel arrays, a simple experiment was conducted to test the TEGs under those conditions. Two TEGs were used for this experiment. The experiment was first conducted with both the TEGs connected in series and then followed by a parallel connection. The setup used for the experiment is shown in the diagram below in Figure 4.26. A 40 mm by 80 mm aluminium cooling water block was used for the cooling of TEGs. Water from the tap in the laboratory was channelled through the cooling block. A constant water flow rate of 20 ml/s was used for the experiment. The 40 mm by 80 mm cartridge heatre block was used to heat the TEGs on the hot side. The input into the cartridge heater was controlled by a variable power supply as shown in the diagram. The variable power supply allows for different heating inputs applied to the cartridghe heater block. G clamps were used to sandwich the TEGs between the water cooling block and the cartridge heater. G-clamps also provides compression needed to minimise the contact resistance of the setup with TEGs. An electronic load was applied to obtain the output current and output voltage for the TEG systems. The data was recorded using a data acquisition system connected to a computer. A set of thermocouples as shown were used to measure the hot and cold side tempearture of the TEGs as well as the water inlet and outlet temperatures. Figure 4.27 shows the schematic of the experimental set up.

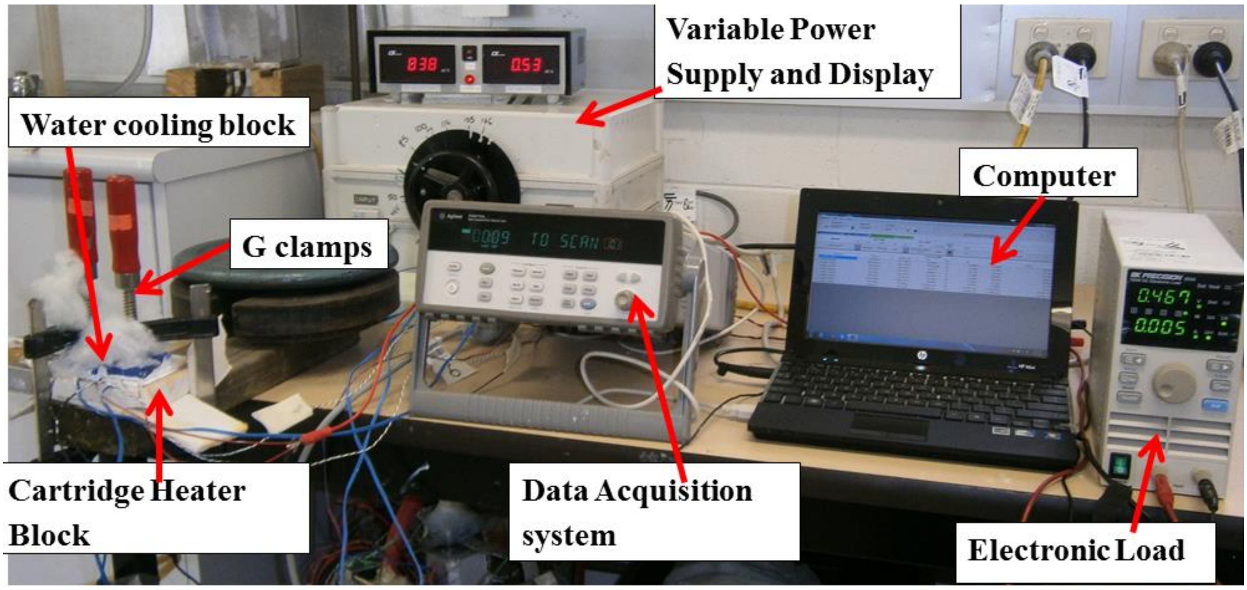

Figure 4.26 Experimental set up for testing of TEG systems operating in series and parallel arrays

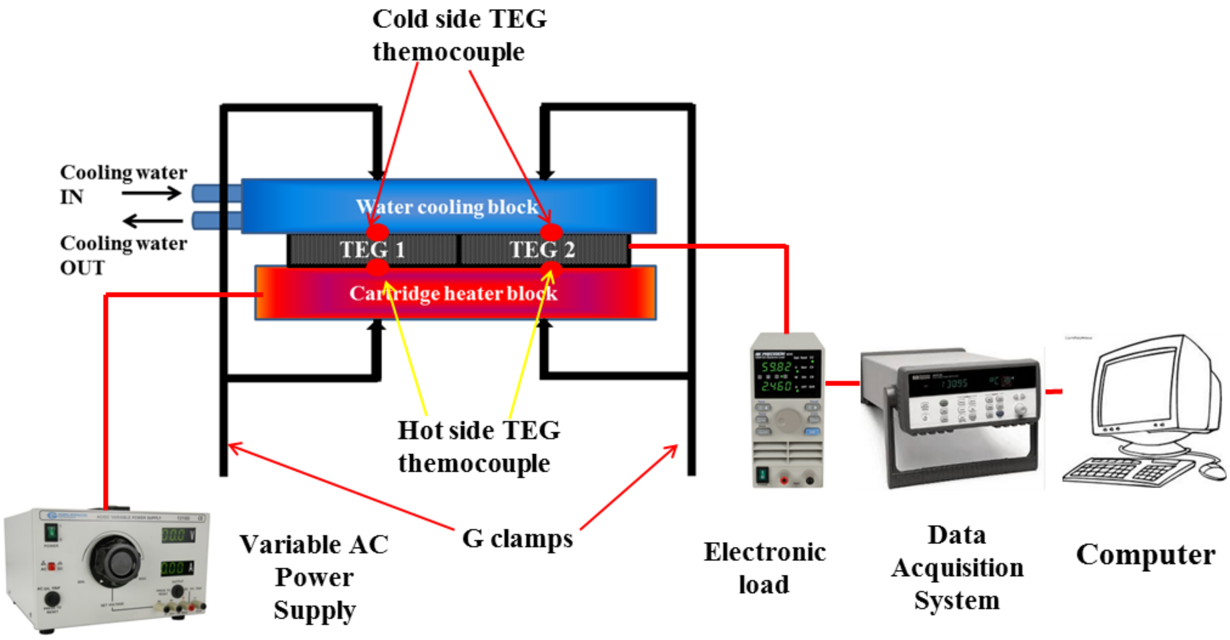

Figure 4.27 Schematic of experimental set up for testing of TEG systems operating in series and parallel arrays

4.5.3 Results and Discussions

Figure 4.28 shows the output power of the TEG arrays arranged in series and parallel versus output voltage. The electronic load was applied to the TEG module systems and varied from the highest to the lowest resistance. When the resistance of the electronic load matched the electrical resistance of the TEG systems, maximum power was obtained as shown in the Figure 4.28. A maximum power output of 5.13 W was obtained from the TEGs connected in series array when 200 W of heat input was applied to the cartridge heater. For the same heat input on the parallel array of the TEG system, a maximum power output of 3.65 W was recorded. The output power from the parallel array TEG system was less than series array by almost 40 %. Although the input power applied to both arrays are similar, the output power from the parallel array shows lower power output. This is due to the effect of Joule heating from the higher output current. As shown in Figure 4.29, the output current for the parallel array is higher than the series array. Figure 4.29 shows the output current versus output voltage of the TEG arrays at different power inputs. The maximum short circuit current observed in the series array was recorded at 2.2 A and 3.3 A was recorded for the parallel array. Similarly, the maximum power point current at maximum power for series array and parallel array was recorded at 1.1 A and 1.6 A respectively. The difference in both these maximum power point current was found to be around 39 %. The higher output current from the parallel array caused losses in terms of Joule heating. Electricity was converted into thermal energy when the electricity flowed through resistance in the connections. The higher the output current form the array, the higher the losses due to the Joule heating as shown by equation 4.26. As a result of that the output power from the parallel array was lower than the series array.

$$P_{loss} = I^2 R_{load} \tag{4.26}$$

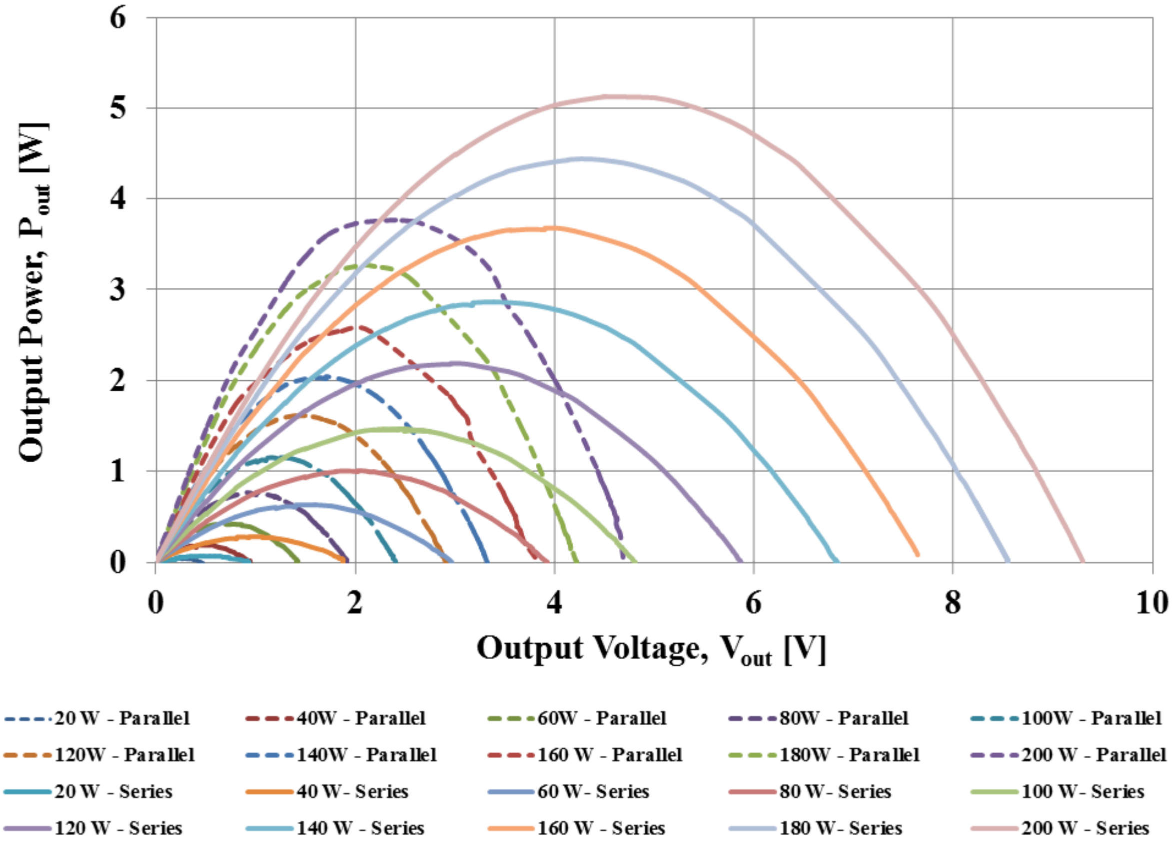

Figure 4.28 Output power of the TEG arrays arranged in series and parallel versus output voltage

From Figure 4.29, we can see that the voltage output from the parallel array is lower than the series array. This is because the voltage in the series array is multiplied by the number of TEG used in the system. For a TEG module producing certain voltage a specified heating conditions, the voltage output will double if two TEGs are connected in series for the same heating conditions. For parallel connection, the above situation will result in twice the original output current of the single TEG. The open circuit voltage for series array was recorded at 9.3 V when 200 W of heating power input applied to the cartridge heater. For the same conditions, open circuit voltage for parallel array connection was recorded at 4.6 V, which was approximately half the open circuit voltage for the TEG system connected in series.

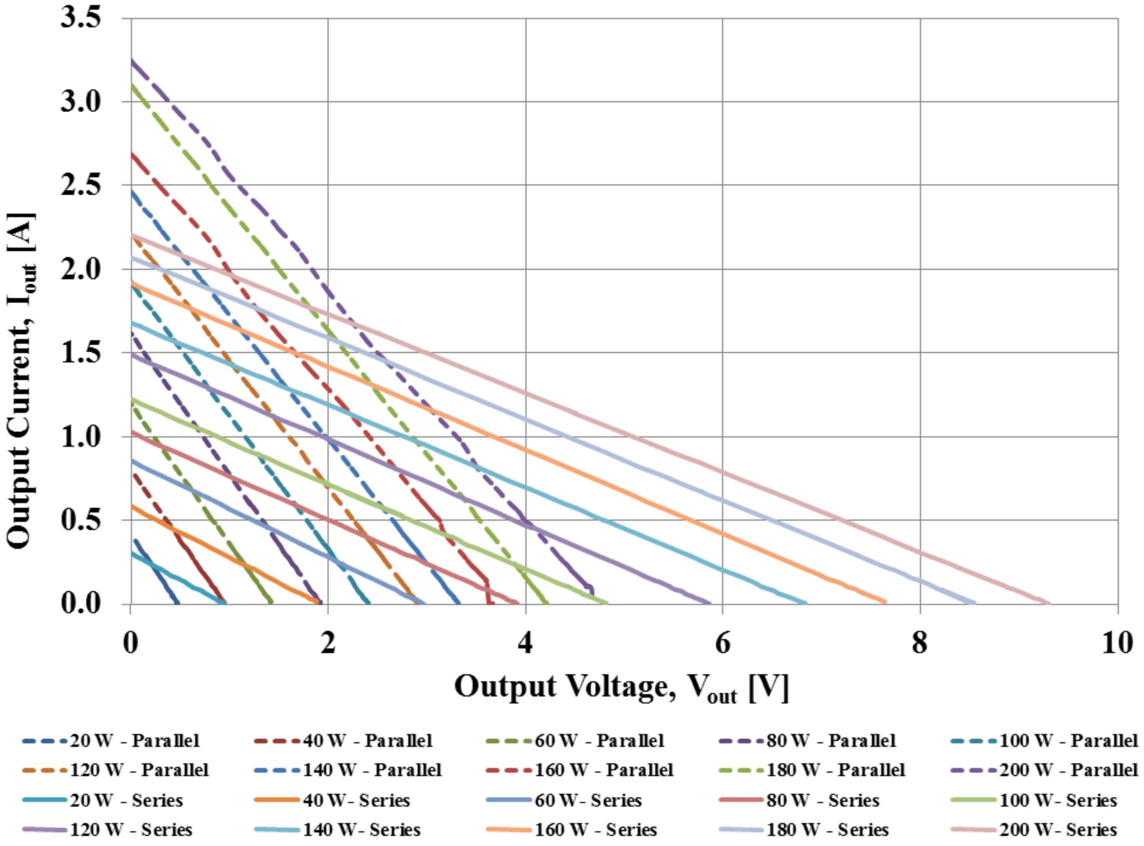

Figure 4.29 Output current of the TEG arrays arranged in series and parallel versus output voltage

Figure 4.30 shows the open circuit voltage and maximum power output versus the temperature difference across TEG arrays connected in series and parallel. Open circuit voltage for series array was observed to be twice the value of open circuit voltage of the parallel array. This is within the expectation as discussed earlier. The power output for the parallel and series array did not differ initially as shown in Figure 4.30. At higher temperature difference, the maximum power output for the series array showed higher output than parallel array at same temperature differences. At lower temperature differences, the output current is low and this results in lower power losses in the circuit. At higher temperature differences, the power loss is significant. The increase in power lost calculated in equation 4.26 shows that the power lost will increase by order of two when output current is increased. This is due to the losses caused by Joule heating as discusses earlier. Furthermore, electronic loads typically measure the power at the load itself. This does not account for the loss of power within the leads and connections. These connections are often made with alligator clips and have a comparatively high resistance. A current flow of 5 A or more through the circuit will lead to significant power lost in the high resistance connection. For example, a connection of only 100 mΩ would lose 2.5 Watts of power (I^2R). A 100 mΩ resistance is not uncommon on alligator clip connections. Even the resistance of the wire itself can be significant. In any thermoelectric system all connections should be soldered to reduce resistance. A more accurate way of measuring the power produced by the module is to use the electronic load to control and measure the current and measure the voltage on the module power leads. Since the voltage measurement draws negligible current, alligator clips are acceptable to be used and since the current is the same no matter where in the circuit it is measured, alligator clips are acceptable to use there. Care should be taken when measuring currents and voltage using electronic load to minimise the power loss from the system.

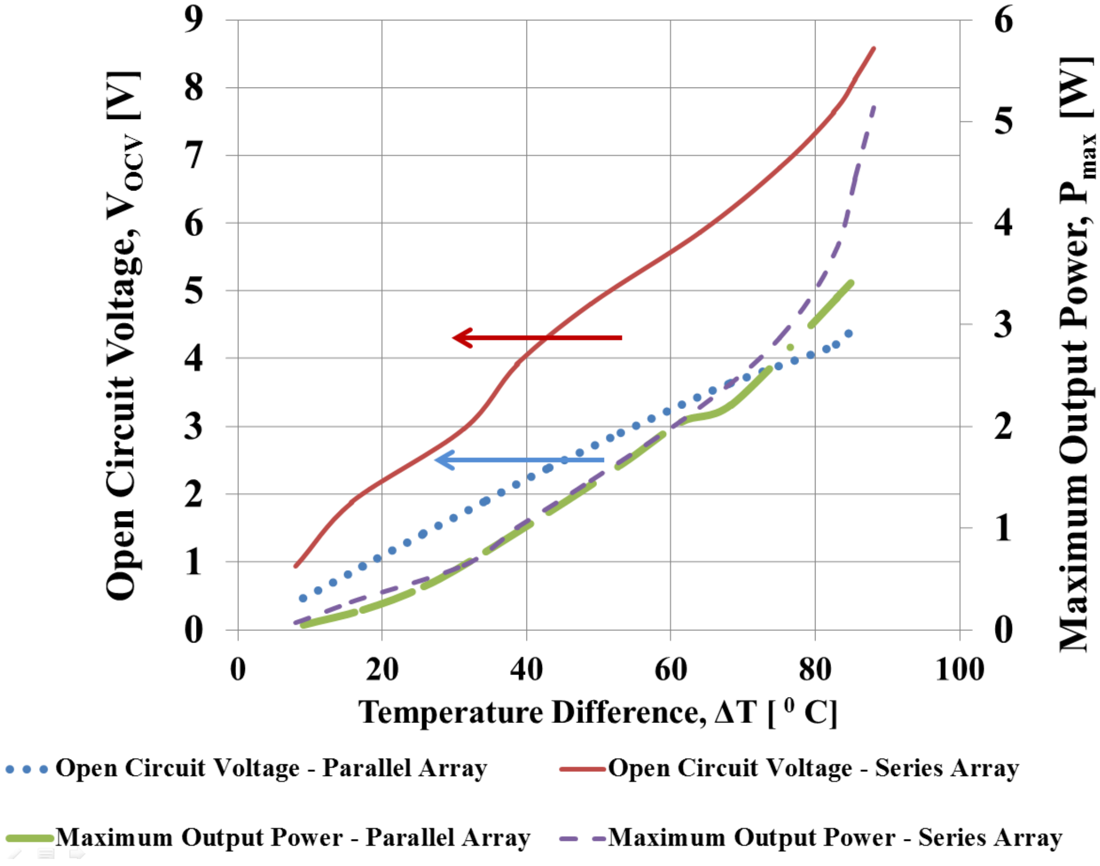

Figure 4.30 Open circuit voltage and maximum power output versus the temperature difference across TEG arrays connected in series and parallel

In practice, several arrays of series and parallel connections are used to achieve the desired application for the TEG systems. For a low cost and effective design of the TEG systems, a balance must be found between the number of arrays of TEG modules connected in series and parallel. The series array connections results in higher output power for the same input heating conditions than the parallel array. However, for reliability of the TEG system, the parallel array connections provide a better alternative than the series array connections. A good TEG system will incorporate a combination of series and parallel array connections to maximise the power output depending on the voltage and current requirements of the final design system. At the same time, care should be taken to minimise the power lost due to the Joule heating and temperature mismatch conditions.

4.6 Experimental Error and Uncertainty

All equipment including electronic load, thermocouples, voltmeter and ammeter used for experiment were calibrated to ascertain their accuracies. The relative uncertainty of the equipment used is defined as

Relative uncertainty = 0.5 x resolution/ (operating or measuring value) (4.27)

Equipment Uncertainty is given in table below

Table 4.1 Equipment uncertainty

Equipment	Operating/Measuring range	Resolution	Relative uncertainty
Cartridge Heater (for current)	0.01 – 250 ^{0}C	0.01 A	0.5 %
Cartridge Heater (for voltage)	0.01 – 240 V	0.01 V	0.5 %
Electronic Load (for voltage)	0.1 – 4.0 A	1 mA	0.5 %
Electronic Load (for current)	0.1 – 12 V	1 mV	0.5 %

The uncertainty of the maximum power is obtained from the following formula (Coleman and Steele, 1989):

$$\frac{\delta P_{max}}{P_{max}} = \left[\left(\frac{\delta V}{V}\right)^2 + \left(\frac{\delta I}{I}\right)^2\right]^{0.5} \tag{4.28}$$

T-type thermocouples were used for measuring the temperature with an intrinsic uncertainty of ±0.5% (Industrial Thermocouple 2012).

The total uncertainty was obtained by combining the sensor accuracy and measuring instruments accuracy using the root sum of square method as follows;

$$\delta_{total} = \sqrt{(\delta_{Sensor})^2 + (\delta_{Instruments})^2} \tag{4.29}$$

Where, δ is the uncertainty of the measured value.

A sample of uncertainty analysis for single TEG testing can be found in Appendix H.

4.7 Chapter Conclusion

From the experiments conducted, it was shown that the TEG can operate with the available low grade heat from solar pond. TEG was able to operate at temperature differences between the hot and cold side ranging from 10˚C to 50˚C. This range of temperature differences is readily available in a solar pond. Even at low temperature differences, TEG was able to generate power.

The experiments also proved that the TEG can be operated without any mechanical fixtures. Thermal adhesive can be used to attach the TEG to heat exchanger for power generation. The use of thermal adhesive is highly advantageous compared to mechanical fixtures for operation in highly corrosive environment of solar pond. This will help to reduce the complexity of the heat exchanger design.

As the TEG modules are highly scalable, the desired output power from the modules can be obtained by arranging them either in series or parallel arrays. Both arrays offer its own advantages and disadvantages. For successful operation of the TEG modules, a combination of series and parallel arrays will ensure power generation depending on the output requirement on voltage and current.

5.0 Thermoelectric Generator Heat Exchanger Designs and Analysis

5.1 Introduction

This chapter focuses on the heat transfer and fluid flow analysis for the heat exchangers used for the power generation with TEGs. Mathematical models using Microsoft Excel sheet workbook were developed to design and verify the heat exchangers used in this project. Three heat exchangers were designed for power generation using TEG. The first heat exchanger was flat plate heat exchanger with sixteen TEGs. Two in-pond heat exchangers, one with square channel and another with nonagon shape were designed for passive cooling water operation in the solar pond. The heat for in-pond heat exchanger was supplied based on natural convection heating from LCZ zone of solar pond. Third heat exchanger with forced convection cooling and heating was designed to maximise the power generation from TEG modules using low grade heat from solar pond.

5.2 Heat Exchanger

5.2.1 Classifications

Heat exchanger is a device used to exchange heat between two fluids at different temperatures and separated by a solid wall between the fluids. Heat exchanger is used for many engineering applications in space heating, air-conditioning, power production, chemical processing, waste heat recovery and many more.

Heat exchanger can be classified according to the flow arrangement and type of construction. The types of heat exchanger are listed as follow:

- Concentric tube/ double pipe heat exchanger
- Shell and tube heat exchanger
- Plate heat exchanger
- Shell and tube heat exchanger
- Plate fin heat exchanger
- Pillow plate heat exchanger
- Spiral heat exchanger
- Direct contact heat exchanger

- Phase-change heat exchanger
- Adiabatic wheel heat exchanger
- Regenerative heat exchanger

The classification of the heat exchangers can be categorised according to the flow arrangement. Generally, three type of flow dominates the flow arrangement in heat exchanger designs as follow:

- Counter flow
- Parallel flow
- Cross flow

Figure 5.1 shows the classification of heat exchanger depending on the flow arrangements, heat transfer mechanisms, and transfer process, number of fluids, surface compactness and construction.

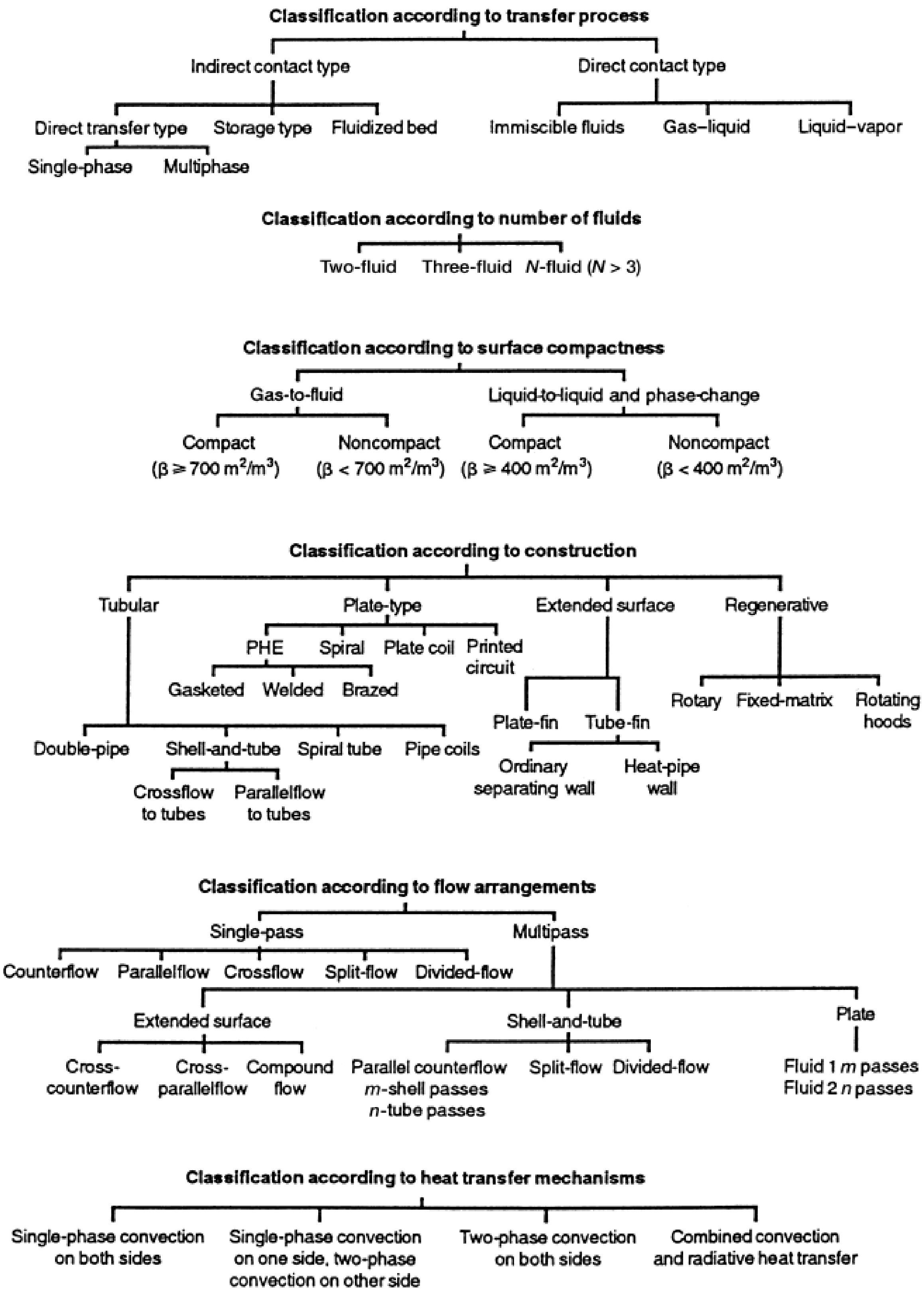

Figure 5.1 Heat exchanger classifications (Shah, 1981)

For this project, the simplest heat exchanger design based on concentric tube/ double pipe heat exchanger and plate heat exchanger was chosen for its ease of design, low cost and ease of fabrication criteria. The hot and cold fluid in this type of heat exchanger can move in the same direction or opposite direction. As shown in Figure 5.2 and 5.3 below, in a parallel flow heat exchanger design, the hot and cold fluid enters the heat exchanger from the same end and flow in the same direction. Both hot and cold fluids exit the heat exchanger in the same direction. In counter flow arrangement, both cold and hot fluid enters the heat exchanger in the opposite direction, flows in opposite direction in the heat exchanger and exits in opposite direction again. The counter flow heat exchanger design provides higher heat transfer due to higher average temperature difference along its unit length when compared to parallel flow heat exchanger.

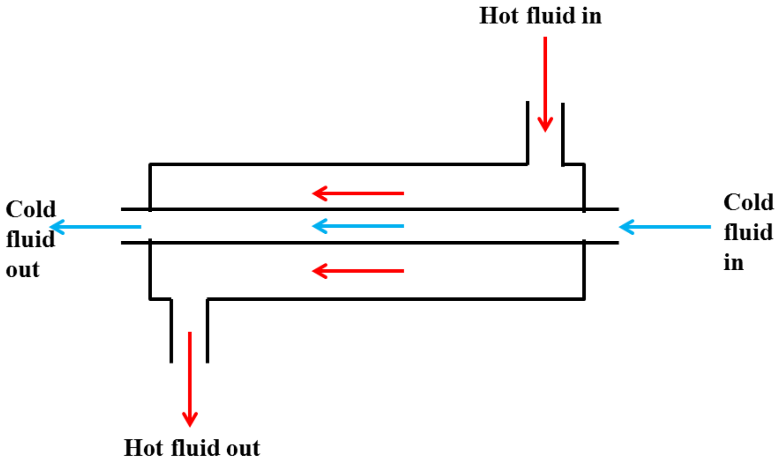

Figure 5.2 Parallel flow arrangements

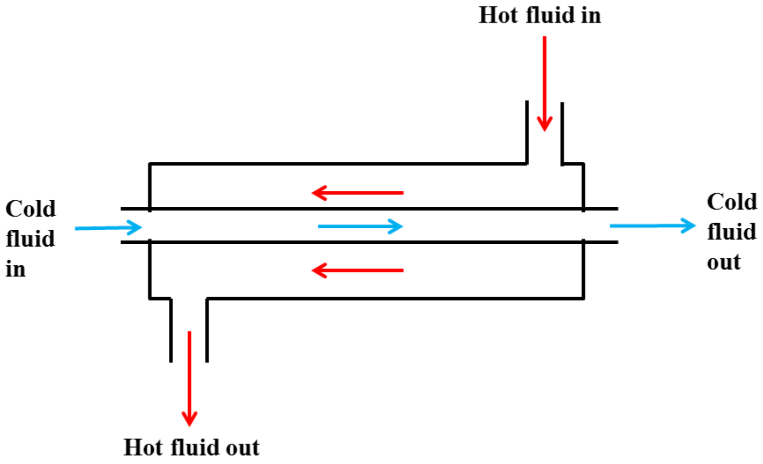

Figure 5.3 Counter flow arrangements

5.2.2 Overall Heat Transfer Coefficient

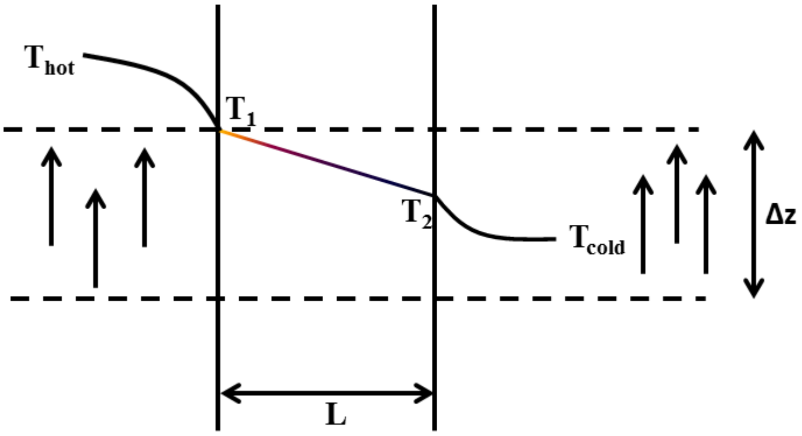

Figure 5.4 Planar wall heat exchanger

Figure 5.4 shows the planar wall of heat exchanger with one side exposed to hot fluid and another to cold fluid. Applying Newton's law of cooling, heat transfer rate from the hot fluid to the heat exchanger wall for a surface area along the length Δz is given by (Incropera et al., 2006):

$$\dot{Q} = h_{conv1} A_s (T_H - T_1) \tag{5.1}$$

Equation (5.1) can be arranged as follow:

$$(T_H - T_1) = \dot{Q} / h_{conv1} A_s \tag{5.2}$$

The conduction equation for the temperature drop across the wall is given by:

$$\frac{d}{dx}\left(k\frac{dT}{dx}\right) = 0 \tag{5.3}$$

The following boundary condition is subjected to equation (5.3)

$$-k\frac{dT}{dx}\bigg|_o = \frac{\dot{Q}}{A_s} \tag{5.4}$$

Integrating equation (5.3)

$$\int_0^{x'} \frac{d}{dx}\left(k\frac{dT}{dx}\right) dx = 0 \tag{5.5}$$

$$k\frac{dT}{dx'} - \mathrm{k}\frac{\mathrm{dT}}{\mathrm{dx}}\Big|_{\mathrm{o}} = 0 \tag{5.6}$$

Substituting equation (5.4) into equation (5.6):

$$k\frac{dT}{dx'} + \frac{\dot{Q}}{A_s} = 0 \tag{5.7}$$

Perform integration to equation (5.7) along the wall thickness, L to obtain the temperature drop across the wall:

$$\int_0^L \frac{dT}{dx'}dx' + \int_0^L \frac{\dot{Q}}{kA_s}dx' = 0 \tag{5.8}$$

From equation (5.7), we obtain:

$$\mathrm{T_1 - T_2} = \frac{\dot{Q}\mathrm{L}}{\mathrm{kA_s}} \tag{5.9}$$

Temperature drop from the wall to the cold fluid is given by the following equation:

$$T_2 - T_C = \frac{\dot{Q}}{h_{conv2}A_s} \tag{5.10}$$

Adding equation (5.7), (5.9) and (5.10), temperature drop from the hot side of the fluid to the cold side through the wall is given by:

$$T_H - T_C = \frac{\dot{Q}}{A_s}\left[\frac{1}{h_{conv1}} + \frac{L}{k} + \frac{1}{h_{conv2}}\right] \tag{5.11}$$

or

$$\dot{Q} = UA_s(T_H - T_C) \tag{5.12}$$

where,

$$U \equiv \left[\frac{1}{h_{conv1}} + \frac{L}{k} + \frac{1}{h_{conv2}}\right]^{-1} \tag{5.13}$$

U (W/m^{2}K) is the Overall Heat Transfer Coefficient.

For a circular tube heat exchanger with inner radius r_1 and outer radius r_2, equation (5.13) can be rewritten as follow:

$$UA \equiv \left[\frac{1}{2\pi r_1 \Delta z h_{conv1}} + \frac{1}{2\pi k \Delta z}ln\left(\frac{r_1}{r_2}\right) + \frac{1}{2\pi r_2 \Delta z h_{conv2}}\right]^{-1} \tag{5.14}$$

The product UA is used to express heat exchanger operation. The heat transfer area of the internal and external of the heat exchanger tube/ cylindrical geometry is different. The following equation can be used to calculate the overall heat transfer coefficient for unfinned, tubular heat exchanger:

$$\frac{1}{UA} = \frac{1}{U_i A_i} = \frac{1}{U_o A_o} \tag{5.15}$$

where subscripts *i* and *o* refer to inner and outer tube surfaces, which may be exposed to either cold or hot fluid. The calculation of UA product depends on whether it is based on hot or cold side surface area, since $U_i \neq U_o$ if $A_i \neq A_o$.

For long term operation of heat exchanger in corrosive environment, unwanted deposits are deposited on the walls of heat exchanger. This can be caused by fluid impurities, rust formation or other reactions between the wall material and fluid. This deposit of film and rust over the surface of heat exchanger can significantly increase the resistance to heat transfer between the fluids. Equation (5.21) can be modified to include the fouling effect by introducing additional thermal resistance, as shown in equation (5.22). Fouling factor, R_f depends on the operating temperature, fluid velocity and length if service of heat exchanger.

$$UA \equiv \left[\frac{1}{2\pi r_1 \Delta z h_{conv1}} + \frac{R_{f1}}{2\pi r_1 \Delta z} + \frac{1}{2\pi k \Delta z} ln\left(\frac{r_1}{r_2}\right) + \frac{R_{f2}}{2\pi r_2 \Delta z} + \frac{1}{2\pi r_2 \Delta z h_{conv2}}\right]^{-1} \tag{5.16}$$

5.2.3 Heat Exchanger Analysis: Log Mean Temperature Difference (LMTD)

It is important to relate the heat transfer rate of a heat exchanger to inlet and outlet fluid temperatures, overall heat transfer coefficient, and the total surface area for heat transfer. The above quantities can be obtained by applying overall energy balances to the heat transfer of hot and cold fluid separated by a wall. This is based on the assumption that the potential and kinetic energy changes are negligible and there is no heat transfer between the heat exchanger and surroundings. Figure 5.5 shows the overall energy balances for the hot and cold fluids in a heat exchanger.

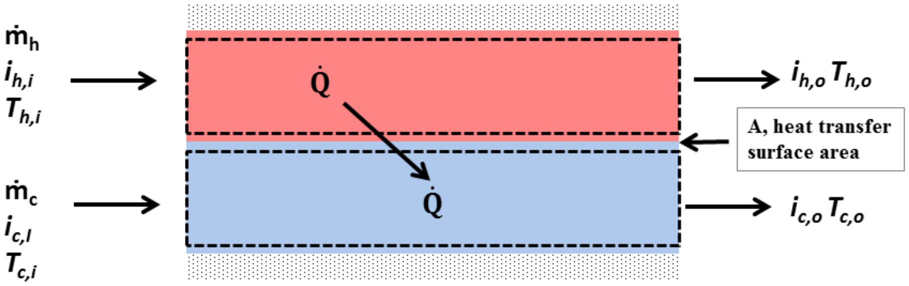

Figure 5.5 Overall energy balances for the hot and cold fluids in a heat exchanger.

Based on the overall energy balance as shown in figure 5.6, the following equation is obtained:

$$\dot{Q} = \dot{m}_h\left(i_{h,i} - i_{h,o}\right) = \dot{m}_c\left(i_{c,o} - i_{c,i}\right) \tag{5.17}$$

where *i* is the fluid enthalpy. The subscript *i* and o refers to the inlet and outlet of the heat exchanger and *h* and *c* refers to the hot and cold fluid.

Equation (5.17) is reduced to equation (5.18) based on the assumption that the fluids are not undergoing any phase change and constant specific heats.

$$\dot{Q} = \dot{m}_h c_{p,h}\left(T_{h,i} - T_{h,o}\right) = \dot{m}_c c_{p,c}\left(T_{c,o} - T_{c,i}\right) \tag{5.18}$$

Equation (5.18) is independent of the flow arrangement and heat exchanger type. The temperatures in the equation are mean fluid temperatures at the designated locations. In a heat exchanger, temperature difference varies with the position in the heat exchanger, it is imperative to use the following equation:

$$\dot{Q} = UA\Delta T_m \tag{5.19}$$

where ΔT_m is the approximate mean temperature differences. The next section establishes the specific form of $\Delta T_{m.}$ Figure 5.6 and 5.7 shows the temperature profile for a double pipe heat exchanger with parallel and counter flow arrangements.

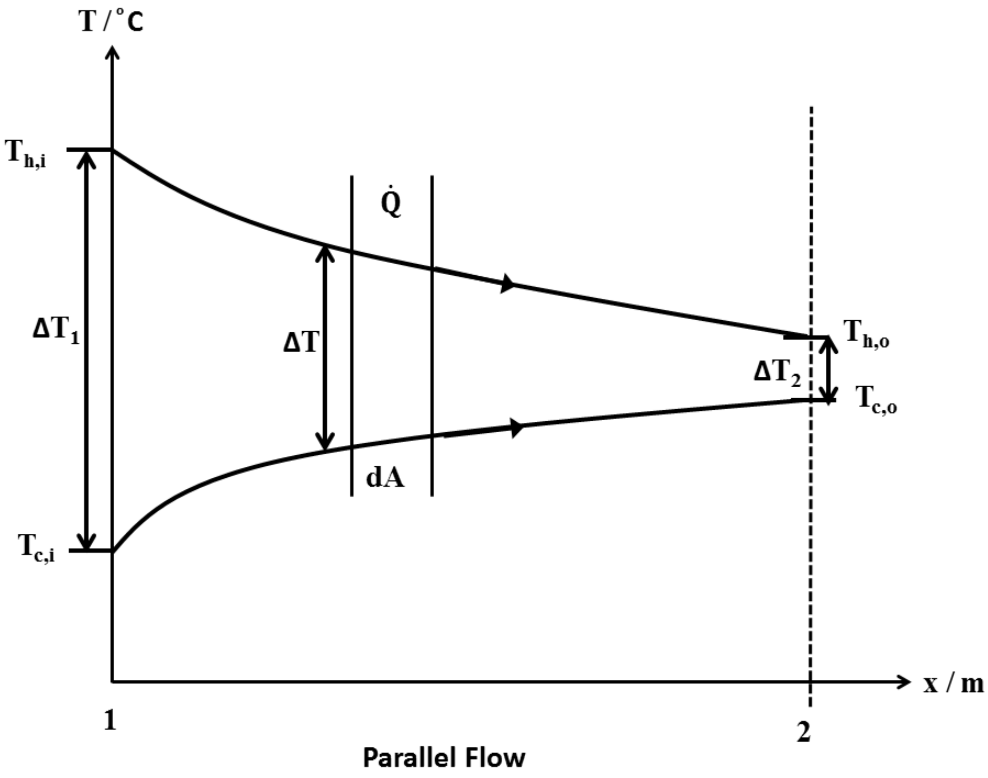

Figure 5.6 Temperature profile for parallel flow double pipe heat exchanger

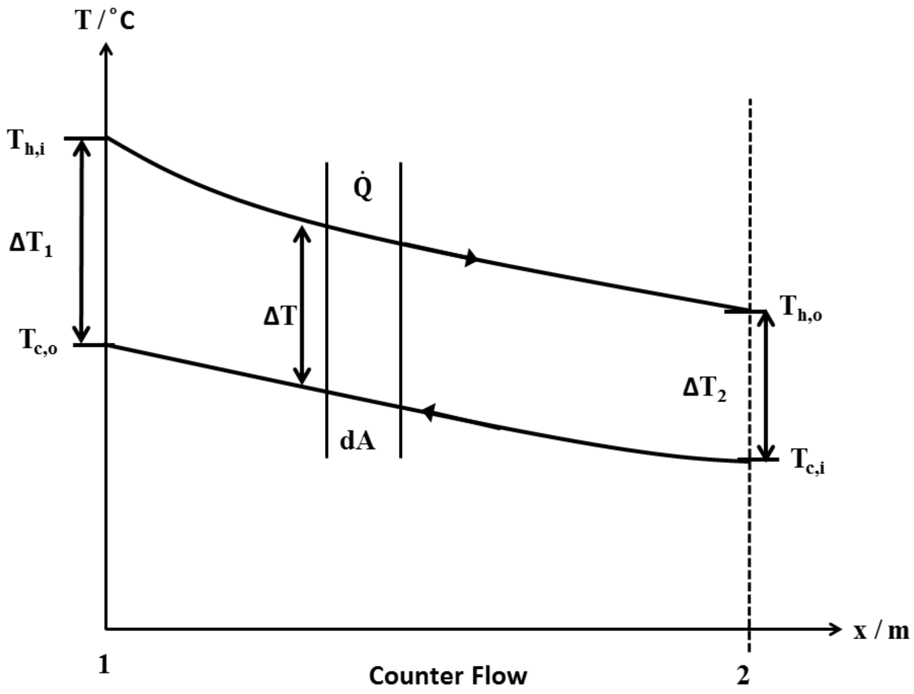

Figure 5.7 Temperature profile for counter flow double pipe heat exchanger

Considering parallel flow arrangement for a double pipe heat exchanger, steady state heat transferred through a differential area, dA is given by:

$$d\dot{Q} = -\left(\dot{m}C_p\right)_h dT_h = \left(\dot{m}C_p\right)_c dT_c \tag{5.20}$$

The heat transfer across this differential area in terms of overall heat transfer coefficient is given by:

$$d\dot{Q} = UdA(T_h - T_c) \tag{5.21}$$

From equation (5.20), we get

$$dT_h = -\frac{d\dot{Q}}{\left(\dot{m}C_p\right)_h} \tag{5.22}$$

and

$$dT_c = \frac{d\dot{Q}}{\left(\dot{m}C_p\right)_c} \tag{5.23}$$

Temperature difference is then is given by following equation based on equation (5.22) and (5.23).

$$dT_h - dT_c = d(T_h - T_c) = -d\dot{Q}\left\{\frac{1}{\left(\dot{m}C_p\right)_h} + \frac{1}{\left(\dot{m}C_p\right)_c}\right\} \tag{5.24}$$

Substituting $d\dot{Q}$ from equation (5.21) results in:

$$\frac{d(T_h - T_c)}{(T_h - T_c)} = -UdA\left\{\frac{1}{\left(\dot{m}C_p\right)_h} + \frac{1}{\left(\dot{m}C_p\right)_c}\right\} \tag{5.25}$$

Integrating the above equation from point 1 to 2 along the length of heat exchanger:

$$\int_1^2 \frac{d(T_h - T_c)}{(T_h - T_c)} = -\int_1^2 UdA\left\{\frac{1}{\left(\dot{m}C_p\right)_h} + \frac{1}{\left(\dot{m}C_p\right)_c}\right\} \tag{5.26}$$

The above equation is then simplified to:

$$ln\frac{(T_h - T_c)_2}{(T_h - T_c)_1} = -UA\left\{\frac{1}{\left(\dot{m}C_p\right)_h} + \frac{1}{\left(\dot{m}C_p\right)_c}\right\} \tag{5.27}$$

Substituting equation (5.24) into (5.27) results in:

$$ln\frac{(T_h-T_c)_2}{(T_h-T_c)_1} = -\frac{UA}{\dot{Q}}[(T_{h1}-T_{h2})+(T_{c2}-T_{c1})] \tag{5.28}$$

Rearranging equation (5.28) gives:

$$\dot{Q} = UA\frac{(T_{h2}-T_{c2})-(T_{h1}-T_{c1})}{ln[(T_{h2}-T_{c2})/(T_{h1}-T_{c1})]} = UA\Delta T_{LMTD} \tag{5.29}$$

Where ΔT_{LMTD} is given by following equation:

$$\Delta T_{LMTD} = \frac{(T_{h2}-T_{c2})-(T_{h1}-T_{c1})}{ln[(T_{h2}-T_{c2})/(T_{h1}-T_{c1})]} \tag{5.30}$$

This can be rewritten as follow to be used for counter flow heat exchanger as well.

$$\Delta T_{LMTD} = \frac{\Delta T_2-\Delta T_1}{ln[\Delta T_2/\Delta T_1]} = \frac{\Delta T_1-\Delta T_2}{ln[\Delta T_1/\Delta T_2]} \tag{5.31}$$

where $\Delta T_1 = T_{h1} - T_{c1}$, $\Delta T_2 = T_{h2} - T_{c2}$.

The LMTD represents the effective, average temperature difference between the two heat transfer fluids over the length of the heat exchanger and though derived here for parallel flow, strictly valid for single phase fluids in double pipe heat exchangers. For counter flow heat exchanger, the change in the temperature differences in the direction of x is not as large as the inlet region of the parallel flow heat exchanger. The outlet temperature of the cold fluid may exceed the outlet temperature of the hot fluid. For same inlet and outlet temperatures, the log mean temperature difference for counter flow exceeds that for parallel flow. This makes counter flow heat exchanger can operate with smaller surface area for specified heat transfer rate similar to parallel flow heat exchanger, assuming the same value of U.

For a given inlet temperature T_{h1} and T_{c1}, for heat exchanger, the outlet temperature T_{h2} and T_{c2} can be obtained using the following equation:

$$T_{h2} = \frac{T_{h1}(R-1)-RT_{c1}\left[1-exp\left[\frac{U_OA_O(R-1)}{\dot{m}_cC_{pc}}\right]\right]}{Rexp\left[\frac{U_OA_O(R-1)}{\dot{m}_cC_{pc}}\right]-1} \tag{5.32}$$

where R’ is the capacity ratio given as follow:

$$R' = \frac{\dot{m}_cC_{pc}}{\dot{m}_hC_{ph}} \tag{5.33}$$

The outlet temperature for cold side can be obtained from the following equation, once T_{h2} is known:

$$T_{c2} = T_{c1} + \frac{T_{h1} - T_{h2}}{R} \tag{5.34}$$

5.3 Pressure Drop and Friction Coefficient in a Pipe Flow

The value of average velocity at stream wise cross-section is determined by the conservation of mass principle. The mass flow rate across a pipe flow is given as follow:

$$\dot{m} = \rho V_{avg} A_c \tag{5.35}$$

The volume flow rate for a flow in a horizontal pipe is given as:

$$\dot{V} = V_{avg} A_c \tag{5.36}$$

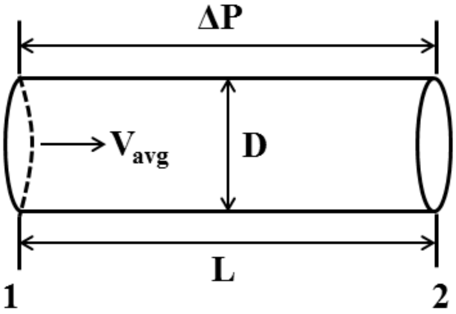

Figure 5.8 Pressure drop in a pipe

Figure 5.8 shows the pressure drop in a pipe from point 1 to 2. Pressure drop, ΔP is a quantity of importance in a pipe flow analysis. This is because pressure drop, ΔP is related to power requirement of pump to maintain the flow. For dP/dx = constant and integrating from $x = x_1$ with pressure is P_1 to x = x+L where the pressure is P_2 gives:

$$\frac{dP}{dx} = \frac{P_2 - P_1}{L} \tag{5.37}$$

V_{avg} is given by the following formula for fully developed laminar flow. R is the radius of the pipe. The pressure gradient is negative as pressure must decrease in the flow direction because of viscous effect.

$$V_{avg} = -\frac{R^2}{8\mu}\left(\frac{dP}{dx}\right) \tag{5.38}$$

Substituting equation (5.37) into equation (5.38),

$$\Delta P = P_1 - P_2 = \frac{8\mu L V_{avg}}{R^2} = \frac{32\mu L V_{avg}}{D} \tag{5.39}$$

The above is the pressure drop equation for laminar flow in a pipe. For practical applications in pipe flow analysis involving both laminar and turbulent flows, circular or non-circular pipes, the following equation can be used to calculate the pressure loss:

$$\Delta P_L = f\frac{L}{D}\frac{\rho V^2}{2} \tag{5.40}$$

For pipe flow analysis, the pressure loss can be expressed in terms of equivalent fluid column height, called the head loss, h_L. Head loss, h_L represents the additional height the fluid needs to be raised by a pump to overcome the frictional losses in the pipe caused by the viscosity of the pipe. It is also directly related to wall shear stress. The equation for head loss, h_L is given as follow:

$$h_L = \frac{\Delta P}{\rho g} = f\frac{L}{D}\frac{V^2}{2g}$$

Reynolds Number, Re is a non-dimensional number used to predict flow pattern at different fluid flow conditions. For a flow in a conduit, Re is defined as:

Reynolds Number, Re = inertia force/viscous force

$$= \rho VD/\mu \tag{5.41}$$

where ρ is the density of fluid in kg/m^3

V is the free stream average velocity in m/s

D is the diameter of the duct in m, or hydraulic diameter, D_h for non-circular duct in m.

μ is the dynamic viscosity of the fluid in N.s/m^2

Friction factor, f is used to calculate the pressure drop in a pipe conduit. It is defined as dimensionless pressure drop for internal flow. The equation for friction factor is given below:

$$f = \frac{\Delta P}{\left(\frac{L}{D}\right)\left(\frac{\rho V^2}{2}\right)} \tag{5.42}$$

where ΔP = pressure difference between two points in the fluid flow in Pa

L is the length of the pipe in m
D is the diameter of the pipe in m
ρ is the density of the fluid in kg/m^3
V is the average velocity of the flow in m/s

For a laminar flow, the friction factor, f is given by:

$$f = 64/Re \tag{5.43}$$

For turbulent flow, the friction factor is given by:

$$f = (0.790 \ln Re-1.64)^{-2} \tag{5.44}$$

or

$$\frac{1}{\sqrt{f}} = -2.0 log\left(\frac{\varepsilon/D}{3.7} + \frac{2.51}{Re\sqrt{f}}\right) \tag{5.45}$$

The above equation is known as Colebrook equation and used to calculate friction factor, f for turbulent flow in pipes in smooth as well as rough pipes. The value for friction factor, f in equation (5.53) can be found from Moody chart as given in appendix 3.

Once the head loss, h_L from the fluid flow id found, the required pumping power for the flow can be calculated as follow:

$$\dot{W}_{pump,L} = \dot{V}\Delta P_L = \dot{m}gh_L \tag{5.46}$$

As the fluid in a heat exchanger passes through various fittings, inlets, exits, contractions, expansions causes additional losses to the flow. These additional losses are minor when compared to the total head loss of the pipe. Minor losses, $h_{L,minor}$ is given by the following equation:

$$h_{L,minor} = K_L V^2/2g \tag{5.47}$$

where K_L is the loss coefficient.

For sudden expansion, the loss coefficient, K_L can be found by using the formula given below:

$$K_L = (1- A_{small}/A_{large})^2 = (1-d^2/D^2)^2 \tag{5.48}$$

where d is the diameter of the smaller section of the pipe in m and D is the diameter of the larger section of the pipe.

The total head loss in a pipe system is given by the total head loss and the total minor losses as shown in the equation below:

$$h_{L,Total} = \sum_i f_i \frac{L_i}{D_i} \frac{V_i^2}{2g} + \sum_j K_{L,j} \frac{V_j^2}{2g} \tag{5.49}$$

The net power output from the TEG heat exchanger can then be calculated based on the equation below:

$$P_{net} = P_{TEG} - P_{Total} \tag{5.50}$$

where, P_{TEG} is the gross power (electrical) delivered by the TEG on the heat exchanger. P_{Total} is the total pumping power required in the heat exchanger, both in the hot and cold section, assuming a pump with an efficiency of 50 %. Total pumping power, P_{Total} is given as follow:

$$P_{Total} = \frac{\dot{W}_{pump,L\,Total}}{\eta_{pump}} \tag{5.51}$$

5.4 Thermal Resistance Network for TEG Heat Exchanger

In order to calculate the heat transfer from the hot fluid to the cold fluid through the TEG, it is important to establish the thermal resistance network for the heat transfer model. Consider Figure 5.9 below showing a single TEG attached to the outer cold fluid pipe. The hot fluid pipe is arranged concentric arrangement.

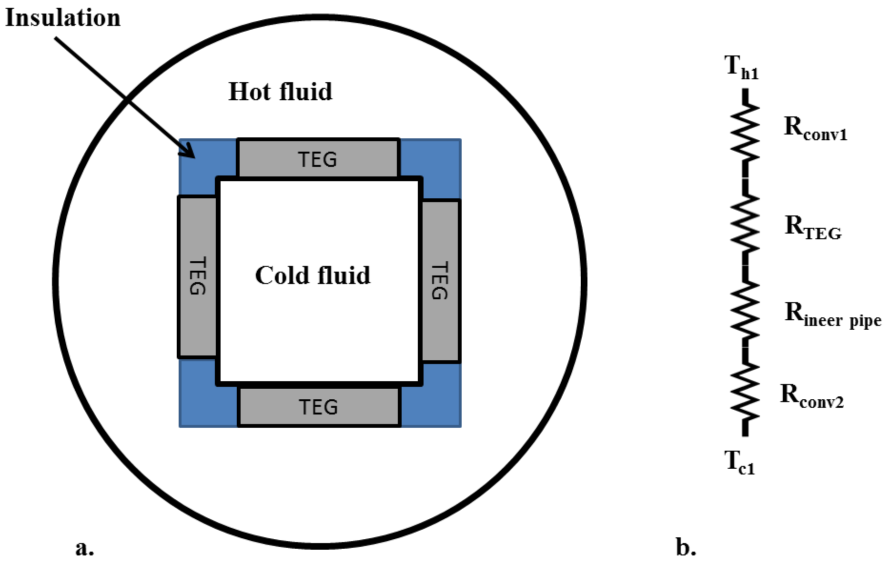

Figure 5.9 a) Cross sectional view of a typical polygon heat exchanger, b) thermal resistance network for heat transfer.

Based on the thermal resistance network shown in figure 5.10, the heat transfer across the TEG can be written as follow (Incropera et al, 2006):

$$Q = \frac{T_{h1} - T_{c2}}{R_{Total}} \quad (5.52)$$

The total resistance is given as :

$$R_{Total} = R_{conv1} + R_{TEG} + R_{Inner\ Pipe} + R_{conv2} \quad (5.53)$$

where R_{conv1} is calculated as follow:

$$R_{conv1} = 1/(h_1 A_{TEG}) \quad (5.54)$$

Nusselt number, Nu provides a measure of the convection heat transfer occurring at the surface. It is also equal to the dimensionless temperature gradient at the surface. It also defines the thermal boundary layer.

Nusselt number is defined as follow:

$$\mathrm{Nu} = \frac{convective\ heat\ transfer}{conductive\ heat\ transfer} = \frac{hL}{k} \quad (5.55)$$

where, h is the heat transfer coefficient of the fluid in W/m^2K

L is the characteristic length in m. For pipe flow, diameter is taken as the characteristic length

k is the thermal conductivity of the fluid in W/mK

Heat transfer coefficient for hot fluid, h_1 is given by following Nusselt number equation:

$$Nu = h_1 D_h / k \qquad (5.56)$$

A Nusselt number close to one indicates that the convection and conduction is of similar magnitude. A large Nusselt number signifies more active convection.

For a pipe flow analysis, the following Nusselt number ralations can be used.

$$Nu = 4.36 \text{ (laminar, fully developed, uniform } q_s\text{)} \qquad (5.57)$$

$$Nu = 3.66 \text{ (laminar, fully developed, uniform } T_s\text{)} \qquad (5.58)$$

$$Nu = \frac{(f/8)(Re-1000)Pr}{1+12.7(f/8)^{0.5}\left(Pr^{2/3}-1\right)} \text{ (turbulent, fully developed flow)} \qquad (5.59)$$

where f is the Darcy friction factor

For vertical cylinder with natural convection, Nusselt number is given as:

$$Nu = \frac{4}{3}\left[\frac{7\,Ra\,Pr}{5(20+21\mathrm{Pr})}\right]^{1/4} + \frac{4(272+315\mathrm{Pr})H}{35(64+63\mathrm{Pr})D} \qquad (5.60)$$

Grashoff number, Gr is generally used for natural convection analysis. Gr helps to approximate the viscous and buoyancy force acting on a fluid. For pipe flow analysis, it is defined as:

$$Gr = \frac{g\beta(T_S - T_\infty)D^3}{\upsilon^3} \qquad (5.61)$$

where g is the gravitational acceleration in m^2/s

β is the volumetric thermal coefficient, taken at 1/T, where T is the absolute temperature in K

T_s is the surface temperature in ˚C

T_∞ is the bulk temeparture of the fluid in ˚C

D is the diameter of the pipe in m (characteristics length)

ν is the kinematic viscosity in m^2/s

Raleigh number, Ra is defined as the product of Grashoff number, Gr and Prandtl number, Pr. Raleigh number is buoyancy driven flow that occurs in natural convection. Under certain critical Ra value, the heat transfer is assumed to be in the form of conduction an otherwise it is assumed to be in the form of convection.

Raleigh number, $Ra = GrPr$ (5.62)

R_{TEG} is taken as the value obtained in chapter 2, with thermal adhesive.

R_{pipe} can be calculated based on the thickness of pipe, L_{pipe} as follow:

$R_{pipe} = L_{pipe}/kA_{TEG}$ (5.63)

R_{conv2} can be obtained by calculating heat transfer coefficient for cold fluid, h_2 similar to the method used for calculating heat transfer coefficient for hot fluid, h_1.

Once R_{Total} is obtained for the heat transfer through a single TEG, then the effective resistance for the entire heat exchanger with n-number of TEGs can be found using the following equation:

$R_{effective} = R_{Total} / n$ (5.64)

Equation (44) can be used to find the overall heat transfer coefficient of the heat exchanger as follow:

$1/ (U_oA_0) = R_{Total} / n$ (5.65)

where A_o is the heat transfer surface area in m^2.

For the total heat transfer across the heat transfer area in the heat exchanger, the heat transfer rate can be calculated as follow:

$$\dot{Q} = \frac{\Delta T_{LMTD}}{R_{effective}} \quad (5.66)$$

5.5 Heat Exchanger Designs

5.5.1 TEG Plate Heat Exchanger (16 TEGs)

An experimental rig was developed to generate electricity from solar pond with a simple plate heat exchanger. An aluminium plate was machined to fit eight TEG modules. The aluminium plate acts as a tablet where two of these plates sandwich eight TEG modules. The tablet design helps in maintaining the TEGs in place. The two aluminium plates are fastened with ten screws around its outer perimeter. The depth of the slot machined on the surface of the aluminium plates is 1.6 mm. This allows for both plates clamped together with enough clearance to fit the TEG modules of 3.2 mm thick between them. The thickness of the machined aluminium plate was measured at 2 mm. This thickness helps in heat transfer required for the power generation. Figure 5.10 shows the CAD model of the machined aluminium plate with dimensions. Figure 5.11 shows the CAD model of an exploded view of arrangements of TEG modules with two aluminium plates.

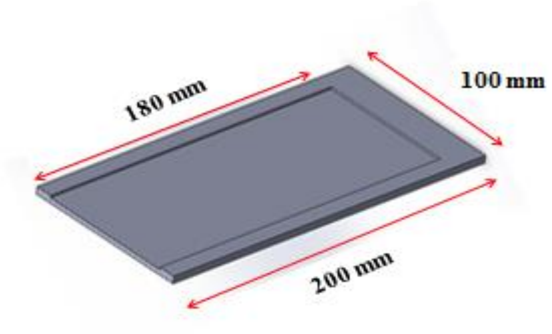

Figure 5.10 CAD model for aluminium plate machined for TEG module attachments

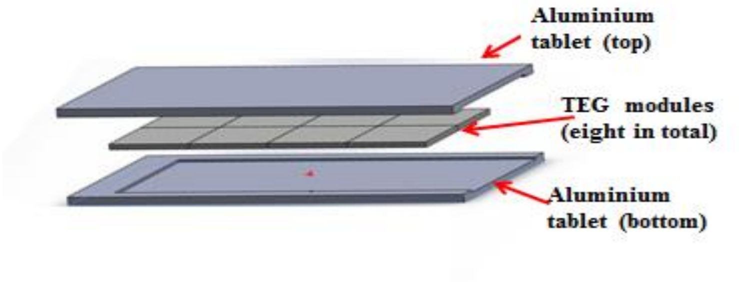

Figure 5.11 Exploded CAD view of aluminium plated with TEG modules

Figure 5.12 shows the actual aluminium tablet with eight TEG modules sandwiched between the aluminium plates. The TEGs are sandwiched with heat transfer paste applied to its surfaces. This helps in heat transfer as the contact resistance is minimised. The terminals of the TEGs are extended and labelled accordingly for experimental analysis.

Figure 5.12 Aluminium tablet with TEG modules

For this project, four aluminium plates that formed two tablets were arranged such that the hot water goes through the central channel and the cold water channelled to the outer two channels, as shown in Figure 5.13. Total of sixteen TEGs were used for the design, with eight TEGs in each tablet. Both the flow in the hot and cold channel was in counter flow arrangement. The heat transfer through the TEGs will be determined by the temperature difference between the hot and cold side of the fluid. Figure 5.13 shows the schematic of cross section view of the TEG experimental setup for power generation. The size of the cold and hot channel is 13 mm x 80 mm and 11 mm x 80 mm, respectively. The length (depth) of both the channels is 160 mm.

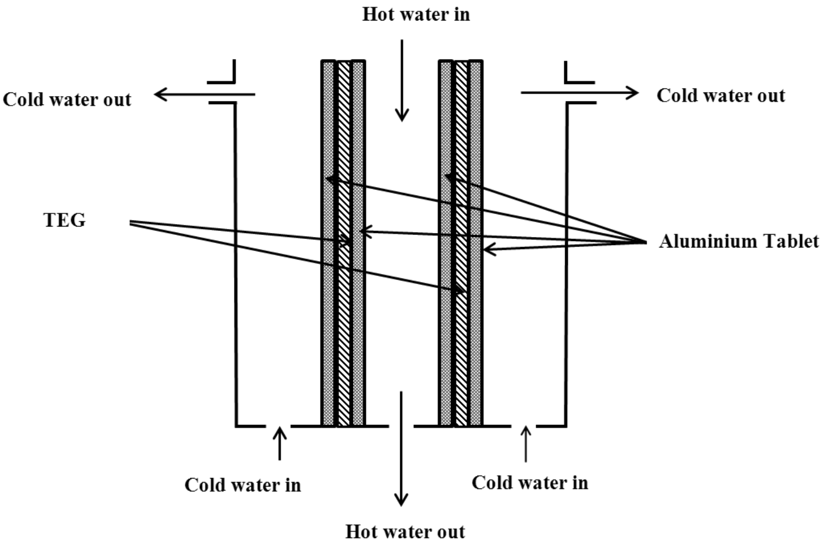

Figure 5.13 Schematic side view of the 16 TEGs setup components with hot and cold water flow arrangements.

Figure 5.14 shows the CAD model of the TEG plate heat exchanger. The flow in hot water channel was introduced from the top and exits from the bottom of the heat exchanger. The cold water enters the heat exchanger from the bottom and exits from the side plates as shown in the diagram. The side plates are made of 15 mm thick Acrylic plates for its insulating properties. Also, the transparent side plates also make it easier to observe the flow in the heat exchanger. Figure 5.15 shows the top view of the actual diagram of the heat exchanger.

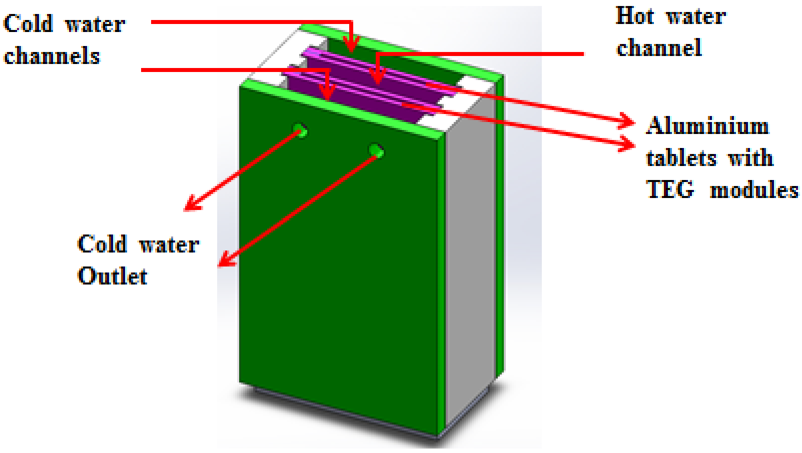

Figure 5.14 CAD model of TEG heat exchanger

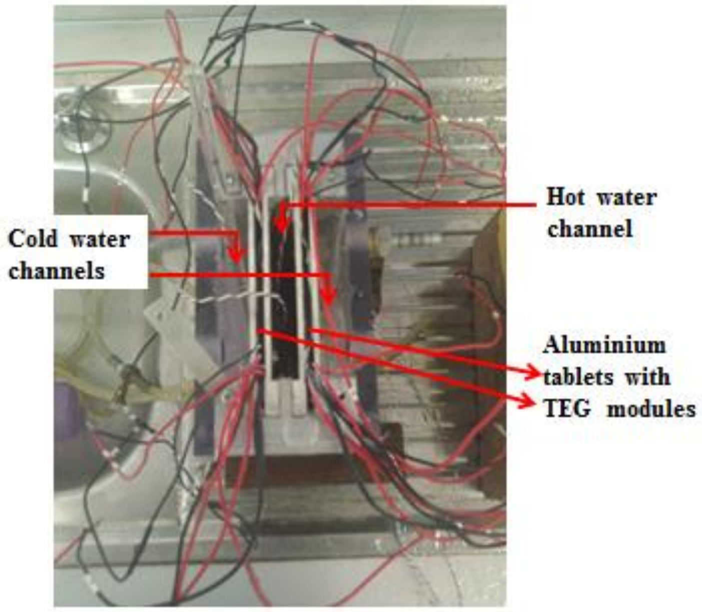

Figure 5.15 Top view of the TEG plate heat exchanger

5.5.2 In-pond Heat Exchanger Designs

5.5.2.1 Square Channel Design (60 TEGs)

In-pond heat exchanger is a simple design that generates electrical power from low grade heat of solar pond. The flow required by the cooling of the TEGs is provided by siphoning effect; this eliminates the need to use any external pumps with electricity. This simple design works seamlessly with the current design of the solar pond. Fresh water is added to the solar pond for surface washing to remove excess salt as a result of salt diffusion from high salinity to low salinity region of solar pond. This extra water from the surface of the solar pond is then channelled into evaporation ponds using gravitational flow. In-pond heat exchanger will utilise this method where the excess water from the surface of the solar pond will be bypassed from the overflow system of the solar pond and channelled directly to the evaporation pond using siphoning effect. This helps to create a passive power generation system, without any external pumping sources from solar pond using TEGs. The net power produced from this system can be utilised fully for any desired application, without compensating for the external pumping system requirements. The heat obtained to power the TEGs in this design was obtained solely from the LCZ section of the solar pond. No heat will be utilised from the NCZ section of the solar pond for this design application. Figure 5.16 shows the conceptual design for the in-pond heat exchanger as described above.

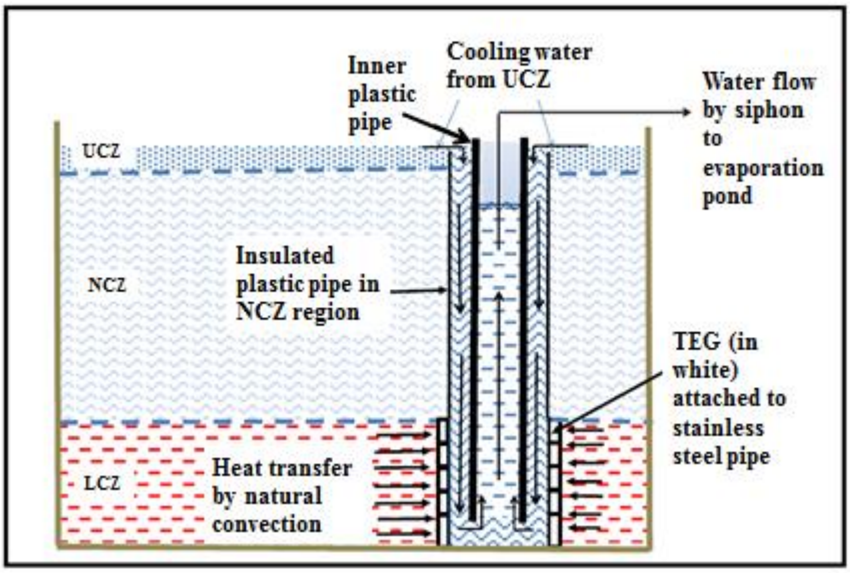

Figure 5.16 Schematic of the in-pond heat exchanger

A stainless steel square channel measuring 50 mm by 50 mm in cross section with a thickness of 2 mm was used to build a heat exchanger for in-pond power generation. The basic concept involves exposing the bottom section of the heat exchanger to the LCZ region of solar pond. The LCZ region in solar pond maintains a uniform highest temperature in a solar pond. Heat can be transferred to the square channel heat exchanger from LCZ to the TEGs attached to the bottom of this heat exchanger. The UCZ region is the lowest temperature region in a solar pond. The heat exchanger was designed such that the water from UCZ can be channelled through the gap in the heat exchanger to provide cooling to the in-pond heat exchanger. The in-pond heat exchanger is 2 m long. This enables the heat exchanger to stand upright in the solar pond and allow water from UCZ to fill the gap at the top opening. To maintain the flow of water in the heat exchanger, water is siphoned out of the in-pond heat exchanger to the evaporation pond.

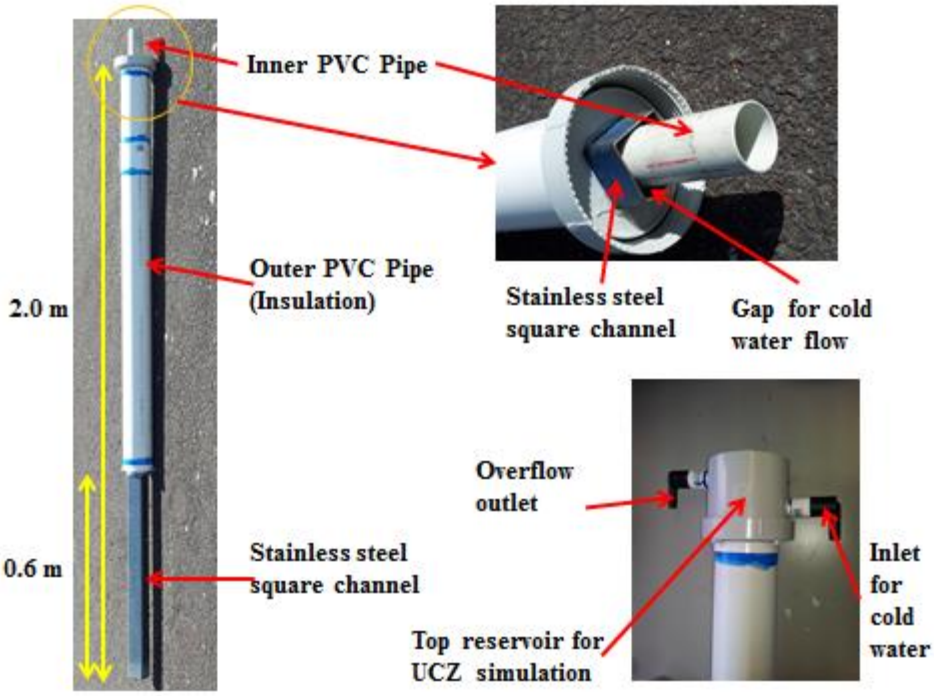

Figure 5.17 In-pond square channel heat exchanger

Figure 5.17 above shows the diagram of the in-pond square channel heat exchanger. The diagram on the left shows the whole in-pond heat exchanger with the bottom exposed for TEG attachments. This section is 0.60 m long to accommodate the LCZ region in the solar pond. The remainder of the heat exchanger is enclosed with a 90 mm outer diameter and 2 mm thick PVC pipe. This outer pipe insulates the heat exchanger from the heat in the NCZ region of solar pond. Another smaller PVC pipe with a length of 2.07 m and 2 mm thick was used to provide the gap between the inner PVC pipe and square channel, as shown in Figure 5.18 on the top right section. The diameter of the inner PVC pipe is 48 mm. The gap allows the cold water from UCZ section to cool the TEGs exposed to the LCZ region of solar pond on the outer surface. This centre PVC pipe is 2 cm above the bottom of the inside of the heat exchanger for the flow of water to reverse it direction upwards. Water is then siphoned out from the canter of the inner PVC pipe into the evaporation pond. To test the heat exchanger in the laboratory, a PVC connector with an outer diameter of 90 mm was used to simulate the UCZ condition of solar pond indoors, as shown in the above figure at the bottom left section. This connector can be easily removed when the heat exchanger is immersed in the solar pond. Figure 5.18 shows CAD model of the square channel designed for this study.

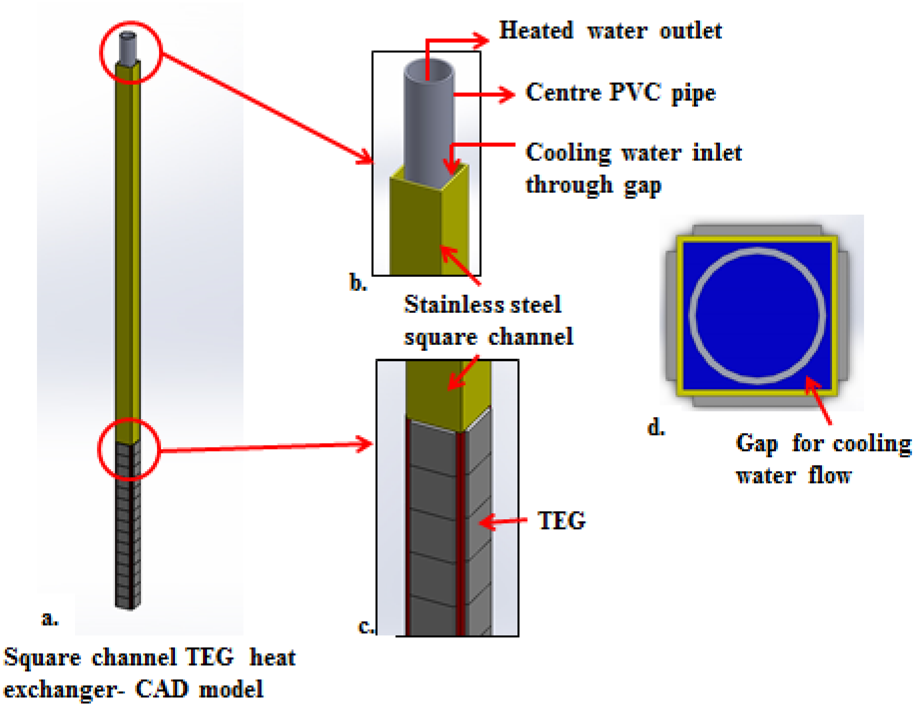

Figure 5.18 a.) CAD model of square channel heat exchanger, b.) Maginified view of the top section of square channel heat exchanger, c.) TEG modules arrangements on the surface of the heat exchanger, d.) Top view of the square channel heat exchanger.

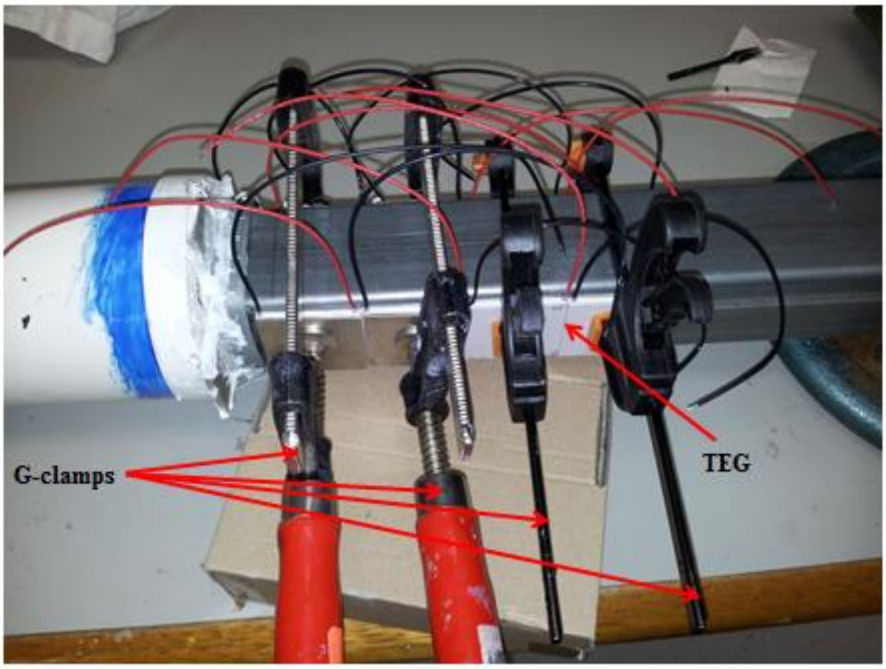

Figure 5.19 G-clamps used to attach TEGs on square channel

The TEGs were attached to the square channel using G-clamps and thermal adhesive, as shown in Figure 5.19. Each TEG is 40 mm by 40 mm in dimension and 15 TEGs are required for the 0.6 m section of the square channel. The TEGs were held with the G-clamps for 8 hours, until the thermal adhesive dries. A total of 15 TEGs were attached on each side of the square channel. This makes a total of 60 TEGs on the whole section of the 0.6 m of the square channel.

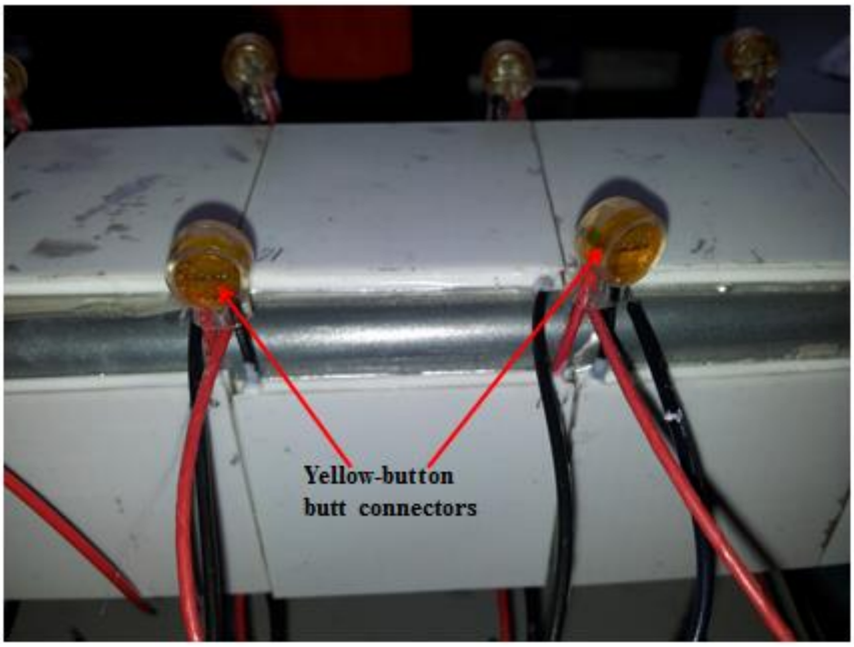

Figure 5.20 Connectors used to connect the terminal of TEGs

Figure 5.20 shows the yellow button butt connectors used to connect the terminals of the TEGs. These connectors were used to connect wires with diameters of 0.4 mm to 0.8 mm. This makes them suitable for connecting TEGs wire terminals as the diameter of these wires falls into the above range. Each connector weighs 22.2 g, with a length of 1.11 cm, width and height of 0.80 cm. Yellow button butt connectors were used for the above purpose because it helps to eliminate the need for soldering terminal connections, which is laborious and time consuming. Two conductors of the terminal are inserted into the two ports of the yellow button butt connectors, and then crimped using a plier. The conductor wires can be either stripped or left with the insulating material on it. The ports of the yellow button butt connectors are filled with gel. This provides with water tight and offer corrosion resistant function to protect the connections against air and moisture. All TEGs in the row section of the square channel design were connected in series. These four rows can then be connected either in series connection or parallel connections.

Figure 5.21 Insulation of the gap using silicone glue

Figure 5.20 also shows the gap between the TEGs rows. This gap can allow heat to be transferred into the cooling water with least resistance compared through TEG itself. To avoid that, these gaps were filled with silicone glue, which has good insulating properties, as shown in Figure 5.21. Silicone glue was used because it can spread easily into the tiny gaps and it is easily applied when compared to other solid insulation materials. It also bonds well with the metallic surface of the heat exchanger. Appendix C shows the drawing for square channel design.

Figure 5.22 Completed section of the heat exchanger with TEGs and insulation

Figure 5.22 shows the completed section of the in-pond heat exchanger together with 60 TEGs, insulation and all connections. Four rows provide four terminals of each positive and negative. These can be connected in series, parallel or individually to meet the application requirements.

5.5.2.2 In-pond Polygon (Nonagon) Heat Exchanger (126 TEGs)

A polygon (nonagon) with nine sides was fabricated to increase the number of TEGs used for power generation from low grade heat of solar pond. A stainless steel sheet metal, grade 316 with a thickness of 2 mm was used to fabricate the nonagon heat exchanger. Three identical different sections were welded together into shape as shown in figure below. Each side is 50 mm in width and 600 mm in length. This will easily accommodate 14 TEGs on each side of the polygon heat exchanger. With nine sides, this gives a total of 126 TEGs on the whole section of the polygon. The heat is obtained only from the LCZ section of the solar pond; hence the length at 600 mm. Figure 5.23 shows sheet metal forming to fabricate the nonagon (polygon) heat exchanger.

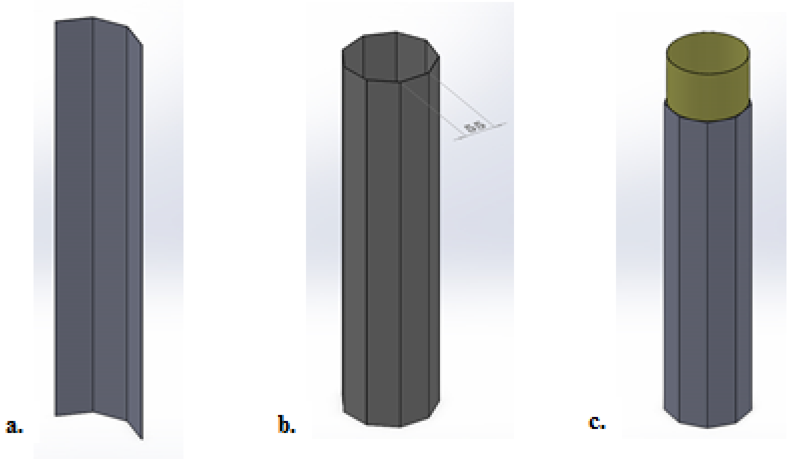

Stainless steel sheet metal formed into three sides

Three stainless steel sheet metal (a.) welded into nonagon polygon shape

Top connector (in green) for outer pipe attachment

Figure 5.23 Stainless steel sheet metal forming for nonagon heat exchanger fabrication

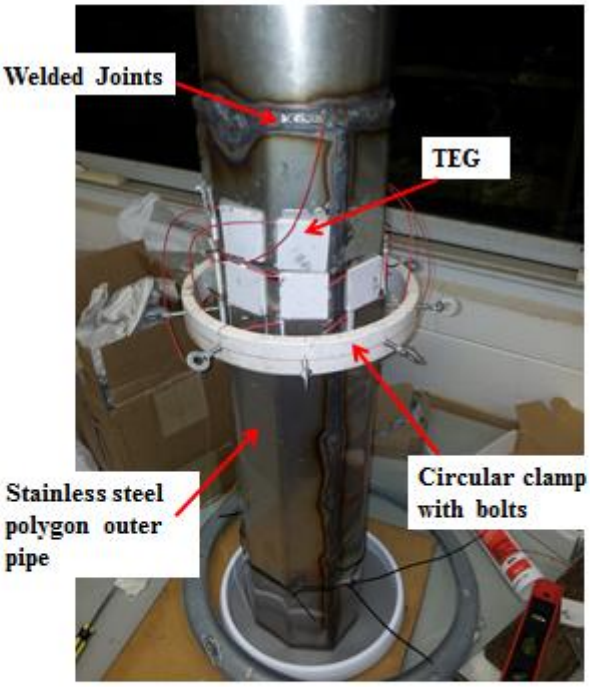

Figure 5.24 Circular clamp used for the attachments of TEGs on polygon heat exchanger

Figure 5.24 shows the diagram where a circular clamp was used to attach the TEGs onto the polygon heat exchanger surface. The circular clamp was held by nine bolts that can be tightened to compress the TEG to the surface of heat exchanger with thermal adhesive. The circular clamp helps to hold the TEGs in place while the thermal adhesive dries over time. A total of nine TEGs were attached at one time and left to dry for 8 hours. Then the whole process is repeated until all 14 TEGs were attached for each row of the polygon heat exchanger. The bolts on the circular clamp can be tightened or loosened by hand. A metallic plate of 4 mm thickness was sandwiched between the TEG and the bolts of the circular clamp to distribute the pressure, and not to crack the TEG ceramic cover with concentrated pressure from the tightening of the bolts.

Figure 5.25 shows the polygon heat exchanger with all one hundred twenty six TEGs attached on each side. The terminals of each of the TEGs were stripped from its plastic insulation.

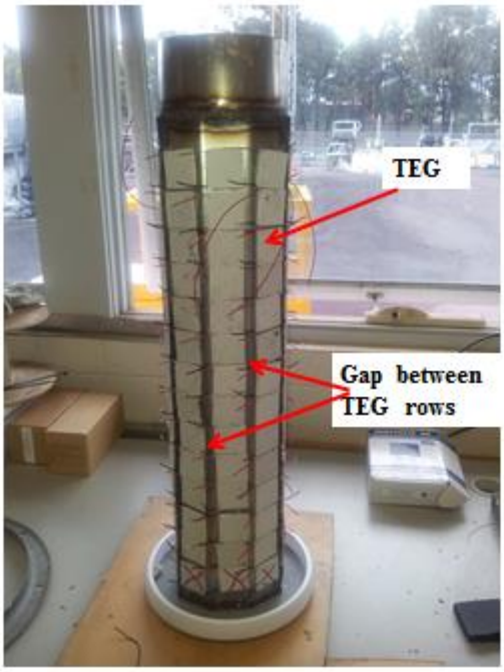

Figure 5.25 Complete TEG attachments to the polygon heat exchanger

These terminals were connected with yellow button butt connectors. From the figure, there were gap between the TEGs for each rows left when all the TEGs were connected. These gaps needed to be filled to reduce the unwanted heat transfer to the cooling fluid. These gaps were filled with silicone glue and the remainder section of the polygon heat exchanger was covered with Armaflex insulation, as shown in Figure 5.26 below. Figure 5.28 shows the CAD model of the polygon in-pond heat exchanger. Three spacers were used to place the inner PVC pipe in place to maintain the gap for cooling water flow. The gap was measured at 4 mm. The inner pipe was cut and then welded into a smaller diameter pipe to fit into the outer pipe. This inner PVC pipe is the same pipe as used for the outer PVC pipe. This is because the next available smaller size of PVC pipe was 98 mm in diameter, which would have resulted in bigger gap for the cold water flow. This would result in lower heat transfer. The bottom of the inner PVC pipe was cut with multiple slots of 40 mm long and 20 mm wide around the perimeter. These slots provided opening for the cold water to change its direction at the bottom to exit the heat exchanger at the top of the inner PVC pipe.

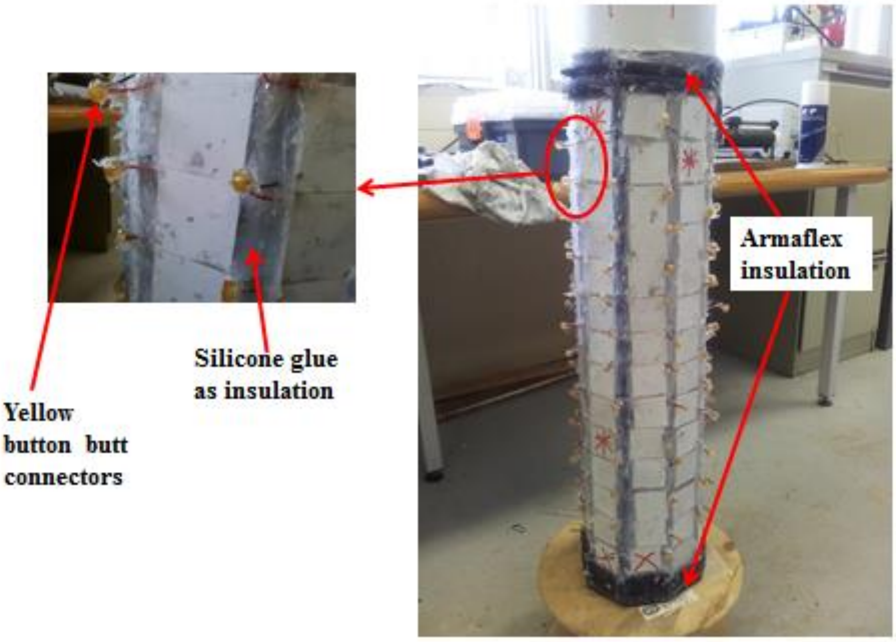

Figure 5.26 Polygon in-pond heat exchanger with 126 TEG modules

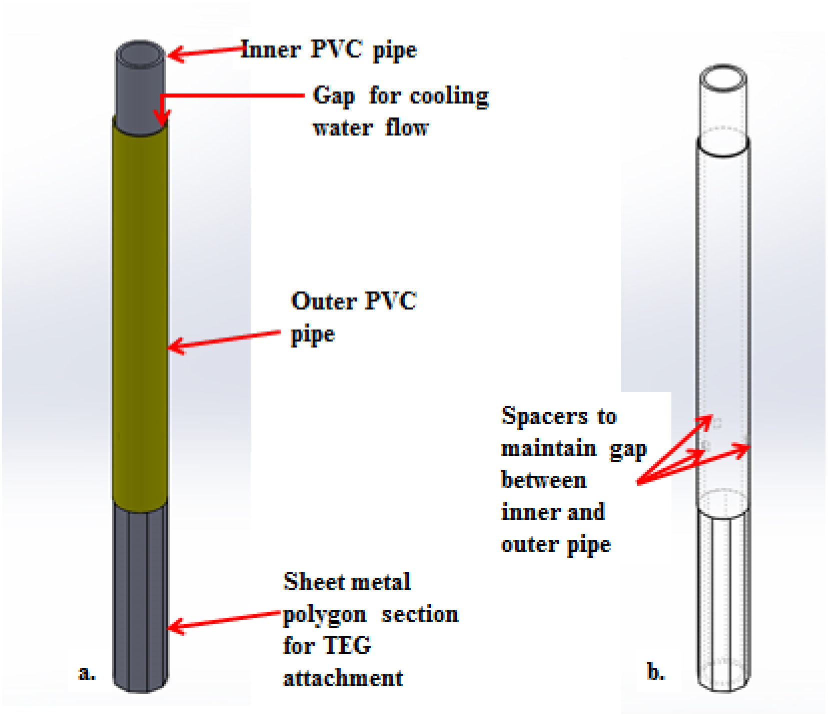

Figure 5.27 CAD model of in-pond heat exchanger with spacers

Figure 5.28 shows the completed polygon heat exchanger. The height of the heat exchanger is not more than 2.0 m in height. This is to allow water from NCZ of the solar pond to flow between the inner gaps of the heat exchanger as cooling water. The figure also shows the inner and outer PVC pipe used to create the gap for cooling water flow rate. The gap was measured at 4 mm. The inner pipe used was 5 mm thick and with outer diameter of 14 cm. The outer pipe was 3 mm thick and with 15.8 cm outer diameter dimension. The outer pipe was fixed to the connector ring of the metal part of the heat exchanger and sealed with silicone adhesive. The flow of cooling water was maintained by the same siphoning action as explained in the section describing square channel heat exchanger. A container was used to simulate the UCZ condition of the solar pond, as shown in the same figure. All TEGs in each row were connected in series. Nine set of terminals were available for connection, either in series, parallel or both, depending on the application requirements. Appendix D shows the drawing for in-pond polygon heat exchanger design.

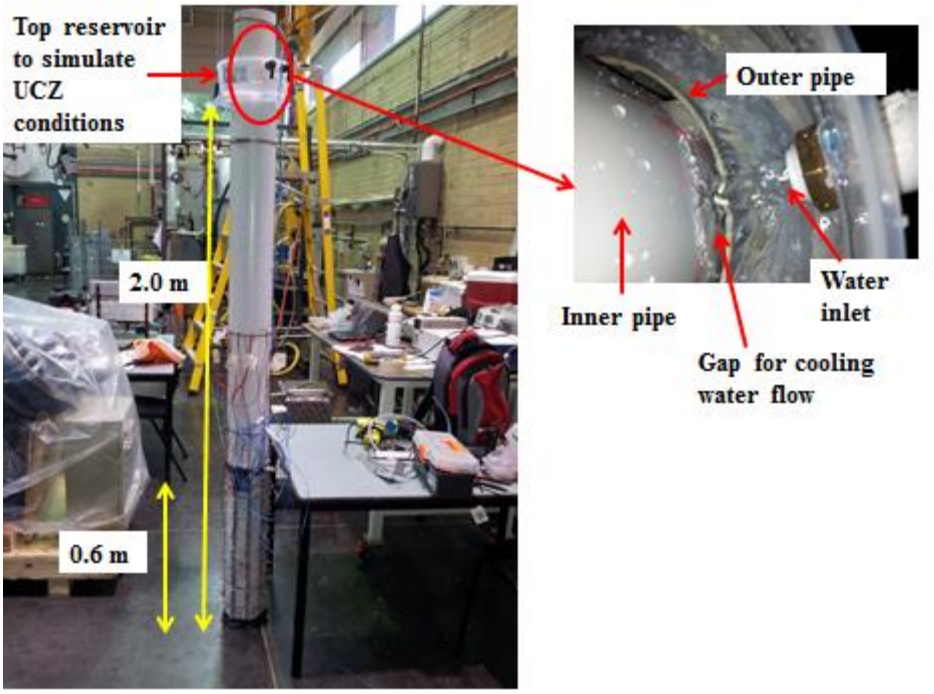

Figure 5.28 Complete polygon heat exchanger setup

5.5.3 Polygon (Decagon) Heat Exchanger with Forced Convection Cooling and Heating (300 TEGs)

Both the in-pond designs described earlier relied on natural convection heating for the hot side TEG section. This is advantageous as the system does not need any external pumping devices to maintain the flow. The siphoning effect was maintained due to the difference in height between the solar pond and evaporation pond. Alternatively, pumps can be used to maintain the hot and cold fluid flow in a TEG based heat exchanger. For power generation from solar pond using low-grade heat, a simple concentric pipe heat exchanger was designed to generate electrical power. The hot fluid for this heat exchanger was pumped using an external pump from the LCZ of the solar pond, and returned back to the same region. Cooling fluid was obtained from the UCZ section of the solar pond, again with an external pump. Both the pumps are direct current (DC) pump, with high flow rate output. Alternatively, the use of cooling water pump can be eliminated if the heat exchanger system were to be connected to the fresh water used for surface washing of solar pond. The heat exchanger can be connected to the fresh water supply and circulated in the heat exchanger, before going into the solar pond for surface washing. This method will help to minimise the power requirement to run the pumps to maintain the flow rate in the TEG heat exchanger.

Figure 5.29 shows the conceptual design of a TEG polygon heat exchanger used for power generation. Hot fluid from LCZ pumped to the hot side of the polygon heat exchanger. The polygon heat exchanger consists of three concentric pipes. The inner most is a thick PVC pipe, followed by a machined stainless steel polygon pipe. TEGs are attached to the machined surface of the stainless steel pipe. The gap between these two pipes will be channelled with hot fluid from LCZ. The outer pipe of the polygon heat exchanger consists of Acrylic pipe. The gap between this Acrylic pipe and the stainless steel pipe will be channelled with cold water flow from the UCZ. The temperature difference between the hot and cold fluid results in power generation from TEGs. This cold water flow can either be pumped by an external pump or supplied by the fresh water used for surface washing of solar pond. This design enhances the heat transfer rate of the heat exchanger as more heat can be transferred by means of forced convection heating and cooling.

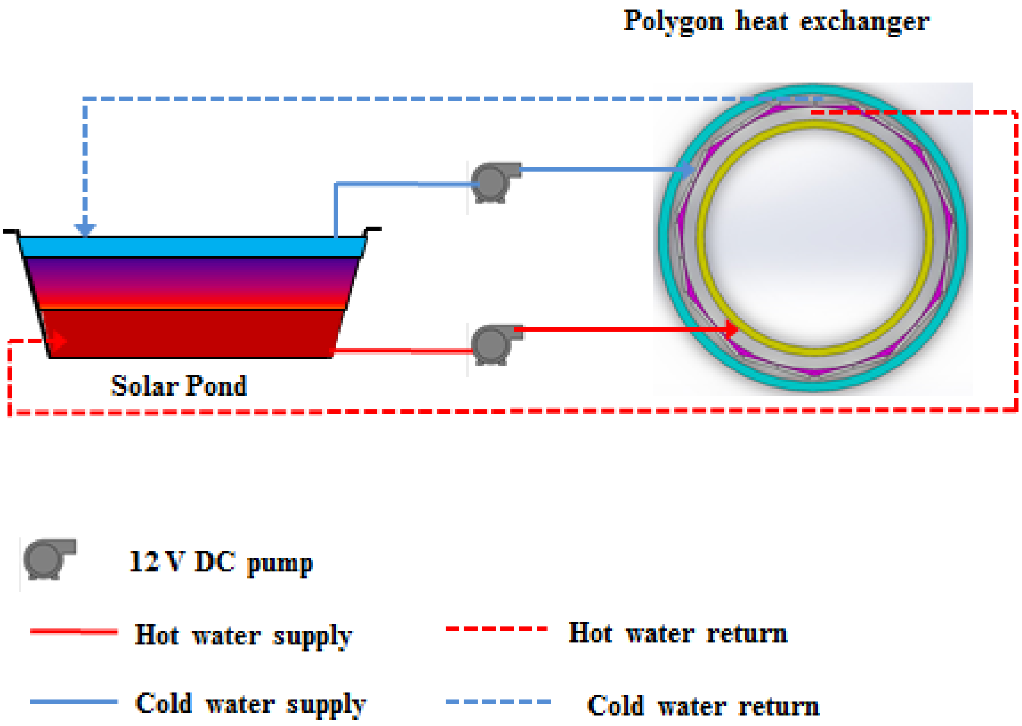

Figure 5.29 Conceptual design for polygon heat exchanger with forced convection cooling and heating.

Figure 5.30 above shows the machined stainless steel polygon pipe. The original pipe was circular in shape. The outer diameter of the pipe was measured at 323.9 mm, with a thickness of 9.5 mm. The pipe was chosen to be thick enough so that it can be machined to flat surfaces as shown in the above figure. The machined sides are 600 mm long and 90 mm wide. Each side of the machined surface can be attached with two rows of 15 TEGs each, so a total of 30 TEGs on one machined face. The whole pipe consists of 10 machined face of equal size. This results in 300 TEGs attachment to the whole polygon stainless steel pipe. The top and bottom surface of the pipe was maintained as a round shape, as shown in the same figure. The depth of this round shape is 15 mm on each side. This is to enable the polygon stainless steel pipe to be covered with end plates on both sides easily. The mass of the stainless steel was measured at 21 kg.

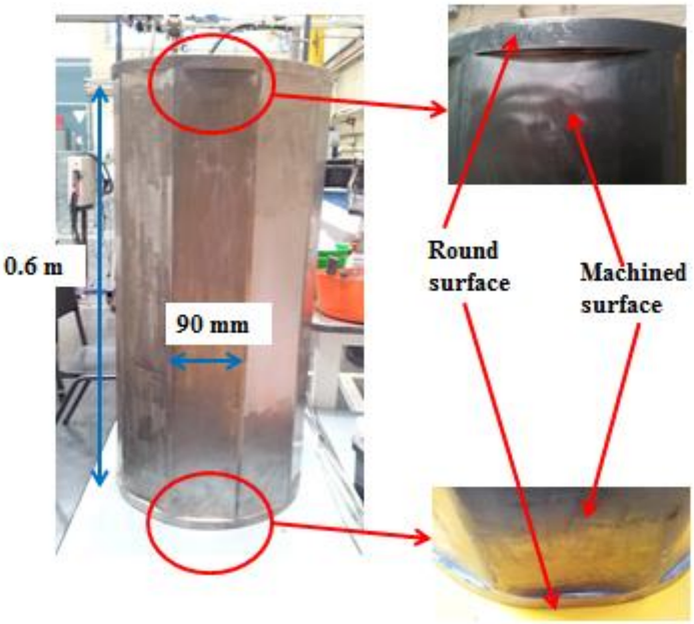

Figure 5.30 Machined stainless steel polygon pipe

Figure 5.31 shows the use of polygon clamp to attach the TEGs on the machined surface of the polygon stainless steel heat exchanger pipe. The same method as discussed in the in-pond nonagon heat exchanger was employed to attach the TEGs. The polygon clamp was adjusted using two stud bolts. A total of twenty bolts on the polygon clamp were used to hold the TEGs around the polygon heat exchanger pipe. Once the thermal adhesive dried, polygon clamp was lowered to attach subsequent batch of the TEGs on the lower part of the heat exchanger.

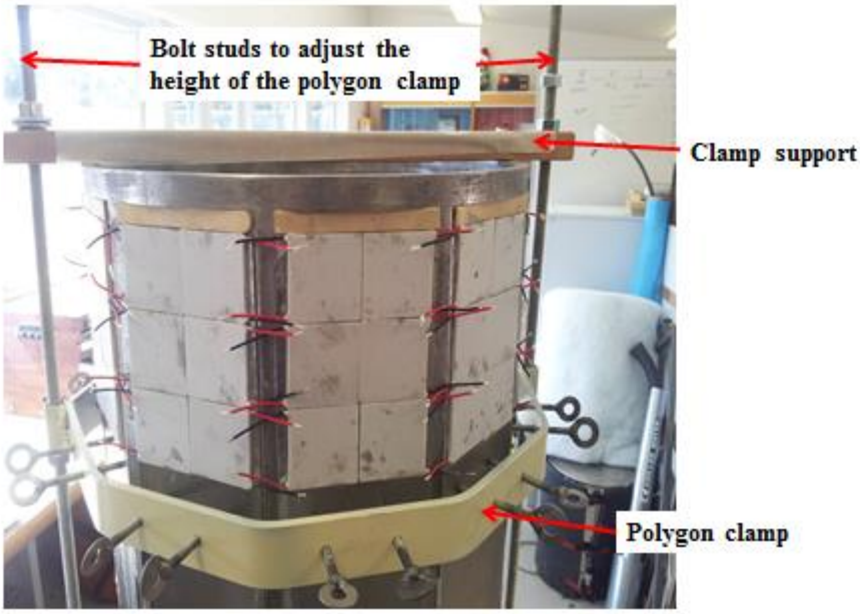

Figure 5.31 Polygon clamp used to attach TEGs

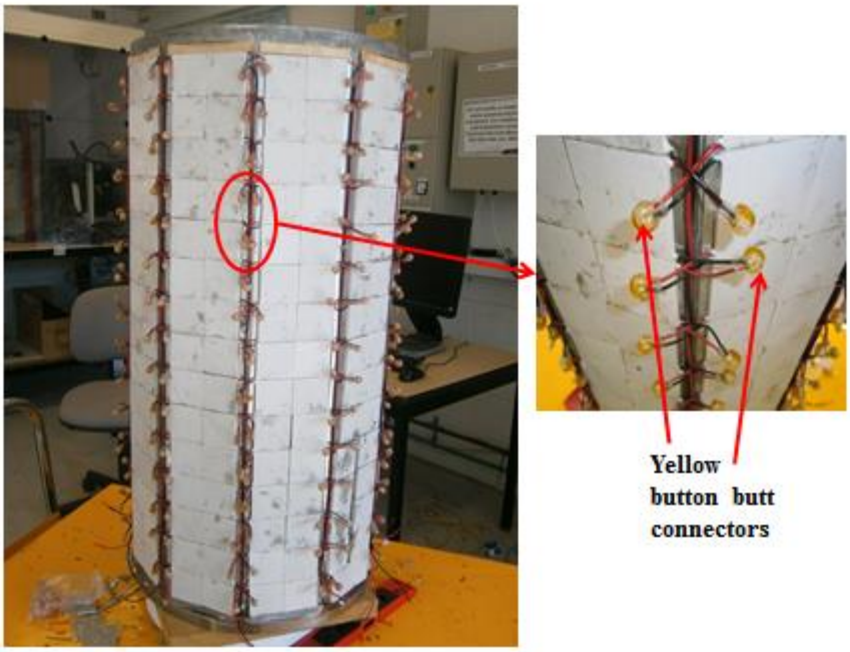

Figure 5.32 300 TEGs attached to the machined section of the stainless steel pipe and terminal connected with yellow button butt connectors

Figure 5.32 shows 300 TEGs attached to the machined section of the stainless steel pipe and terminal connected with yellow button butt connectors. A total of twenty rows of TEGs with 15 TEGs in each row were connected in series. Each machined surface of the polygon stainless steel pipe was attached with twenty TEGs in two rows, with ten TEGs in each row. The gaps between the rows were filled with silicone glue, which acts as insulation.

Acrylic end plate was machined to fit all three pipes to construct the heat exchanger. This acrylic plate was measured to be 30 mm thick, with equal length and width of 500 mm. Three circular slots were machined into the one end of this acrylic sheet to fit all three pipes, with a depth of 15 mm. At the bottom of these slots, a 4 mm thick rubber seal was inserted to act as seal to prevent any water leaking from the heat exchanger. Six holes were drilled around the end plates to fit in the stud bolts. These stud bolts were used to join the end plates and the pipes in to position and also to provide a tight and water leak proof fitting. At one side of the end plate, ten cable glands were fitted to bring out the TEGs conductor wires for testing and connection purposes. To provide hot and cold water to the heat exchanger, twelve hose tailed barbed connector, each for the cold and hot side channel were fitted at equal spacing around the end plates. These hose tailed barbed connector provides the inlet and outlet for the hot and cold water flow from the polygon heat exchanger.

Figure 5.33 below shows the arrangement of the three pipes used to construct the heat exchanger. As seen from the same figure in the diagram on left, the gap between the inner PVC pipe and stainless steel pipe was filled with hot water flow and the gap between stainless steel pipe and outer acrylic pipe was filled with cold water flow. When covered with end plate as shown in the figure on right, the pipes were placed in position by the slots in the end plates. The gaps were 12.2 mm, 8.6 mm for hot and cold channel respectively. Hose tailed barbed connectors are placed at equal spacing at 30° all along the hot water and cold water channel of the heat exchanger.

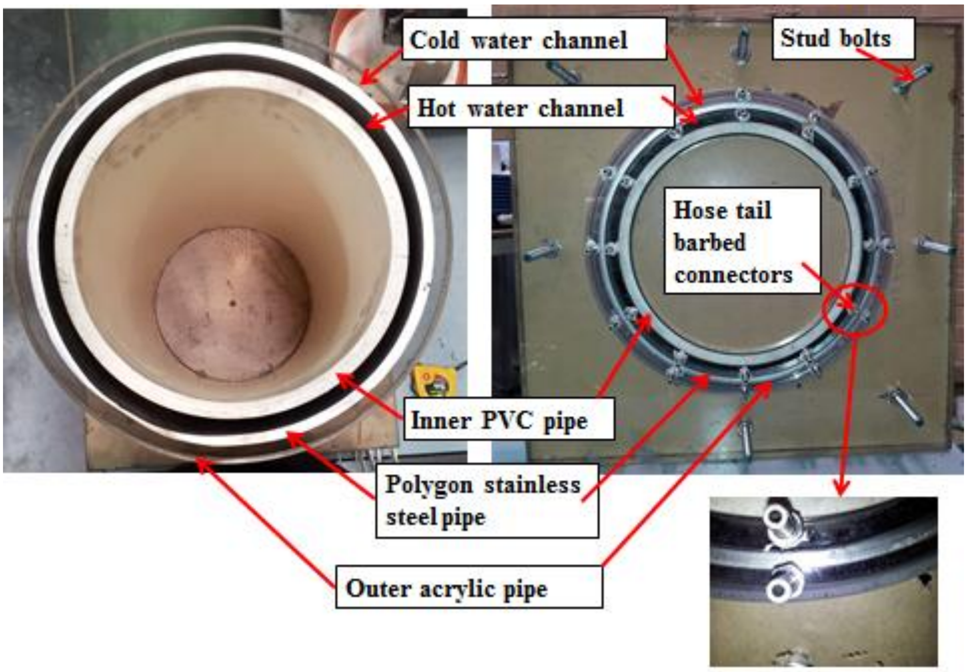

Figure 5.33 Arrangements of pipes in polygon TEG heat exchanger

Figure 5.34 shows a CAD model for acrylic end plate used to hold the heat exchanger together. Figure 5.35 shows the actual diagram of the acrylic end plate with connectors and cable glands. Three slots of depth of 15 mm were machined to fit the inner PVC pipe, stainless steel pipe with TEG modules and outer acrylic pipe. Both the length and width of the end plate was 500 mm. The thickness of the end plate was 30 mm. Six holes with a diameter of 10 mm were drilled on the end plate. This is to hold both the end plates with the heat exchanger together with stud bolts. For the hot and cold water channels, twelve holes with a diameter of 8 mm were drilled. Extra ten holes were drilled on the cold channel part of the end plate to fix cable glands. Cable gland, as shown in figure 5.36 was used to bring out the terminal wires of the TEG for experimental analysis.

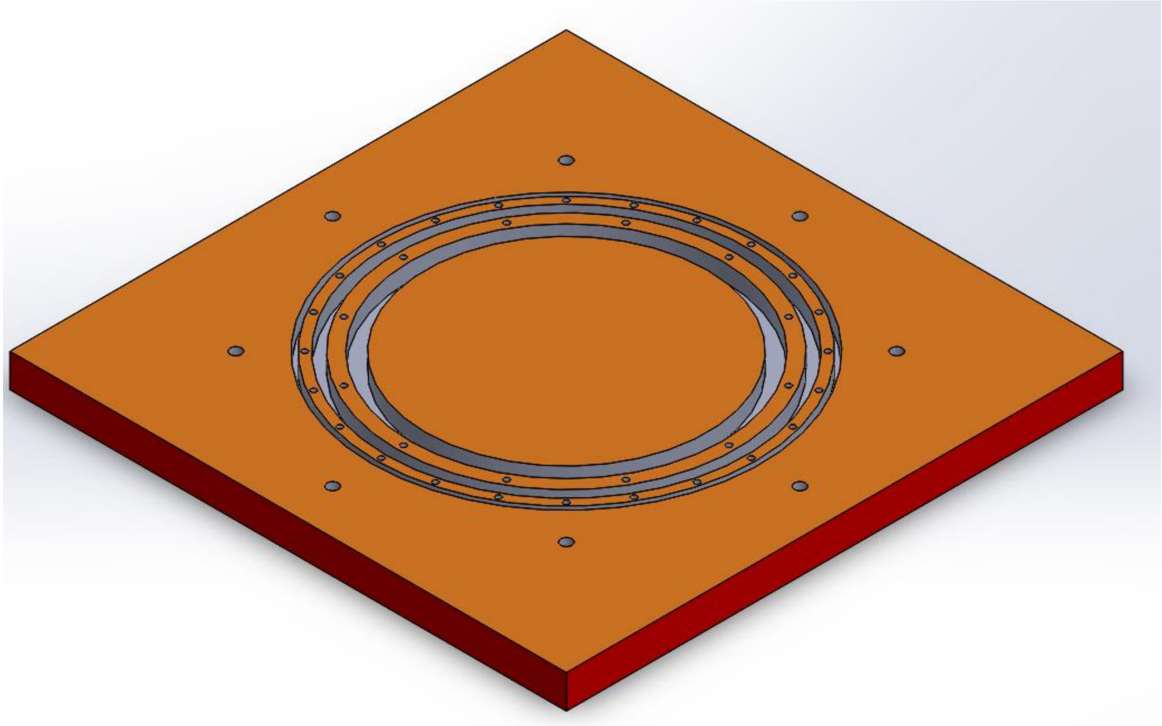

Figure 5.34 CAD model of acrylic sheet end plate (Appendix E)

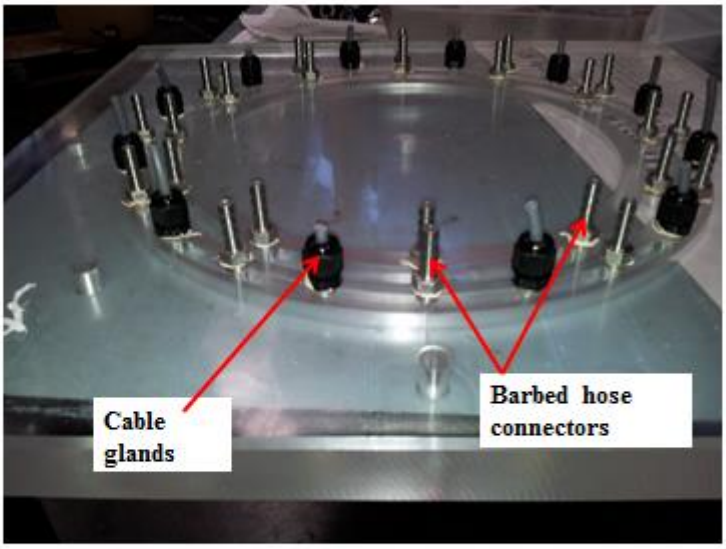

Figure 5.35 Acrylic end plate with connectors and cable glands

Figure 5.36 Cable gland used for acrylic end plate

Figure 5.37 shows twelve outlet water manifolds used to supply hot and cold water for the hot and cold side of the polygon heat exchanger. The twelve outlet manifold helps to supply hot and cold water evenly around in the TEG polygon heat exchanger. Plastic heat resistance (up to 90°C) tubes were used for the inlet and outlet of the heat exchanger. A 12 V DC pump was used to supply hot water to the hot side of the heat exchanger. The cooling water was supplied by the tap water located in the lab.

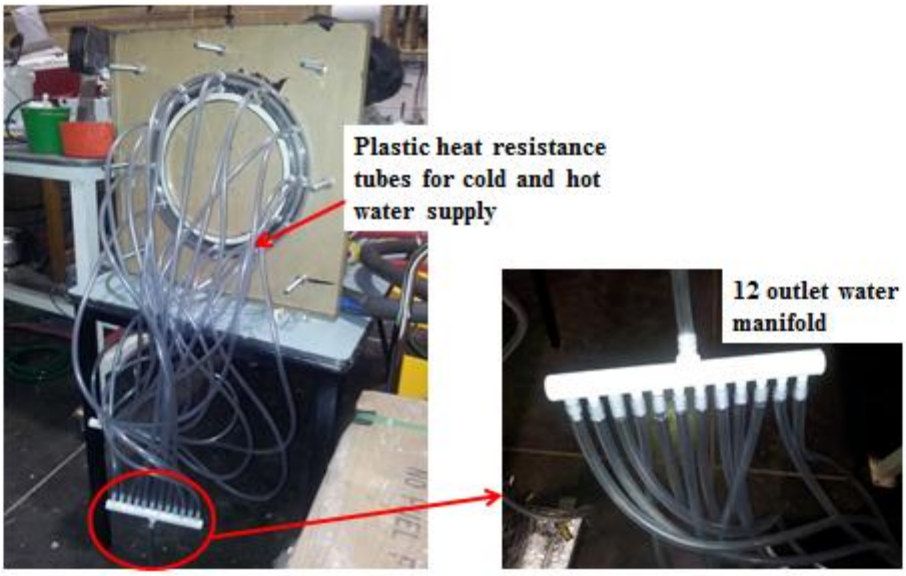

Figure 5.37 Twelve outlet manifold for hot and cold water inlet and outlet

Figure 5.38 below shows the completed set up of the polygon heat exchanger used for power generation with three hundred TEGs. Appendix F shows the drawing for the polygon TEG heat exchanger.

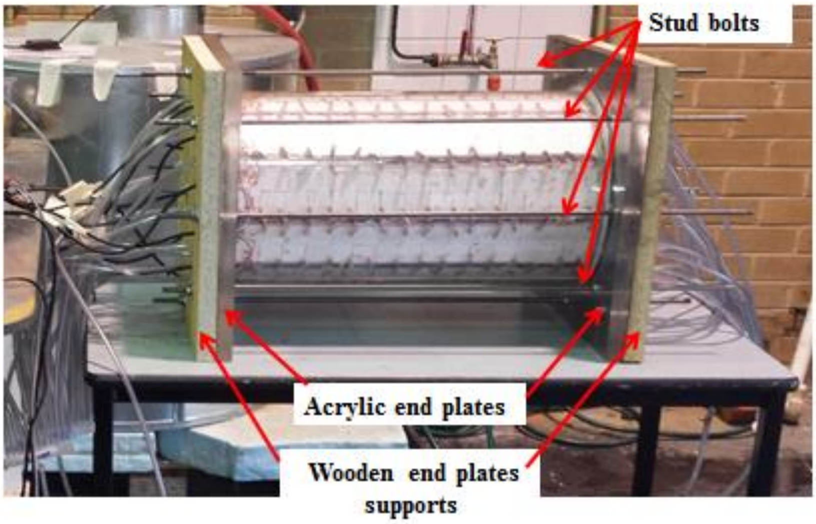

Figure 5.38 Completed TEG heat exchanger

5.6 Chapter Conclusion

In this chapter, the mathematical analysis used to model the TEG plate and polygon heat exchanger was presented. The mathematical analysis helped in designing the TEG heat exchangers as well as to help to verify the experimental results obtained.

Three configurations designs were used to test the TEGs for power generation from low grade heat of solar pond. Both passive and active designs were considered, depending on the application of the power generation. These designs are simple, low cost and easy to manufacture.

6.0 TEG Heat Exchangers – Results and Discussion

6.1 Introduction

This chapter presents the results obtained for TEG power generation using different TEG heat exchanger designs. A plate heat exchanger with counter flow arrangement was tested in the laboratory to predict the performance of TEG using low grade heat below 100 ˚C. In-pond TEG heat exchangers were tested in both laboratory and in an actual solar pond. In-pond heat exchanger provides power generation without any pumping devices. The cooling water needed for the heat transfer was provided by the UCZ section of solar pond and transferred to evaporation pond through siphoning effect, without compromising the overall operation of the solar pond. Finally, a TEG heat exchanger with forced convection cooling and heating was tested in the laboratory with three hundred TEG modules. All results are discussed in this chapter and compared with theoretical model developed using analytical simplified model in Excel spread sheets.

6.2 TEG Plate Heat Exchanger

6.2.1 Experimental Set Up

A laboratory experimental set up was used to test TEG plate heat exchanger. Figure 6.1 shows the TEG plate heat exchanger. A hot water urn was used as a reservoir for hot water utilisation in the experiment. The temperature in hot water urn was controlled using a temperature controller with a sensor submerged in the hot water urn. Temperature controller with the sensor helps to maintain a constant temperature in the hot water bath. A flow meter with a flow range of 0 – 30 L/min was used to measure the hot water flow rate. This flow meter monitors real-time flow rate and total flow over a period. A 12V DC pump was used to pump hot water from the hot water urn to TEG plate heat exchanger. The 12V DC pump has the capacity of providing a mass flow rate up to 0.2 kg/s. The cold water was supplied by the tap water supply located in the laboratory. An electronic load was used to apply variable external resistance to the TEG connections. The output from the TEG modules was connected to a data logger and computer system. Figure 6.2 shows the schematic of the TEG plate heat exchanger.

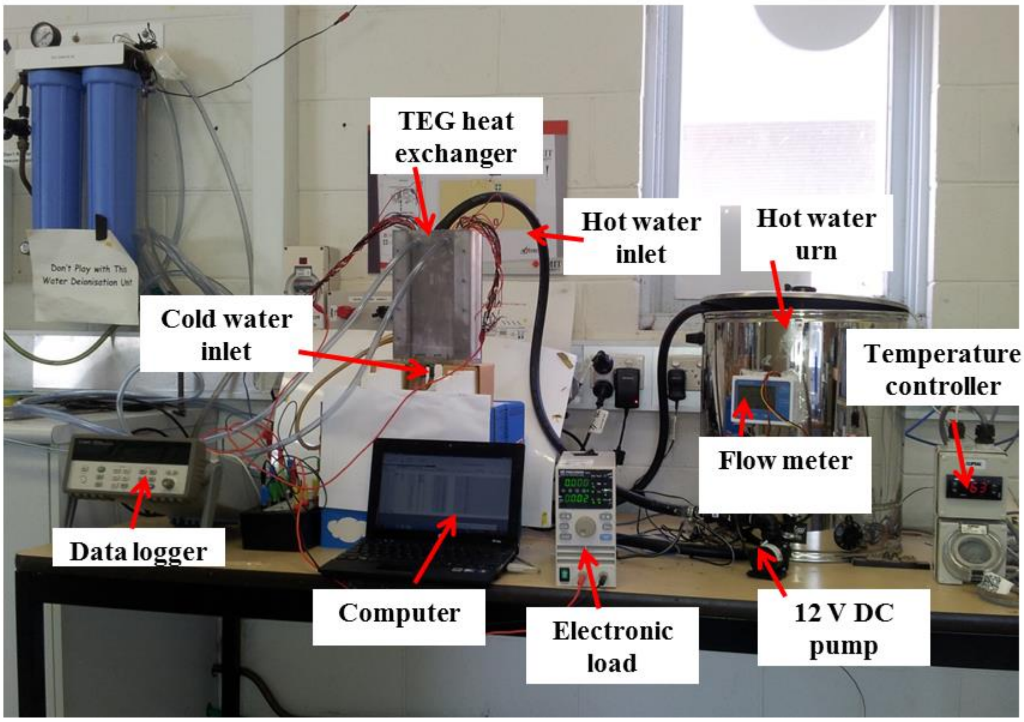

Figure 6.1 Experimental set up for TEG plate heat exchanger for laboratory testing

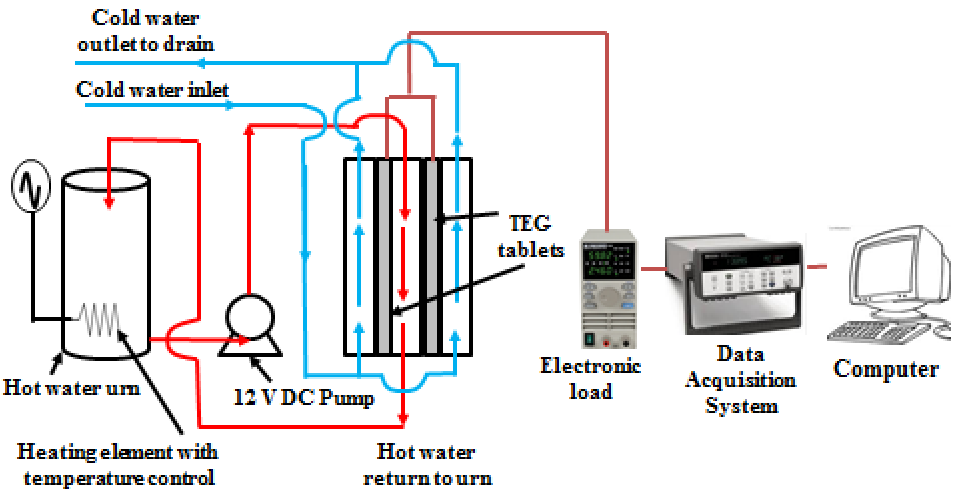

Figure 6.2 Schematic set up for the TEG plate heat exchanger used for laboratory testing

6.2.2 Results and Discussions

A plot of output current, I_{out} [A] versus output voltage, V_{out} [V] is shown in Figure 6.3. The graph was plotted for bulk fluid temperature differences of 20˚C, 30˚C, 40˚C, 50˚C, 60˚C, 70˚C and 80˚C. The cold side water temperature was constant at 20˚ C and the hot side water temperature was fixed at 40˚C, 50˚C, 60˚C, 70˚C, 80˚C, 90˚C and 100˚C respectively to obtain the bulk fluid temperature differences above. From figure 6.3, it is shown that the relationship between current output, I_{out} [A] and voltage output, V_{out} [V] is linear. All TEG modules were connected in series. An increase in the temperature difference between the cold and hot side of the fluid increases, will cause the output current, I_{out} [A] and output voltage, V_{out} [V] to increase proportionally. This increase in heat transfer is due to the larger temperature differences across the TEGs, resulting in increase of electrical energy generated by the TEGs.

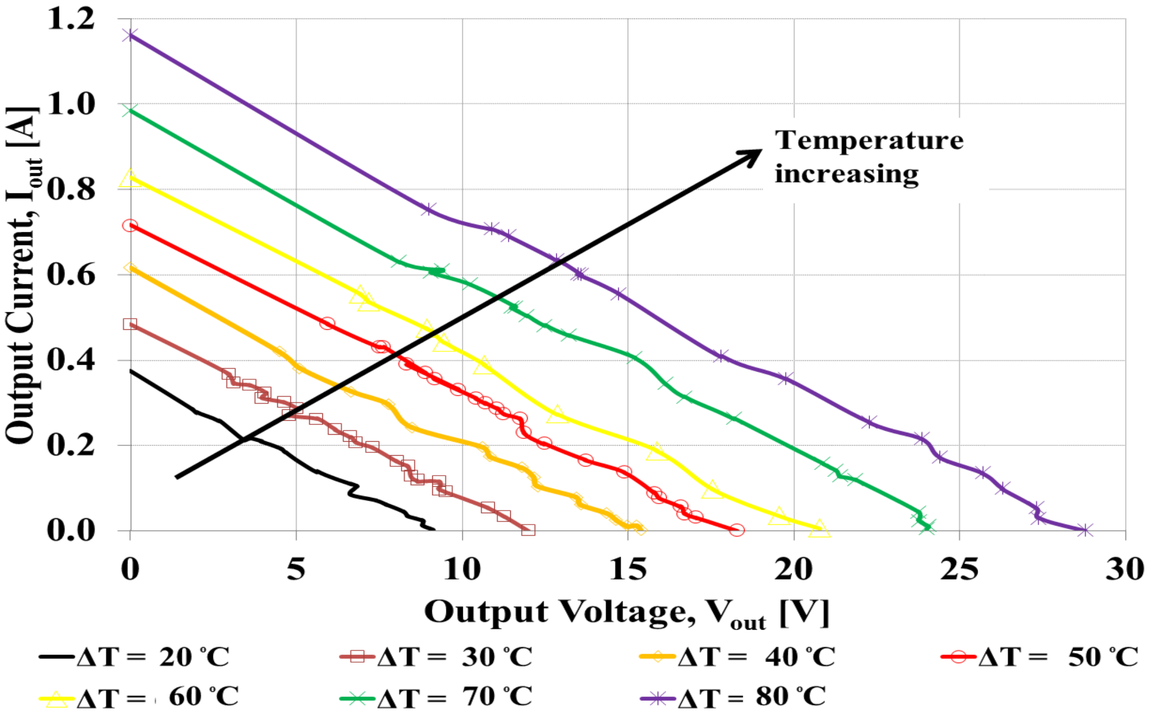

Figure 6.3 Output current versus output voltage for several fluid bulk temperature differences

From Figure 6.3, a high linearity in all I/V plots with the same slope can be observed. This shows that the internal resistance of the TEGs was constant with the fluid bulk test temperatures and the load applied to the TEGs. This results in clear existence in clusters of internal resistances as shown in Figure 6.4.

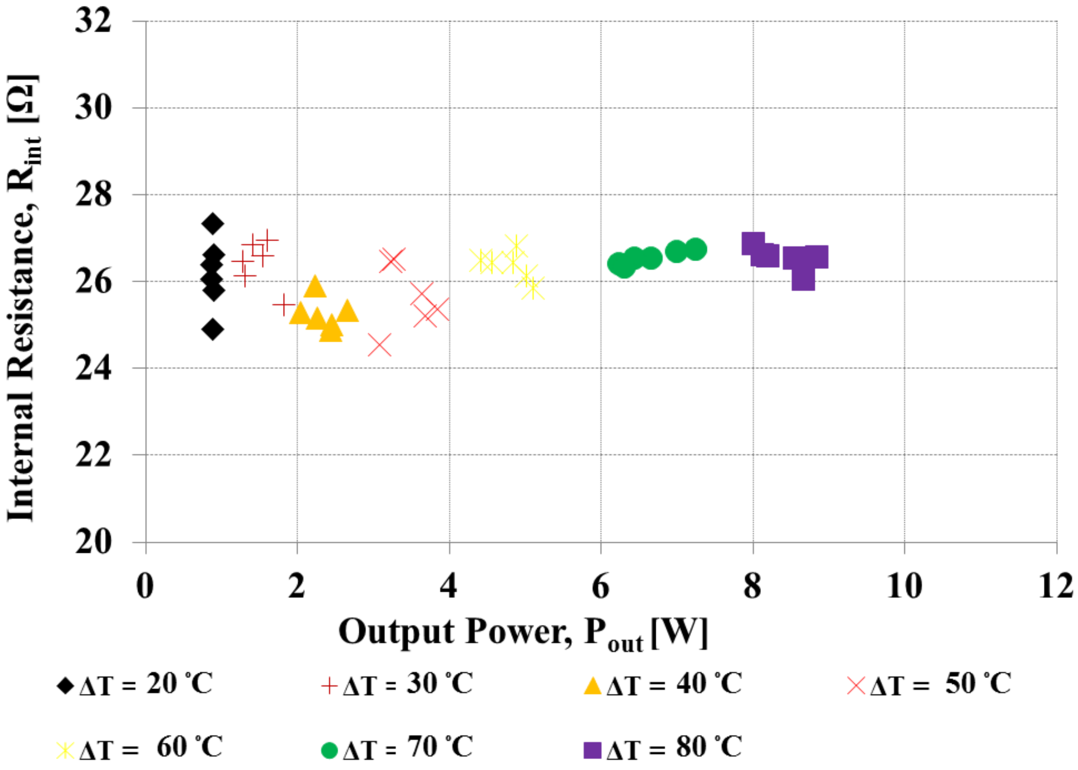

Figure 6.4: The internal resistance of TEGs versus the output power for several fluid bulk temperature differences

In order to calculate the statistical behaviour of these clusters, their medium ($\mu_i \in$ 26.2, 26.4, 25.3, 25.6, 26.4, 26.5, 26.5 Ω) and standard deviation ($\sigma_i \in$ 0.8, 0.5, 0.3, 0.8, 0.3, 0.2, 0.3, 3.3 Ω) was calculated. From this analysis, the internal resistance of the analysed TEGs is equal to $R_0 = 26.1$ Ω, with a tolerance equal to $\Delta R_{int} = 0.3$ Ω, thus $R_{int} = R_0 \pm \Delta R_{int} =$ 26.1±0.3 Ω. Figure 6.5 shows Output Power, P_{out} [W] change as a function of Electrical Resistivity, Ω [Ohm]. Power output increases with increasing the hot fluid temperature at different load resistance. The peak of the measured power curves occurs where the load resistance is in the range of about 20-30 Ω, which falls in the range as calculated earlier. Maximum power of TEG module was achieved when load resistance equals the effective internal resistance of the TEG modules. The output power of TEG can be optimized by balancing the internal and external resistance in real application practice.

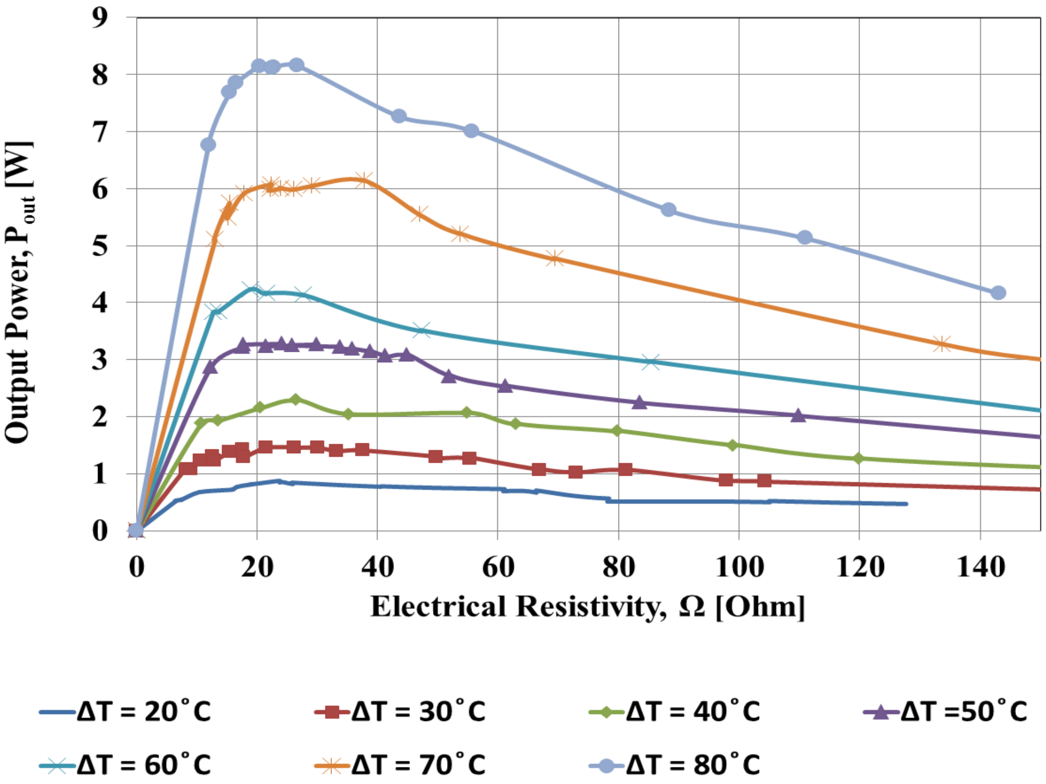

Figure 6.5 Power change as a function of electric resistivity

It was also observed from Figure 6.3 that the output power increases with the increase in temperature. This is due to the rise in output voltage, V_{out} [V] as the temperature gradient, $\Delta T = T_H - T_C$ [˚C] increases. This will then result in an increase in the output current, I_{out} [A]. The dissipated power corresponds to the external load resistance applied, R_L [Ω]. Maximum power occurs when the external load resistance R_L [Ω] is equal to the internal resistance, R_{int} [Ω] of the TEG, e.g, $P_{out} = V_{out}I_{out}$ [W]. Figure 6.6 shows the output power P_{out} [W] versus the output voltage V_{out} [V]. The output power increases P_{out} [W] with the increase in bulk fluid temperature difference, $\Delta T = T_H - T_C$ [˚C] to the hot side of the TEG. The increase in the temperature difference between the hot fluid and cold fluid increases the power produced by the TEGs. In Figure 6.6, a maximum power curve was obtained when the load resistance matches the resistance of the TEGs connected in series. For a temperature difference of 20˚C, 30˚C, 40˚C, 50˚C, 60˚C, 70˚C and 80˚C. Maximum powers obtained was 0.9 W, 1.5 W, 2.4 W, 3.4 W, 4.4 W, 6.2 W and 8.2 W respectively. All maximum output was recorded at external load resistance between 25.8 to 26.4 ohms, [Ω].

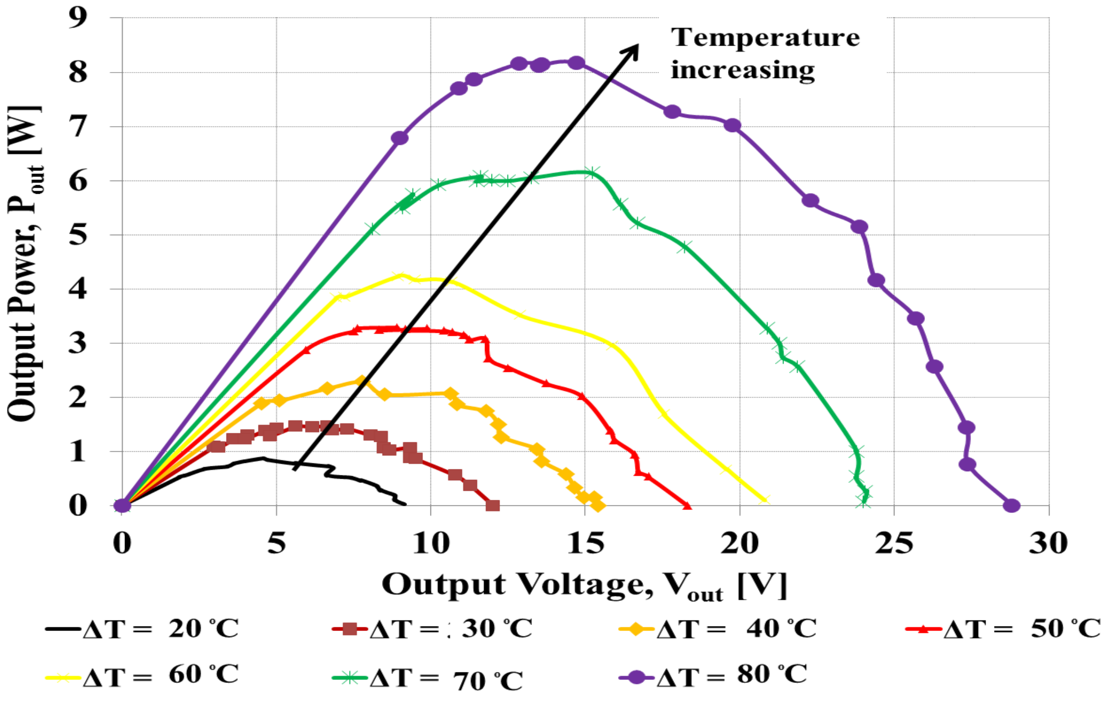

Figure 6.6 Output power versus output voltage for several fluid bulk temperature differences

Figure 6.7 shows the power output for a combination of connections of the TEG modules for plate heat exchanger.

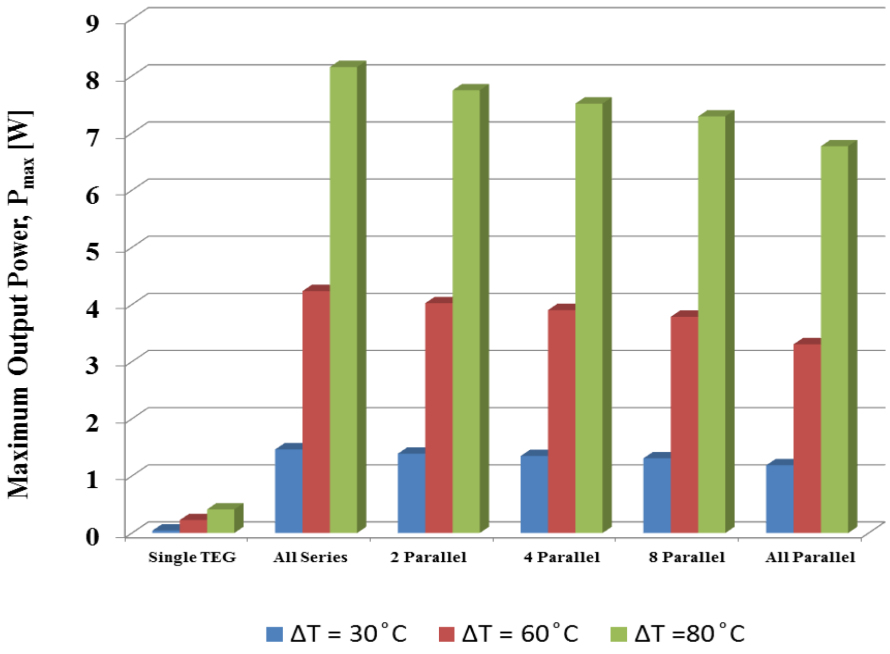

Figure 6.7 Maximum output power versus parallel/series connections

Maximum power output from a single TEG was obtained and recorded for three temperature differences as shown in the figure. Then, all sixteen TEG modules were connected in series to obtain the maximum power output. This was followed by having two TEG modules connected in parallel, which results in eight parallel connections. These eight parallel connections were then connected in series. Same method as above was applied to four TEGs connected in parallel and eight TEGs connected in parallel. Finally, all sixteen TEGs were connected in parallel and power outputs from these connections are shown in Figure 6.7.

From Figure 6.7, it can be shown that the power output was maximum when all TEG modules were connected in series and lowest when all TEGs were connected in parallel. The maximum output power reduces with the number of parallel connections used for the TEG plate heat exchanger. The difference between the series and parallel connections was at 17 %. For TEG modules, temperature difference was proportion to the voltage developed. Heat flux is proportion to the current flowing through the cell. Current flow will also be inversely proportion to the resistance of the cell. When TEG modules were connected in series, total resistance will be sum of individual cell thermal resistance, and voltage will also add up. When cells connected in parallel total thermal resistance will be low and, between thermal resistance of one module and total sixteen modules. Therefore, we move from all series (where open circuit voltage is highest) towards parallel combination, where the output power is going down due to large reduction of the circuit voltage. Compared with single TEG module in terms of voltage with the current, it can be seen that current output is very low. Hence overall output power is larger function of voltage as a result, and reduction in power was experienced. Also, the applied heat or flux is constant; therefore change in current will not be very much. In actual life system, one need to put some modules in series to make an array, to get the required voltage (for example 12 Volt) and then number of these arrays in parallel to get the required current (and this necessary power) (e.g. 60 W = 12 V x 5 Amp).

Figure 6.8 shows the connection of the open circuit volatge, V_{ocv} [V] and temperature difference of the fluid used in the experiment. The correlation between the open circuit voltage, V_{ocv} [V] and temperature difference is linear. This proves that the open circuit voltage, V_{ocv} [V] will vary correspondingly with the temperature difference. A linear equation can be obtained from the results of this experiment from Figure 6.8 and is shown below.

$$V_{oc} = 0.36\ \Delta T \tag{6.1}$$

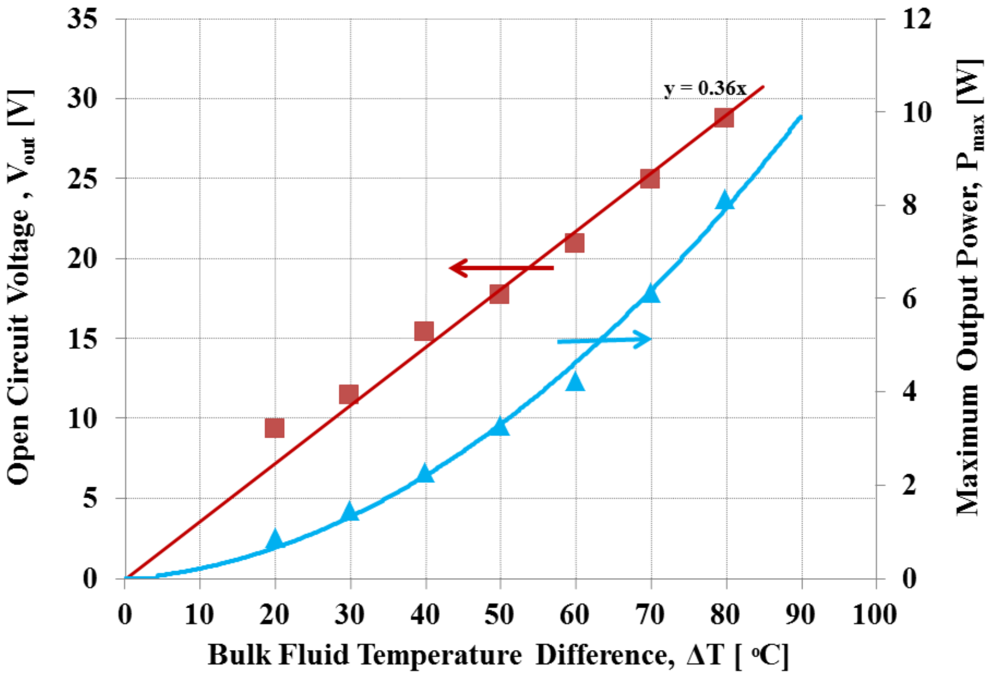

Figure 6.8 Open circuit volatge and maximum output power versus several fluid bulk temperature differences

Figure 6.8 also shows the plot for maximum power output, P_{max} [W] versus several fluid bulk temperature differences, ΔT [˚C]. This maximum output power P_{max} [W] was obtained when the resistance of the electronic load was equal to the resistance of the sixteen TEGs, all connected in series. From the plot, we can see that the maximum power output, P_{max} [W] increases with the increase in fluid bulk temperature differences, ΔT [˚C]. For the solar pond power generation application, the required temperature differences for the TEGs lies between 20-60˚C. The high temperature at LCZ and low temperature at UCZ in the solar pond can be used to power the TEGs. From the same figure, it is shown that the power generation solar pond using TEGs can be achieved not only during summer but also in the winter when the temperature of the pond drops according to the ambient temperature. The minimum temperature difference between the LCZ and UCZ in the winter season is around 24˚C. From the experiment conducted, the TEGs will not only be able to generate electricity in summer, where the temperature difference is highest, but also during winter when the difference of temperature recorded temperature is lowest. This provides an added advantage for power generation from solar pond using TEGs compared to ORC engines, as the latter will not be able to operate using the low temperature heat from solar pond during winter.

The above results show that the power generation from SGSP using TEGs provides a competitive alternative to the other solar based power generation systems. The power produced is lineal to the temperature difference across the TEGs. Even a small temperature differences is possible to generate power from TEGs. A maximum power of 8.2 W was observed from this experiment. This was obtained at when the temperature difference of the bulk fluid for the maximum power output was set at 80 °C for all the sixteen TEGs. The voltage and current recorded for the above power output was at 12.8 V and 0.6 A respectively. The open-circuit voltage and the short circuit current values of 28.8 V and 1.2 A respectively were obtained. The proposed TEGs heat exchanger will be useful for power generation for small scale application using the heat stored in SGSP.

6.3 Polygon TEG Heat Exchanger

6.3.1 Experimental Set Up

A laboratory experimental set up with three hundreds TEGs was used to test polygon (decagon) TEG heat exchanger performance. Figure 6.9 shows the polygon TEG heat exchanger. A four hundred litres, eight kilowatts hot water tank was used to supply hot water used in the experiment. The temperature in the hot water urn was controlled using a temperature controller with a sensor submerged in the hot water urn. Temperature controller with the sensor helps to maintain a constant temperature in the hot water bath. A 12V DC pump was used to pump hot water from the hot water tank to polygon TEG plate heat exchanger. The 12V DC pump has the capacity of providing a mass flow rate at 40 L/min. The cold water was supplied by the tap water supply located in the laboratory. An electronic load was used to apply variable external resistance to the TEG connections. The output from the TEG modules was connected to a data logger and computer system. Figure 6.10 shows the schematic of the TEG plate heat exchanger.

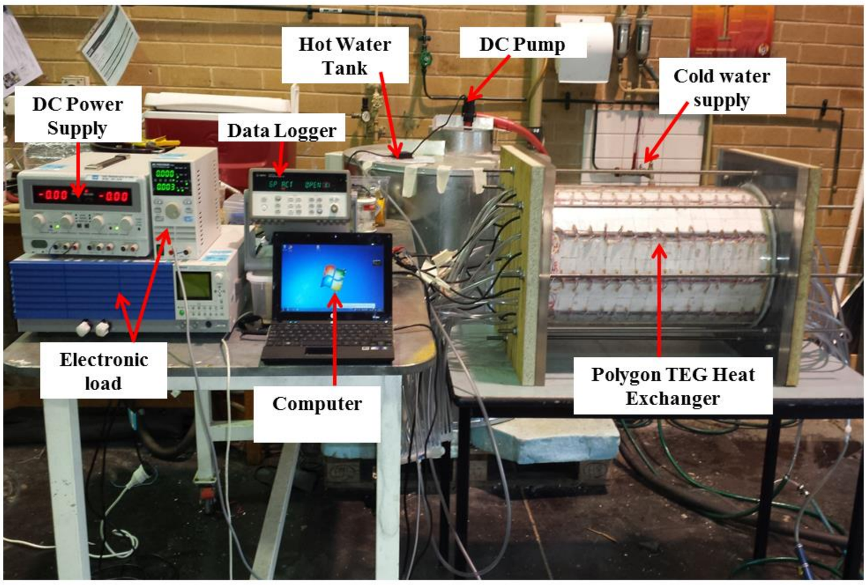

Figure 6.9 Experimental set up for polygon TEG plate heat exchanger for laboratory testing

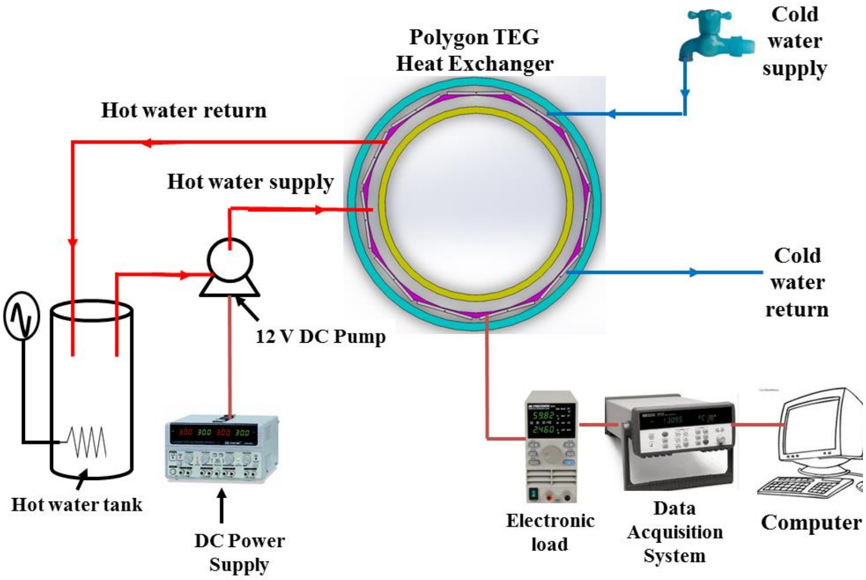

Figure 6.10 Schematic set up for the polygon TEG plate heat exchanger used for laboratory testing

6.3.2 Results and Discussions

Figure 6.11 shows the theoretical total heat transfer from the polygon TEG heat exchanger with different gap sizes for cold and hot water channel for different water mass flow rates. The hot water and cold water temperatures were fixed at 65˚C and 25˚C for modelling of the TEG heat exchanger with a total length of 0.6 m. The analytical results were obtained by using analytical computer model developed using Excel. Same mass flow rates were used for the hot and cold water channel of the polygon TEG heat exchanger. The lower gap sizes for the hot and cold channel results in higher heat transfer as shown in figure 6.11. As shown in the figure, as the gap sizes of cold and hot channel of the heat exchanger increases, the heat transfer from the hot fluid to cold fluid drops. This is due to of reduced turbulence for the fluid in the heat exchanger due to bigger gap sizes. For all gap sizes, it can be shown from the figure that the flow changes from laminar to transitional flow with low mass flow rate and then changes to turbulent flow as the mass flow rate increases. The increase in mass flow rate helps in increasing the total heat transfer rate due to the rise in convective heat transfer coefficient. For this project, a mass flow rate of not more than 1 kg/s and gap size of not more than 20 mm were chosen for the final design. The mass flow rate was limited by the availability of DC pumps for high flow rates. Furthermore, the available materials to build the heat exchanger again limit the gap sizes needed for the TEG heat exchanger. Based on the analytical model, the maximum electrical power obtained from TEG heat exchanger was around 190 W when the flow rate was set at 6 kg/s with a gap size of 1 mm, where two percent thermal to electrical efficiency was considered. As the gap sizes increases, the power output drops as the heat transfer was reduced by due to lower turbulent mixing in a bigger gap.

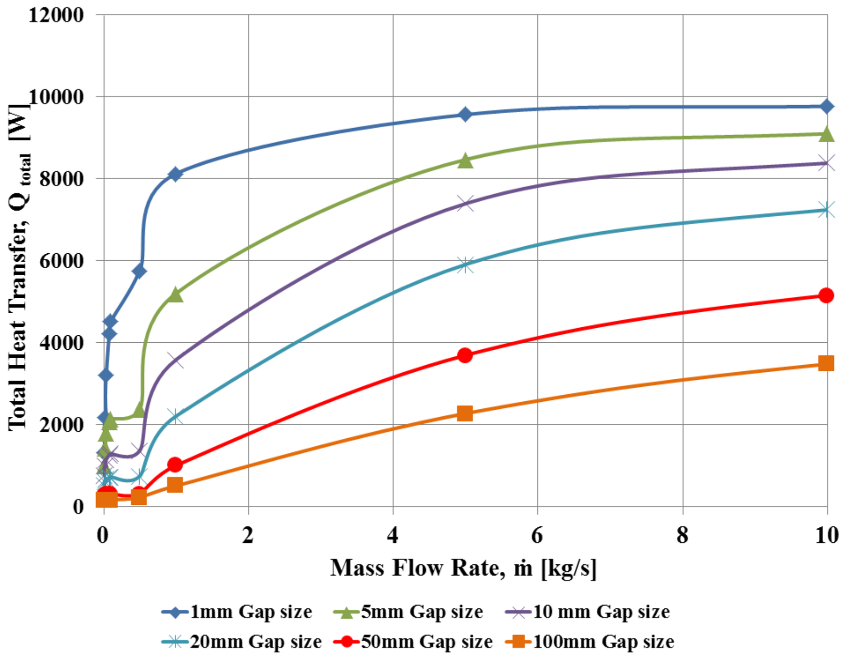

Figure 6.11 Total heat transfer rate versus the mass flow rates for different gap size

Figure 6.12 shows the theoretical analysis for total head loss versus mass flow rate for the TEG heat exchanger. As shown in the figure, the total head loss for the polygon TEG heat exchanger increases exponentially as the mass flow rate increases for 1 mm gap size. This is because of a strong boundary layer interaction between the flow and the inner surface of the heat exchanger. This results in higher friction for the flow rate in a small gap sizes. This is due to higher wall shear stress between the fluid and the walls of the heat exchanger at lower gap sizes. As the gap sizes increases, the total head losses in the heat exchanger reduce as the friction and viscous effect are reduced with a bigger gap sizes. This allows the fluid to flow between the inner surfaces of the heat exchanger with lower viscous effects. Also, the rough surfaces of the inner pipe increase the energy loss at a significant rate for lower gap sizes. The sudden jump in the rate of heat transfer beyond 0.4 to 0.8 kg/s of mass flow rate was due to flow regime change from laminar to turbulent. For a bigger gap sizes, the total head loss is lower than 10 m and further reduces to a lower value as the gap size increases. Similar trends were obtained for the total pressure loss and total pumping power versus mass flow rate, as shown in Figure 6.13 and 6.14. This shows that the optimum gap size for the heat exchanger is between 5 mm to 20 mm for reasonably lower head loss, pumping power and pressure loss.

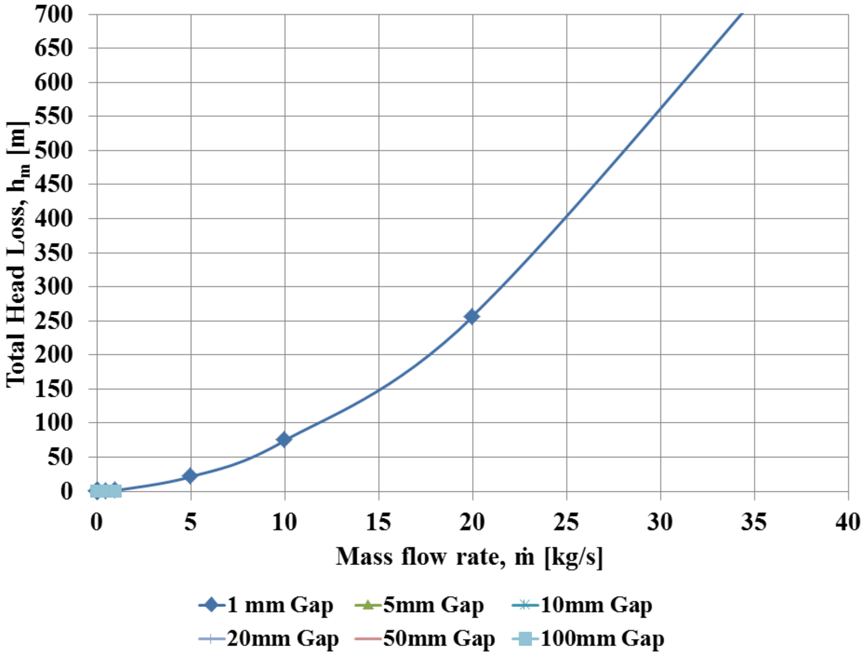

Figure 6.12 Total head loss versus mass flow rate for different gap Sizes

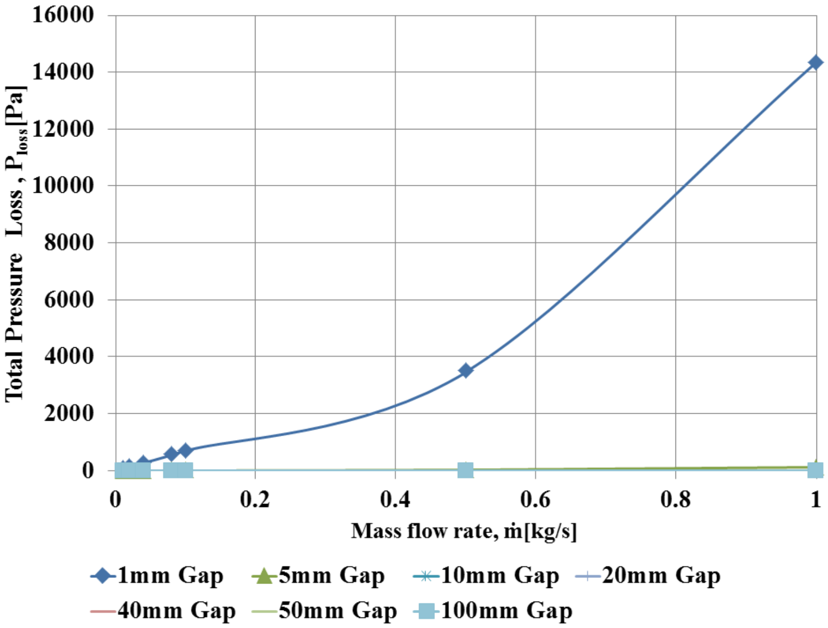

Figure 6.13 Total pressure loss versus mass flow rate for different gap sizes

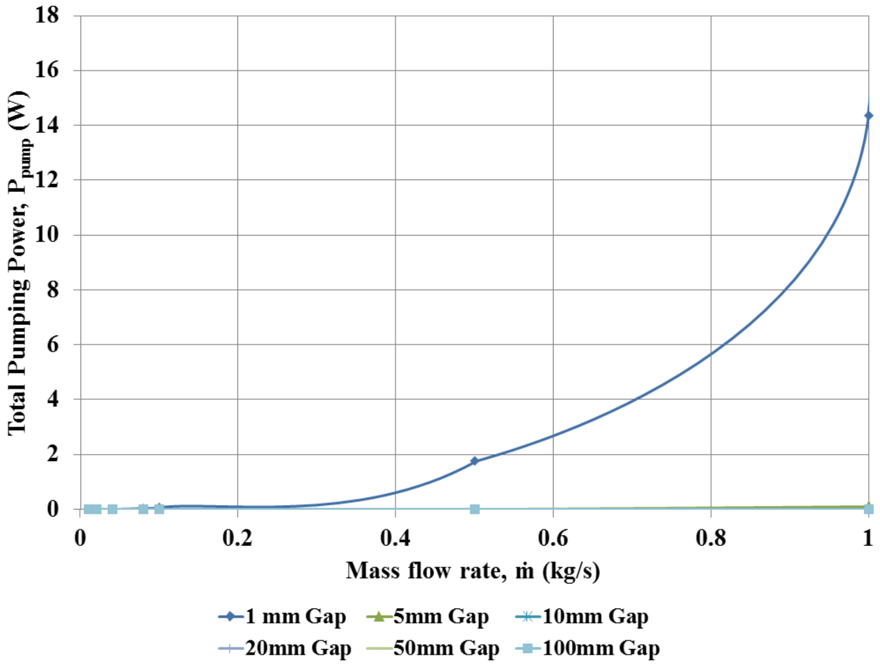

Figure 6.14 Total pumping power versus mass flow rate for different gap sizes

Figure 6.15 shows the theoretical results for net power generated by the TEG modules versus mass flow rate of the hot and cold water in the TEG heat exchanger. The theoretical analytical result was obtained by assuming pump efficiency of 50 %. Net power was obtained by subtracting the total pumping power required for the hot and cold water flow rate. As shown in the figure, the maximum net power obtained was at 160 W when the gap size was set at 10 mm with a mass flow rate of 8 kg/ s. The figure shows that all the graphs initially showed increase in the net power output to a maximum point and then it reduces as the mass flow rate increases. For a gap size of 1 mm, the friction caused by a small gap increases the pumping power exponentially as the mass flow rate increases. This result in more energy needed to pump the fluid in the heat exchanger. When the mass flow rate increases, the net energy reduces because the total pumping losses increases to a point where it is higher than the gross energy produced by the TEG modules. For a design of TEG heat exchanger, an optimum value for the gap size is needed to obtain a maximum possible output power with least head loss, pumping power losses and pressure losses. The mass flow rate needed to maintain the hot and cold water flowrate needs to be at an optimum level where the output power is optimum with minimum losses.

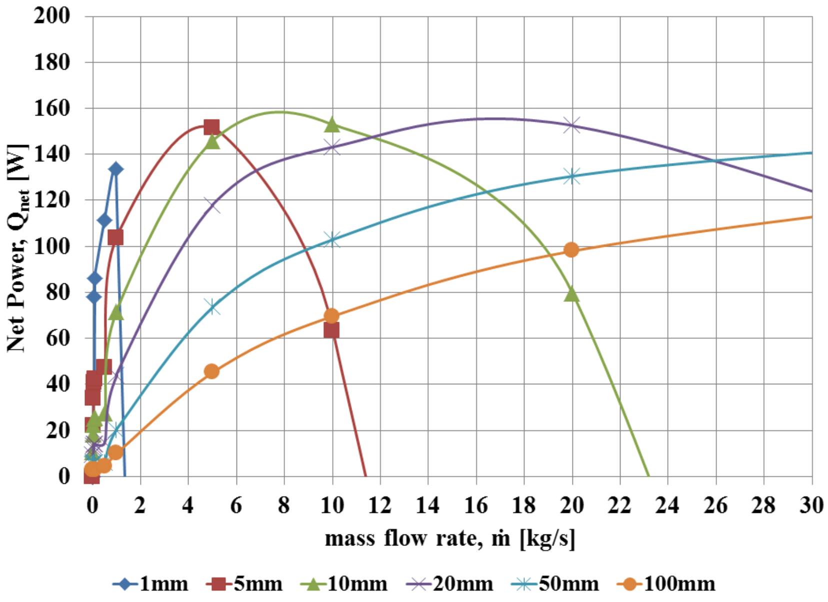

Figure 6.15 Net power versus mass flow rate for different gap sizes

Based on the theoretical analytical results, it was evident that a gap size of 3 mm to 20 mm results in lower head losses as well as lower pressure and pumping power losses. Mass flow rate of not more than 1 kg/s was chosen as this was limited by the available 12 V DC pump. The hot side gap size was set at 12.6 mm. This is because of the availability of stainless steel pipe and PVC pipe used to make the hot water channel from the market. This gap was then reduced to 3 mm by wrapping the inner PVC pipe with 9.5 mm thick Armaflex insulation to reduce the gap size. This allows us to perform the experiment for a lower gap size with higher heat transfer coefficient due to a lower gap size. The gap size for the cold water flow was set at 8 mm throughout the experiment.

Figure 6.16 shows the open circuit voltage for two gap sizes versus average temperature difference across TEG on the primary axis. As shown in the figure, the open circuit voltage increases linearly with increase in the hot water flow rate. Hot water flow rate at 40 ˚C to 80 ˚C with increments of 10 ˚C were used for the hot water flow rate. The cold water flow rate was measured at approximately around 19 ˚C to 20 ˚C based on the tap water source available at the laboratory. The maximum flow rate of the cold water was measured to be 0.3 kg/s and a 12V DC pump (Appendix G) used for the experiment provided a constant flow rate of 0.5 kg/s throughout the experiment. The TEG modules were connected in series in the length direction of the heat exchanger and then connected in parallel with other rows of TEG modules around the TEG heat exchanger. The maximum open circuit voltage was recorded at 28 ˚C with average temperature differences across TEG modules at 11 ˚C, with a gap size of 12.6 mm. The hot water and cold water inlet temperature was measured at 81 ºC and 20 ˚C, respectively. When the gap size was reduced to 3 mm for hot water flow rate, the open circuit voltage increased to 38.93 V with an average temperature difference across TEG modules at 18 ˚C. The hot water and cold water inlet temperature at 3mm gap size was measured at 81 ˚C and 20 ˚C, respectively. This shows that the reduced gap size helps to increase the power output from the TEG modules due to higher turbulence caused by a smaller gap size in the hot water channel. This results in higher heat transfer coefficient that results in higher heat transfer across the TEG that results in higher average temperature difference across TEG modules for the same hot and cold water temperatures.

Figure 6.16 also shows the efficiency of the TEG heat exchanger system on the secondary axis. The highest efficiency was recorded at 1.5 % for the 3 mm gap size construction while the efficiency of the TEG modules at 12.6 mm gap size was measured at 1.3 %. The reduction in the gap size increased the efficiency of the system by 12.6 % without any adverse effect on the flow conditions of the heat exchanger. This is advantageous as a slight modification can result in higher efficiency of the system will result in beneficial return in terms of cost of running the system over a period of time.

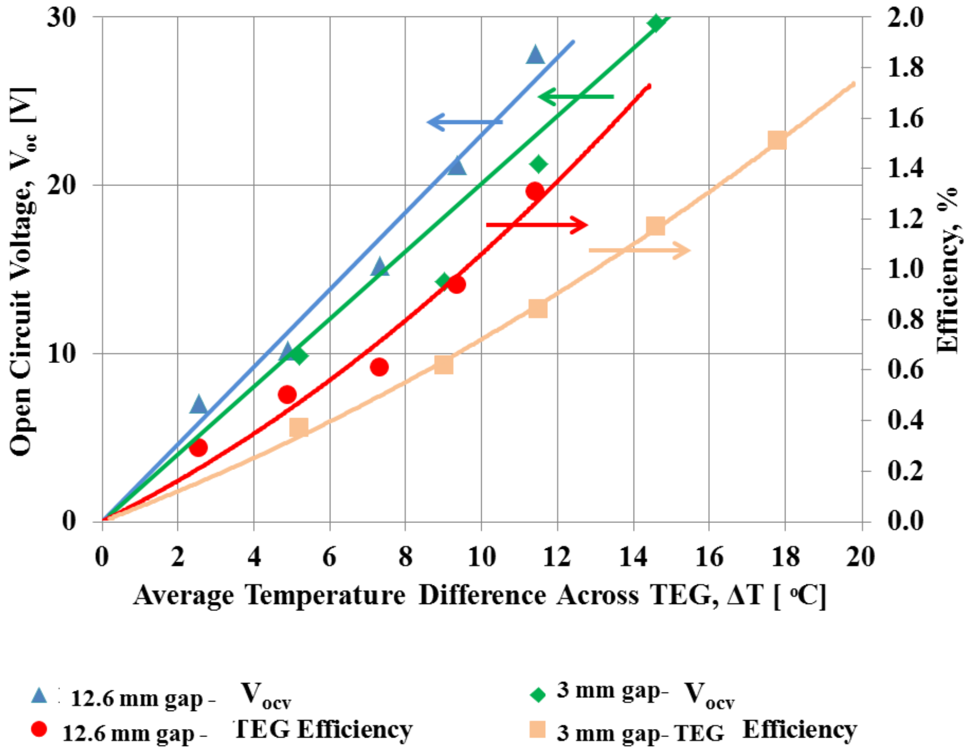

Figure 6.16 Open circuit voltage and TEG modules efficiencies versus average temperature differences across TEG modules

Figure 6.17 shows the maximum power output from the TEG modules versus average temperature differences across TEG modules. Both the experimental and theoretical results showed similar trends where the output power from the TEG modules increased with average temperature differences across TEG modules. This is because the higher temperature differences across the TEG modules results in higher output power. The maximum power output was obtained for the 3 mm gap size hot water channel for the heat exchanger at 78.9 W. The maximum power output for 12.6 mm gap size was measured at 48.1 W for the same hot and cold water conditions as the 3 mm gap size. The smaller gap size results in higher maximum power output due to higher heat transfer, as discussed above. The differences between the theoretical and experimental results were not more than 18 %. This discrepancy was caused by many factors, including the assumptions used in the theoretical model that underestimates the heat transfer coefficient of the heat exchanger. Besides that, the equations used for theoretical modelling approximates the flow and heat transfer conditions based on optimised constraints and approximation

.

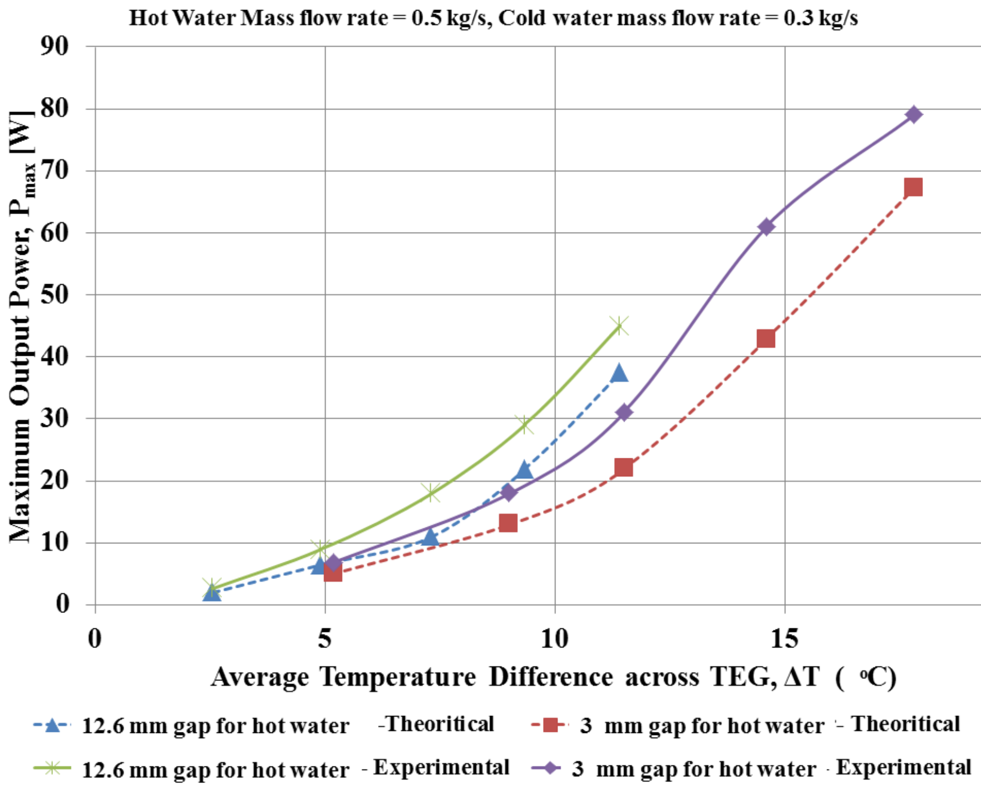

Figure 6.17 Maximum output power (Theoretical and Experimental) versus average temperature differences across TEG modules

6.4 In-pond TEG Heat Exchanger

6.4.1 Experimental Set Up

Figure 6.18 below shows the laboratory setup of TEG in-pond square channel heat exchanger. The top of the rig is fitted with a PVC connector to simulate the UCZ section of the solar pond. Tap water supply was used to supply the cooling water flowing through the gap. The PVC connector was always full by controlling the flow rate of the water into the system and the outflow from the system through siphoning action. A hose was used to siphon the water out of the PVC pipe. A valve was located at the end of this hose to control the flow rate from the siphon. Three thermocouples were located in the TEG heat exchanger. One thermocouple was located at the start of the section where the TEG was attached and another one at the bottom part of the inside of the square channel. The difference between the two temperatures will determine the amount of heat transfer into the channel. Another thermocouple was attached at the top of the PVC connector to measure the temperature of the incoming water. The same arrangement of set up was used for the TEG in-pond polygon (nonagon) heat exchanger. All rows of the TEG can be either connected in series or parallel for power generation. Maximum power was generated when the external load applied by the electronic load matches the load of the TEG connection. The hot water temperature in the tank that simulates the LCZ section of the solar pond was controlled by a thermostat. A temperature range for the hot water between 40 ˚C to 100 ˚C was used to test the system. Data from the thermocouples and the TEG were recorded on the computer using Agilent 349070A data logger unit. The maximum power output was determined by a digital rheostat (model: BK Precision 8540, 150W DC). Figure 6.19 below shows the schematics of the experimental setup used for the experimental analysis.

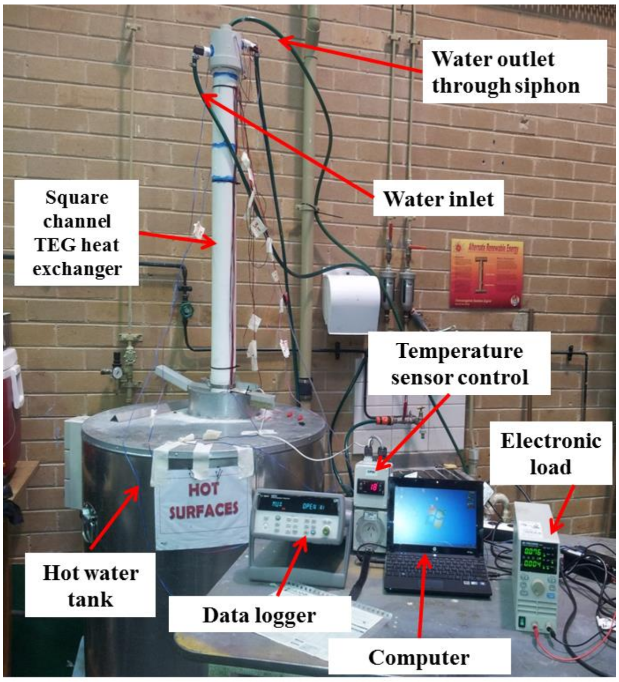

Figure 6.18 Laboratory setup of the TEG experimental rig.

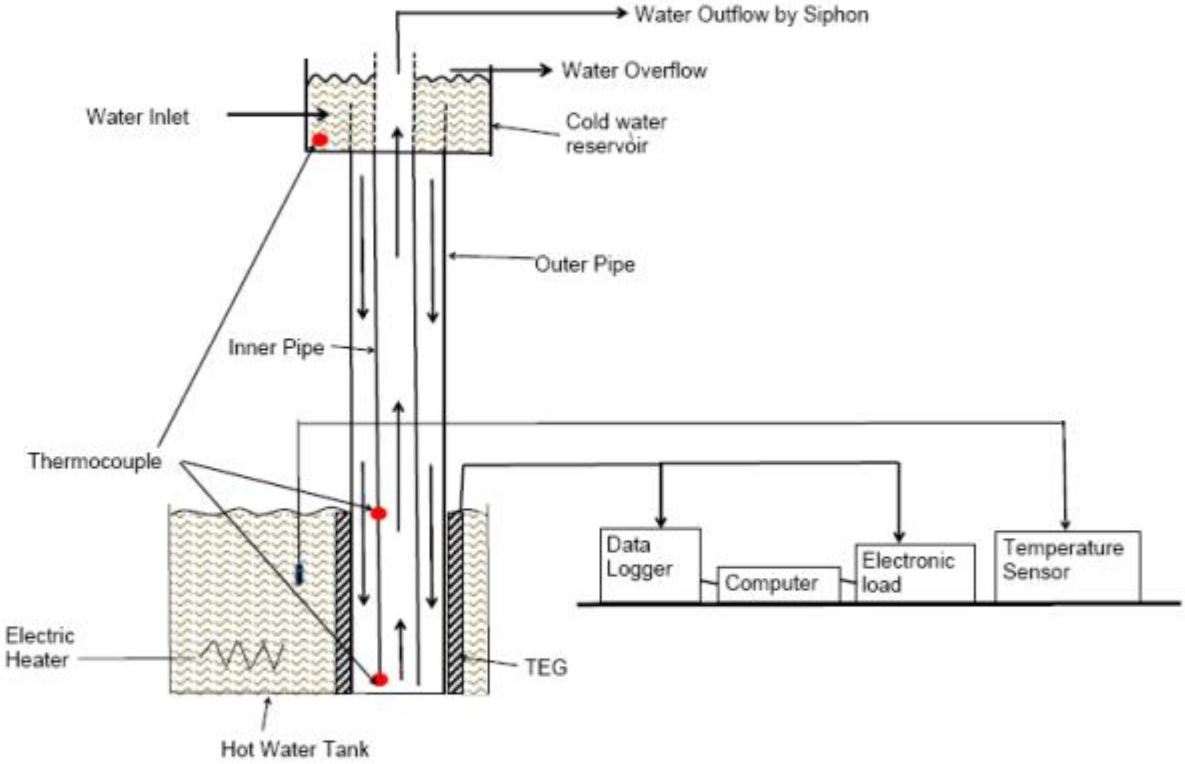

Figure 6.19 Schematics of the laboratory setup TEG in-pond experimental rig

6.4.2 Results and Discussions

Figure 6.20 shows the temperature profile of the cooling water in in-pond square channel heat exchanger from the top to bottom of the LCZ section. This section was chosen to be 600 mm to fit the LCZ section in the solar pond. As seen from the figure, the temperature cooling water in the gap at the top is lower than the temperature at the bottom of the LCZ section of the heat exchanger. This is because the heat transfers to the cooling water flow rate from the hot water outside the heat exchanger. This type of temperature profile results in a mismatch conditions for the TEG modules attached to the heat exchanger, if not connected properly. TEG modules attached to the heat exchanger can either be connected in series in column (vertical) or row (horizontal) direction. These connections were then connected in parallel for higher reliability for long term operation. If the TEG modules are arranged in series in the row (horizontal) direction, then the voltage output produced will result in mismatch that will affect the power generation from the TEG modules. There is a need to apply minimal voltage mismatch conditions to the individual TEG for optimum power output.

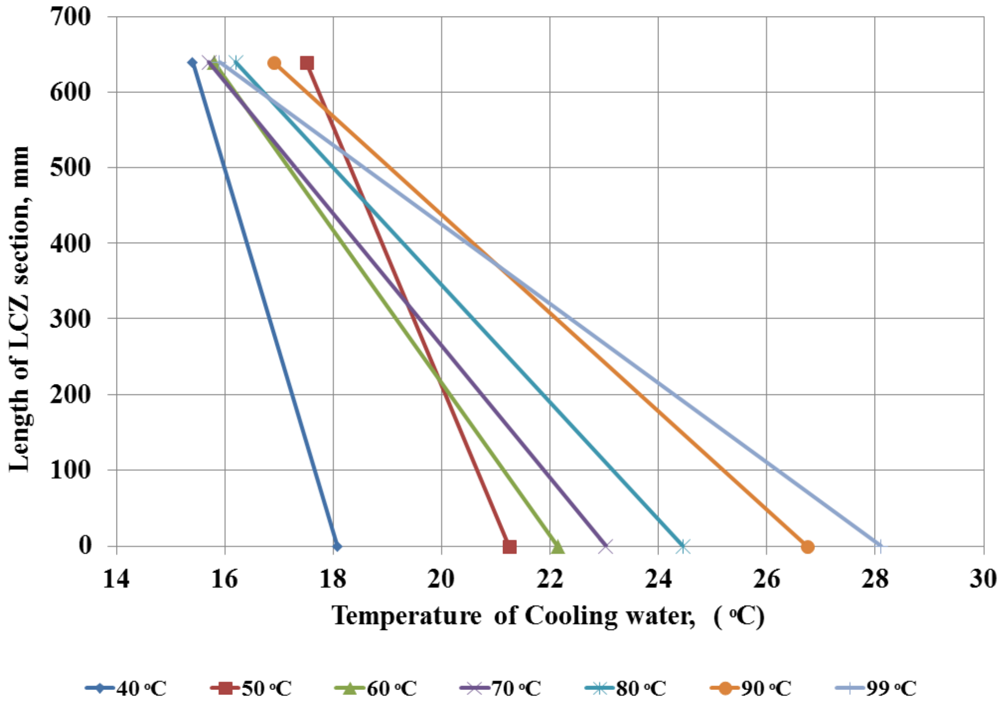

Figure 6.20 Temperature variations along the length of LCZ section for different temperatures

As shown in Figure 6.21, the figure shows the open circuit voltage of TEG modules connected in series in the column direction. For the square channel design, each column with fifteen TEGs each was connected in series, with four columns of sixty four TEGs. Results shown in Figure 6.21 shows that the voltage differences between the columns of TEGs were minimal with maximum differences of only 2.5 %. This was because the average temperature difference between the TEGs in the columns is constant. This result in almost constant voltage output from the TEG modules connected in series in the column direction. All four columns can then be connected either in series or parallel connection without compromising the output performance of the set up.

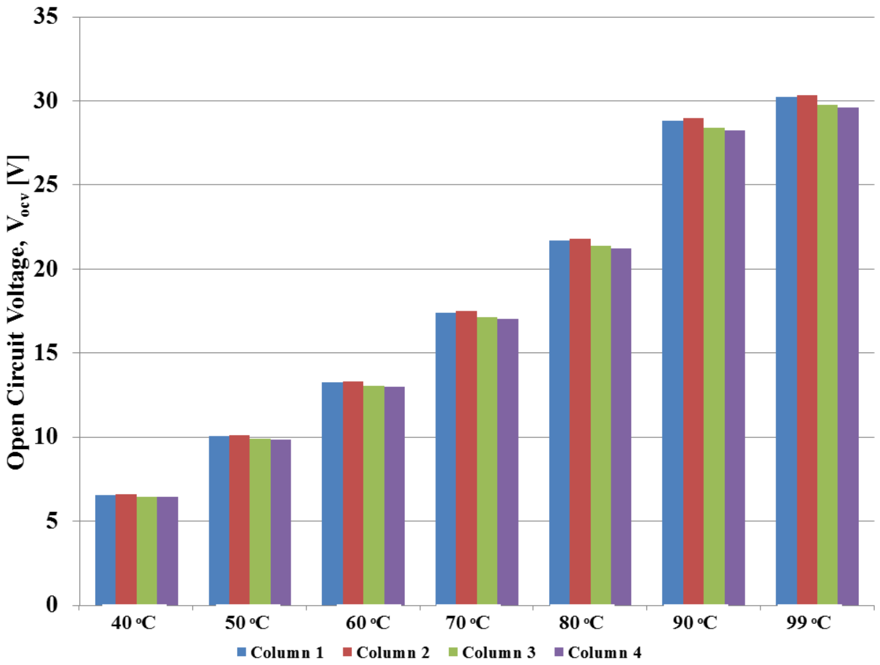

Figure 6.21 Open circuit voltage for TEG modules in columns connected in series

On the other hand, when the TEG modules were connected in series in row direction, the open circuit voltage was not constant for all the rows, as shown in Figure 6.22. Four TEGs were connected in series in rows for the square channel in-pond heat exchanger. This resulted in fifteen rows of four TEG modules connected in series. As seen from the temperature profile in Figure 6.20 earlier, the temperature differences in the LCZ section of the heat exchanger reduces as we travel down from the top to bottom of the LCZ section. The temperature on the outer side was constant and the cooling water was heated as it flows down the heat exchanger. This results in lower temperature difference at the bottom for the TEG modules. As a result of this, the voltage output reduced in accordance to the temperature drop in the system. This caused the voltage output from the TEG modules connected in rows drops with the drop in the temperature difference in the heat exchanger. The maximum difference between the voltage differences was recorded at 25.7 % for the first row at the top and the last row at the bottom. The voltage mismatch produced will be high and affect the performance of TEG modules for power generation when connected in parallel. Based on the results, it is better to connect the TEGs in column direction than in row direction to minimise the voltage mismatch problem. Alternatively, if the TEG modules needed to be connected in series in the row direction, there must be higher number of TEGs for the subsequent bottom rows to match the voltage of the upper rows. This results in a conical heat exchanger design as shown in Figure 6.23, which will increase the manufacturing cost and design complexity.

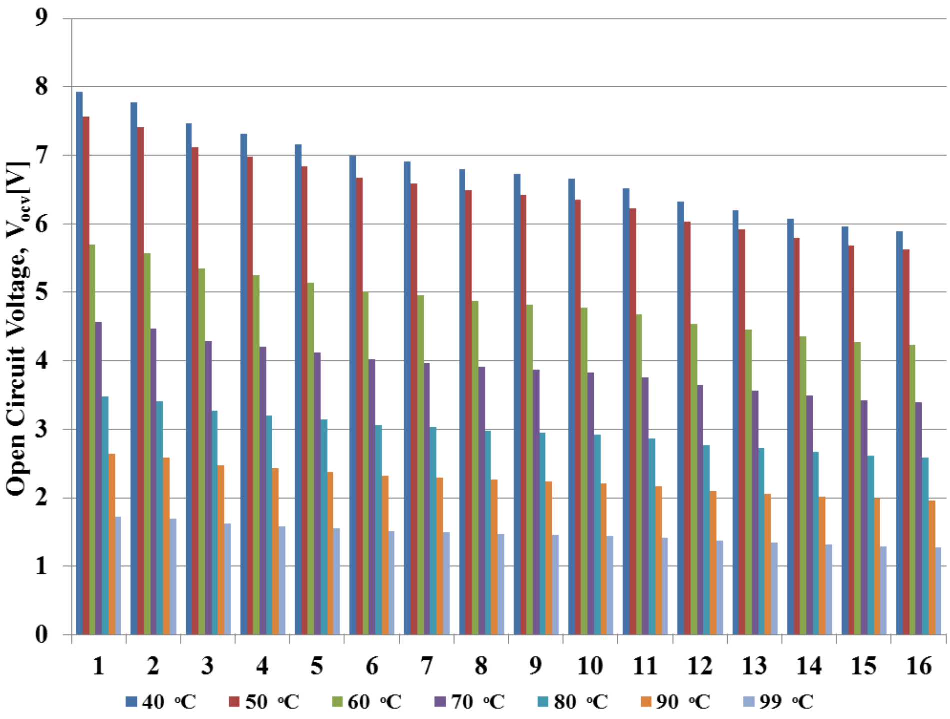

Figure 6.22 Open circuit voltage for TEG modules in rows connected in series

Figure 6.23 Conical heat exchanger

Figure 6.24 shows theoretical results obtained for TEG maximum power output versus cooling water flow rate for different gap sizes between the inner pipe and outer pipe of the in-pond heat exchanger. The outer diameter of the outer stainless steel pipe was set at 100 mm with a thickness of 2 mm. The gap was varied to obtain the maximum power output for 100 TEGs attached to the LCZ section of the TEG heat exchanger. The conversion of thermal to electrical efficiency was set at 2 %. From theoretical results obtained, it can be seen that the lower gap sizes produced higher maximum power output and increases with higher cooling water flow rate. After about 0.4 kg/s mass flow rate of cooling water, the output power from the TEG did not show any significant rise. For a gap size of 1mm, the maximum power output from TEG modules was obtained at 37 W and 32 W for 20 mm gap size. But at lower flow rate of cooling water at 0.2 kg/s, the difference for both the above gap sizes were at 76 %. This is because the flows in a bigger gap in the laminar region at lower than 0.2 kg/s has lower heat transfer coefficient. With gap sizes reducing, the viscosity effect increases the disturbance of water molecules in smaller gap sizes which improves heat transfer. This results in higher heat transfer across TEG module to produce higher power output with the same flow rate. This was due to the flow regime changes from laminar to turbulent beyond 0.4 kg/s. This shows that the limiting cooling water flow rate was around 0.4 kg/s for all gap sizes. But, lower gap sizes at 1 mm produces high friction coefficient which will limit the cooling water flow rate, as the flow rate of the cooling water was maintained by siphoning effect alone. The in-pond heat exchanger was designed with a gap size of between 3 mm to 5 mm gap to maximise power generation and minimise frictional losses in the heat exchanger.

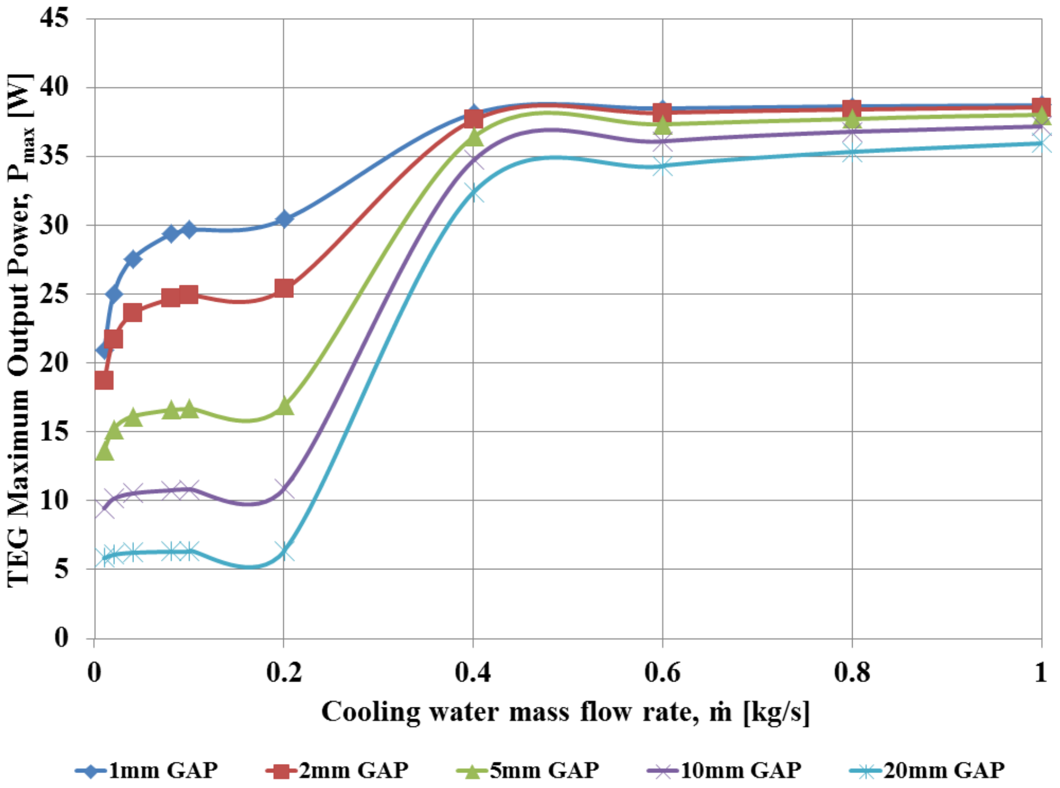

Figure 6.24 Theoretical results obtained for TEG maximum power output versus cooling water flow rate for different gap sizes between the inner pipe and outer pipe of the in-pond heat exchanger

Figure 6.25 shows TEG maximum power output versus average temperature difference across TEG modules. The results shows that the maximum power output for series connection were higher for both cooling water flow rate when compared to parallel connections. All four columns from the in-pond TEG were first connected in series and then in parallel. For cooling water flow rate of 0.16 kg/s and average temperature difference across TEG at 35 ˚C, the maximum power output from the series connection was recorded at 34 W. Parallel connections for the same condition above produced maximum power output at 29 W, which were 14 W lower than the output of series connections. Lower output from the parallel connections was expected due to the higher output current from the connections. For a reliable and long term applications of the TEG systems, it is advantageous to use a combination of parallel and series connection to meet the end application requirements. Parallel connections require lower resistance to operate and the operation of the parallel TEG system operates even with some damaged TEG modules when compared to TEG systems with series connections.

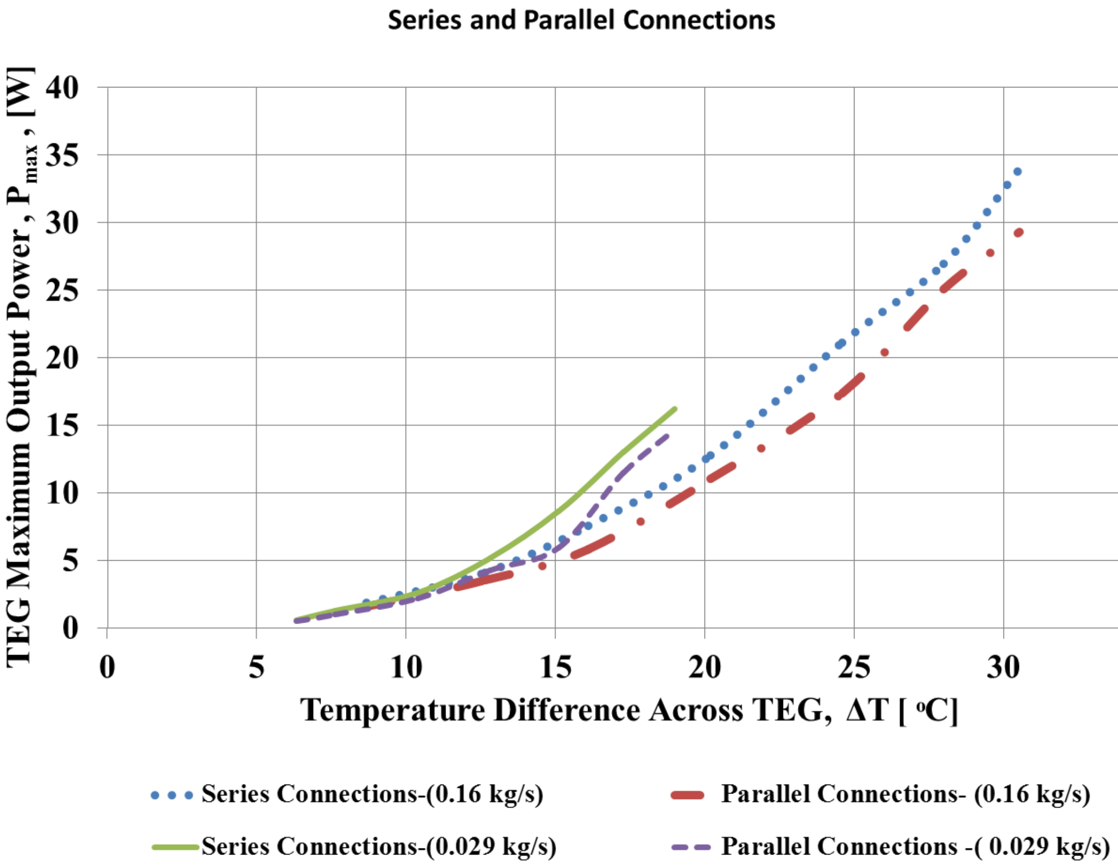

Figure 6.25 Experimental TEG maximum power output versus average temperature difference across TEG modules

Figure 6.26 shows the TEG maximum power output versus the average temperature differences across the TEG module at 0.16 kg/s and 0.029 kg/s cold water flow rate. The TEG modules for all the columns of the square channel heat exchanger were connected in series. The maximum output power increased with the increase in the hot water temperature and cold water flow rate as the temperature difference between the hot fluid and cold fluid increased, the amount of power generated also increased. The maximum power was obtained by varying the resistance from the electronic load connected to the experimental setup. Maximum power was obtained when the resistance of the electrical load applied matched the resistance of the TEGs connected in series used in the experimental setup. For a cooling water flow rate of 0.16 kg/s and a temperature difference across TEG of 9˚C, 13 ˚C, 16 ˚C, 20 ˚C, 25 ˚C, 38 ˚C and 31 ˚C, the maximum power obtained was 2 W, 4 W, 8 W, 13 W, 21 W, 26 W and 34 W respectively. All maximum output was recorded at external load resistance between 96 to 106 ohms, [Ω]. It can be seen from the figure that the maximum power output increases with the temperature difference across TEG. The maximum output power from the TEGs relates linearly to the temperature difference applied across them. Theoretical results for both cooling water flow rate showed similar trends with a maximum differences of not more than 16.4 %. Higher flow rate of the cold water allows the TEG to generate higher output power. This is because the increase in the flow rate increases the heat transfer across the TEGs. For the solar pond power generation application, the required temperature differences for the TEGs lie around 20 – 60 °C. The high temperature at LCZ and low temperature at UCZ in the solar pond can be used to power the TEGs. From the same figure, it is shown that the power generation solar pond using TEGs can be achieved not only during summer but also in the winter when the temperature of the pond drops according to the ambient temperature. The minimum temperature difference between the LCZ and UCZ in the winter season is around 24 °C.

From the experiment conducted, the TEGs will not only be able to generate electricity in summer, where the temperature difference is highest, but also during winter when the difference of temperature recorded temperature is lowest. This provides an added advantage for power generation from solar pond using TEGs compared to ORC engines, as the latter will not be able to operate using the low temperature heat from solar pond during winter. The maximum efficiency for the thermal energy to electrical energy was observed at 1.4 % and 1.2 % for 0.2 kg/s and 0.03 kg/s cold water flow rate, respectively.

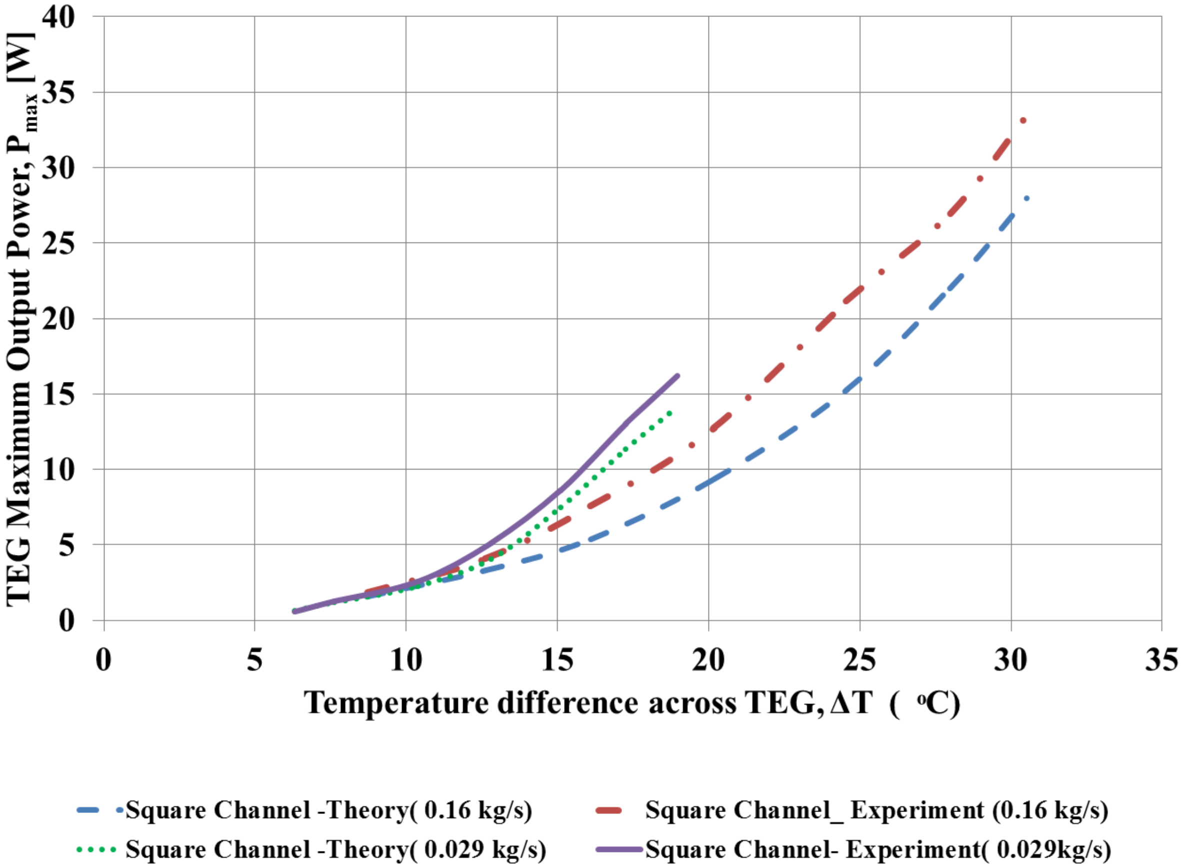

Figure 6.26 TEG maximum power output versus the average temperature differences across the TEG module at 0.16 kg/s and 0.029 kg/s cold water flow rate

Figure 6.27 shows the plot for maximum power output versus average temperature difference across TEG for polygon (nonagon) in-pond heat exchanger. From the plot, we can see that the maximum power output increases with the temperature difference across TEG. The maximum output power from the TEGs relates linearly to the temperature difference applied across them. Higher flow rate of the cold water allows the TEG to generate higher output power. This was because the increase in the flow rate increases the heat transfer across the TEGs. The maximum efficiency for the thermal energy to electrical energy was observed at 1.5 % and 1.2 % for 0.28 kg/s and 0.16 kg/s cold water flow rate, respectively

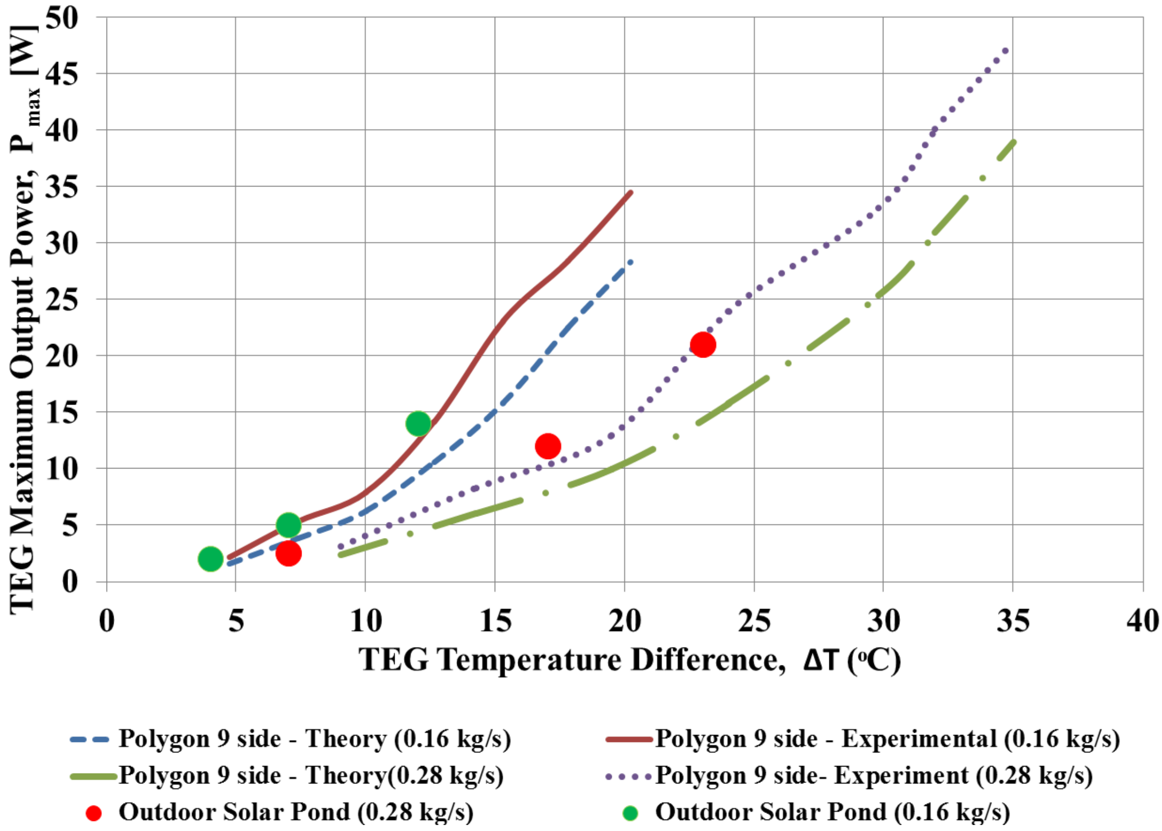

Figure 6.27 Maximum power output versus average temperature difference across TEG for polygon (nonagon) in-pond heat exchanger

Figure 6.27 also shows the result for the experiment done outdoor in a solar pond, as shown by the red and green dots. Three data were obtained for February, March, and July 2014. The average LCZ temperatures for those months were 72 ˚C in February, 54˚C in March and 26 ˚C in July. The results matches with the laboratory experimental results, as shown in figure 6.27. For lower temperatures of the LCZ section in July, the TEG was able to generate electrical power even with low temperature diffrences. With suitable scalability for TEG modules, the power output can be increased to meet the desired application needs even in winter months with LCZ temperatures in the lower 30˚C. Figure 6.28 shows the experimental setup used for solar pond outdoor power generation using polygon TEG heat exchanger. Figure 6.29 shows the 12V LED bulb and LED display powered by in-pond polygon TEG heat exchanger that proves that low grade heat can be converted into electricity using TEGs. Total of 9 W of electricity was generated by 5 rows of TEGs from the heat exchanger to light the LED bulb and display.

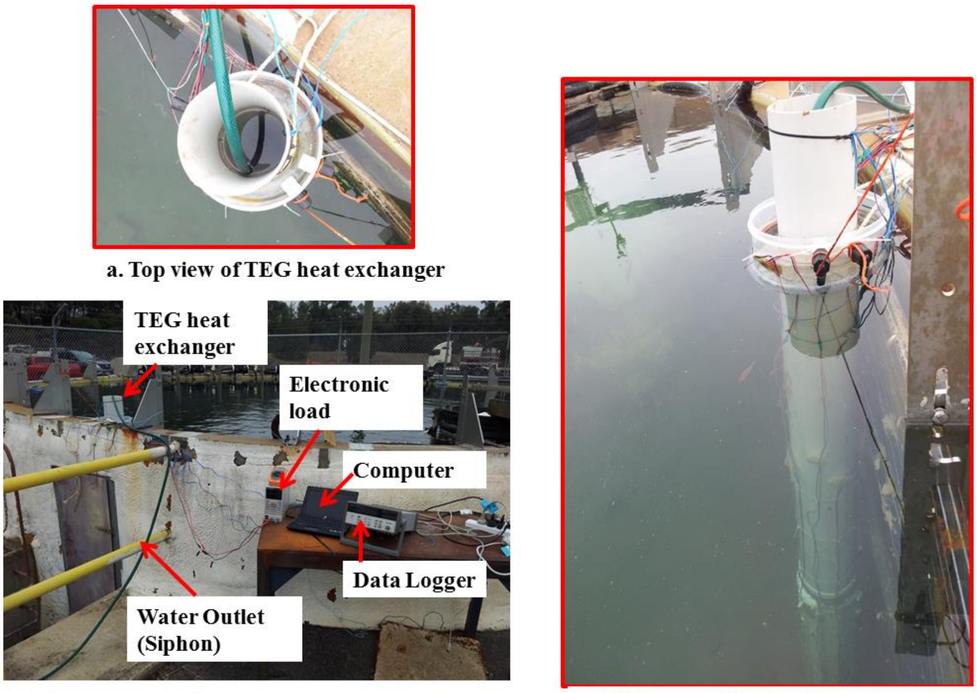

a. Top view of TEG heat exchanger

b. Experimental set up

c. TEG in-pond heat exchanger

Figure 6.28 Outdoor solar pond in-pond polygon TEG heat exchanger set up

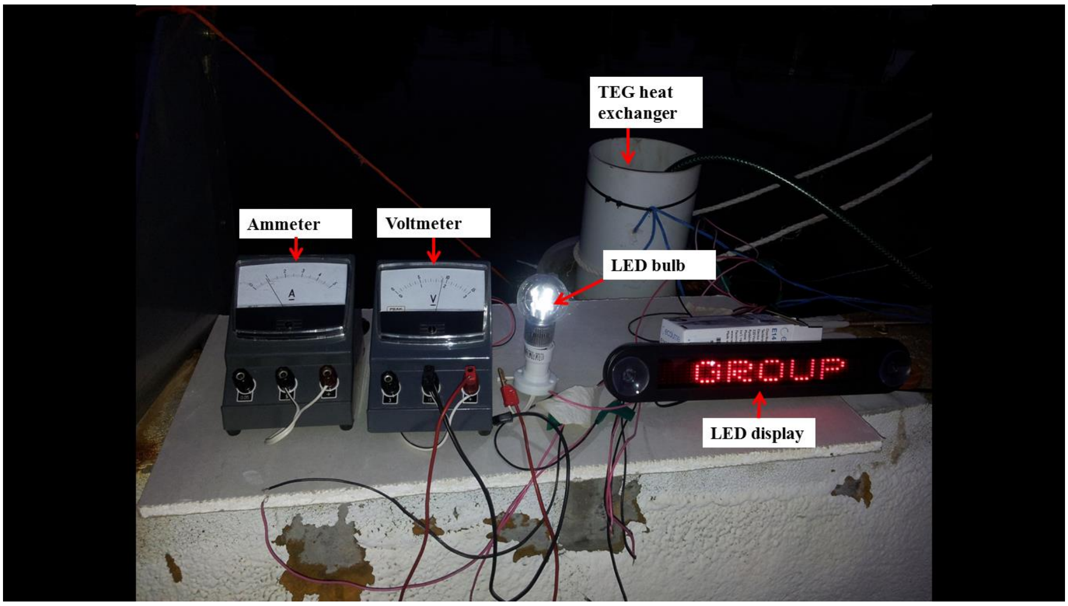

Figure 6.29 Electrical power generation from solar pond using polygon TEG heat exchanger

6.5 Chapter Conclusions

Three different types of TEG heat exchangers were tested in the laboratory with low grade heat of less than 100 ºC. All TEG heat exchangers showed good potential in terms of power generation from solar pond using low grade heat. These heat exchangers can either be used passively or by having active cooling and heating mechanisms. Actual testing of the In-pond TEG heat exchanger showed that the thermal energy from low grade heat can be converted to electricity. Although the efficiency of the heat exchangers were lower than 2 %, but availability of abundant free solar energy and stable and cheap thermal storage system in solar pond makes TEG technology a better alternative to ORC engines. The long term operations and relatively low maintenance system for the TEG system makes this technology a good candidate to replace ORC engines for power generation from solar pond using low grade heat.

7.0 Conclusion and Recommendations

7.1 Conclusions

The proposed TEG heat exchanger with various designs was studied in this research work. The main aim of the research was to generate electricity from a low grade heat source. TEG modules were found to be effective in converting the low grade heat from solar pond into electricity. TEG modules are resilient and robust operating in a corrosive salty environment.

As an integral thermal collector and storage system, solar pond proves to be a low cost and simple technology. The available thermal energy in the storage zone varies with the change in season. The temperature at the storage zone is found to be stable due to the large thermal mass of water of storage zone. With regular maintenance of the solar pond in terms of salt replenishment and clarity of water, the performance of solar pond as a thermal collector can be operated at its optimum level. TEG modules are able to work with the temperature differences available in the solar pond between the storage zone and UCZ. The minimum and maximum average monthly temperatures differences between LCZ and UCZ zone available in the RMIT solar pond in winter and summer are 16˚C and 47˚C, respectively.

Even with low temperature differences between the storage zone and UCZ in winter months, TEG modules are able to generate electricity. This would have been impossible with the conventional ORC engines due to the requirements of certain threshold temperature for the organic fluid evaporation. Alternatively, during low solar insolation period in winters, solar collectors can be utilised to provide heat for the storage zone in a solar pond. Augmentation of solar evacuated tube collectors with solar pond allows for thermal heat gain of the storage zone during low solar insolation. The contribution of the heat addition system in adding heat to the pond was found to be 31 %. A new automatic surface washing control system also reduces the fresh water consumption. The proposed control system is relatively simple and does not need any monitoring by human. Besides that, the control system was able to control the water flow automatically based on the conditions of water level and salinity.

TEG modules can operate with the available low grade heat from solar pond at temperature differences between the hot and cold side ranging from 10˚ C to 50˚C. This range of temperature differences is readily available in a solar pond. Even at low temperature differences, TEG was able to generate power. When compared to other vapour compression heat engines, TEG module works well even with low temperature differences. This makes TEG module one of the best technology that can generate electricity from very low temperature differences. Bismuth Telluride (Bi_2Te_3) TEG modules are found to be competitive for low temperature and low cost applications.

TEG modules can be scaled up into any required numbers to fulfil the desired output required by the end applications. A number of TEG modules can be connected in series and parallel for providing the required output power. Both arrays offer its own advantages and disadvantages. But, for reliability, TEG modules are best arranged in a combination of series and parallel arrangements. The experiments also proved that the TEG can be operated without any mechanical fixtures. Thermal adhesive can be used to attach the TEG to heat exchanger for power generation. The use of thermal adhesive is highly advantageous compared to mechanical fixtures for operation in highly corrosive environment of solar pond. This will help to reduce the complexity of the heat exchanger design. A maximum of 80 W of electrical energy was obtained from polygon TEG heat exchanger with conversion efficiency of 1.51 %.

The design of a TEG heat exchanger affects the rate of heat transfer. Theoretical modelling developed showed that the gap sizes for the hot and cold water flow rate can result in significant change in heat transfer rate of a TEG heat exchanger. From the theoretical results, it was found that the smallest gap sizes results in higher heat transfer. But, at the same time, the smaller gap sizes cause very high pumping power and head losses. This was due to very high turbulent shear stress with high friction caused by the small gap sizes. This was further aggravated by high mass flow rates. To overcome the problem, an optimum gap size was chosen with a compromise to lower heat transfer and reasonable pumping power and head losses. This led to TEG heat exchanger designs with passive and active hot and cold water flow. A gap size between 3 mm to 12 mm was chosen for the designs based on the available materials to construct the TEG heat exchanger.

TEG modules attached to the heat exchangers needs to be connected in a combination of series and parallel connections. For in-pond designs with constant hot side temperature, the cooling water flow rate causes uneven temperature distribution in the vertical direction from top to bottom. This results in voltage mismatch for the output from the TEG modules. It is best to connect TEG modules in series in the same direction (column) of the vertical temperature distribution to provide significantly lower mismatch in terms of the output from the modules. This will improve the performance of the TEG heat exchanger when the columns of the modules are connected in parallel. It was found that the mismatch for the output can be as high as 25 % if not connected properly. With uneven temperature distribution of and incorrect connections of TEG modules will result in reverse currents flowing back into the TEG modules. This will make the modules to work as a load and it must be avoided.

With several TEG heat exchangers tested for power generation from solar pond, it was found that the low grade heat from solar pond converted into electrical energy was successfully demonstrated through this research. Both passive and active fluid flow designs are simple and reliable for long term power generation from solar pond. This new method can revolutionise the power generation from solar pond using TEG as a sustainable and clean renewable energy applications and replace fossil fuel power generation in the future.

7.2 Recommendations

With positive outcome from the results obtained through this work, there is a need still a lot of improvement that needs to be carried out for the designs of the TEG heat exchangers as well as operation of the solar pond as a source of low grade heat. Further work needs to be done in this area to explore a wide scale application of the outcome of the research.

Augmentation of solar collectors with solar pond proves to be a good application to store thermal energy in winter months. This will enable the solar pond to operate at a higher storage temperature in winter conditions. Furthermore, this method can also be used to boost the temperature in summer months to a maximum temperature close to 100˚C. This will enhance the performance of the solar pond and provide a better efficiency for thermal to electrical conversion at high temperatures. Automation for obtaining density and temperature profiles, as well as surface washing need to be explored on a larger scale to make solar pond a truly simple and cost effective technology.

The geometrical designs of the TEG heat exchanger need to be studied further. This will enable for a more compact and high power density design for power generation application from low grade heat of solar pond. Various designs used in this experiment can be used as benchmarks for better and more effective designs with higher output. Possibility of a micro grid connected system needs to be explored to prove the viability of TEG power generation for future applications. This will encourage the development of low grade heat transformation from not just solar pond, but from other abundant resources of low grade heat currently wasted into atmosphere.

Maximum power point tracker (MPPT) allows for optimum operation TEG modules. MPPT should be explored to be integrated with the overall designs of the TEG heat exchanger system. This will allow for an autonomous operation of the TEG modules at maximum power output, similar to PV systems. MPPT integrated with TEG modules allows the system to operate at higher efficiency and performance. This will result in a more stable output and induce more widespread interest for this technology for low grade heat applications. Low cost electronics with simple software programming can result in an efficient and low cost MPPT system for TEG power generation.

Various other heat exchanger designs with better heat transfer capability at low temperatures need to be investigated for future applications. Methods to improve the heat transfer coefficients with improved designs and surface treatment will result in better performance in terms of the output from TEG heat exchanger. New designs of heat exchanger that can withstand corrosive environment of solar pond and with high effectiveness will result in higher performance of the overall system.

Application of thermo siphon flow can be used to design a passive TEG heat exchanger. By utilising the difference in buoyancy of water at different temperatures, the cooling water flow can be induced by this difference in the buoyancy of water for in-pond heat exchanger. With a large thermal mass of solar pond, the cooling of water from the heat exchanger by the UCZ will not affect the performance of solar pond. But it will ensure a fully passive design for the in-pond TEG heat exchanger design.

Thermal resistance across TEG modules reduces the temperature difference required for the output power from the module. This will reduce the performance of the TEG modules. Thermal adhesives available in the market allows for attachment of the modules without any mechanical fixtures, but the added cost due to the thermal adhesive for a large scale application can be of concern. New adhesive or techniques need to be explored so that TEG modules can be attached with a minimum fuss for an overall low cost design of the TEG heat exchanger.

A computer model based on the commercial software in the market can be utilised for a better understanding of the flow and heat transfer in a TEG heat exchanger. Computational Fluid Dynamics (CFD) software can be used for a more vigorous and detailed design to optimise the performance and output of the TEG heat exchanger. This will enable a researcher to compute various design criteria of a heat exchanger designs and obtain the result and visualise the shortcomings, so that a better and improved design can be obtained at initial stage before embarking on fabrication and application. With the advance of CFD software, the implementation of a design problem using computational methods reduces the time and also enables one to simulate real conditions using a computer programme. It also helps in better and a faster design.

REFERENCES

Aggarwal, R.K. and Markanda, S. (2012). “A review on thermocouple for power generation.” Int. Journal of Applied Sciences and Engineering Research 1: 98-105.

Ahn, J., Shao, Z., Ronney, P.D., and Haile, S.M. (2007). "A thermally self-sustaining miniature solid oxide fuel cell." The 5th International Fuel Cell Science, Engineering & Technology Conference (Fuel Cell 2007), 250832.

Akabarzadeh, A., J. Andrews and P. Golding (2005). “Integration of solar ponds in salinity mitigation schemes to produce low grade heat for industrial process heating, desalination and power.” Solar World Congress Bringing Water to the World, Orlando, Florida.

Akbarzadeh, A., J. Andrews and P. Golding (2005). “Solar Pond Technologies: A Review and Future Directions.” Advance in Solar Energy. 16: 233-294.

Akbarzadeh, A., J. Andrews and P. Golding (2005). “Solar Pond Technologies: A review and Future Directions. Advances in Solar Energy.” London, UK, Earthscan. 16: 233–294

Akbarzadeh, A., P. Johnson and R. Singh (2009). "Examining potential benefits of combining a chimney with a salinity gradient solar pond for production of power in salt affected areas." Solar Energy 83(8): 1345-1359.

Al Jammal, K. and Kasshan, S. (1996). "Effect of energy extraction on solar pond performance." Energy Conversion and Management 39: 559-566.

Alagao, F. B., A. Akbarzadeh and P. W. Johnson (1994). "The design, construction, and initial operation of a closed-cycle, salt-gradient solar pond." Solar Energy 53(4): 343-351.

Alagao, F. B., Akbarzadeh, A and Johnson, P.W. (1994). "The design, construction, and initial operation of a closed-cycle, salt-gradient solar pond." Solar Energy 53(4): 343-351.

Bass, J. C., Elsner, N. B. and Leavitt, F. A (1994). "Performance of the 1kW thermoelectric generator for diesel engines." Proceedings of the 13th International Conference on Thermoelectrics: 295-298.

Boegli, W.J., Dahl, M.M., and Remmers, H.E. (1982). " Preliminary study of solar pond for stability control in the Colorado River Basin." Bureau of Reclamation Report No. REC-ERC-82-19.

Böer, K.W (2005). " The Fifty Years History of ISES and Its National Sections." vol. 1, ch. 17. Boulder, American Solar Energy Society, Inc.

Bojić, M., Savanović, G., Trifunović, N., Radović, L and Šaljić, D (1997). "Thermoelectric cooling of a train carriage by using a coldness-recovery device." Energy 22: 493-500.

"Bose, B.K., (2013). "Global Energy Scenario and Impact of Power Electronics in 21st Century." IEEE Transactions on Industrial Electronics, 60 (7) : 2638-2651.

Boukai, A.I., Bunimovich, Y., Tahir-Kheli, J., Yu, J.K., GoddardIii, W.A. and Heath, J.R. (2008). "Silicon nanowires as efficient thermoelectric materials." Nature 451:168-171.

Bronicki, L.Y. (1986) " Method of an appartusfor treating the water in a solar power plant." U.S Patent No. 4571947.

Butti, K., Perlin, J (1977). " Solar heaters in California, 1890–1930." Coevolution Quarterly Issue 15: 4–13.

Chavez, E.A., Vorobiev, Y.V., Bulat, L.P (2012). " Slar hybrid systems with thermoelectric generators." Solar Energy 86: 369-378.

Cohen, Y. (1981) " Method and means of reducing turbidity in a standing body of brackish water." Australian Patent No. 76320/81.

Coleman, H.W. and Steele Jr, W.G. (1989). " Experimentation and uncertainty analysis for engineers." Wiley New York.

Collins, R.B (1983). "Alice Spring solar pond project." Proc. Int. Sol. Energy Soc. Perth 102: 281.

Collin, R.B (1985). "The advanced Alice Spring solar pond." Proc. Int. Sol. Energy Soc. Montreal:1479.

Dai, Y.J., Wang, R.Z., Ni, L (2003). "Experimental investigation on a thermoelectric refrigerator driven by solar cells." Renewable Energy 28: 949-959.

Date, A., Yaakob, Y., Date, A, Krishnapillai, S. and Akbarzadeh, A. (2013). " Heat extraction from non-convective and lower convective zones of the solar pond: A transient study." Solar Energy 97: 517-528

Dickinson, W.C., Cheremisinoff, P.N (1980). " Solar Energy Technology Book, Part A: Engineering Fundamentals." Butterworths, New York: Marcel Dekker, Inc.

"Ellabban, O., Haitham. A.B., Blaabjerg, F (2014). ""Renewable energy resources: Current status, future prospects and their enabling technology."" Renewable and Sustainable Energy Reviews 39: 748-764.

Elwell, D.L., Short, T.H., and Badger, P.C (1977). " Stability criteria for solar (thermal-saline) ponds. Proc. Am. Sec. Int. Sol. Energy Soc: 391.

Ewert, M.K. (1998) "Terrestrial anda erospace solar heat pump development : past, present and future." International Solar Energy Conference Albuquerque,NM (USA): ASME Solar Engineering: 375–82.

Federici, J.A., Norton, D.G., Gruggemann, T., Voit, K.W., Wetzel, E.D., Vlachos, D.G (2006). " Catalytic microcombustor with integrated thermolectric elements for portable power production." Journal of Power Sources 161: 1469-1478.

Felix, E.A. and Rushworth, S.R. (1979). "The algal flora of the Great Salt Lake, Utah." Nova Hedviga 31.

Fiorenza, G., Sharma,V.K., Braccio, G (2006). "Techno-Economic Evaluation of salt gradient solar pond: A potential energy source for seawater desalination and power generation." International Energy Journal 7

Fynn, R.P., Short, T.H., and Shah, S.A., "The practical opeartion and maintenance of a solar pond for green house heating." Proc. Int. Sol. Energy Soc: 531.

Gasulla, N., Y. Yaakob, J. Leblanc, A. Akbarzadeh and J. L. Cortina (2011). "Brine clarity maintenance in salinity-gradient solar ponds." Solar Energy 85(11): 2894-2902.

Geddes, M.C. (1981) "The brine shrimp Artemia and Paratemia." Hydrobiologica 81.

Ghosh, A (2012). "Thermoelectricity: Source of Sustainability." online document viewed 23rd December 2013. <URL:www. themichigantimes.com/article/2013/12/thermoelectricity source-of-sustainability>.

Glosch, H (1999). "A thermoelectric convereter for energy supply, sensors and actuators." A. Physical 43:246-250.

Golding, H.P. and Swift, A (1991). Method for monitoring stability within a Salinity Gradient Solar Pond. Solar Engineering 1991. Reno, NV, USA, ASME, Solar Energy Div; Japan Solar Energy Soc; JSME: 75-82.

Goldsmid, H.J., Giutronich, J.E and Kaila, M.M (1980). “ Solar thermoelectric generation using Bismuth Telluride alloys.” Solar Energy 24: 435-440.

Goswami, Y.D., Kreith, F. and Kereider, J.F (1999). " Principles of Solar Engineering." Philadelphia, PA: Taylor & Francis.

Grossman, G (1999). "Israeli section of the International Solar Energy society." ISES Solar World Congress, 1st Edition ISBN-9780080951782.

Hara, T., Azuma, H., Shimizu, H., Obora, H. and Sato, S (1998). " Cooling performance of solar cell driven, thermoelectriccooling prototype headgear." Appl. Therm. Eng. 18:1159–1169.

Haruyama, T (2001). "Performance of Peltier elements as cryogenic heat flux sensor at tempearture down to 60 K." Cryogenics 41:335-339.

He, W., Su, Y., Wang, Y.Q., Riffat, S.B.and Ji, J (2012). "A study on incorporation of thermoelectric modules with evacuated-tube heat-pipe solar collectors." Renew. Energy.37:142–149.

Heremans, J.P., Jovovic, V., Toberer, E.S., Saramat, A., Kurosaki, K. and Charoenphakdee, A. (2008). " .Enhancement of thermoelectric efficiency in PbTe by distortion of the electronic density of states." Science 321:554–547.

Hsu, C.T., Huang, G.Y., Chu, H.S., Yu, B., and Yao, D.J. (2011). "Experiments and simulations on low-temperature waste heat harvesting system by thermoelectric power generators." Applied Energy 88: 1291-1297.

Hsu, K.F., Loo, S., Guo, F., Chen, W., Dyck, J.S. and Uher, C (2004). "Cubic AgPb SbTe2 : Bulk thermoelectric materials with high figure of merit." Science 303: 818-821.

http://www.kelk.co.jp/english/useful/netsuden3.html

Hull, J. R. (1989). Maintainance of brine tranparency in salinity gradient solar ponds. 11th Annual Solar Energy Conference. San Diego, CA, ASME Solar Energy Division.

Hull, J.R. (1980). "Computer simulation of solar pond thermal behaviour." Solar Energy 25.

Hull, J.R. and Mehta, J.M. (1987). " Physical model of gradient zone erosion in thermohaline systems." Int. J. Heat and Mass Transfer 30.

Hull, J.R., Nilesen, C.E. and Golding, P (1989). "Salinity gardient solar ponds." CRC Press Inc

Hull, J.R., Scranton, A.B. and Kasza, K.E (1985). "Solar pond heat removal using submerged heat exchanger." Proc. Int. Sol. Energy Soc: 1505.

Hull, J.R., Scranton, A.B., Mehta, J.M., Cho, S.H. and Kasza, K.E (1986). " Heat extraction from the ANL Research Salt Gradient solar pond." Report no. ANL-86-17, Argonne National Laboratory, Argone, Illinois.

Incropera, F.P., Dewitt, D.P., Bergman, T.L. and Lavine, A.S (2006). “Fundamentals of Heat and Mass Transfer.” 6^{th} Edition, John Wiley and Sons, New York.

Jaefarzadeh, M.R. (2005). "Thermal behaviour of a large salinity-gradient solar pond in the city of Mashhad." Iranian Journal of Science & Technology, Transaction B, Engineering 29:219-229.

Jo, S. , Kim, M., Kim, M., Kim, H. and Kim, Y (2012). " Human body heat energy harvesting using flexible thermoelectric generator for autonomous microsystems." 16th International Conference on Miniaturized Systems for Chemistry and Life Sciences :839-841.

Kalecsinsky, V (1902). "Uber die ungarischen warmen und heissen Kochalzseen als naturliche Warmeaccumulatoren." Ann. Physik 7: 408.

Kannan, S., Dewsbury, J and Lane, S.G. (2014). " A simple heat and mass transfer model for salt gradient solar ponds." World Academy of Science Int. J. of Mech. Ind. And Mecha. Eng. 8: 27-33.

Kapur,J (1984). " Surya, maker of the seasons, giver of life, Lord of planets." SunWorld 8: 2–4.

Kim, H., Kaviany, M., Thomas, J.C., Vander Ven, A., Uher, C. and Huang, B. (2010). "Structural order–disorder transitions and phonon conductivity of partially filled skutterudites." Phys. Rev. Lett. 26:265901.

Kirk, J.T.O. (1980) " Light and photosynthesis in aquatic ecosystem." Cambridge University Press, Cambridge.

Kishi, M., Nemoto, H., Hamao, T., Yamamoto, M., Sudou, S., Mandai, M and Yamamoto, S (1999). "" Micro thermoelectric modules and their application to wristwatches as an energy source."" Eighteenth International Conference on Thermoelectrics Proceedings, ICT’99: 301-307, Kraemer, D., Poude, I.B., Feng, H.P., Caylor, J.C., Yu, B. and Yan, X. (2011). "High-performance flat-panel solar thermoelectric generators with high thermal concentration." Nat. Mater. 10:532–538.

Kumar, A., Kishore, V.V.N (1999). "Construction and operational experience of a 6000m2 solar pond at Kutch, India. " Solar Energy 65: 237-249.

Leblanc, J., A. Akbarzadeh, J. Andrews, H. Lu and P. Golding (2011). "Heat extraction methods from salinity-gradient solar ponds and introduction of a novel system of heat extraction for improved efficiency." Solar Energy 85(12): 3103-3142.

Lertsatitthanakorn, C (2007). "Electrical performance analysis and economic evaluation of combined biomass cook stove thermoelectric (BITE) generator." Bioresource Technology 98: 1670-1674.

Lesino, G., L. Saravia and D. Galli (1990). "Industrial production of sodium sulfate using solar ponds." Solar Energy 45(4): 215-219.

Liu, C., Chen, P. and Li, K (2014) “A one kW thermoelectric generator for low-temperature geothermal resources.” Proceedings of thirty-ninth Workshop on Geothermal Reservoir Engineering Stanford University, Stanford, California.

Lodhi, M.A.K (1996). "Solar Ponds in a alkaline lake and oil well regions." Energy Conversion and Management 12: 1677-1694.

Lu, H., A. H. P. Swift, H. D. H. Jr. and J. C. Walton (2004). "Advancements in salinity gradient solar pond technology based on sixteen years of operational experience." ASME Journal of Solar Energy Engineering 126(2): 759 - 767.

Malik, N., A. Date, J. Leblanc, A. Akbarzadeh and B. Meehan (2011). "Monitoring and maintaining the water clarity of salinity gradient solar ponds." Solar Energy 85(11): 2987-2996.

Maneewan, S., Kheadri, J., Zeghmati, B., Hirunlabh, J., Eakburanawat, J (2004). "Investigation on generated power of thermoelectric roof solar collector." Renewable Energy 29: 743-752.

Mekhilef, S., Saidur, R and Safari. A (2011). " A review on solar energy use in industries." Renewable and Sustainable Energy Reviews 15: 1777-1790.

Mills, D.R (2001). " Solar thermal electricity." Gordon J (ed.) Solar Energy, the State of the Art, 706pp. Chicago, IL: ISES.

Myre, E. and R. Shaw (2006). The turbidity tube: Simple and accurate measurement of turbidity in the field, Michigan Technological University: 1-17.

Naskar, P.J., Kulkarni, R.S (2011). "Theritical performance prediction of a doesel locomotive based thermoelectric generator." International Conference on Sustainable Energy and Intelligent System (SEISCON) : 695-699.

Natito, H., Kohsaka, Y., Cooke, D. and Arashi, H (1996). "Development of a solar receiver for a high-efficiency thermionic/thermoelectric conversion system."Solar Energy 58:191-195.

Newell, T.A., Cowie, R.G., Cler, G.L. and Gorham, R.S (1987). " The University of Illinois one-half acre salt gradient solar pond." Proc. Am. Sol. Energy Soc : 483.et al 1987p20, n46

Nielsen, C. E. (1975). "Salt gradient for solar ponds for energy utilization." Environment Conservation 2: 289-292.

Nielsen, C.E (1980). " Design and initial opeartion of a 400 m2 solar pond ." Proc. Am. Sec. Int. Sol. Energy Soc: 381.

Nolas, G.S., Sharp, J. and Goldsmid, H.J. (2001). "Thermoelectrics : Basic principles and new materials developments." Springer.

Nuwayhid, R.Y., Hamade, R (2005). "Design testing of a locally made loop-type thermosyphon heat sink for stove-top thermoelectric generators." Renewable Energy 30: 1101-1116.

Post, F.J., Borowitzka, L.J., Borowitzka, M.J., Mackay, B. and Moulton, T (1983). "The protozoa of western Australian hypersaline lagoon." Hydrobiologia 95.

Rabl, A. and Nielsen, C.E. (1975). " Solar Ponds for space heating." Solar Energy 19: 321.

Reid, R.L., Swift, A.H.P., Boegli, W.J., Castaneda, B.A. and Kane, V.R (1986). " Design construction and initial opeartion of 3355m2 solar pond in El Paso." Proc. ASME Sol. Energy Div. Conf. 304.

Remeli, M.F., Date, A., Singh, B., Tan, L and Akbarzadeh, A. (2014). "" Power Generation and Heat Recovery Using Heat Pipe Thermoelectric Generator (HPTEG)."" Proceedings of the 52nd Annual Conference, Australian Solar Energy Society (Australian Solar Council)"

Riffat, S.B. and Ma, X. (2003). " Thermoelectrics : A review of present and potential applications." Applied Thermal Engineering 23: 913-935.

Rinalde, G.F., Juanico, L.E., Taglialavore, E., Gortari, S., Molina, M.G (2010). "Development of thermoelectric generators for electrification of isolated rural homes." Hydrogen Energy 35: 5818-5822.

Robinson, N (1956). " Solar machines." Proceedings of the World Symposium on Applied Solar Energy :43–46.

Romdhane, M., Gourdon, C. and Casamatta, G (1995). "Development of a thermoelectric sensor for ultrasonic intensity measurement." Ultrasonics 33: 139-146.

Rothmeyer, M. (1980). " The soret effect and salt gradient solar ponds." Solar Energy 25:567.

Rowe, D.M. (1995)."CRC handbook of thermoelectrics." CRC Press.

Sark, W.G.J.H.M (2011). "Feasibility of photovoltaic – Thermoelectric hybrid modules." Applied Energy 88 :2785-2790.

Schladow, S. G. (1984). "The upper mixed zone of a salt gradient solar pond: Its dynamics, prediction and control." Solar Energy 33(5): 417-426.

Schnitzer, M. (1978). " Humic substances: chemistry and reactions." Soil Mechanics, S.U. Eds. Elsevier.

Schot, J. (1973) " Sur la mesure des coefficient de Soret par la methode thermogravitationnell." C.R.Acad.Sc.Paris. Ser.C.

Singh, R., S. Tundee and A. Akbarzadeh (2011). "Electric power generation from solar ponds using combined thermosyphon and thermoelectric modules." Solar Energy 85: 371-378.

Smith, R.C. and Baker, K.S. (1981). "Optical properties of the clearest natural waters (200-800nm)." Appl. Opt. 20:177.

Snyder, G.J. (2008). "Small thermoelectric generators." Electrochem. Soc. Interface 17: 54-56

Stachowiak, H. and Lassue, S. (1998). “A thermoelectric sensor for fluid flow measurement. Principles, calibration and solution for self temperature compensation.” Flow, Measurement and Instrumentation 9:135-141.

Stewart, W.D.P. and Pearson, H.W. (1970) "Effects of aerobic and anaerobic conditions on the growth and metabolism of blue green algae." Proc. Royal. Soc.B.

Swift, A. H. P., R. L. Reid, M. P. Sewell and W. J. Boegli (1987). Operational Result for 3355 m2 Solar Pond in El Paso, Texas. Solar Engineering, American Society of Mechanical Engineers. 1: 287-293.

Tabor, H. (1963). "Large area solar collector for power production." Solar Energy 7(4): 189-194.

Tabor, H. and Z. Weinberger (1981). "Non Convecting Solar Ponds." Solar Energy Handbook. J. F. Kreider and F. Kreith. New York, McGraw Hill.

Tabor, H. Z. and B. Doron (1990). "The Beith Ha'arava 5MW(e) Solar Pond Power Plant (SPPP) - Progress Report." Solar Energy 45(4): 247-253.

Tackaert, W.S., (1993). The Use of Brine Shrimps Artemia in Biological Management of Solar Salt Works in Seventh Symposium on Salt.

Tundee, S., P. Terdtoon, P. Sakulchangsatjatai, R. Singh and A. Akbarzadeh (2010). "Heat extraction from salinity-gradient solar ponds using heat pipe heat exchangers." Solar Energy 84: 1706-1716

US Energy Information Administration 2011, online document viewed 2nd January 2013 <URL:http://www.eia.gov/>

Vancauwenberghe, O., Short, J., Giehler, E., Bildstein, P., Ancey, P. and Gschwind. M (1996). "Microsensor for the preventive detection of water condensation: operating principle and interface electronics." Sensors and Actuators A. Physical 53: 304-308.

Vedernikov, M.V., Iordanishvili, E.K. (1998). " A.F. Ioffe and origin of modern semiconductor thermoelectric energy conversion." 17th International Conference on Thermoelectrics : 37-42.

Vijay, D., Mansoor, A., Soma, S.S.R.D., Robert C.G., Douglas, N, Craig, N (2013). "Solar energy:Trends and enabling technologies." Renewable and Sustainable Energy Reviews 19: 555-564.

Walsch, G.E. (1972) "Effects of herbicides on photosynthesis and growth of marine unicellular algae." J. Haycinth. Control.

World Energy Outlook 2012, online document viewed 25th June 2013 <URL:www.worldenergyoutlook.org/publications/weo-2012/>

www.bom.gov.au (2013). Bureau of Meteorology, Australia.

http://www.worldenergyoutlook.org/

Xi, H., Luo, L. and Fraisse, G. (2007) ""Development and applications of solar-based thermo-electric technologies."" Renewable and Sustainable Energy Review 11:923–936.

Xu, H., J. Sandoval, H. Lu, A. Ybarra, P. Golding and A. Swift (1993). "Operating Experience with the El Paso Solar Pond." Proceeding of the3rd International Conference on Progress in Solar Ponds.

Yaakob, Y. (2014). “An Innovative Approach to Heat Extraction from a Salinity Gradient Solar Pond to Enhance Overall Efficiency.” PhD Thesis, RMIT University.

Yaakob, Y., A. Date and A. Akbarzadeh (2011). Heat extraction from gradient layer using external heat exchangers to enhance the overall efficiency of solar ponds. IEEE First Conference on Clean Energy and Technology (CET)

Yodovard, P., Khedari, J. and Hirunlabh, J (2001) "The potential of waste heat thermoelectric power generation from diesel cycle and gas turbine cogeneration plants." Energy Sources 23:213-224.

Zangrando, F. (1979). Observation and Analysis of a Full Scale Experimental Salt Gradient Solar Pond. PhD, New Mexico.

Zangrando, F. (1980). "A simple method to establish salt gradient solar ponds." Solar Energy 25: 467-470.

Appendix A

Description: Meteorology data

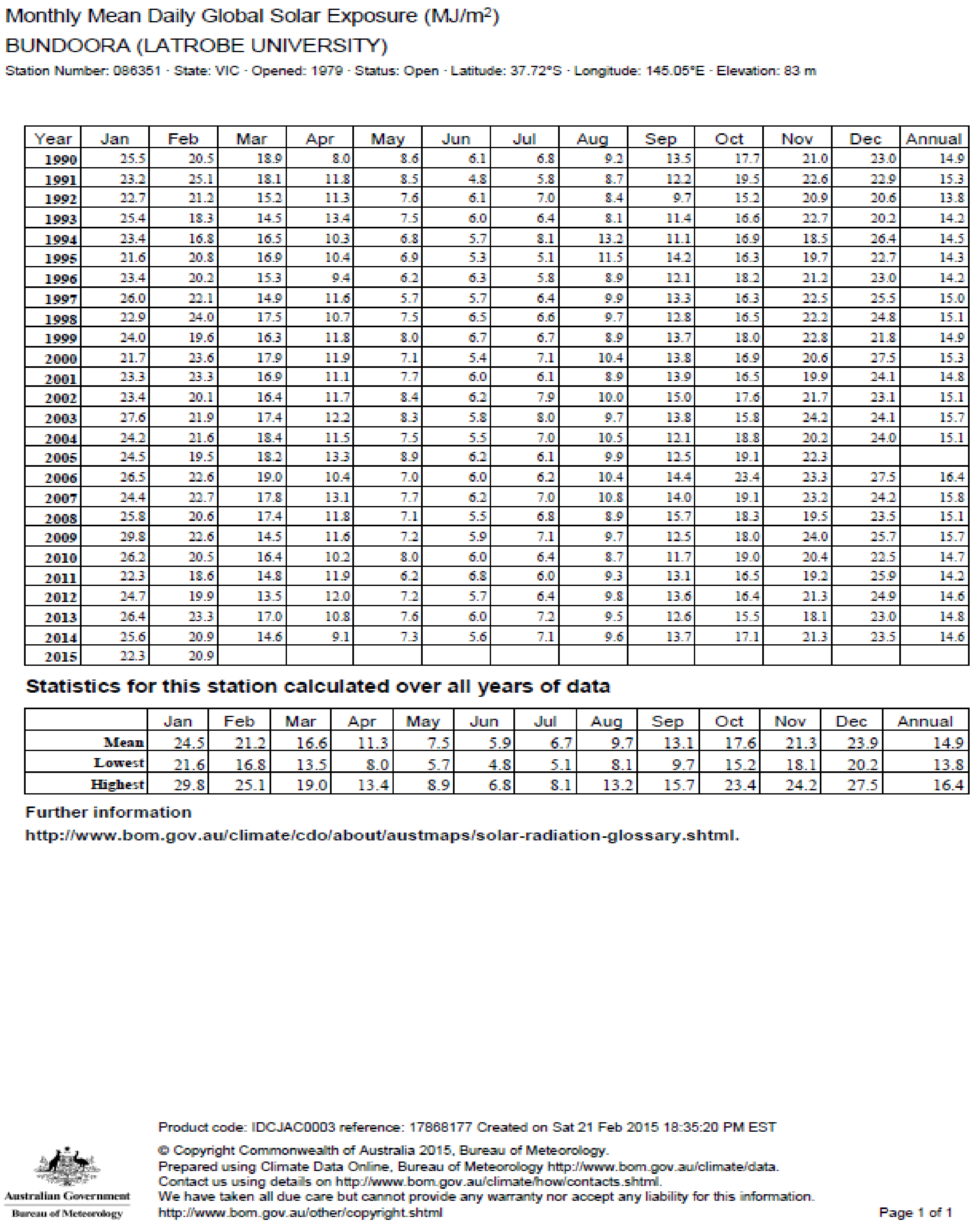

Monthly Mean Daily Global Solar Exposure (MJ/m^2)

BUNDOORA (LATROBE UNIVERSITY)

Station Number: 086351 · State: VIC · Opened: 1979 · Status: Open · Latitude: 37.72°S · Longitude: 145.05°E · Elevation: 83 m

Year	Jan	Feb	Mar	Apr	May	Jun	Jul	Aug	Sep	Oct	Nov	Dec	Annual
1990	25.5	20.5	18.9	8.0	8.6	6.1	6.8	9.2	13.5	17.7	21.0	23.0	14.9
1991	23.2	25.1	18.1	11.8	8.5	4.8	5.8	8.7	12.2	19.5	22.6	22.9	15.3
1992	22.7	21.2	15.2	11.3	7.6	6.1	7.0	8.4	9.7	15.2	20.9	20.6	13.8
1993	25.4	18.3	14.5	13.4	7.5	6.0	6.4	8.1	11.4	16.6	22.7	20.2	14.2
1994	23.4	16.8	16.5	10.3	6.8	5.7	8.1	13.2	11.1	16.9	18.5	26.4	14.5
1995	21.6	20.8	16.9	10.4	6.9	5.3	5.1	11.5	14.2	16.3	19.7	22.7	14.3
1996	23.4	20.2	15.3	9.4	6.2	6.3	5.8	8.9	12.1	18.2	21.2	23.0	14.2
1997	26.0	22.1	14.9	11.6	5.7	5.7	6.4	9.9	13.3	16.3	22.5	25.5	15.0
1998	22.9	24.0	17.5	10.7	7.5	6.5	6.6	9.7	12.8	16.5	22.2	24.8	15.1
1999	24.0	19.6	16.3	11.8	8.0	6.7	6.7	8.9	13.7	18.0	22.8	21.8	14.9
2000	21.7	23.6	17.9	11.9	7.1	5.4	7.1	10.4	13.8	16.9	20.6	27.5	15.3
2001	23.3	23.3	16.9	11.1	7.7	6.0	6.1	8.9	13.9	16.5	19.9	24.1	14.8
2002	23.4	20.1	16.4	11.7	8.4	6.2	7.9	10.0	15.0	17.6	21.7	23.1	15.1
2003	27.6	21.9	17.4	12.2	8.3	5.8	8.0	9.7	13.8	15.8	24.2	24.1	15.7
2004	24.2	21.6	18.4	11.5	7.5	5.5	7.0	10.5	12.1	18.8	20.2	24.0	15.1
2005	24.5	19.5	18.2	13.3	8.9	6.2	6.1	9.9	12.5	19.1	22.3		
2006	26.5	22.6	19.0	10.4	7.0	6.0	6.2	10.4	14.4	23.4	23.3	27.5	16.4
2007	24.4	22.7	17.8	13.1	7.7	6.2	7.0	10.8	14.0	19.1	23.2	24.2	15.8
2008	25.8	20.6	17.4	11.8	7.1	5.5	6.8	8.9	15.7	18.3	19.5	23.5	15.1
2009	29.8	22.6	14.5	11.6	7.2	5.9	7.1	9.7	12.5	18.0	24.0	25.7	15.7
2010	26.2	20.5	16.4	10.2	8.0	6.0	6.4	8.7	11.7	19.0	20.4	22.5	14.7
2011	22.3	18.6	14.8	11.9	6.2	6.8	6.0	9.3	13.1	16.5	19.2	25.9	14.2
2012	24.7	19.9	13.5	12.0	7.2	5.7	6.4	9.8	13.6	16.4	21.3	24.9	14.6
2013	26.4	23.3	17.0	10.8	7.6	6.0	7.2	9.5	12.6	15.5	18.1	23.0	14.8
2014	25.6	20.9	14.6	9.1	7.3	5.6	7.1	9.6	13.7	17.1	21.3	23.5	14.6
2015	22.3	20.9											

Statistics for this station calculated over all years of data

	Jan	Feb	Mar	Apr	May	Jun	Jul	Aug	Sep	Oct	Nov	Dec	Annual
Mean	24.5	21.2	16.6	11.3	7.5	5.9	6.7	9.7	13.1	17.6	21.3	23.9	14.9
Lowest	21.6	16.8	13.5	8.0	5.7	4.8	5.1	8.1	9.7	15.2	18.1	20.2	13.8
Highest	29.8	25.1	19.0	13.4	8.9	6.8	8.1	13.2	15.7	23.4	24.2	27.5	16.4

Further information

http://www.bom.gov.au/climate/cdo/about/austmaps/solar-radiation-glossary.shtml.

Australian Government
Bureau of Meteorology

Product code: IDCJAC0003 reference: 17868177 Created on Sat 21 Feb 2015 18:35:20 PM EST

Prepared using Climate Data Online, Bureau of Meteorology http://www.bom.gov.au/climate/data.
Contact us using details on http://www.bom.gov.au/climate/how/contacts.shtml.

Page 1 of 1

Appendix B

Description: TEG data sheet

Beijing Huimao Cooling Equipment Co.,Ltd
TEC1-12710T125 Specification
Hot side temperature is 25 C,
Imax(最大电流)： 10A，
Umax（最大电压）: 15.2V
Qmax(最大产冷量)：105.8W
Delta T max（最大温差)： 67 C
ACR（交流电阻)：1.08 to 1.13 Ohm
Size (尺寸) ： 40x40x3.2mm

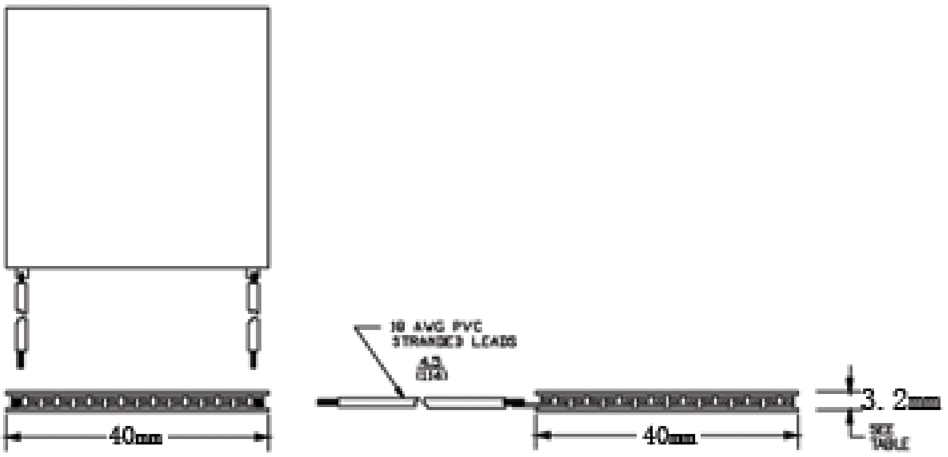

Ceramic Material: Alumina (97% Al_2O_3, 3% Strontiumcarbonate,nanometre)
Solder Construction: 138ºC, (99.3% Sn , 0.7% Cu)

Operation Tips:

- Max Operating Temperature: 125 ºC
- Do not exceed Imax or Vmax when operating module.
- Please consult Beijing Huimao Cooling Equipment Co.,Ltd modules for moisture and corrosion protection options.
- Solder tinning also available on metallized ceramics

Appendix C

Description: In-pond square channel heat exchanger drawing

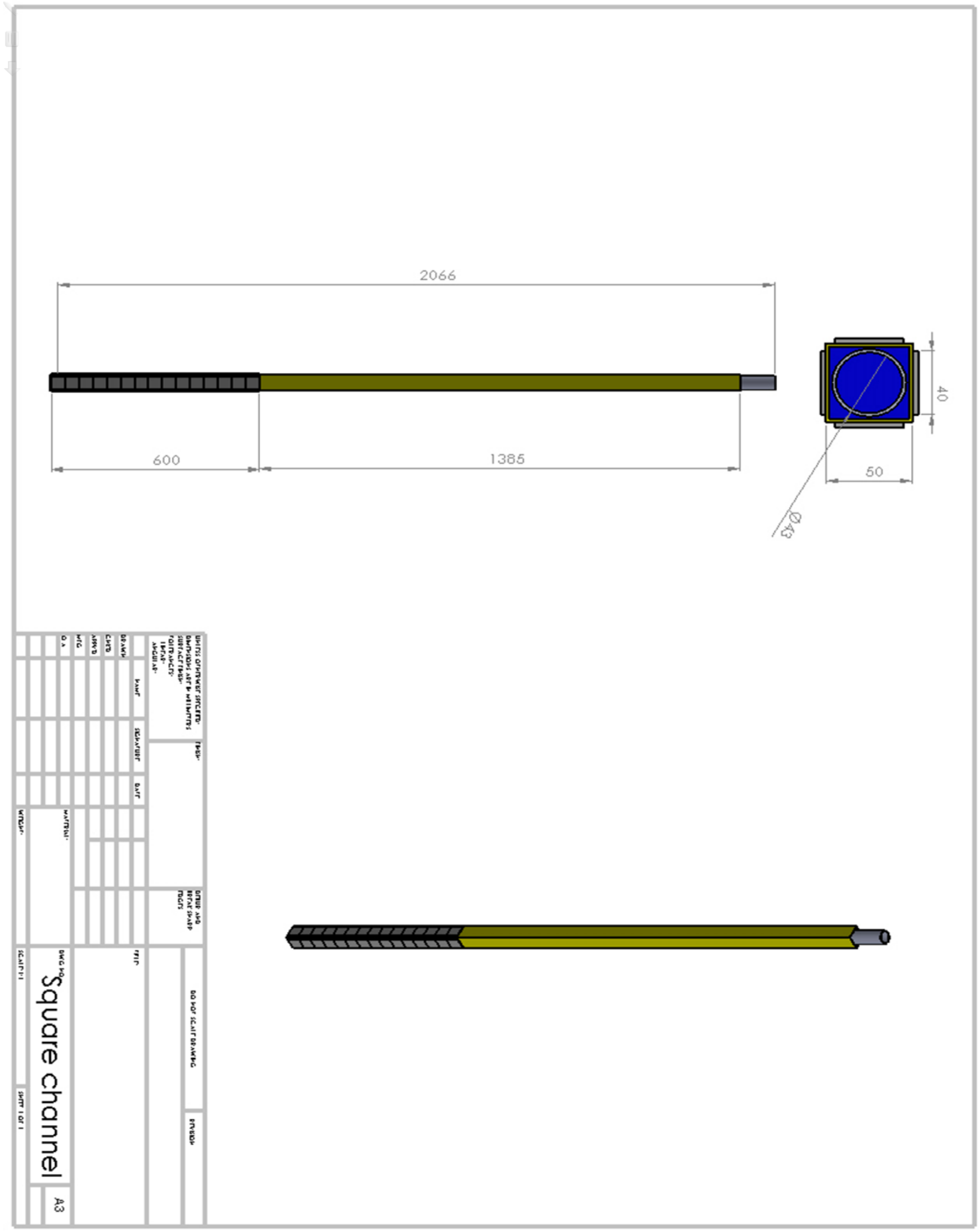

Appendix D

Description: In-pond polygon channel heat exchanger drawing

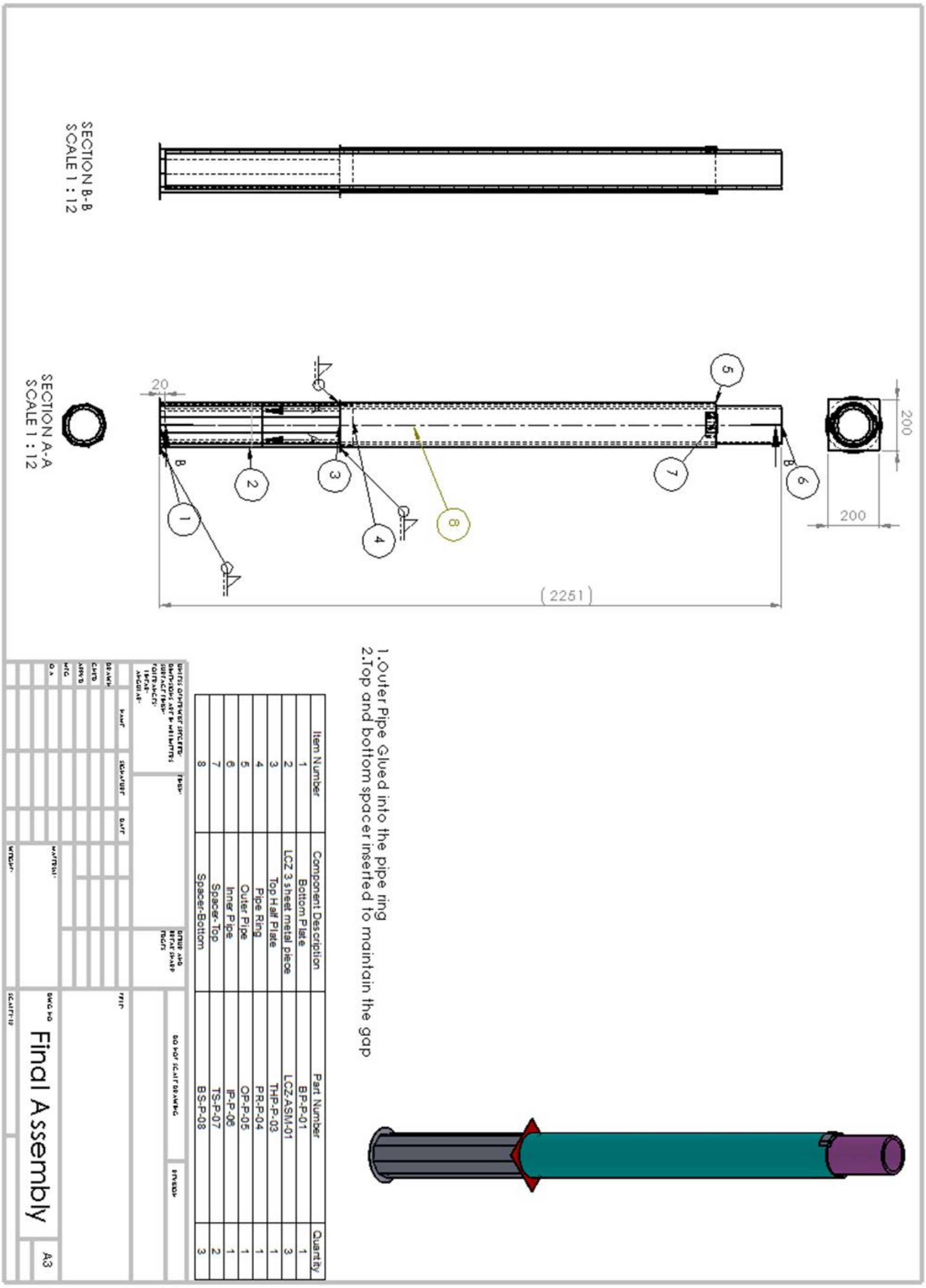

1.Outer Pipe Glued into the pipe ring
2.Top and bottom spacer inserted to maintain the gap

Item Number	Component Description	Part Number	Quantity
1	Bottom Plate	BP-P-01	1
2	LCZ 3 sheet metal piece	LCZ-ASM-01	3
3	Top Half Plate	THP-P-03	1
4	Pipe Ring	PR-P-04	1
5	Outer Pipe	OP-P-05	1
6	Inner Pipe	IP-P-06	1
7	Spacer-Top	TS-P-07	2
8	Spacer-Bottom	BS-P-08	3

Appendix E

Description: Acrylic end plate drawing

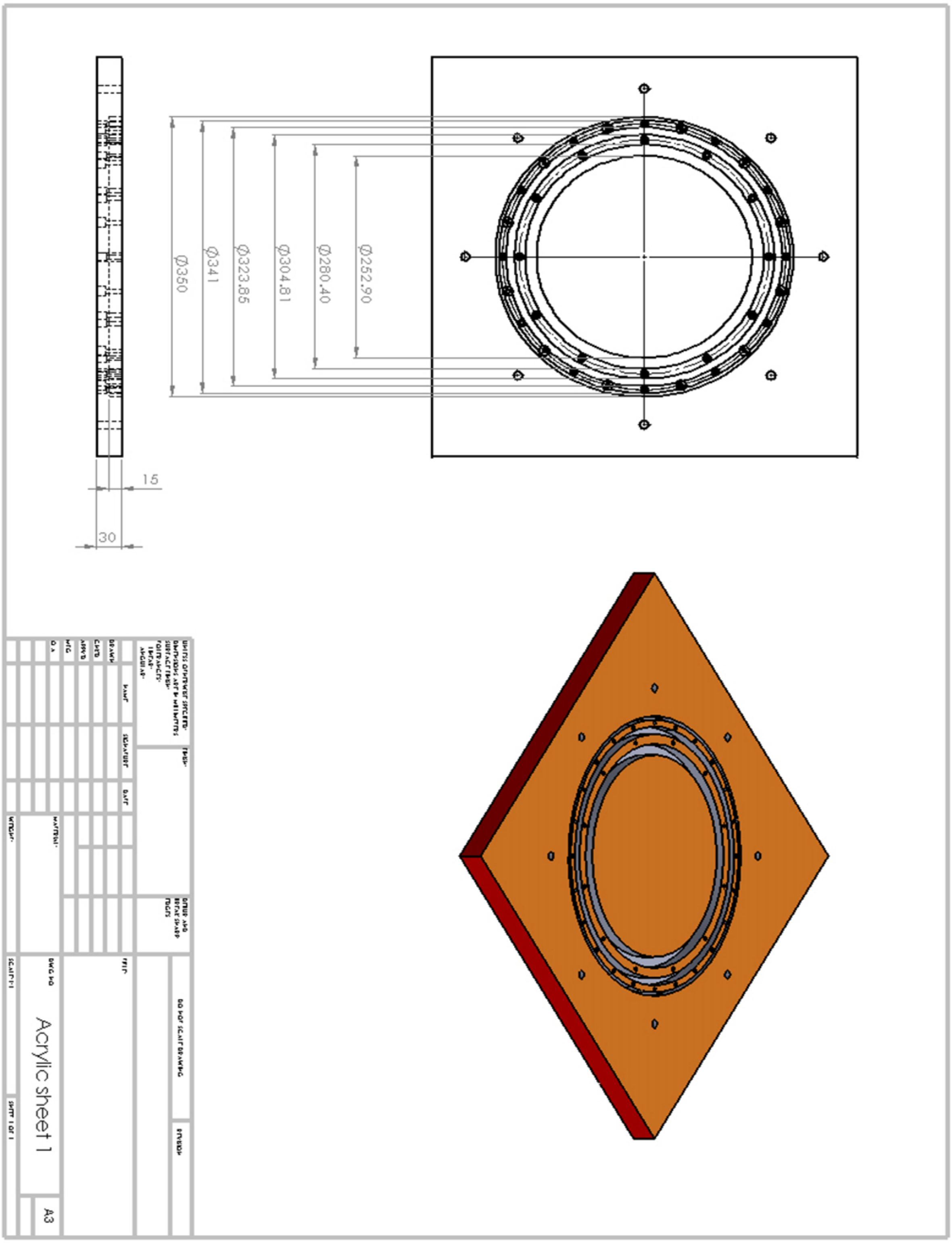

Appendix F

Description: Polygon TEG heat exchanger

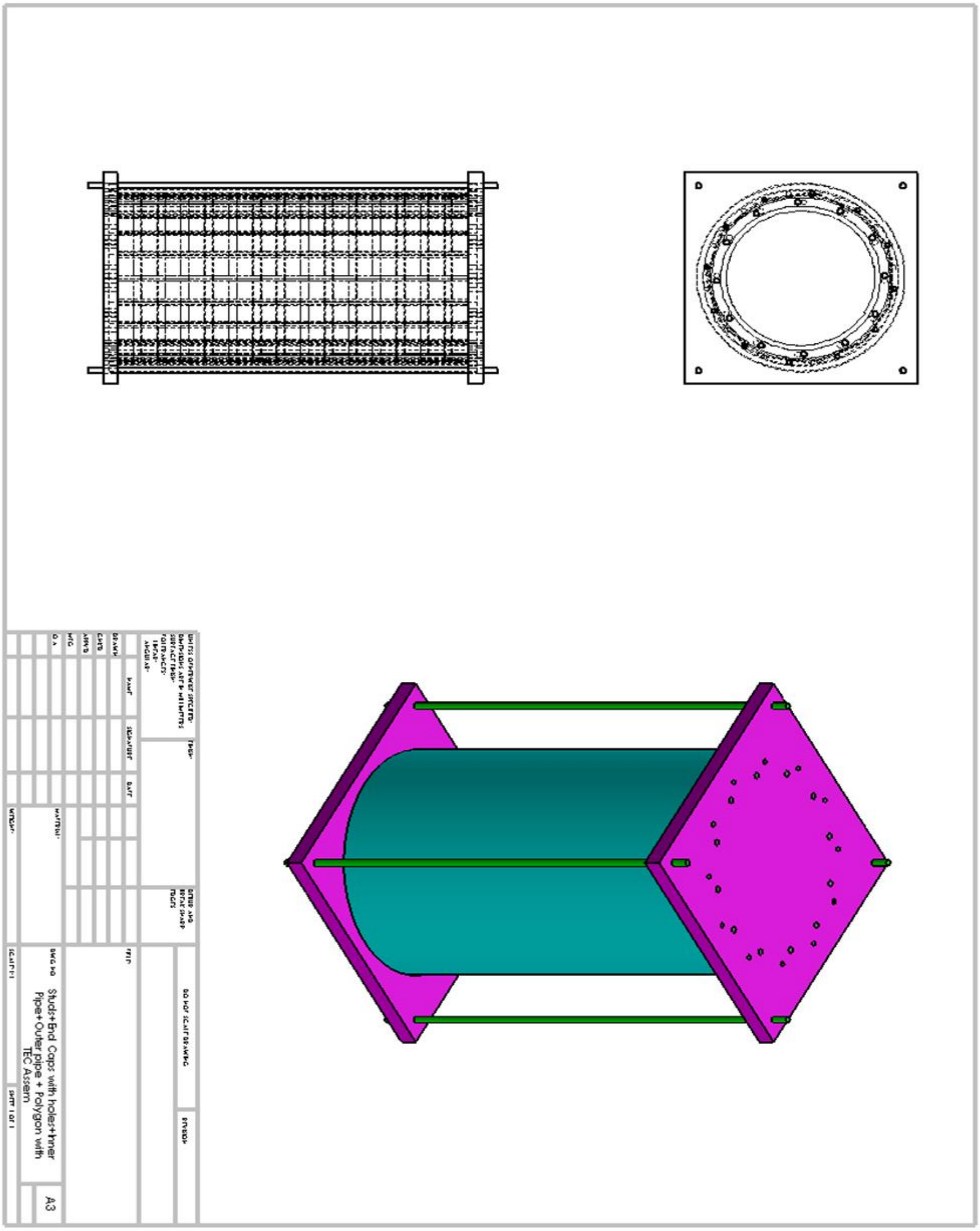

Appendix G

Description: 12 V DC pump information

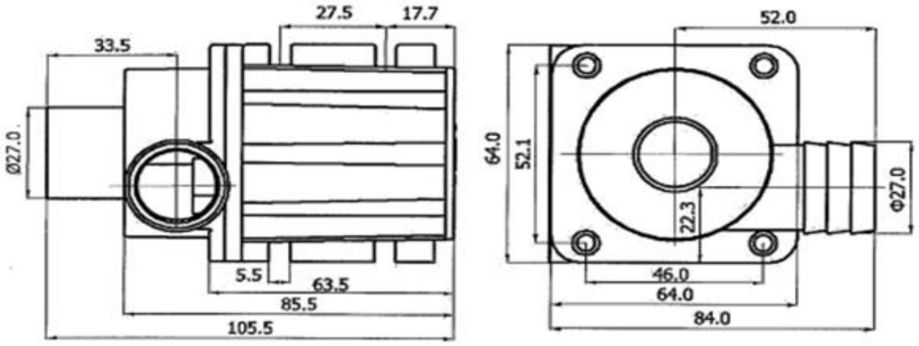

※DC50A Series:

We have a wide range of water pumps with different specifications, please find the following list of all DC50A Series for your reference:

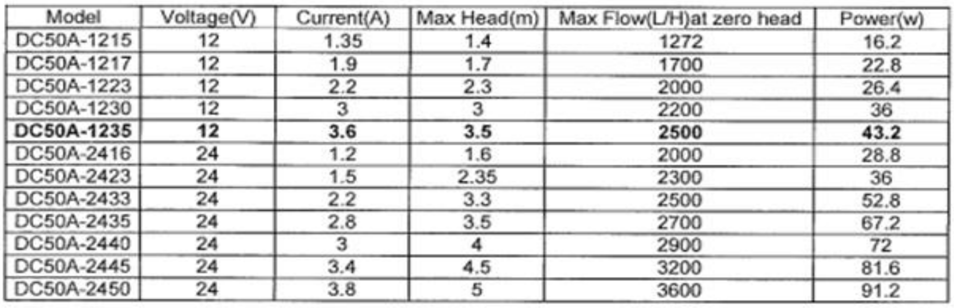

Model	Voltage(V)	Current(A)	Max Head(m)	Max Flow(L/H)at zero head	Power(w)
DC50A-1215	12	1.35	1.4	1272	16.2
DC50A-1217	12	1.9	1.7	1700	22.8
DC50A-1223	12	2.2	2.3	2000	26.4
DC50A-1230	12	3	3	2200	36
DC50A-1235	**12**	**3.6**	**3.5**	**2500**	**43.2**
DC50A-2416	24	1.2	1.6	2000	28.8
DC50A-2423	24	1.5	2.35	2300	36
DC50A-2433	24	2.2	3.3	2500	52.8
DC50A-2435	24	2.8	3.5	2700	67.2
DC50A-2440	24	3	4	2900	72
DC50A-2445	24	3.4	4.5	3200	81.6
DC50A-2450	24	3.8	5	3600	91.2

Note: Maximum liquid temperature: 100°C, 212F

Head-Flow Curve Graph:

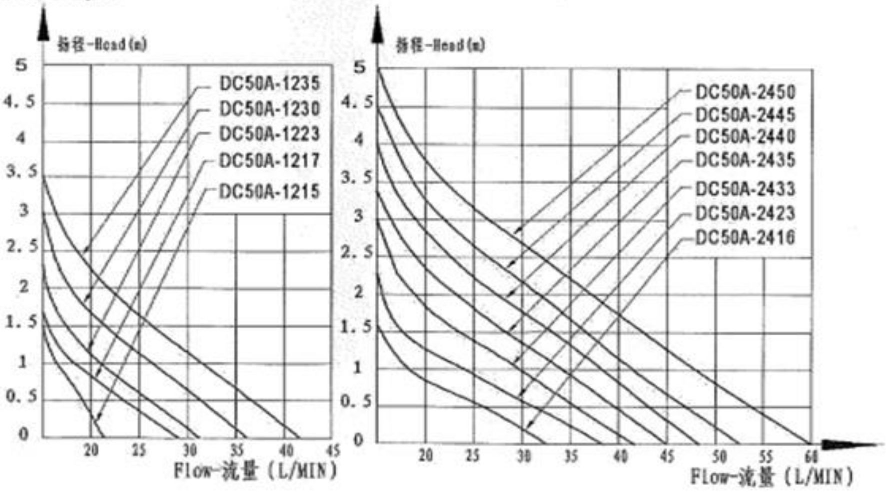

Appendix H

Description: Uncertainty calculation for single TEG testing

Table H1: Experimental uncertainty for single TEG with 20 W power input

Parameter	**1st Measurement**	**2nd Measurement**	**3rd Measurement**	**Mean**	**Standard Deviation**	**Uncertainty (%)**
T_{hot} (˚C)	45.6	46.3	45.0	45.6	0.65064	1.43
T_{cold} (˚C)	29.0	29.8	28.7	29.2	0.56862	1.95
V_{ocv} (V)	0.932	0.965	0.983	0.960	0.02570	2.68
I_{sc} (A)	0.435	0.452	0.433	0.440	0.01034	2.35
V_{mpp} (V)	0.342	0.339	0.340	0.340	0.00141	0.42
I_{mpp} (A)	0.277	0.279	0.270	0.275	0.00475	1.72

Table H2: Experimental uncertainty for single TEG with 40 W power input

Parameter	**1st Measurement**	**2nd Measurement**	**3rd Measurement**	**Mean**	**Standard Deviation**	**Uncertainty (%)**
T_{hot} (˚C)	67.5	68.3	67.0	67.6	0.65737	0.97
T_{cold} (˚C)	33.8	34.0	34.6	34.1	0.40452	1.18
V_{ocv} (V)	1.896	1.905	1.991	1.931	0.05243	2.72
I_{sc} (A)	0.857	0.911	0.909	0.892	0.03058	3.43
V_{mpp} (V)	0.854	0.844	0.869	0.856	0.01258	1.47
I_{mpp} (A)	0.421	0.447	0.432	0.433	0.01303	3.01

Table H3: Experimental uncertainty for single TEG with 60 W power input

Parameter	**1st Measurement**	**2nd Measurement**	**3rd Measurement**	**Mean**	**Standard Deviation**	**Uncertainty (%)**
T_{hot} (˚C)	86.9	87.2	86.5	86.9	0.35119	0.40
T_{cold} (˚C)	38.8	39.8	39.0	39.2	0.54455	1.39
V_{ocv} (V)	2.799	2.807	2.901	2.836	0.05672	2.00
I_{sc} (A)	0.857	0.864	0.875	0.865	0.00904	1.04
V_{mpp} (V)	1.203	1.224	1.208	1.212	0.01096	0.90
I_{mpp} (A)	0.623	0.651	0.649	0.641	0.01565	2.44

Table H4: Experimental uncertainty for single TEG with 80 W power input

Parameter	**1st Measurement**	**2nd Measurement**	**3rd Measurement**	**Mean**	**Standard Deviation**	**Uncertainty (%)**
T_{hot} (˚C)	103.2	100.3	104.0	102.5	1.95042	1.90
T_{cold} (˚C)	43.7	43.4	44.0	43.7	0.30000	0.69
V_{ocv} (V)	3.501	3.565	3.551	3.539	0.03365	0.95
I_{sc} (A)	1.385	1.490	1.404	1.426	0.05595	3.92
V_{mpp} (V)	1.688	1.732	1.771	1.730	0.04165	2.41
I_{mpp} (A)	0.693	0.688	0.720	0.700	0.01721	2.46

Table H5: Experimental uncertainty for single TEG with 100 W power input

Parameter	**1st Measurement**	**2nd Measurement**	**3rd Measurement**	**Mean**	**Standard Deviation**	**Uncertainty (%)**
T_{hot} (˚C)	123.1	121.2	122.0	122.1	0.93302	0.76
T_{cold} (˚C)	49.9	51.3	50.9	50.7	0.74333	1.47
V_{ocv} (V)	4.552	4.611	4.587	4.583	0.02961	0.65
I_{sc} (A)	1.676	1.600	1.688	1.655	0.04768	2.88
V_{mpp} (V)	1.970	1.998	1.908	1.959	0.04611	2.35
I_{mpp} (A)	0.853	0.833	0.842	0.843	0.01027	1.22

Table H6: Experimental uncertainty for single TEG with 120 W power input

Parameter	**1st Measurement**	**2nd Measurement**	**3rd Measurement**	**Mean**	**Standard Deviation**	**Uncertainty (%)**
T_{hot} (˚C)	135.8	134.9	136.3	135.7	0.70767	0.52
T_{cold} (˚C)	54.1	53.7	54.8	54.2	0.55365	1.02
V_{ocv} (V)	5.324	5.300	5.388	5.337	0.04542	0.85
I_{sc} (A)	2.085	2.093	2.112	2.097	0.01383	0.66
V_{mpp} (V)	2.889	2.798	2.842	2.843	0.04541	1.60
I_{mpp} (A)	0.911	0.928	0.927	0.922	0.00965	1.05

Table H7: Experimental uncertainty for single TEG with 140 W power input

Parameter	**1st Measurement**	**2nd Measurement**	**3rd Measurement**	**Mean**	**Standard Deviation**	**Uncertainty (%)**
T_{hot} (˚C)	145.8	146.2	147.0	146.3	0.61978	0.42
T_{cold} (˚C)	59.2	58.3	59.8	59.1	0.75222	1.27
V_{ocv} (V)	5.880	5.832	5.838	5.850	0.02614	0.45
I_{sc} (A)	2.642	2.749	2.731	2.707	0.05711	2.11
V_{mpp} (V)	2.982	2.877	2.852	2.904	0.06915	2.38
I_{mpp} (A)	1.208	1.249	1.228	1.228	0.02035	1.66

Table H8: Experimental uncertainty for single TEG with 160 W power input

Parameter	**1st Measurement**	**2nd Measurement**	**3rd Measurement**	**Mean**	**Standard Deviation**	**Uncertainty (%)**
T_{hot} (˚C)	158.8	159.1	158.3	158.7	0.40596	0.26
T_{cold} (˚C)	64.3	65.7	64.2	64.7	0.84654	1.31
V_{ocv} (V)	6.255	6.334	6.432	6.340	0.08867	1.40
I_{sc} (A)	2.790	2.767	2.783	2.780	0.01179	0.42
V_{mpp} (V)	3.147	3.238	3.252	3.212	0.05713	1.78
I_{mpp} (A)	1.332	1.313	1.339	1.328	0.01345	1.01